Investigation of the laminar and turbulent combustion behavior in a one-cylinder internal combustion engine

Dissertation
zur Erlangung des Doktorgrades
der Mathematisch-Naturwissenschaftlichen Fakultät
der Christian-Albrechts-Universität zu Kiel
vorgelegt von

Alexander Thrun
Institut für Physikalische Chemie

Kiel 2016

Erster Gutachter: Prof. Dr. Friedrich Temps
Zweiter Gutachter: Prof. Dr. Gernot Friedrichs

Tag der mündlichen Prüfung: 16.09.2016
Zum Druck genehmigt: 16.09.2016

gez. Prof. Dr. Natascha Oppelt, Dekanin

Erklärung

Hiermit erkläre ich, dass die vorliegende Abhandlung - abgesehen von der Beratung durch meinen Betreuer Prof. Dr. Friedrich Temps - nach Inhalt und Form meine eigene Arbeit ist. Diese Arbeit hat weder in Auszügen noch in ganzer Form einer anderen Stelle im Rahmen eines Prüfungsverfahrens vorgelegen. Sie wurde in ihrer Gesamtheit nicht veröffentlicht und auch nicht zur Veröffentlichung eingereicht. Teile dieser Arbeit wurden in einer fachwissenschaftlichen Zeitschrift veröffentlicht. Dies bezieht sich auf die turbulenten Druckmessungen und Teile der LIF und PIV-Messungen.

A. Thrun, F. Temps, J. Bauer, „Investigation of Turbulent Combustion and Flame Extinction in a One-Cylinder Internal Combustion Engine“, *VDI-Berichte* **2015**, *2267*, 723 - 728 (2015).

Die Arbeit ist unter Einhaltung der Regeln guter wissenschaftlicher Praxis der Deutschen Forschungsgemeinschaft entstanden.

Kiel, im Juli 2016

Alexander Thrun

Abstract

This Thesis deals with the analysis of the combustion behavior of a gas-fueled one-cylinder internal combustion engine used in a commercially available nail gun (*BeA Gasnagler*). The main focus was laid on the difference in combustion under laminar and under turbulent conditions, the latter induced by solid obstacles in the chamber or by a small electrical fan located in the top of the cylinder head. Additionally, different fuel compositions, consisting of either propane-air or propene/1-butene-air, were investigated. A major part of the Thesis was the design and setup of the required optical and electronic detection systems as well as the re-design of the engine electronics and housing for their implementation in the experimental detection systems. The combustion process was investigated for pressure-time traces, piston velocity and flame expansion characteristics. For the latter, two detection systems were developed. The whole flame structure was imaged using the flame's chemiluminescence, while the two-dimensional flame could be visualized using the fluorescence of OH radicals around λ = 314 nm probed at λ = 283.01 nm by a laser-induced fluorescence (LIF) system. For the characterization of the fan-induced turbulent flow, a particle image velocimetry (PIV) setup was built. In comparison to laminar conditions, the fan-induced turbulence enhanced the combustion efficiency drastically, as indicated by an increase of the rate of pressure rise in the chamber by a factor of 10 to $(\mathrm{d}p/\mathrm{d}t) \approx 1300$ bar s^{-1}. Turbulent combustion was investigated for flame quenching effects, as a strong decrease of ignition probability of premixed propane-air fuels was found for a fan start Δt_{fan} = -250 ms before ignition, corresponding to a fan speed of $u_{\mathrm{fan}} \approx$ 10,000 rpm and a Reynolds number of $Re \approx$ 40,000. This effect could not be observed for the unsaturated fuel, which was externally injected using pre-filled cartridges. The turbulence intensities of the flow without ignition $u^{'}$ exceed the laminar flame speed u_{l} by a factor of 10, which leads to an increase of the minimum ignition energy. Additionally, a decrease of the integral length scale was found for high turbulence, which suggest that the engine operates at the transition from the wrinkled flame regime towards the well stirred reactor, where the flame can be quenched by turbulence.

Zusammenfassung

Diese Arbeit beschäftigt sich mit der Analyse des Verbrennungsverhaltens eines gasbetriebenen Ein-Zylinder-Verbrennungsmotors, welcher in Nagelpistolen verwendet wird (*BeA Gasnagler*). Das Hauptaugenmerk wurde auf den Unterschied der Verbrennung unter laminaren und unter turbulenten Bedingungen gelegt. Letzere wurden durch das Einrbingen von festen Hindernissen in der Kammer oder durch ein elektrisch betriebenes Flügelblatt, welches sich im oberen Teil des Zylinderkopfs befindet, erzeugt. Zusätzlich wurden unterschiedliche Treibstoffmischungen von Propan in Luft bzw. Propen/1-Buten in Luft untersucht. Ein wichtiger Teil der Arbeit bestand darin, die optischen bzw. elektronischen Detektionssysteme zu entwerfen und aufzubauen, sowie die Ansteuerung und den optischen Zugang zum Motor der Detektion entsprechend zu überarbeiten. Zur Analyse des Verbrennungsprozesses wurde der Druckverlauf in der Kammer, die Kolbengeschwindigkeit und das Ausbreitungsverhalten der Flammenfront untersucht. Die gesamte Flammenstruktur wurde mithilfe eines Chemolumineszenz-Detektionssystems abgebildet, während zweidimensionale Schnitte durch die Flammenstruktur anhand Laser-induzierte Fluoreszenz (LIF) um $\lambda = 314\,\mathrm{nm}$ von OH-Radikalen bei einer Anregungswellenlänge von $\lambda = 283.01\,\mathrm{nm}$ realisiert wurden. Zur Messung des durch das Flügelrad hervorgerufene turbulente Strömungsfeld wurde ein Particle Image Velocimetry-System (PIV) aufgebaut. Im Vergleich zwischen laminarer und turbulenter Verbrennung zeigte sich, dass die Verbrennung unter turbulenten Bedingungen um das zehnfache auf eine Druckanstiegsgeschwindigkeit von $(\mathrm{d}p/\mathrm{d}t) \approx 1300\,\mathrm{bar\,s^{-1}}$ gesteigert wurde. Für zu starke Turbulenzen wurde ein deutlicher Abfall der Zündwahrscheinlichkeit festgestellt. Dies konnte bei Propan-Luft-Zusammensetzungen ab einem Startzeitpunkt des Flügelrads $\Delta t_{\mathrm{fan}} = -250\,\mathrm{ms}$ vor der Zündung beobachtet werden, was einer Umdrehungsgeschwindigkeit von $u_{\mathrm{fan}} \approx 10\,000\,\mathrm{rpm}$ bzw. einer Reynoldszahl von $Re \approx 40\,000$ entspricht. Für den ungesättigten Treibstoff, welcher durch eine Kartusche eingespritzt wurde, konnte dieser Effekt nicht beobachtet werden. Die Turbulenzintensität, welche ohne Zündung ermittelt wurde, übersteigt die laminare Flammengeschwindigkeit um das Zehnfache und führt somit zu einem starken Anstieg der Mindestzündenergie. Zusätzlich konnte gezeigt werden, dass die Turbulenzlängenskala mit zunehmender Turbulenz sinkt. Dies führt dazu, dass während der Verbrennung ein Übergang vom Bereich der getrennten Reaktionszonen zum homogenen Reaktor stattfindet, was somit ein Erlöschen der Flamme zur Folge haben kann.

Contents

Introduction

1

Finding a sufficient and sustainable supply of energy is one of the biggest challenges of the 21st century. According to the U.S. Energy Information Administration, the world energy consumption increased from 512 EJ to 553 EJ between 2008 and 2012, which is attributed to the growth of economy and population.[1] Due to the limited supply of fossil fuels and the demand for the reduction of greenhouse gases (GHGs), especially CO_2, the attention has shifted significantly towards renewable sources, e.g., wind power, hydro power and solar energy. In 2015, 30% of the electricity generated in Germany arose from renewable sources, second only to the electricity generated by coal-fired power plants that accounted for 42.2% (see Fig. 1.1a). This picture changes drastically for the total amount of consumed energy. As shown in Figure 1.1b, fossil fuels made up the major share of energy sources in Germany. The combustion of fuels such as oil, gas and coal were responsible for 79.5% of the energy consumed in 2015, while renewable sources formed only a minor part (12.5%).[2] To reduce the amount of GHG emission, the European Commission

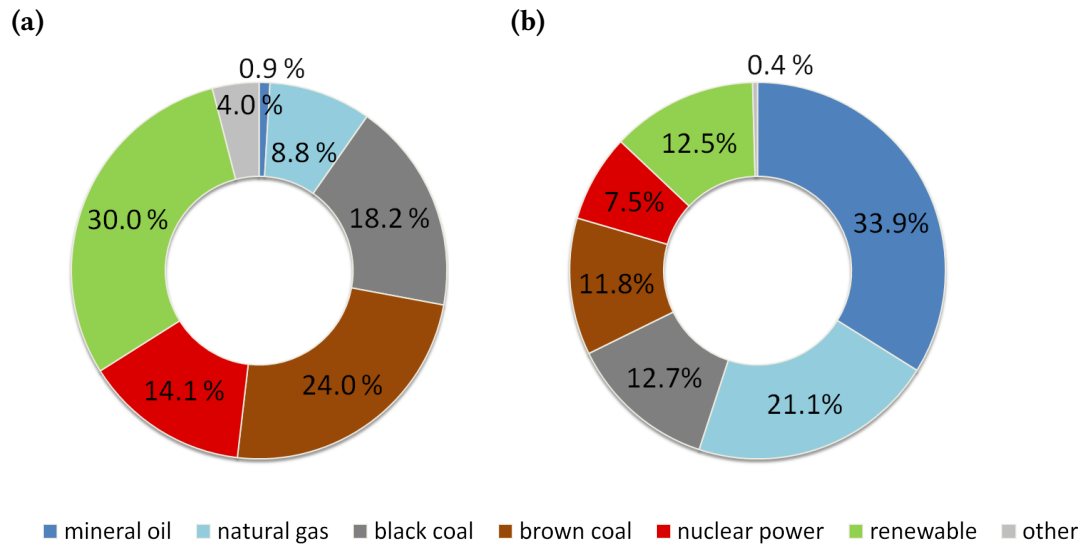

Figure 1.1: (**a**) Primary sources of electricity generation and (**b**) energy consumption in Germany, 2015.[2]

created a roadmap that suggested decreasing the carbon emission to 80% below the levels of 1990 by 2050.[3] In 2013, fuel combustion processes and fugitive emissions from fuels were responsible for 79% of the GHG emission in Europe. Of these 79%, 25% are due to the sector of road transportation, which can be split into light-duty vehicles (LDVs) such as cars and vans, and heavy-duty vehicles (HDVs), e.g., trucks, tractors, coaches and buses.[4–6]

The fuel efficiency, and thus the carbon footprint for LDVs, improved significantly over the course of 15 years. According to the German Federal Motor Vehicle Office, the average amount of fuel consumed by Diesel and gasoline vehicles dropped from 8 L/100 km in 1998 below 6 L/100 km in 2013.[7] Part of this accomplishment can be attributed to the so-called engine downsizing. The principle of engine downsizing is the reduction of engine capacity and weight without loss of power compared to larger engines. The use of boosting devices, e.g., turbochargers, and improved injection technologies enhanced the efficiency and reduced carbon emissions.[8] Downsized engines (Ford EcoBoost 1.0l, VW 1.4l TSI, Fiat Twin-Air 875cc) can be found in an abundance of mid-sized cars. Despite the evident advantages, improved efficiency can often be achieved only for partial-load operations, while under full load the fuel efficiency may increase.[9] For Diesel engines, the downsizing often leads to an increase in combustion temperature and thus formation of NO_x. In recent years, engines of car manufacturers like Opel and Volkswagen revealed the use of so-called defeat devices to match the NO_x emissions permitted by law,[10,11] while Mitsubishi used a fuel consumption test that differed from the Japanese standards to improve their alleged fuel efficiency.[12]

Despite the trend of increasing sales numbers of hybrid and electric cars, the demand for combustion based vehicles is still high. Cars propelled by electric motors offer higher efficiency compared to gasoline and Diesel engines, but suffer from the increased weight of the equipped rechargeable batteries, low availability of recharging stations and long refueling times. The latter especially becomes important in fields of application with demand for quasi-nonstop operation, such as HDVs used for public transportation or construction equipment, where Diesel engines are still the most common engines due to their high fuel-efficiency.[13,14]

Another, albeit less influential, sector of GHG emissions arises from the widespread use of so-called power tools, which includes all tools that are actuated by a power source other than manual labor. While power tools, e.g., chainsaws, lawn mowers, leaf blowers, string trimmers or nail guns are often powered by electric motors, the use of combustion-driven tools offers significant advantages under certain conditions. Comparable to HDVs, easy access to fuel in combination with quick refueling makes them ideally suited for outdoor use and the cordless operation offers a high freedom of movement. This mobility is also influenced by the size and weight of the tool and thus requires high performance from engines as small as possible.

The nail gun investigated in this Thesis is shown in Figure 1.2 and was provided by *BeA fastening systems Germany*. Combustion-driven nail guns use compressed gas such as propane, butene or mixtures of propene/1-butene. The compressed gas is injected into the combustion chamber prior to ignition and then mixed with the

available fresh air using a small fan connected to an electric motor, which is located in the cylinder head. The fan also acts as agitator to enhance the combustion by turbulence. After spark ignition, the piston is pushed down by the gas expansion and drives a nail. Afterwards, the piston moves up again and a valve is opened, through which the exhaust gases can be released. Simultaneously, the chamber is filled with fresh air from the surrounding.

One of the first patents for gas-fueled nail guns was applied for in 1981.[15] Since then, this patent was referenced in more than 300 additional worldwide patents, covering the ongoing development of this power tool, e.g. fan placement, fuel composition, chamber geometry or safety measures.[16]

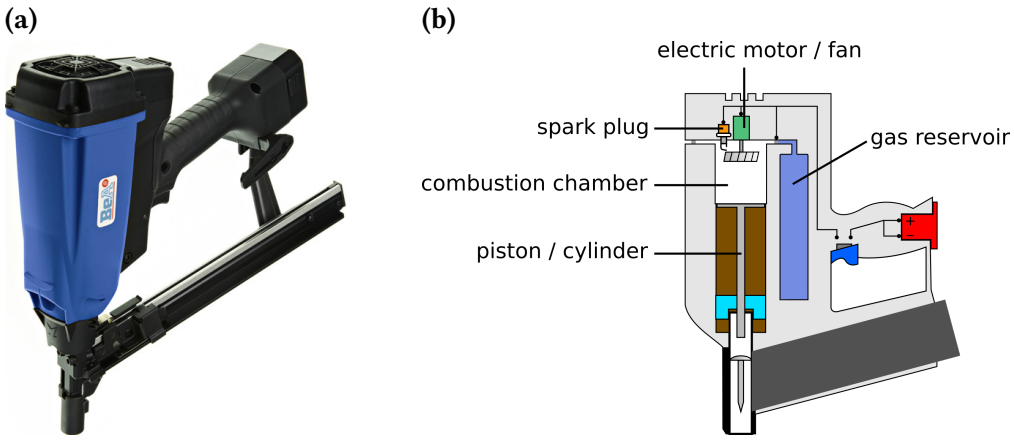

Figure 1.2: (**a**) Commercially available nail gun by the BeA company.[17] (**b**) Schematic drawing of the combustion-fueled nail gun.

The present Thesis describes the basic investigations of the fundamental combustion processes inside the nail gun engine shown in Figure 1.2a. For a better understanding, the basic physical, chemical and fluid dynamical concepts of these processes will also be explained. Experimental emphasis is put on the investigation of the premixed combustion of gaseous hydrocarbon fuels under laminar and turbulent conditions. Turbulent conditions are induced by using (*i*) stationary obstacles in form of grids or the fan in the combustion chamber and (*ii*) the rotation of the fan located in the cylinder head. Therefore, the Thesis is divided into three main parts: In Chapter 2, the theoretical background of combustion processes and their study using two selected laser-based detection techniques – laser-induced fluorescence (LIF) and particle image velocimetry (PIV) – is explained.

Chapter 3 presents the technical modifications of the combustion engine shown in Figure 1.2 and their implementation into the experimental detection systems. A major part of this Chapter explains the set-up of the LIF and PIV units and their key parameters for the successful investigation of interactions between flame front and surrounding fluid.

In Chapter 4, the data for the combustion behavior under laminar and turbulent conditions are presented. Integral parts of this Chapter cover the interpretation of pressure-time traces and flame expansion during the combustion and the influence of turbulence characteristics on the combustion behavior.

Theoretical Background

2

2.1 Fundamental combustion phenomena

To qualitatively and quantitatively understand combustion several fundamental concepts of different combustion processes were developed over the last 100 years. This Section will give an overview over the basic concepts of combustion, both for laminar and turbulent conditions.

Combustion phenomena arise from the interaction of physical properties of the flow with the chemical processes.[18–24] While combustion starts with the occurrence of a self-supporting exothermic reaction, the transport of matter, energy and thus the flame front itself is governed by physical/fluid dynamical properties. Depending on the conditions, one property might dominate over the other and consequently alter the combustion process dramatically.[19]

For any given combustion process, it is always the question which amount of fuel and oxidizer are necessary to obtain the preferred combustion conditions. While engines are often designed for maximum performance, nowadays the demand for the reduction of exhaust gases or soot formation is emphasized. Under ideal combustion conditions, the entire fuel, in this case based on a hydrocarbon C_nH_m, and oxidizer oxygen are consumed and only CO_2 and H_2O are formed:

$$\mathrm{C}_n\mathrm{H}_m + \left(n + \frac{m}{4}\right)\mathrm{O}_2 \rightarrow n\,\mathrm{CO}_2 + \frac{m}{2}\mathrm{H}_2\mathrm{O}\,. \tag{2.1}$$

This mixture is called stoichiometric and yields the maximum flame temperature, because all the chemical energy is transferred into released heat $\dot{Q}$. Nevertheless, under real conditions, it is rarely just oxygen that is present during the reaction and the conditions differ from stoichiometric combustion. To account for inert gases like N_2 from air used as oxidizer and deviations from stoichiometric conditions towards oxidizer-rich or lean mixtures, the general equation for hydrocarbon combustion is[25]

$$\begin{aligned}\mathrm{C}_n\mathrm{H}_m + \lambda\left(n + \frac{m}{4}\right)\left(\mathrm{O}_2 + \frac{79}{21}\mathrm{N}_2\right) \rightarrow \\ n\,\mathrm{CO}_2 + \frac{m}{2}\mathrm{H}_2\mathrm{O} + (\lambda - 1)\left(n + \frac{m}{4}\right)\mathrm{O}_2 + \lambda\frac{79}{21}\left(n + \frac{m}{4}\right)\mathrm{N}_2\,.\end{aligned} \tag{2.2}$$

Premixtures of fuel and air are characterized by the air equivalence ratio or air number λ

$$\lambda = \frac{\chi_{\text{air}}/\chi_{\text{fuel}}}{\chi_{\text{air,stoich}}/\chi_{\text{fuel,stoich}}}, \tag{2.3}$$

or the reciprocal value, the so-called fuel equivalence ratio $\phi = 1/\lambda$, where χ is the molar fraction of the compound. Depending on the composition of the fuel, the combustion can be divided into three premixed regimes depending on the air-to-fuel ratio: For *stoichiometric* combustion, the equivalence ratio is unity, $\lambda = \phi = 1$. For $\lambda > 1$ ($\phi < 1$), more air than needed for a complete combustion is present, leading to *lean* combustion. For $\lambda < 1$ ($\phi > 1$), an excess of fuel is present and the regime is called *rich*. In this case, the products may contain CO, unburned fuel or other species like soot or degradation products from the fuel itself. The reaction for a simple fuel like hydrogen ($2\ H_2 + O_2 \rightarrow 2\ H_2O$) consists of nearly 40 elementary reactions, the combustion of hydrocarbon fuels is even more complex. The auto-ignition of Diesel fuel, which consists mainly of $C_{16}H_{34}$, is described by several thousand elementary reactions, whose interactions govern the combustion process. Figure 2.1 shows the flow analysis and general combustion mechanism for C_1 and C_2 hydrocarbons.[23,26,27] Combustion of methane in oxygen occurs via chain

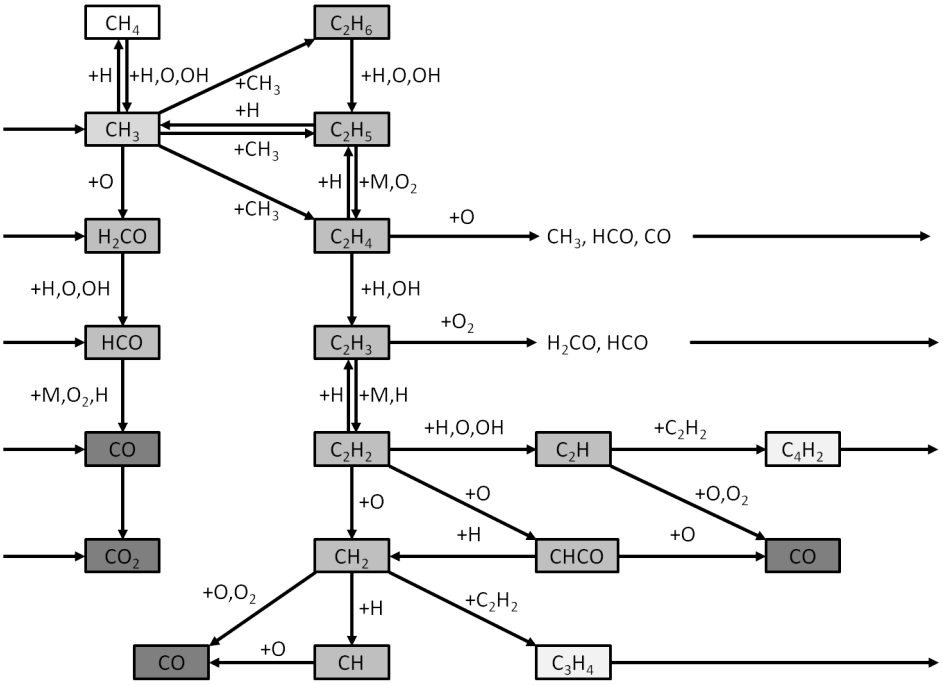

Figure 2.1: Mechanism and flow diagram for C_1/C_2 hydrocarbon combustion, starting with methane as primary fuel. First, the methyl radical is formed, which can undergo oxidation to form CO_2 or side branching reactions to form higher alkanes. Adapted from Warnatz.[23,26,27]

reactions of many intermediate radicals. The first step is initiated by hydrogen abstraction. At high temperatures, the initial reaction is a thermal decomposition,

CH_4 + M → CH_3 + H + M, at lower temperatures the hydrogen can, in principle, be abstracted by oxygen, CH_4 + O_2 → CH_3 + OOH. With the presence of H atoms at higher temperatures, the H_2-O_2 chain branching mechanism starts to form a pool of H, O and OH radicals. These radicals initiate further fast H abstraction reactions. The oxidation of methyl radicals via formaldehyde to CO and finally CO_2 is slow and the amount of CH_3 increases, favoring the recombination of two methyl radicals, 2 CH_3 → C_2H_6. Due to the higher bond energy of the methyl system, the oxidation of higher hydrocarbons differs from the formation of CO_2 via the direct methyl pathway. Additionally, the reaction pathway of C_x compounds becomes more and more complicated due to the instability of higher-order alkyl radicals. This leads to a high degree of side branching reactions as indicated for the ethyl reaction path in Figure 2.1. Nevertheless, the general mechanism for oxidation can be divided into three coupled reaction zones: In region I, the primary fuel is decomposed without energy release and (un)saturated hydrocarbons together with hydrogen atoms are formed. Afterwards, the unsaturated hydrocarbons are oxidized to give CO and H_2 in region II and the hydrogen is simultaneously consumed to form H_2O. Region III produces the majority of the heat release rate and the high abundance of CO is oxidized to CO_2 via CO + OH → CO_2 + H. This reaction occurs after the primary fuel is nearly completely consumed because of the higher reaction rate of hydroxyl radicals with fuel compounds.[24]

Depending on the fuel-to-air ratio the oxidation reactions involving oxygen are stalled and the formation of soot precursors like polycyclic aromatic hydrocarbons (PAHs), e.g via the HACA (H-abstraction-C_2H_2-addition)[28] mechanism, is favored.[29]

2.1.1 Laminar flame

In premixed combustion, fuel and oxidizer are mixed before the combustion starts and ignition will occur, if the ratio of fuel to oxidizer lies within the flammability limits. Enough energy has to be applied using an external heat source. The flame starts to propagate through the combustible mixture and a burned state, categorized by a chemical equilibrium, is reached downstream of the flame front. The remaining unburned state lies in the upstream part of the mixture. Thus, a premixed flame can also be seen as a deflagration wave that propagates through the mixture of fuel and oxidizer. The mechanism of the propagation can be described by the following simplified steps: Once enough energy is applied to the fuel, reactions in the adjacent layer of the combustible mixture are initiated by heat and radicals, most importantly by hydrogen atoms diffusing into O_2. Then, the layer itself

becomes the source of heat and radicals, which initiate reactions in the next layer and the flame propagates due to molecular transport and chemical reactions.

While this model holds true for an ideal laminar flame, which is characterized by a planar, 1-dimensional structure, adiabatic flame temperature and spatially uniform combustion products, a real flame will always be disturbed by heat loss and flow and mixture non-uniformities, which result in flame curvature.[30] Nevertheless, theory of the inner structure and propagation mechanism of a laminar, premixed flame can be described using the adiabatic flame model, based on the theories developed by Zeldovich, Frank-Kamenetsky and Semenov.[31,32] Figure 2.2 shows the internal structure of a premixed flame, which is separated into four regions: The preheating zone, the inner layer, the oxidation layer and the equilibrium zone, where the temperature of the flame reaches its maximum. In the preheating

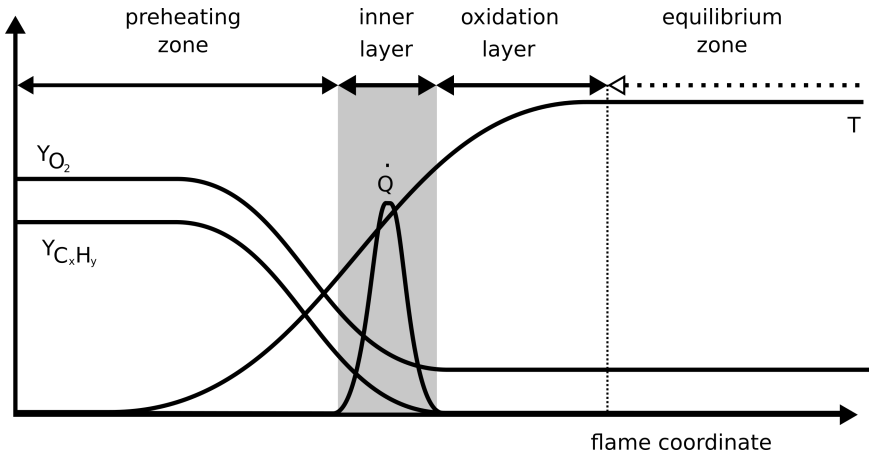

Figure 2.2: Internal structure of a premixed flame, showing the preheating zone, inner layer, oxidation layer and equilibrium zone. While the mass fraction of the fuel $Y_{C_xH_y}$ and oxygen Y_{O_2} decrease due to the formation of radicals in the preheating zone and finally reach their minimum values in the inner layer, the temperature reaches its maximum in the oxidation layer and is assumed to be constant afterwards. The heat release rate $\dot{Q}$ has its maximum in the inner layer. Adapted from Peters.[33]

zone, the products are heated up due to heat conduction and the temperature reaches ignition conditions. This zone makes up the majority of the overall flame thickness. The *inner layer* is the zone, where most of the fuel is consumed and hence most of the radicals for the chain branching reactions are formed. The inner layer is also the zone of maximum heat release, despite being the smallest zone in the flame front. Its thickness δ_i, usually 1/10th of the laminar flame thickness δ_l, is in the order of a few micrometers and decreases with increasing pressure.[33]

In the *oxidation layer*, the CO produced in the inner layer is oxidized to CO_2, $OH + CO \rightarrow CO_2 + H$. Depending on the fuel-to-air ratio, the inner layer and oxidation zone are responsible for the formation and depletion of the radicals that make

up the characteristic flame luminosity. For fuel-rich mixtures, an excess of carbon-containing radicals and intermediates like CH, C_2, CHO, CH_2O (see Figure 2.1) or even soot particles are formed. The formation of higher carbon-containing species leads to the specific yellowish-orange glow of fuel-rich flames. Leaner mixtures lead to an increase of electronic excited OH radicals via the reaction $CH + O_2 \rightarrow CO + OH^*$, one of the most important reactions in hydrocarbon flame chemistry.[34] The formation of C_1 intermediates is favored, and the chemiluminescence of oxygen-rich flames is shifted towards the UV wavelength range.

The emission spectrum of an oxygen-rich propane gas flame is shown in Figure 2.3 and the most important emission bands are noted. Oxygen rich flames generate an abundance of C_2^*, CO_2^*, but mostly CH^* and OH^* that all emit light in the blue wavelength region below $\lambda = 450$ nm.[35] The C_2^* emission at $\lambda > 500$ nm is more pronounced in fuel-rich flames. While the *equilibrium zone* is not of

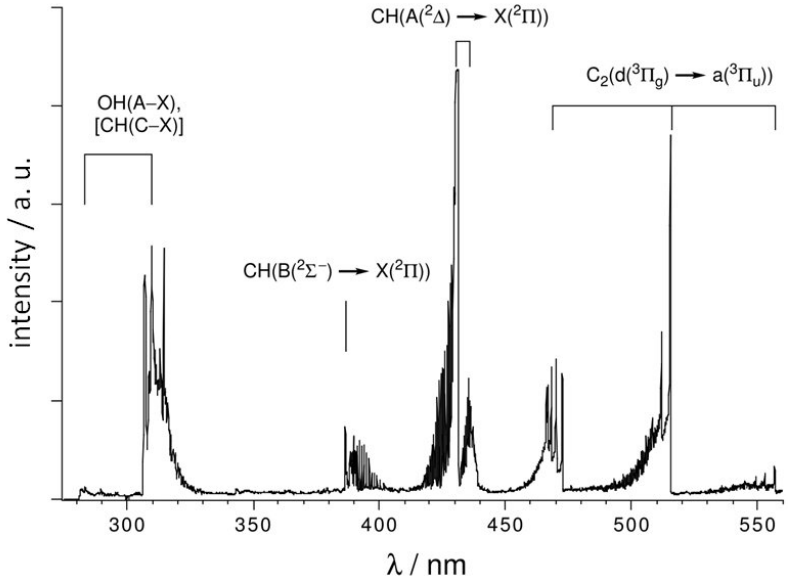

Figure 2.3: Emission spectrum of oxygen-rich propane gas flame from a gas burner. Emission from the flame source upward (about 2 cm) is recorded. The observed molecular emissions are indicated. Adapted with permission from Ref. [36]. Copyright 2000 American Chemical Society.

importance for the chemical reaction, it is usually the zone of highest temperature and marks the end of all reactions that are supposed to be in an equilibrium at this point.

2.1.2 Spark discharge process

Explosive gas mixtures can be ignited using a broad spectrum of sources, for example open flames, hot solid surfaces or by compression of the gas up to its self-ignition temperature, as it is used in Diesel engines. The most common application for ignition is still the use of an electric spark discharge, whose energy is stored either in a capacitor or the inductance of a coil. During the work of this Thesis, an ignition coil was used for all combustion experiments. The spark-discharge process can be divided into four different phases that will be discussed in the following Section: The *pre-breakdown*, the *breakdown*, the *arc* and the *glow phases.* All consist of different spark plasma characteristics.

In the *pre-breakdown phase*, the insulating gas in the spark gap region is ionized due to the linear rise of the applied spark voltage. Electrons that are randomly created by the UV-background radiation, are accelerated towards the anode and excite or even ionize more gas molecules. This process continues until a self-sustained electron avalanche is created. During the pre-breakdown phase, the temperature and electron density of the surrounding gas stays at its initial conditions. Only in places of high electric field strengths enough electrons are produced to start the ionization processes. The electric field itself depends strongly on the applied voltage and shape of the electrodes.

During the *breakdown phase*, the spark voltage drops from values of a few kV to ≈ 100 V, hence the name breakdown. The electric field creates a plasma channel of ≈ 40 µm along the path of the highest conductivity, which is not necessarily the shortest distance. Due to the differences in conductivity of the gas mixture, the location and voltage of the spark is exposed to fluctuations. The breakdown phase is characterized by a high current of several hundreds of Ampere and a rapid temperature and pressure rise in the cylindrical channel up to $T = 60{,}000$ K and $p = 200$ bar. The event of breakdown occurs on timescales of a few nanoseconds, during this time nearly all the energy supplied is stored in the gas due to dissociation and ionization processes. The heat transfer loss due to conduction to the electrodes and by radiation is less than 5%.[37,38]

After the short breakdown phase, the longer lived *arc phase* starts and can last up to a few milliseconds. The arc voltage is below $U = 100$ V, while the current magnitude is determined by the circuit properties. To sustain the arc, the cathode must still emit electrons, mainly from hot and molten spots of a few µm in diameter. Due to heat conduction and mass diffusion, the plasma channel expands and exhibits a much lower amount of dissociated species and thus the temperature drops to values of $T = 6000$ K. The overall energy in the plasma drops to 50% or

less, the rest is lost via heat transfer to the electrodes. Nevertheless, the kernel consists of several radical species that, together with the high temperatures, provide conditions for the start of the combustion.

When the voltage at the electrodes starts to rise up to a few hundred Volt, the *glow discharge phase* starts and marks the remainder of the spark duration. This phase can last for more than 1 ms and is characterized by a temperature of 3000 K and low currents below 200 mA. Due to the long lifetimes of the glow discharge phase, the majority of the spark energy is released during this time, albeit the energy loss rises to 70%. In case of cross-flows, the glow plasma can be transported away from the electrodes forming so-called hairpin structures. If the voltage of these structures exhibits the voltage for breakdown between the electrodes directly, a shortcut is built and the process can be repeated, until the stored electric energy is used up. The combination of cross-flow and glow discharge can lead to a 20-fold extension of the spark gap, which highly effects the ignition probability.[39]

2.1.2.1 Minimum ignition energy and quenching distance

Ignition will occur if the added energy e.g., via spark, laser or compression, raises the gas kernel temperature above the adiabatic flame temperature T_a in a region d comparable in size to the flame thickness l_f. The energy release by the source must be sufficiently fast to overcome the loss by heat transfer and conduction. The rate of heat release by the chemical reactions exceeds the rate of heat loss, the kernel grows in size and eventually fills the entire combustion volume. If the heat release is slower than the heat conduction at the kernel surface, the kernel temperature starts to drop until the burning temperature is too low to maintain chemical reactions and the flame extinguishes. Thus, the kernel size that enables the flame to propagate unaided is defined as the quenching distance d_q. For flame propagation in tubes, the quenching distance is usually a parameter of the distance between the walls, for spark ignition the crucial parameter is the distance between the spark electrodes. The energy that has to be supplied to the system to reach this critical size is the minimum ignition energy (MIE). The MIE is connected with the quenching distance via:[40,41]

$$E_\mathrm{min} = \frac{1}{6}\pi d_\mathrm{q}^3 \rho_\mathrm{b} \cdot C_\mathrm{av} \Delta T \,. \tag{2.4}$$

Here, ρ_b is the molar density of the burned gas, C_av the average molar heat capacity of the gas for the temperature difference ΔT between flame T_b and unburned mixture T_u.

The minimum ignition energy for quiescent propane/air mixtures near 5.0 Vol% at atmospheric pressure is in the order of 0.02 mJ, while the quenching distance was determined to be 1.8 mm.[42] The MIE is not only a function of the quenching distance, but varies with pressure and percentage of fuel, oxygen and species of inert gas, e.g., N_2, Ar or CO_2. More important, the fuel-air equivalence ratio ϕ for the MIE increases with increasing carbon number of the fuel and shows a steady shift towards more fuel-rich compositions. Hydrogen and methane have their MIE at $\phi < 1$ due to their higher diffusivity compared to air, while higher alkanes like propane or butane have their MIE around $\phi \approx 1.2$.[43] Nevertheless, for practical applications the most effective spark gap length d_{gap} is often greater than the quenching distance d_{q}. A spark plug with tightly spaced electrodes can act as heat sink and remove a greater amount of heat from the developing flame kernel. The increase in spark gap leads to a change of the spark shape. For small gap distances, the resulting flame kernel is comparable to a spherical form, the increase of d_{gap} leads to a more line-shaped structure, which is less effective for ignition. For electrodes in a non-parallel plane orientation, ignition can even occur for distances smaller than d_{q}.[44]

While these theories are true for quiescent conditions with a laminar flame speed u_{l}, the influence of turbulence intensity or scale $u^{'}$ can drastically change the ignition behavior. Usually, the strain on the flame kernel is increased with an increase in $u^{'}$, which requires a higher ignition energy to overcome the heat loss from the flame kernel.[45,46] Depending on the Kolmogorov scale of the turbulence, this is not always the case. For small turbulence intensity, $u^{'} \leq 2u_{\mathrm{l}}$, the MIE decreases slightly with an increase of turbulence scale, while an increase of the MIE is only observed for $u^{'} \geq 2u_{\mathrm{l}}$. In between these extremes lies a range of conditions, where the MIE is independent of turbulence scale.[47,48] To account for these effects, the definition of the minimum ignition energy for turbulent mixtures can be rewritten as:

$$E_{\mathrm{min}} = \frac{1}{6}\pi \left[\frac{Bk/\left(C_{\mathrm{av}}\rho_{\mathrm{b}}\right)}{u_{\mathrm{l}} - a \cdot u^{'}} \right] \rho_{\mathrm{b}} \cdot C_{\mathrm{av}} \cdot \Delta T \,. \tag{2.5}$$

B is the ratio of quenching distance to flame thickness, a the ratio of the eddy diffusivity to the turbulence intensity and eddy length. Nevertheless, the exact effect on the combustion is hard to predict because of the broad range of variables responsible for the change of MIE and quenching distance and often have to be determined individually in the experiment.

2.1.2.2 Ignition delay time and ignition limits

While for purely thermal ignition processes an instantaneous increase in temperature is observed, for hydrogen and hydrocarbon explosions the temperature rise, and thus the reaction, starts after a certain amount of time, the so-called ignition delay time τ_{id}. The ignition delay time contains an overlap of a series of physical and chemical processes with different time scales and thus depends apart from the molecular properties of the fuel also on pressure, temperature and, for non-laminar conditions, on the fluid flow field.[23]

At the chemical level, the ignition delay time is defined by the important chemical reactions of the fuel that is the formation of radicals and chain branching reactions. But even though radicals are formed at an exponential rate, the amount of fuel consumed and energy released is too small to detect for $t < \tau_{\mathrm{id}}$, and for short reaction times the temperature stays constant. Finally, when the radical pool is large enough and enough energy is released, the reactions will sustain themselves and auto-ignition will take place. If the mixture is not ignited by itself, but locally by an external ignition source like a spark plug, the process is called induced ignition. Here, just a small volume of the fuel is heated up above the ignition temperature and ignition starts locally and the flame starts to propagate through the unburned mixture.[23,49] Experimentally, the measurement of ignition delay times is not universally defined and different methods are common (temperature or pressure increase, CH or OH chemiluminescence).[50] Besides parameters like MIE, quenching distance, temperature and pressure, the fuel-to-air ratio plays an important role, because not all fuel-air mixtures will burn or explode. If a stoichiometric mixture is exposed to an external ignition source or the mixture is heated up to the ignition temperature, the mixture moves into the explosive regions and starts to burn, even if the ignition source is removed. The mixture produces a self-sustaining flame. For mixtures with a low or high amount of fuel, this might not be the case and the flame extinguishes. The minimum amount of fuel needed for combustion is called lower flammability limit (LFL), the upper limit upper flammability limit (UFL).[1] The flame is quenched if the heat-release-rate to heat-loss-rate ratio $\dot{Q}_{\mathrm{rel}}/\dot{Q}_{\mathrm{loss}}$ is less than unity. The heat loss depends on the thermo-physical properties of the unburned mixture. For lean mixtures, the limits in oxygen and air are usually the same because of their similar specific heat, while for richer mixtures the limits are higher in pure oxygen, which is related to higher temperatures due to a lack of nitrogen. Depending on the composition of the inert gases present in the mixture, the required amount of oxygen to establish flame

[1] Depending on the literature, lower and upper explosion limit (LEL and UEL) are used instead of LFL and UFL

propagation can change dramatically. For the $CH_4/O_2/N_2$ system, the minimum oxygen amount is 12.1 %. When O_2 is replaced by CO_2, the limit increases to 14.6 %, and for the $CH_4/O_2/Ar$ system the amount of oxygen needed is less than 10 %. The reason for a stronger influence of the rich limits can be explained by two important competing reactions: Free hydrogen atoms can recombine via three body collision $H + H + M \rightarrow H_2 + M$ or increase the amount of radicals for chain branching via $H + O_2 \rightarrow OH + O$. The recombination increases with decreasing temperature and increasing amount of M, which are the conditions for rich combustion limits.[24]

Due to the delayed formation of a self-sustainable flame kernel, the early stages of ignition are susceptible to a lot of external forces, like heat loss to surfaces and surroundings or strain due to turbulence, all of which might lower the temperature below the ignition limit and quench the flame.[51] To get a deeper understanding of the mechanism involving flame quenching, the next Section will discuss the interaction of turbulent flows with flame chemistry and propagation.

2.1.3 Turbulent combustion

In technical processes, combustion nearly always happens within a turbulent environment rather than in a laminar flow field, especially in internal combustion engines. Turbulent processes enhance mixing of injected fuel and oxidizer, which are seldom stored premixed before ignition due to safety reasons. Additionally, the heat released by combustion often leads to flow field instabilities, thus making a transition from laminar to turbulent processes unavoidable. For engine operation, turbulent conditions enhance the overall efficiency.

The main requirement for combustion is the mixing of fuel and oxidizer at the molecular level. Because diffusion as mixing process takes too long for operation under high repetition rates, e.g., in automotive engines, the turbulent mixing process is of high interest in combustion diagnostics. The general mechanism of turbulent mixing is based on the breakdown of induced eddies or vortices[1]. These eddies induce strain and shear forces, which are responsible for steep concentration gradients at the reactant flow interface and increase the molecular inter-diffusion drastically. Nevertheless, turbulence can also result in the opposite effect: Once an ignitable mixture is created, a stable propagating flame can only be established, if the heat transfer and transport of radicals from the reaction zone to the unburned mixture is sustained. If the gradients become too steep, the temperature might

[1] While eddies are a direct result of pressure difference due to flow over the edge of an object, vortices can also be created by, e.g., confluent flows. Because most of the turbulence interactions investigated in this thesis arise from the flow around objects, both terms will be congruent.

drop below the crossover temperature, the chemical reactions are quenched and the flame extinguishes. The investigation of turbulence and flame chemistry still is an ongoing research topic in the combustion community and not all turbulent flame interactions are qualitatively and quantitatively understood. Until this point in time, experimental work on turbulence is an indispensable tool to gain better insights into the underlying mechanisms and to improve combustion models.

Even though mixing is often favorable, technical combustion processes are generally divided into three classes: Premixed, non-premixed, or, although not as common, partially premixed turbulent combustion.[33] An overview of different applications for laminar and turbulent combustion depending upon the mixing of fuel and oxidizer is given in Table 2.1 and will be shortly discussed in the following.

Table 2.1: Examples of different combustion systems ordered by types of premixing and fluid motion.[23,52,53]

Fuel/Oxidizer Mixing	Motion of the fluid	Examples
premixed	turbulent	spark-ignition gasoline engine low NO_x gas turbine
	laminar	flat flame burner Bunsen burner
non-premixed	turbulent	Diesel engine aircraft turbine
	laminar	wood fire candle flame
partially premixed	turbulent	partially-premixed and gasoline direct-injection compression-ignition

2.1.3.1 Premixed turbulent combustion

The probably most common application for turbulent premixed combustion is the spark-ignition combustion engine like a four-stroke Otto engine. Here, the fuel and air are injected premixed or separately during the compression stroke and mixed at the molecular level for the duration of the stroke by turbulence. The ideally homogeneous mixture is then ignited using a spark plug that generates a

flame which first grows in a laminar fashion and then, once a stable flame kernel is established, by turbulent flame propagation. This is only possible when the fuel-to-air ratio lies between the lower and upper flammability limits. For propane, the ignition limits lie between 2.1 vol% and 9.5 vol%, which correspond to fuel-to-air equivalence ratios of $\phi_{\mathrm{LFL}} = 0.51$ to $\phi_{\mathrm{UFL}} = 2.50$.[54,55] Premixed combustion is often applied when high heat release rates are preferable, especially in small devices with low residence time. Premixed conditions offer the possibility of lean combustion and thus reduce the formation of soot, while the comparably low temperatures enable low NO_x formation.[23,56] The use of lean combustion is always a compromise, because the stability limits are narrow and flames in low-emission gas burners are susceptible to blow-off.[57]

2.1.3.2 Non-premixed turbulent combustion

Turbulent non-premixed flames are of great interest in practical combustion applications. Non-premixed flames are safer to handle, because the fuel is separated from the oxidizer until the moment of ignition. The spectrum of non-premixed flows ranges from jet engines, steam boilers, furnaces to Diesel engines. Often, the process is called diffusive combustion or combustion in diffusion flames, because the diffusion of fuel and oxidizer is the rate-determining process. Apart from safety reasons, non-premixed combustion in Diesel engines offer a much higher efficiency than gasoline-fueled Otto engines, $\eta_{\mathrm{Diesel}} \approx 45\%$ vs. $\eta_{\mathrm{Otto}} \approx 30\%$. Less fuel has to be burned to reach the same work, the engine operates at higher temperature of combustion and higher work load. Additionally, the amount of CO_2 produced per unit distance is smaller, which results also from incomplete combustion at high loads and an increase of CO formation. The inherent high temperatures in Diesel engines favor the production of NO_x, which can only be reduced with engine modifications like exhaust gas recirculation (EGR), selective catalytic reduction (SCR), e.g., AdBlue, or lean NO_x traps (LNTs), of which the latter are known to fail under high-load, real-life conditions.[58] The distinction between premixed and non-premixed combustion is not always clear when mixing times are in the order of the reaction times. Fuel and air can mix in a flame after extinction of the local non-premixed flame and are reignited by adjacent flame zones. This process is more clearly described by the definition „partially premixed“and different theoretical approaches have to be applied. The reaction products of non-premixed flames appear on both sides of the reaction zone, because the flame is only established at the fuel-oxidizer-surface. It does not propagate, or propagates only if fuel and air

are moving due to convection, and is therefore much easier to model and describe as a premixed flame.[23]

2.1.3.3 Partially premixed turbulent combustion

In many burners, and to a lesser extent in internal combustion engines, the heat release from the combustion happens neither in fully premixed nor non-premixed conditions. Even if fuel and air are premixed like in a lean gas turbine, the mixture composition is inhomogeneous and shows spatial variation of $\phi(\mathbf{x}, t) < 1$. This behavior, which only occurs for lean or rich mixtures, is often called stratified. The same applies for direct injection gasoline engines, if the interval between injection and spark ignition is too short for a complete mixture. Compared to spark ignition engine, the fuel is directly injected into the chamber and not mixed in the intake manifold. The flame kernel then travels through an environment of highly inhomogeneous fuel compositions, with different areas of lean or rich compositions.[30] For automotive engines, this concept can be seen as a hybrid of homogeneous charge compression ignition (HCCI) and Diesel CI. While in the first the fuel and air are completely mixed and ignited by compression, the fuel is injected into the compressed oxidizer in the latter. In a partially premixed combustion engine, fuel is injected into a lean, non-combustible mixture. The ignition delay is extended to some crank angle degree (CAD) after injection and combined with using exhaust-gas recirculation (EGR) oder low compression techniques. The advantages are low NO_x, even without catalytic converter, and soot emission, low acoustic noise and high running loads.[53]

2.1.4 Fluid dynamics of turbulence

Turbulent flows, both reacting and unreacting, are characterized by different length and time scales, fluctuations and non-dimensional numbers. They are transitory, highly diffusive, seemingly random and chaotic. Turbulent flows always occur at high Reynolds numbers. The Reynolds number Re is used for the characterization of laminar or turbulent flow. It is defined as the ratio of inertial or momentum forces to viscous forces:[59,60]

$$Re = \frac{\text{inertial forces}}{\text{viscous forces}} = \frac{\rho v^2/L}{\mu v/L^2} = \frac{\rho v L}{\mu} = \frac{vL}{\nu}. \tag{2.6}$$

Here, v is the maximum velocity of the fluid (or an object relative to the fluid), L is the characteristic dimension of the system, e.g., pipe or impeller diameter, μ and ν the dynamic and kinematic viscosities and ρ the fluid density. If the system is a stirred vessel or reactor, the Reynolds number can be calculated in relation to the turbine or propeller:

$$Re = \frac{\rho N D^2}{\mu}. \tag{2.7}$$

N is the rotational speed in rpm and D the diameter of the agitator. For low Reynolds numbers, the system can be characterized as laminar. The viscous forces are dominating over inertial forces and disturbances of the flow can be damped out, which prohibits any growth and self-sustaining of disturbances. The opposite effect is true for high Reynolds numbers. If the viscosity is less important than inertia, disturbances can be perpetuated and are not damped out. For regimes with Reynolds numbers above $Re \geq 10000$, the flow is considered to be turbulent.[61]

Another important property of turbulent flow is its velocity fluctuation over time, which is often used to categorize turbulence intensity. Figure 2.4 shows the time series for the axial component of the flow velocity $u_{\mathrm{x}}(t)$, observed from a fixed position x in the flow field. The instantaneous velocity $u_{\mathrm{x}}(t)$ fluctuates around a mean velocity value $\langle u_{\mathrm{x}} \rangle_{\mathrm{t}}$. This applies for nearly all variables of turbulent

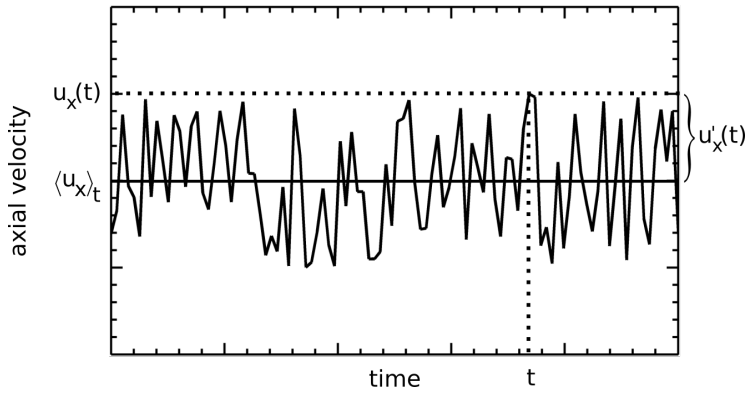

Figure 2.4: Typical time series of the axial component of the flow velocity at a fixed position x in a turbulent flow field. The mean value $\langle u_{\mathrm{x}} \rangle_{\mathrm{t}}$ is shown as the black line, the difference between the mean and the actual velocity $u_{\mathrm{x}}(t)$ marked by the dashed line is the fluctuating component $u_{\mathrm{x}}^{'}(t)$.

flows. The general procedure is to split the variable into a (probability weighted average) mean and the variance (mean square fluctuations). As an example, the velocity component can be decomposed into the sum of the mean value and the instantaneous deviation from the mean $u_{\mathrm{x}}^{'}(t)$:

$$u_{\mathrm{x}}(t) = \langle u_{\mathrm{x}} \rangle_{\mathrm{t}} + u_{\mathrm{x}}^{'}(t) \ . \tag{2.8}$$

The intensity of the turbulence is calculated as the root-mean-square of the deviation from the mean, because the linear average would be zero:[38]

$$u'_{\mathrm{x,rms}} = \sqrt{\langle u'^2_{\mathrm{x}} \rangle_{\mathrm{t}}} \,. \tag{2.9}$$

This also holds true for ensemble averaging, if the turbulence increases over time. The procedure is called Reynolds averaging.[62]

A lot of flow properties can be deduced from Newtons second law for incompressible fluids that relates the fluid particle acceleration $\mathrm{D}U/\mathrm{D}t$ to the surface and body forces experienced by the fluid. Here, the material or substantial derivative of a macroscopic scalar or vector field Φ is defined as:

$$\frac{\mathrm{D}\Phi}{\mathrm{D}t} \equiv \frac{\partial \Phi}{\partial t} + U_i \frac{\partial \Phi}{\partial x_i} = \frac{\partial \Phi}{\partial t} + \mathbf{U} \cdot \nabla \Phi. \tag{2.10}$$

If the surface forces are of molecular origin and can be described using a stress tensor τ_{ij} and the body force by a gravitational potential g, the momentum equation can be written as[63]:

$$\rho \frac{\mathrm{D}U_j}{\mathrm{D}t} = \frac{\partial \tau_{ij}}{\partial x_i} - \rho \frac{\partial g}{\partial x_j} \,. \tag{2.11}$$

Considering that the stress tensor is a function of pressure and the velocity field is selenoidal, $\nabla \cdot U = 0$, the general Navier-Stokes equation can be written as:

$$\rho \frac{\mathrm{D}U_j}{\mathrm{D}t} = \mu \frac{\partial^2 U_j}{\partial x_i \partial x_i} - \frac{\partial P}{\partial x_j} - \rho \frac{\partial g}{\partial x_j} \,. \tag{2.12}$$

or, with the modified pressure $p = P + \rho g$

$$\frac{\mathrm{D}U_j}{\mathrm{D}t} = -\frac{1}{\rho} \nabla p + \nu \nabla^2 U \,. \tag{2.13}$$

One of the fundamental performers in turbulent fluid mechanics are vortices, as they develop almost everywhere in turbulent fluid motion. A vortex is a region in a medium, in which the fluid particles rotate around an axis, as it is known from smoke rings, whirl pools around boat engines or paddles or storms like Jupiter's great red spot. When a vortex is formed, it can undergo a lot of different fluid interactions, like stretching, moving and interacting with other vortices and often carries important quantities like mass, energy or momentum. In an ideal fluid, the vortex energy due to the circular motion cannot be dissipated and the vortex would survive forever. However, due to the viscosity of real fluids, the energy is dissipated in the fluid and often vortex stretching occurs. Vortex stretching steepens the velocity gradient and leads to smaller and smaller vortex structures.[64] One concept for the description of vortices is the vorticity $\vec{\omega}$.

Vorticity is a pseudo-vector field $\vec{\omega}$ that describes the local spinning motion of a continuum near some point as seen by an observer located at that point moving with the flow. Mathematically, it is defined as the curl of the flow velocity $\vec{v}$ and can be expressed as:

$$\vec{\omega} = \nabla \times \vec{v} = \left(\frac{\partial}{\partial x}, \frac{\partial}{\partial y}, \frac{\partial}{\partial z}\right) \times (v_\mathrm{x}, v_\mathrm{y}, v_\mathrm{z}) \tag{2.14}$$

$$= \left(\frac{\partial v_\mathrm{z}}{\partial y} - \frac{\partial v_\mathrm{y}}{\partial z}, \frac{\partial v_\mathrm{x}}{\partial z} - \frac{\partial v_\mathrm{z}}{\partial x}, \frac{\partial v_\mathrm{y}}{\partial x} - \frac{\partial v_\mathrm{x}}{\partial y}\right). \tag{2.15}$$

In a two-dimensional flow or when the out-of-plane velocity component cannot be measured, the vorticity vector is always parallel to the z-axis and therefore can be expressed as a scalar field multiplied by a constant vector $\vec{z}$:

$$\vec{\omega_\mathrm{z}} = \nabla \times \vec{v} = \left(\frac{\partial}{\partial x}, \frac{\partial}{\partial y}, \frac{\partial}{\partial z}\right) \times (v_\mathrm{x}, v_\mathrm{y}, 0) = \left(\frac{\partial v_\mathrm{y}}{\partial x} - \frac{\partial v_\mathrm{x}}{\partial y}\right) \vec{z}\,. \tag{2.16}$$

Vorticity is an important concept for the study of turbulence-flame interactions, since high fluctuations of the flow might lead to flame instabilities and determination of vortex regions and their strengths is a key to determine combustion instabilities and improve the overall combustion process.

The energy dissipation mentioned earlier can be explained using two important theories to describe turbulent interactions: The energy cascade and the Kolmogorov microscale. The latter quantifies the picture of the cascade drawn by Richardson in the early 1920s, who summarized turbulence as a phenomenon in a poem:

> Big whirls have little whirls that feed on their velocity
> And little whirls have lesser whirls and so on to viscosity.[65]

The general idea behind this is that the kinetic energy, produced by some mechanism like stirring, is introduced at the largest scale of motion into the system. The energy is then transferred to smaller and smaller scales and structures by inviscid effects and finally at the smallest scales it is dissipated due to viscosity. The smallest scale in the flow is also known as Kolmogorov microscale.[66,67] While the flow shows a continuous spectrum of scales, three distinctive regimes can be identified in the turbulence spectrum and characterized by their kinetic energy $E(\kappa)$ as a function of eddy wavenumber $\kappa = l^{-1}$, which is the inverse of the length scale. Figure 2.5 shows a logarithmic sketch of the turbulent energy as a function of the wavenumber. The *energy containing range* consists of the largest scales l_t, $\kappa = l_\mathrm{t}^{-1}$, in the energy spectrum. The eddies obtain the energy from the flow and are of the size of the apparatus as mentioned in Equation 2.7, $l_\mathrm{t} \approx D$. Therefore, the Reynolds number of this range is large and direct effects of viscosity

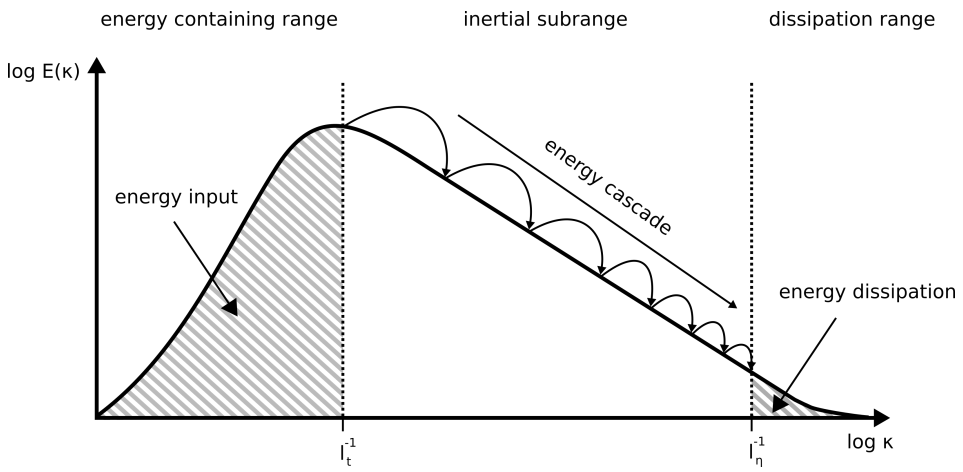

Figure 2.5: Sketch of the turbulent energy spectrum E(κ) as a function of the wavenumber of the eddies $\kappa = l^{-1}$. The energy is put into the system at the largest scales l_t and the created eddies are reduced in size in the inertial subrange until they are small enough to dissipate their energy to the surroundings at the Kolmogorov scale l_η due to viscosity. Adapted from Ref. [63].

are negligibly small.
In the *inertial subrange*, the energy depends on the energy dissipation rate ϵ and wavenumber κ

$$E(\kappa) = C\epsilon^{2/3}\kappa^{-5/3}. \tag{2.17}$$

The dissipation rate can be estimated using[68]

$$\epsilon = \frac{u'^3}{l_\mathrm{t}} \tag{2.18}$$

and the time scale of the turbulence is

$$\tau_\mathrm{t} = \frac{l_\mathrm{t}}{u'}. \tag{2.19}$$

When the eddies become small enough, their Reynolds number is close to unity and viscous effects take over. At this Kolmogorov scale η or *dissipation range*, the eddies are of size l_η and are defined only by the viscosity ν and dissipation rate ϵ

$$l_\eta = \left(\frac{\nu^3}{\epsilon}\right)^{1/4}. \tag{2.20}$$

All eddies are supposed to be isotropic and their properties like velocity u_η and time scale τ_η (eddy turnover time) can be determined using a dimensional analysis:

$$u_\eta = (\nu\epsilon)^{1/4}, \tau_\eta = \left(\frac{\nu}{\epsilon}\right)^{1/2}. \tag{2.21}$$

While the size of the smallest scales is very small, it is far larger than any molecular scale.[66] Using Equation 2.18, the Kolmogorov microscales can be estimated from measuring the fluid velocity, e.g., by means of particle image velocimetry (PIV).

2.1.4.1 Turbulent combustion regimes

The impact of turbulence intensity u' and microscale l_t on the flame structure is often shown in relation to the laminar flame velocity u_l and thickness δ_l. Depending on the ratio of turbulence intensity to laminar flame velocity u'/u_l and microscale to flame thickness $l_\mathrm{t}/\delta_\mathrm{l}$, flames can be divided into five different regimes. These are shown in the so-called non-dimensional Borghi diagram (see Fig. 2.6) and will be explained in the following:

The time scale for a flame to move a distance equal to its own thickness can be written as

$$\tau_\mathrm{c} = \frac{\delta_\mathrm{l}}{u_\mathrm{l}}\,. \tag{2.22}$$

Thus, τ_c can be interpreted as the chemical time scale of the flame. The ratio of turbulent flow scale τ_t for the larger eddies to the chemical time scale τ_c is the dimensionless Damköhler number Da:

$$Da = \frac{\tau_\mathrm{t}}{\tau_\mathrm{c}} = \frac{l_\mathrm{t}}{\delta_\mathrm{l}}\frac{u_\mathrm{l}}{u'}\,. \tag{2.23}$$

For $Da \gg 1$, the chemical times are much shorter than the eddy turnover time, and the flame front structure is not affected by turbulence. If $Da < 1$, the flame front is disturbed by the large eddy structures and therefore starts to wrinkle.

To compare the chemical reaction to the small scale turbulence, the dimensionless Karlowitz number Ka is introduced. Ka is the ratio of the chemical time scale to the Kolmogorov time scale:

$$Ka = \frac{\tau_\mathrm{c}}{\tau_\eta} = \frac{\delta_\mathrm{l}}{l_\eta}\frac{u'}{u_\mathrm{l}} = \frac{\sqrt{\frac{\epsilon}{\nu}}}{\frac{u_\mathrm{l}}{\delta_\mathrm{l}}}. \tag{2.24}$$

For high Karlowitz numbers ($Ka > 1$), the thin reaction zone interferes with the smallest eddies in the turbulent flow field, $Ka < 1$ denotes an undisturbed flame front. According to Borghi and Peters, the five regimes are:[69,70]

1. **Laminar flames**: In the laminar flame region, denoted by the turbulent Reynolds number $Re_t < 1$, the turbulent fluctuations are so small that the flame is completely undisturbed and the flame propagates as a laminar flame.

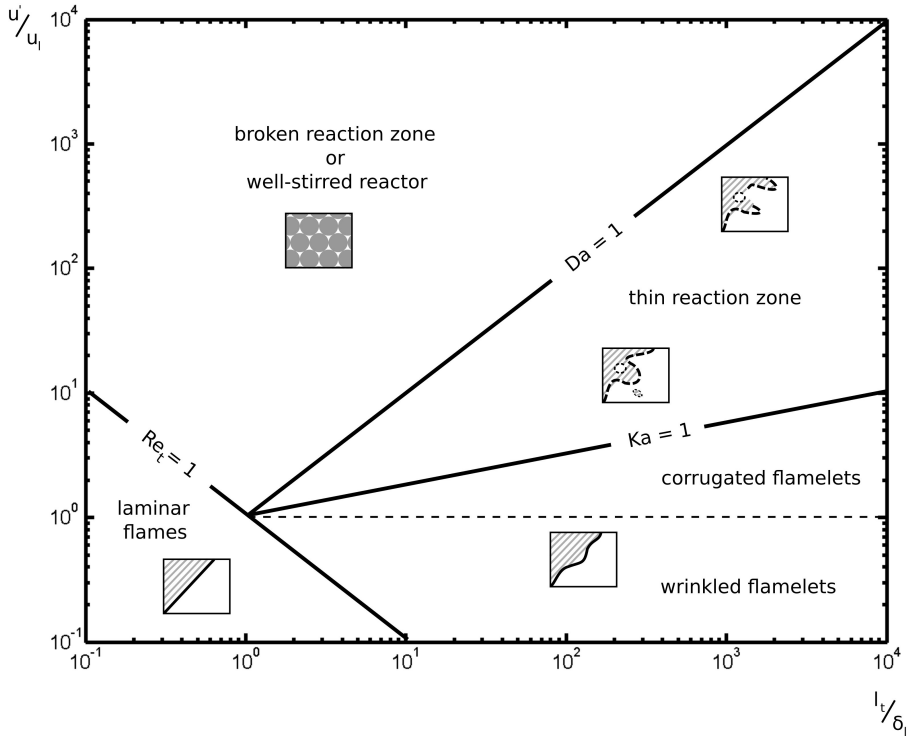

Figure 2.6: Borghi diagram to describe five different regions of combustion depending the ratio of turbulence intensity to laminar flame velocity $u^{'}/u_{\mathrm{l}}$ and microscale to flame thickness $l_{\mathrm{t}}/\delta_{\mathrm{l}}$. For high turbulence intensities ($Da < 1$, $Ka > 1$), the flame front is broken up completely, leading to the broken reaction or well-stirred reactor zone. Adapted from Peters and Borghi.[33,69]

2. **Wrinkled flamelets**: In the wrinkled flame regime, the turbulence intensity $u^{'}$ is small compared to u_{l}, the laminar flame speed is still the dominating quantity ($Ka < 1$). The flame is slightly wrinkled, but the laminar flame structure is still upheld.

3. **Corrugated flamelets**: With higher turbulence intensity, the wrinkling of the flame increases, but the size of the smallest eddies is still bigger than the thin reaction zone and cannot influence the combustion. Nevertheless, small pockets of burned and unburned gases can form. The boundary of this regime to the thin reaction zone is reached at $Ka = 1$, when $\delta_{\mathrm{l}} \equiv \eta$.

4. **Thin reaction zone**: In this regime the turbulent integral time scale is larger than the chemical time scale ($Da > 1$), but the Kolmogorov scales are smaller than the overall flame thickness ($Ka > 1$). While the inner layer of the flame cannot be disturbed by the smallest eddies, it shows laminar conditions only locally, because diffusion and heat transfer are enhanced by turbulence and the flame is thickened. For high stretch induced by the Kolmogorov eddies

$\sqrt{\epsilon/\nu}$, the flame can be quenched locally, which marks the transition to the broken reaction zone.[71]

5. **Broken reaction zone**: In the broken reaction zone regime, often called well-stirred reactor conditions, eddies can enter the inner layer of the flame ($Da < 1$, $Ka > 1$). The reaction zone breaks down locally because of an increase in heat loss to the preheating zone. The stretch of the flame alters along the flame front, but the positive stretch brings more reactants towards the flame, increasing the gradients at the flame front. Finally, the finite rate of the kinetics becomes slower than the reactant delivery rate. This causes a drop in temperature and hence a loss of radicals. The turbulent mixing is faster than the flame chemistry. Additionally, fuel and oxidizer might interdiffuse and mix again at lower temperatures not high enough for reactions.[72]

It should be noted that the Borghi diagram is an oversimplification, since turbulence is rarely represented by single values of u' and l_t and the transitions between the lines is not sharply defined.[73] Kolmogorov vortices may suffer from a short life-time due to dissipation and might even be too small or have too small velocities to affect the flame noticeably. Nevertheless, the influence of Kolmogorov vortices constitutes the most effective mechanism affecting the flame front because of the high degree of induced strain rate.[71]

For every combustible mixture, there is a certain level of turbulence intensity that generates a maximum of turbulent flame speed, a further increase of u' first leads to a drop-off in speed, followed by the extinction of the flame. This is often interpreted using the flamelet model and flamelet wrinkling process, which does not only depend on the local turbulence level, but also on the complex geometry of shear layers, walls, flame-flame interaction and, in case of burners, the anchor location of the flame.[72,74]

To understand the complex interactions of a laminar flame front with different turbulent flow structures, it is often necessary to model the system with a reduced set of variables. This can be the interaction of a laminar propagation flame front, or even simpler of a small flame segment, with a single vortex structure, which has the same size as the segment. A so-called canonical counter-rotating vortex pair can be used to explain the effects of strain rate and eddy interaction with a laminar flame. Figure 2.7 shows a two-dimensional cut through an artificial vortical structure. The vorticity $\vec{\omega}$ of the structure (Fig. 2.7a) and resulting strain rate magnitude S (Fig. 2.7b) is overlayed by the velocity vectors to visualize the flow of the fluid. The strain rate magnitude was calculated according to $S = (S_{xy} S_{xy})^{1/2}$. While the vorticity has its maximum at the center of the particular eddies, the strain rate maximum is reached at the top and bottom between the two eddies, where the

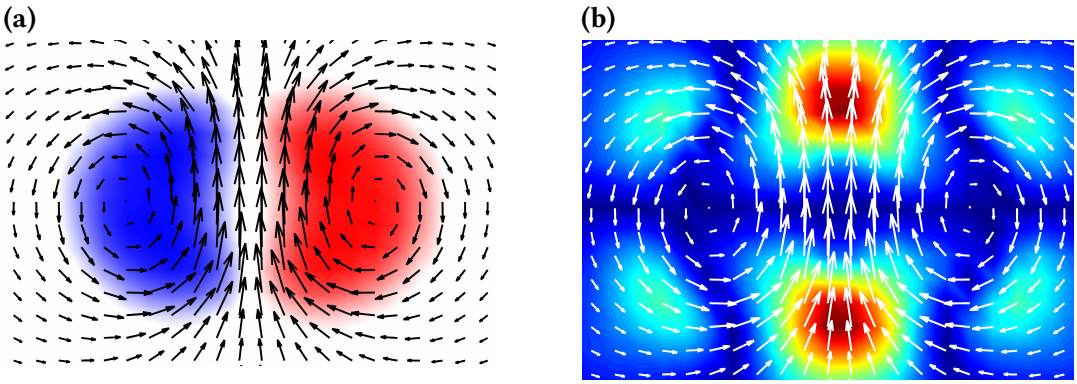

Figure 2.7: **(a)** Counter-rotating vortex pair with overlayed velocity field, the clockwise rotating vorticity $\vec{\omega_z}$ is shown in red. **(b)** Contour plot of the strain rate magnitude induced by the vortex pair. The strain magnitude was calculated according to $S = (S_{xy}S_{xy})^{1/2}$. The vector field was calculated from artificial images generated by PIVlab.[75]

flow starts to move outwards. The maxima are associated to the trailing (bottom) and leading (top) strain structures.

This results in a more strongly wrinkled flame and in an increase of flame surface of the now turbulent flame front.[76] The vortex/strain-interaction of a flame segment, traveling with the laminar flame speed u_l is shown schematically at four different time steps t_0 – t_3 in Figure 2.8. A more detailed theoretical and experimental study of the interactions is discussed in the work of Steinberg and Driscoll.[77] At time t_0, the flame segment, depicted by the gray bar, is still undisturbed and propagates downwards with a laminar flame velocity u_l. Between t_0 and t_1 the flame front starts to propagate off the leading strain structure and the flame segment is exposed to a positive strain rate $+S$. This results in an elongation of the segment, which is still considered laminar. The wrinkling of the flame is induced by the interaction of the strained flame with the counter-rotating eddies at t_2 and a cusp is formed. When the flame has passed the eddy structure and reaches the trailing strain structure at t_3, the flame segment is shortened due to negative strain $-S$. Even if the straining rates of leading and trailing structures are of the same magnitude before the flame interaction, they do not compensate each other and thus the stretching of the flame is not reversed. According to Steinberg and Driscoll, this is attributed to the amplification of turbulence itself by the interaction between turbulence and hot flame and $+S$ dominates over $-S$, leading to an increase of the flame surface. If the strain rates are sufficiently high enough, the flame front can be locally quenched as it was shown for the broken reaction zone regime.

Because of the high degree of different time scales and non-planarity of turbulent flows, it is obvious that interactions between the flow field and flame under

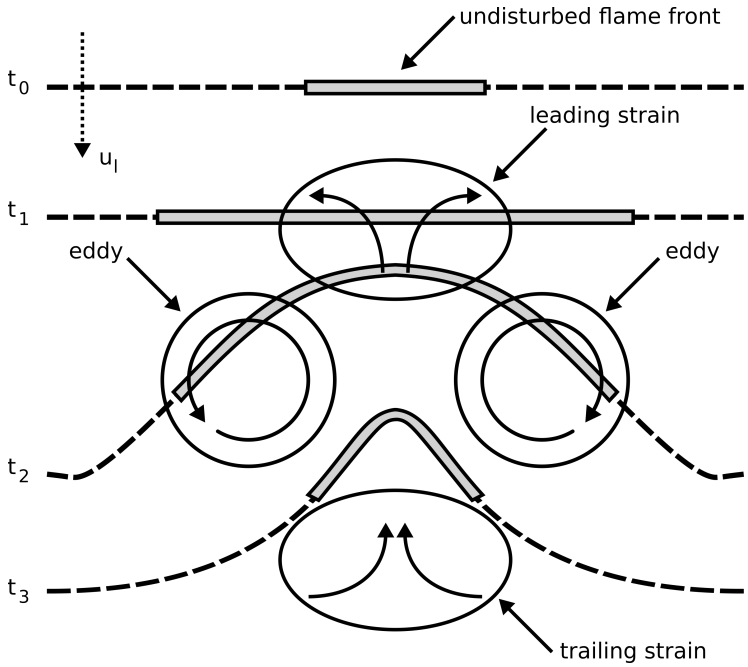

Figure 2.8: Schematic representation of the interaction between a laminar flame front traveling at the speed u_l with a canonical counter-rotating vortex pair. A segment of the flat flame is shown in grey. Due to the interactions of the leading strain element at t_1, the segment of the flame is stretched. At t_1, the stretched element is wrinkled by the vortical eddies and at the end (t_3) compressed by the trailing strain element. Adapted from Steinberg and Driscoll.[77]

highly turbulent conditions, as they occur in combustion engines, are still challenging to model using today's computer processing power.

2.2 Laser-based combustion diagnostics

As seen in the previous Chapter, small influences on the flame environment can alter the properties of the system dramatically. Before the widespread use of laser-systems for combustion diagnostics, physical properties had to be recorded using intrusive methods,[78,79] which often rely on single-point instead of multi-dimensional detection. To measure the temperature, thermocouples have to be placed inside the flow at one or more positions, if the temperature distribution is of interest. Fluid velocities are often determined using hot-wire anemometry (HWA).[80] This method uses a fine wire, heated up to temperatures above ambient conditions. If the wire is exposed to a moving fluid, it is cooled and according to the change of resistance with temperature, this can be correlated with the fluid velocity. Although thermocouples and HWA instruments offer high-frequency responses,

are easy to calibrate and demand low maintenance, they still have to be in direct contact with the fluid. Nowadays, Laser-based methods on the other hand have surpassed the traditional probe methods because of their high temporal and spatial resolution, their excellent sensitivity and in particular their chemical selectivity and non-intrusive nature. Various parameters such as particle and droplet size, temperature, concentration distributions and velocities can be determined.
Laser-based methods can be separated into two categories: Single-point and two- or more dimensional systems. Laser-Doppler anemometry to determine the fluid velocity or Rayleigh scattering, coherent anti-stokes raman scattering (CARS) and degenerate four-wave mixing (DFWM) for temperature and species concentration measurements are often used as single-point techniques, whereas (planar) laser-induced fluorescence ((P)LIF) and particle image velocity (PIV) are usually the methods of choice for multi-dimensional experiments (see Fig. 2.9). The next sections will give an overview of the two laser-based techniques used in this Thesis, PLIF and PIV.[81–83]

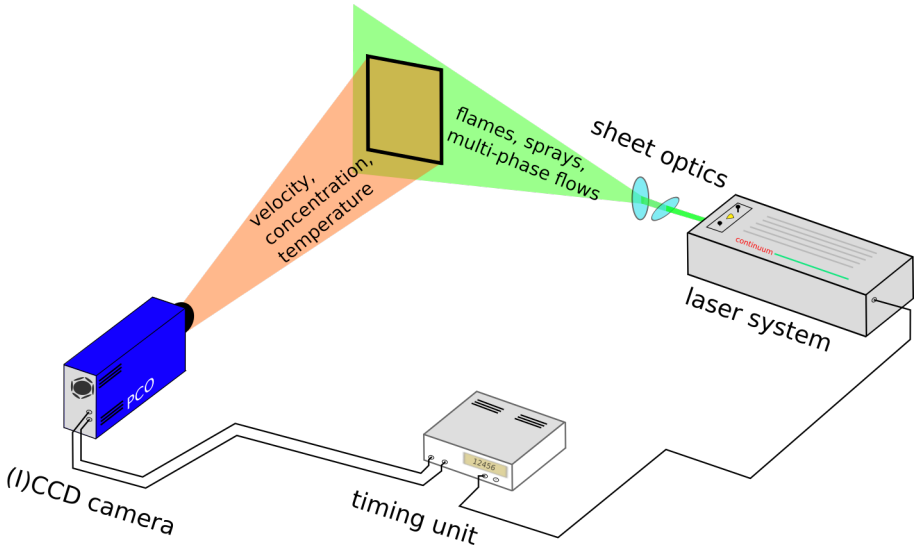

Figure 2.9: Schematic principle of two-dimensional imaging systems. The laser beam is expanded into a light sheet of several centimeters height and compressed below 1 mm in width using a combination of cylindric lenses. Scattered light or fluorescence usually is detected at a right angle.

2.2.1 Laser-induced fluorescence

The wide-spread use of tunable lasers with small spectral linewidths below 0.1 cm^{-1} and short pulse durations enable the electronic excitation of specific molecules in a mixture with also rotational selectivity, including short-lived intermediate species.

An important advantage in comparison with classical absorption techniques is the good spatial resolution, when the laser light is expanded into a light sheet and the fluorescence is detected at right angles with respect to the laser beam direction. In terms of data evaluation and experimental work, LIF experiments are rather simple; they require neither the use of multiple laser beams nor complex theoretical considerations.[83]

Before dealing with the important species used for LIF detection, an overview of the mathematical background for the use of LIF as a qualitative and quantitative detection scheme for species concentration and temperature will be discussed.[84–86]

2.2.1.1 Quantification of LIF signals

Figure 2.10 shows anharmonic potential energy surfaces for the electronic ground state X and first and second excited state A and B of a molecule, respectively. Upon irradiation, the molecule is excited from an electronic state 1 to an electronic state 2. b_{12} corresponds to the Einstein coefficient for absorption B_{12} using $b_{12} = B_{12} I_\mathrm{v}/c$, where I_v is the spectral irradiance of the light source.

After excitation, several processes for energy distribution or dissipation are possible:

i Stimulated emission upon absorption of a second photon b_{21} to the ground state

ii Collisional quenching $Q_{\mathrm{v,r}}$: Rotational (RET) or vibrational energy transfer (VET) in the excited state or electronic quenching to the ground state Q_{21}. Q_{21} heavily depends on the concentration and cross-section of other species present as well as the temperature.

iii Predissociation, if the molecule is excited near the crossing of a repulsive electronic state (predissociation rate P).

iv Absorption of a second photon with high energy which then ionizes the molecule (photoionization rate W).

v Spontaneous emission of a photon and return to the electronic ground state (A_{21}), the so-called fluorescence.

Collecting the photons emitted from the measurement volume using a light-sensitive quantum detector, e.g., an ICCD camera, the concentration of the fluo-

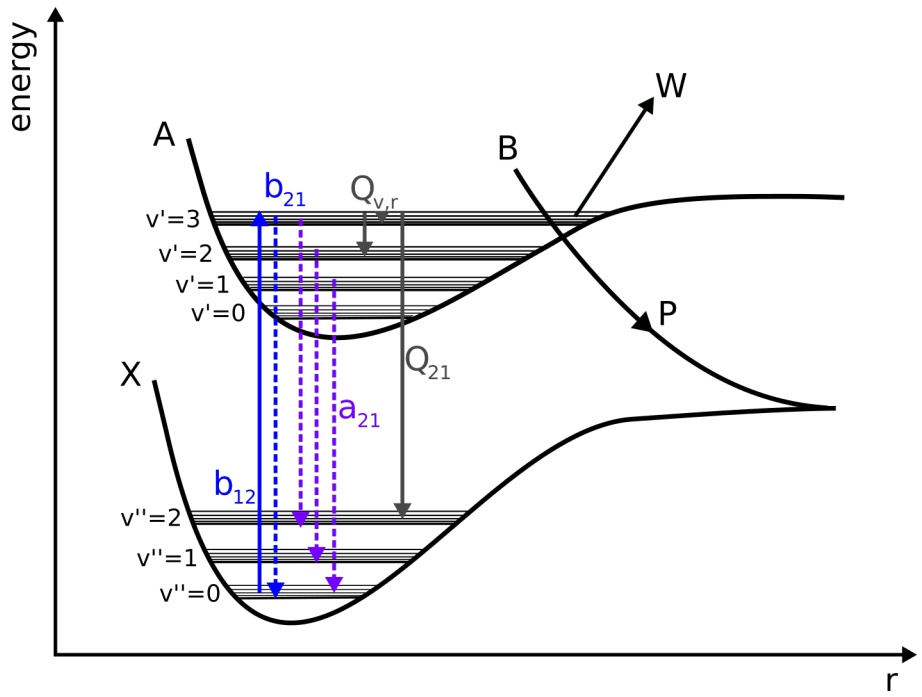

Figure 2.10: Three-level scheme for a two-atomic molecule upon irradiation. After excitation from the electronic ground state X into the first excited state A, the molecule can undergo transitions to the ground state via stimulated emission b_{21}, spontaneous emission a_{21}, collisional quenching Q_{21} or, if the excitation energy is high enough, be photoionized W or excited to a predissociative state B.

rescing species can be calculated. The rate equations for the change of population of the ground state can be written as

$$\frac{dN_1}{dt} = -N_1 b_{12} + N_2 \left(b_{21} + A_{21} + Q_{21}\right) . \tag{2.25}$$

If the excitation wavelength and intensity is chosen right, predissociation and photoionization can be neglected and the rate equation for the depopulation of the excited state can be written as

$$\begin{aligned} \frac{dN_2}{dt} &= N_1 b_{12} - N_2 \left(b_{21} + A_{21} + Q_{21} + P + W\right) \\ &\approx N_1 b_{12} - N_2 \left(b_{21} + A_{21} + Q_{21}\right) . \end{aligned} \tag{2.26}$$

The initial population of the excited state N_2 at the beginning of irradiation is small compared to the ground state population N_1 and since the rate of photoionization $W = 0$ results in population conservation, the overall number of population N is

$$N_1 + N_2 = const. = N = N_1^0, \tag{2.27}$$

where N_1^0 is the ground state population before irradiation. Using Equations 2.26 and 2.27 and solving for N_2 gives

$$N_2(t) = b_{12} N_1^0 \cdot k^{-1} \left(1 - e^{-(k \cdot t)}\right) , \tag{2.28}$$

with $k = b_{12} + b_{21} + A_{21} + Q_{21}$. For times shorter than the duration of the laser pulse, the population of the excited state rises linearly and reaches a constant value for $k \cdot t \gg 1$. Using $b_{12} = B_{12} I_\mathrm{v}/c$, N_2 can be rewritten as

$$N_2 = \frac{b_{12} \cdot N_1^0}{b_{12} + b_{21} + A_{21} + Q_{21}} = N_1^0 \cdot \frac{B_{12}}{B_{12} + B_{21}} \cdot \frac{I_\mathrm{v}}{I_\mathrm{v} + I_\mathrm{v,sat}} . \tag{2.29}$$

$I_\mathrm{v,sat}$ is the saturation intensity and is defined as

$$I_\mathrm{v,sat} = c \cdot \frac{A_{21} + Q_{21}}{B_{12} + B_{21}} . \tag{2.30}$$

The number of detectable photons, that is the fluorescence signal S_LIF, is proportional to the population density in the first excited state N_2 and the Einstein coefficient for spontaneous emission A_{21}

$$S_\mathrm{LIF} \propto N_2 A_{21} . \tag{2.31}$$

With experimental parameters, i.e. the photon energy $hc\nu$, the detection angle Ω, the measurement volume V and an efficiency constant for the collection optics ϵ, the fluorescence signal becomes

$$S_\mathrm{LIF} = hc\nu \frac{\Omega}{4\pi} \epsilon V \cdot N_1^0 A_{21} \frac{B_{12}}{B_{12} + B_{21}} \frac{I_\mathrm{v}}{I_\mathrm{v} + I_\mathrm{v,sat}} . \tag{2.32}$$

If the laser intensity I_v is much smaller than the saturation intensity $I_\mathrm{v,sat}$, the fluorescence signal S_LIF rises linearly with the laser intensity and can be reduced to

$$S_\mathrm{LIF} = hc\nu \frac{\Omega}{4\pi} \epsilon V \cdot N_1^0 \frac{B_{12}}{c} \frac{A_{21}}{A_{21} + Q_{21}} I_\mathrm{v} . \tag{2.33}$$

The LIF intensity is proportional to the number of molecules in the measurement volume $N_0^1 V$, but also depends strongly on the so-called Stern-Vollmer factor $A_{21}/(A_{21} + Q_{21})$, which gives the efficiency of the fluorescence. Since the quenching rate is usually much faster than the spontaneous emission – the fluorescence quantum yield in flames at atmospheric pressures is below 1 % –, the overall fluorescence intensity is weak. However, to quantify the species concentration, the quenching rate must be calculated using thermochemical data, which can be a challenging task. To make S_LIF independent of Q, the laser intensity must be

high enough to reach saturated conditions. In the so-called saturation LIF, the fluorescence signal simplifies to

$$S_{\mathrm{LIF}} = hc\nu \frac{\Omega}{4\pi} \epsilon V \cdot N_1^0 A_{21} \frac{B_{12}}{B_{12} + B_{21}} \,. \tag{2.34}$$

Under experimental conditions, this approach is difficult to obtain, because the laser pulse has to reach saturated properties in spectral, temporal and spatial dimensions. The laser intensities needed for a complete saturation are often higher than the damage threshold of the optical elements, and can lead to photoionization of the molecules. A third method is the use of fluorescence from a predissociative state, usually named LI(P)F. Here, the predissociation rate P cannot be neglected and the fluorescence signal depends on

$$S_{\mathrm{LIF}} = hc\nu \frac{\Omega}{4\pi} \epsilon V \cdot N_1^0 A_{21} \frac{B_{12}}{P_2 \cdot c} I_{\mathrm{v}} \,. \tag{2.35}$$

Albeit avoiding the aforementioned drawbacks of linear and saturation LIF, predissociative states usually have a low quantum yield, limiting the detectability of the desired molecule. The approach of the two-level LIF for molecules is not so good. The electronic states consist of several vibrational and rotational sublevels, which are coupled via collisional energy transfers. In thermal equilibrium, the population can be described using Boltzmann statistics and the relative population is

$$\frac{N_{\mathrm{J}''}}{N} = \frac{2J'' + 1}{kT} \exp\left(-\frac{E_{\mathrm{J}''}}{kT}\right) = P\left(T\right) \,, \tag{2.36}$$

where $N_{\mathrm{J}''}$ is the population in a rotational sublevel J'' and $E_{\mathrm{J}''}$ its energy. To avoid changes in fluorescence intensity due to changes in temperature during combustion, it is feasible to excite rotational lines that are nearly unaffected by temperature. The relative populations of the $\mathrm{Q}_1(6)$ and $\mathrm{Q}_1(8)$ line in the $\mathrm{A}^2\Sigma^+ \leftarrow \mathrm{X}^2\Pi$ (1,0) OH radical transition at 283.01 nm vary by less than 10 % in the temperature range between 1500 K and 2000 K (values calculated using LIFBASE[87]). The connection of LIF signal to the species concentration can be used to derive a second interesting quantity in combustion diagnostics, the temperature. Since the LIF signal is correlated to the population of the ground state, the signal strength also depends on the Boltzmann distribution

$$S_{\mathrm{LIF}} \propto P\left(T\right) \,. \tag{2.37}$$

If two different transitions 1 and 2 are excited, the ratio of the two LIF signals is[88,89]

$$R_{12} = \frac{\epsilon_1 I_1 \cdot g_1 \exp\left(-E_1/kT\right) \cdot B_1 \Gamma_1\left(p,T\right) A_1/\left(A_1 + Q_1\left(p,T\right)\right)}{\epsilon_2 I_2 \cdot g_2 \exp\left(-E_2/kT\right) \cdot B_2 \Gamma_2\left(p,T\right) A_2/\left(A_2 + Q_2\left(p,T\right)\right)} \tag{2.38}$$

where g_i is the degeneracy of the state i, E_i the energy of the state and Γ the laser overlap. Assuming that the quenching rate Q dominates over A and is independent of rotational quantum numbers and the laser overlap is independent of T and p, the temperature is a function of

$$T = \frac{-\Delta E_{12}/k}{\ln\left(R_{12}/C\right) - \ln\left(I_1/I_2\right)}\,. \tag{2.39}$$

C is a calibration parameter for the experimental setup and ΔE_{12} is the energy difference between the two lower absorbing levels. If a species, e.g., an aromatic hydrocarbon, has a broad emission spectrum, the temperature can be measured using a so-called single-excitation/two-color detection scheme that exploits the redshift. The molecule is excited by a single laser pulse and two different emission wavelengths, called "blue" and "red" channel, are detected simultaneously using spectral filtering.[90] The signal ratio then reduces to

$$\frac{S^\mathrm{red}}{S^\mathrm{blue}} = c\frac{\phi^\mathrm{red}}{\phi^\mathrm{blue}} = f\left(T\right) \tag{2.40}$$

which only needs a calibration curve to determine temperatures from the signal ratios.

2.2.1.2 Fluorescent species used for LIF in combustion diagnostics

The following Section gives an overview of several molecules used in combustion diagnostics for a broad variety of different chemical and physical properties of the reacting flows, e.g., flame front imaging for laminar and turbulent interactions, concentration measurements of pollutants and calculation of heat release rate and temperature. Besides „intrinsic“molecules that are formed during the decomposition of the fuel, the use of added particles, so-called tracer molecules, will be discussed with regard to their photophysical properties and application advantages.

OH: The hydroxyl radical (OH) plays an important role during the combustion of hydrocarbons (see Figure 2.1), since it is the main radical doing the abstraction of H atoms. OH is formed at temperatures above 1500 K close to the main reaction

zone. Behind the main reaction zone, the oxidation zone starts, where the hydroxy concentration is lowered due to reactions with CO forming CO_2. Since OH radicals show high concentration in the burned gas, OH LIF can be used to distinguish between unburned mixture and the burned gas.[91] During the formation of an electric spark, the OH concentration rises to values of 4.5%.[92]

OH radicals can be electronically excited using several schemes. Figure 2.11a

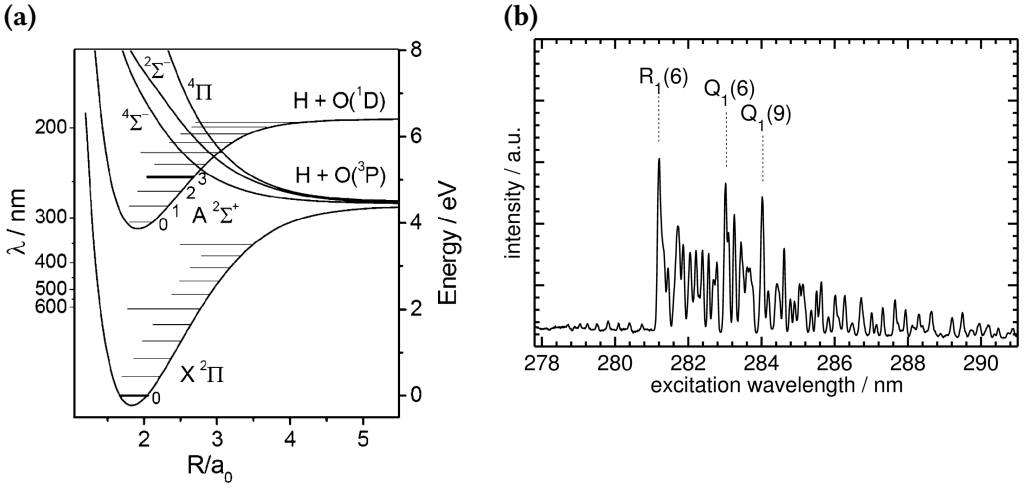

Figure 2.11: (a): Potential energy curves for different electronic states of the OH radical. Reproduced from Ref. [93] with permission from the PCCP Owner Societies. **(b)**: Excitation spectrum of OH radicals in a methane-air flame. The emission in an interval from 305 nm to 317 nm was averaged after excitation of the radical to the $A^2\Sigma^+(1,0)$ and (2,1) states.[94,95]

shows the calculated potential energy curves for the electronic ground state ($X^2\Pi$) and first excited state ($A^2\Sigma^+$) as well as the first three predissociative states.[93] An experimental excitation spectrum of OH in a methane-air flame at ambient pressure is shown in Figure 2.11b.[94,95] The radicals were excited from the electronic ground state to the first excited state using the $A \leftarrow X\,(1,0)$ transition, starting at 278.5 nm and $A \leftarrow X\,(2,1)$ transition starting at 287.4 nm. The emission was collected over a wavelength range of $302\,\text{nm} < \lambda < 333\,\text{nm}$. The most intensive transitions belong to the $R_1(6)$ rotational line at 281.22 nm, the $Q_1(6)$ line at 283.01 nm and the $Q_1(9)$ line at 284.01 nm. All the lines benefit from a small population change of less than 5 % over a temperature range of 1300 K – 2000 K, but are close to the maximum of the distribution. For quantitative measurements, it must be checked that the absorption does not significantly attenuate the laser power.[96]

The (3,0) band is, despite of its low transition probability of $5.717 \cdot 10^{-5}$, still a very interesting target for LIF measurements because of two important characteristics: First, it coincides with the central wavelengths of KrF excimer lasers at 248 nm, making it experimentally easily accessible. Second, the higher rotational levels of the (3,0) band offer access to a predissociative state $A^4\Sigma^-$ that minimizes the effect

of fluorescence quenching. An overview of the most common A–X transitions and the corresponding transition probabilities is given in Table 2.2.

Table 2.2: Experimental vibrational transition probabilities $p_{\nu'\nu''}$ for the most common OH $A^2\Sigma^+ \leftarrow X^2\Pi$ transitions and their corresponding wavelength.

$\nu' \leftarrow \nu''$	λ_{trans} / nm	$p_{\nu'\nu''}$ [87]
0,0	308	$1.073 \cdot 10^{-2}$
1,0	281	$2.613 \cdot 10^{-3}$
1,1	314	$6.775 \cdot 10^{-3}$
2,0	262	$4.058 \cdot 10^{-4}$
2,1	287	$4.147 \cdot 10^{-3}$
3,0	245	$5.717 \cdot 10^{-5}$

Due to its ubiquitous occurrence in flames, the OH radical is used in a wide range of application fields and techniques for combustion research.[83] As shown in Figure 2.12, OH detection techniques can be divided into temporal categories, using either single pulse measurements or averaging over several laser pulses, and spatial categories, e.g., two- or even three-dimensional imaging,[97] or single-point measurements. The applications range from fundamental kinetics to discover details of chemical mechanisms at low pressures[98] to the investigation of the interaction of the flame chemistry and the flow field and diagnostics in technical combustion chambers[92,99–101] or burners[102,103] at high pressures, often by combining 2D LIF with other non-intrusive methods like PIV.[91,104,105] Nonetheless, it should be noted that the edges of the OH distribution may not always correspond to the flame front. Especially at high Reynolds numbers in turbulent flows, where the flame can be distorted or multiple folded, the flame front may not be located at the edge of the OH radicals.[91]

CH: CH is an intermediate in Fenimore NO_x forming processes,[106] takes part in the decomposition reaction of the primary fuel and plays an important role in pollutant formation.[107,108] In addition, CH is implicated in soot formation in hydrocarbon flames.[109] Furthermore, it is often used as a flame front marker, especially for the investigation of turbulent flame structures,[110,111] since CH is directly formed in the reaction zone of a flame and relatively short-lived.[110] When CH is measured, the discontinuities in the CH field are often attributed to localized extinction in laminar and turbulent flames. To expose flames to unsteady strain and curvature, flame-vortex interactions provide a well-controlled environment to evaluate CH radicals as flame front markers.[110] Even with this broad spectrum of feasible applications, the detection of CH is still a challenging task. In a laminar methane-air flame, the concentration of CH reaches a maximum of 6 ppb in an

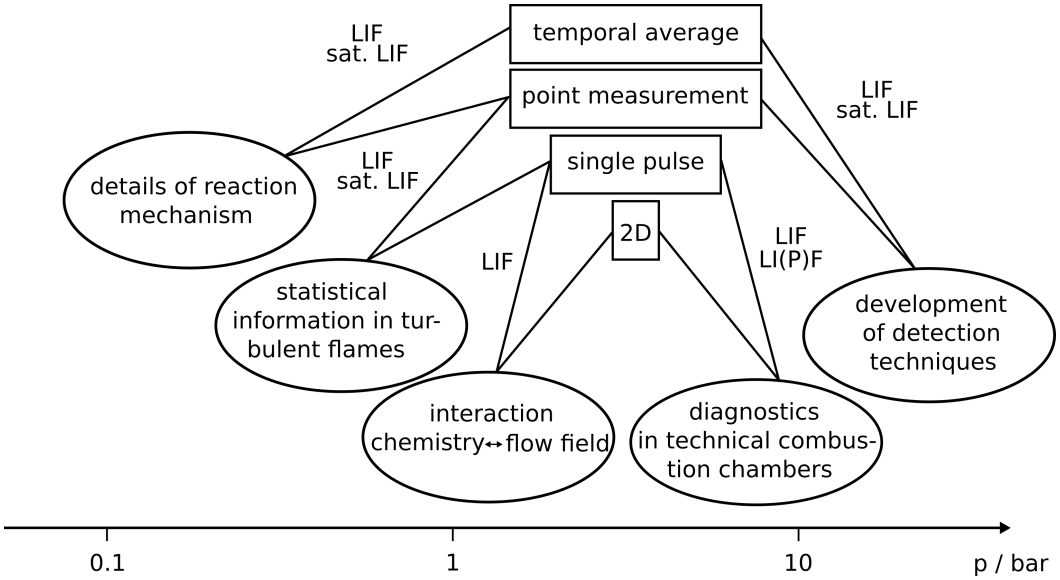

Figure 2.12: Overview of common applications for OH LIF detection techniques in different combustion environments, ranging from sub-atmospheric pressure measurements for the investigation of chemical reaction mechanism to high-pressure detection in technical combustion chambers. Adapted from Kohse-Höinghaus.[83]

approximately 0.2 mm thick layer. With this low abundance, the CH radical reaches only 1 ppm of the concentration of OH even under ideal conditions.[112]

The excitation and detection schemes cover a broad spectral range. One common scheme uses the $R_2(5)$ transition of the $B^2\Sigma^- – X^2\Pi$ (0,0) band near 387.3 nm and broadband fluorescence from the B–X (0,1), A–X (1,1) and A–X (0,0) bands overlapping at around 431 nm.[91,108,110] CH can also be used for pre-dissociation LIF, using the $C^2\Sigma^+ – X^2\Pi$ band for excitation, although this suffers from significant reduction of the fluorescence signal due to weak transition probabilities of the off-diagonal transitions.[108] Detection of the diagonal (1,1) and (0,0) bands after excitation of the $A^2\Delta – X^2\Pi$ (1,0) band suffers from the same effect.[113] For excitation of the A–X (0,0) transition and detection from the same band, a series of narrowband interference filters have to be used to transmit the Q-branch emission while blocking scattered laser light, reducing the fluorescence signal as well.[114] Due to these problems, CH PLIF is still limited to applications for turbulent flame structures due to its finite detection limits,[115] and often a combination of different species detection like OH and CH_2O LIF has to be applied.[91]

CHO: Flame properties like the heat release rate cannot be imaged directly and must be inferred from images of other physical or chemical properties.[116] As shown by Najm and co-workers, chemiluminescence measurements are generally not reliable for monitoring of the heat release rate,[117] OH LIF lacks the contrast to uniquely identify the thin flame front and the OH radical is an insensitive indicator

of the local heat release rate. The CH concentration is not directly correlated to the heat release rate and as CH is often used to display the shape of the flame, it may wrongly correlate the breaking of the surface to the heat release rate. Finally, the formyl radical CHO was identified to correlate well with the temporal and spatial maximum heat release rate for three reasons:[107,117] (*i*) The decomposition of CHO to CO and H is faster than its formation rate, thus the CHO concentration is directly proportional to the production rate. (*ii*) A substantial part of the carbon reacting from fuel to products flows through the CHO channel, making CHO a good monitor for the carbon fuel. (*iii*) The CHO production depends mainly on the concentration of formaldehyde, which in turn is formed through the reaction $CH_3 + O \leftrightarrows CH_2O + H$, which shows the largest fractual influence on heat relase.[117] Like the CH radical, CHO suffers from low concentrations that lead to low signal-to-noise ratios even at frame averaging.[116] Additionally, the formyl radical reacts also a pollutant similar to NO, as it is a contributor to photochemical smog.[118]

CH_2O: Formaldehyde is a typical first-step intermediate that appears in the cold regions before CHO is formed. This happens mainly in the beginning of the flame front, which makes formaldehyde an ideal target to detect early, unwanted stages of combustion, e.g., engine knock phenomena[112] or to study geometry effects of the combustion chamber at the start of the combustion process.[119] Collin et al. showed that at early compression stages in a HCCI engine, the OH- and CH_2O LIF signal never appear at the same local region, making formaldehyde an ideal target for distinction of low- and high temperature reactions.[100] According to Paul et al., the product of OH and CH_2O concentrations is proportional to the reaction rate of $CH_2 + OH \rightarrow H_2O + CHO$ and can be used to estimate the production rate of CHO.[116] Due to the high abundance of CH_2 and OH in the flame front region, this provides an attractive choice for single-shot flame front detection in highly turbulent systems.[120] Formaldehyde is usually detected using excitation of the 4_0^1 band (355 nm) as well as the $4_0^1 2_0^1$ band (339 nm) and detected over a broad wavelength range (360–550 nm).[120,121] However, quantification of the CH_2O fluorescence is complicated, especially at engine conditions. Spatial filters to single out wavelength bands have to be applied and the remaining spatially resolved light is then interpreted to stem from formaldehyde. This is not necessarily true, because a large variety of heavier species like polycyclic aromatic hydrocarbons (PAHs), which, build up during the start of combustion, fluoresce over a broad wavelength range.[121,122]

NO: The strict regulation of NO_x emission is a major challenge for designers of automotive engines. In Diesel engines, the overall air/fuel ratio deviates from unity, making the treatment of the exhaust gases difficult. Therefore, the overall amount of NO_x emission has to be decreased by reducing the amount of NO formed during

the fuel combustion. Therefore, to monitor the physical and chemical processes leading to NO formation, the understanding and development of low-emission IC engines could be considerably enhanced.[123] Different attempts for NO detection have been used over the years. Excitation at 193 nm using the D-X (0,1) band suffers, despite the high intensities of ArF excimer lasers, from strong attenuation within the combustion chamber. The data have to be corrected for variations of laser intensity assuming homogeneous distribution of particles, which is not always true,[124] thus making the interpretation of the fluorescence images difficult.[14] This drawback can be avoided using the A–X (0,0) transition around 226 nm, generated by an optical parametric oscillation (OPO) system and the utilization of partially oxygenated fuels lacking the production of soot particles.[125] Due to its wide availability, the use of KrF excimer laser for probing the A–X (0,2) band at 248 nm is still the most favorable excitation in IC engine applications. Additionally, the (0,1) band can be used for the detection of NO. This strongly discriminates NO against interfering LIF of hot oxygen and intermediate hydrocarbons.[123]

The NO radical is also conveniently used for LIF thermometry. While the use of the OH radical for thermometry in lean and non-sooting combustion is a common task, its concentration under fuel-rich conditions drops significantly due to the low temperatures and low levels of oxidizing species.[126] For applications of LIF in those flames, tracer can be seeded into the fuel to increase the fluorescence signal. However, it is essential for the seeded particles not to interfere with the combustion process, which makes the use of native tracers favorable.[127] While seeding of NO to the flame is a commonly accepted procedure for two-line thermometry both in pre- and post-flame zones,[128,129] reduction of the NO concentration can occur in fuel-rich flames.[130] This is due to a large influence of NO reburning through the reactions NO + CH $\rightarrow$ HCN + O and NO + CH_2 $\rightarrow$ HCNO + H and HNC + OH, increasing the oxidation of soot particles.[131]

Tracer molecules: Tracer molecules are used for a broad range of applications, e.g., visualization of the fuel/air equivalence ratio or mixture fraction, thermometry or to distinguish between burned and unburned fuel. Usually, there are two cases that require the addition of fuel tracers to measure the fluid field. First, the components of the fuel do not fluoresce or fluoresce only weakly, for example air and exhaust gases like CO_2 and H_2O, which have accessible red-shifted spectra for combustion diagnostics only at high temperatures. The second case includes fuels that contain too many fluorescent species, which tend to overlap in their spectral properties, as it is often the case for commercial fuels. The requirements for the added tracers range from being chemically inert to absence of interference with the flame chemistry to lack of decomposition at elevated temperatures for distinguishing between burned and unburned fractions. Depending on the ap-

plication, tracers should behave exactly like the fluid in terms of their physical properties like droplet formation, evaporation, diffusion, or chemical parameters like reactivity and reaction rate. Additionally, the ideal tracer should yield a LIF signal that is directly proportional to the desired information. The LIF signal of aromatic tracers is strongly affected by quenching of oxygen, thus making the LIF signal not only dependent on the tracer concentration, but also inversely on the oxygen content. This can be exploited by using the LIF signal as indicator for the fuel/air ratio.[86,132] To avoid quenching and decomposition of the tracer, metal atoms like rubidium, thallium, indium or lead can be added to the fuel.[133,134] Indium is an established tracer for two-line atomic thermometry, often in sooting flames, where intrinsic tracers suffer from low abundance or collisional quenching effects.[135] The spin-orbit coupling of the 5P indium ground state leads to a spacing of the energy levels that allows for measurements over a wide temperature range from 1000 K – 3000 K.[89] The lines used for thermometry at 410.18 nm ($5P_{1/2}$–$6S_{1/2}$) and 451.13 nm ($5P_{3/2}$–$6S_{1/2}$) are commonly excited using dye or extended cavity diode laser systems.

Toluene: Toluene is often chosen because it fits well with the evaporation and ignition behavior of gasoline fuels. The fluorescence quantum yield of the $S_1 \leftarrow S_0$ ($\pi\pi^*$) transition is fairly high ($\phi \approx 0.3$) compared to other tracer molecules, with one of the main absorption bands near the wavelength of the fourth-harmonic of a Nd:YAG laser (266 nm).[136] Nevertheless, the absorption cross-section of toluene changes drastically in the temperature range of 300 – 1000 K and the quantum yield decreases by more than two orders of magnitude. In the absence of oxygen, toluene is a sensitive molecule for single line thermometry in homogeneously seeded environments.[137]

3-pentanone: For fuels like iso-octane, non-aromatic ketones are well suited as tracer molecules because of their similar evaporation properties. Furthermore, the influence of collisional quenching by oxygen is reduced compared to aromatic compounds due to their lifetimes being controlled by rapid intersystem crossing. 3-pentanone exhibits an absorption spectrum between 220 nm and 340 nm ($n\pi^*$ transition) with a peak near 280 nm. The influence of temperature can be minimized when the tracer is excited near the maximum of the absorption band, allowing for a direct measurement of fuel-tracer number density.[132,138,139]

Acetone: Another commonly used non-aromatic ketone for fluorescence tracing is acetone, which shows similar photophysical properties to 3-pentanone. The excitation wavelengths range from 225 nm to 320 nm, and the fluorescence occurs between 350 nm and 550 nm.[140] While the absorption spectrum shows a strong red-shift with temperature, the emission spectrum is largely unaffected by temperature

changes, making both acetone and 3-pentanone useful for two-line excitation and single-line detection techniques.[141,142] Compared to other ketones, acetone has a much higher vapor pressure, which makes is suitable for LIF under ambient conditions. Acetone decomposes when it is exposed to temperatures above 1000 K so that no acetone fluorescence is observable in the combustion zone.[143–145] For cold regimes, like the conditions at the intake stroke of an IC engine, acetone has been used for simultaneous measurements of temperature and fresh air fraction in a direct injection spark ignition (DISI) engine with exhaust gas recirculation (EGR).[146]

2.2.2 Particle image velocimetry

Laser-induced fluorescence is a versatile tool used for flow visualization, even for extremely complicated flow fields. The use of fluorescent tracers enables researchers to perform the measurement of mixing and mixing velocity of the fluids.[147,148] Nevertheless, in case of just one fluid compound or premixed fluids, different techniques have to be applied. Laser-based velocity measurements often rely on seeded solid or liquid tracer particles for the elastic scattering of light, which is detected using the Doppler-shift of two crossed laser beams at a single point. This technique is called laser Doppler anemometry (LDA). To obtain multi-dimensional information, the scattered light of at least two temporally delayed laser light sheets have to be recorded and the velocity of the fluid U_f can be calculated measuring the displacement Δx of particles in a given time interval Δt.[149] This method is called particle image velocimetry (PIV). The experimental setup of a PIV system can be divided into several subsystems: (*i*) The particle generator adds the tracer particles to the flow. (*ii*) The particles have to be illuminated by a plane of light at least twice by a short (pulsed) light source. (*iii*) The scattered light by the particles has to be recorded either in one frame (single-frame/double exposure, 1F2E) or in a sequence of frames (double-frame/single exposure, 2F1E). (*iv*) Based on the detection technique, different evaluation schemes have to be applied.[150] The following Chapter gives an overview of the experimental prerequisites and the data evaluation for the flow measurements.

2.2.2.1 PIV methods

For the flow-field measurements performed in this Thesis, the double-frame/single exposure method was used. Figure 2.13 shows the difference between 1F2E (a)

and 2F1E (b). For the first, the scattered light of a particle is recorded at a time

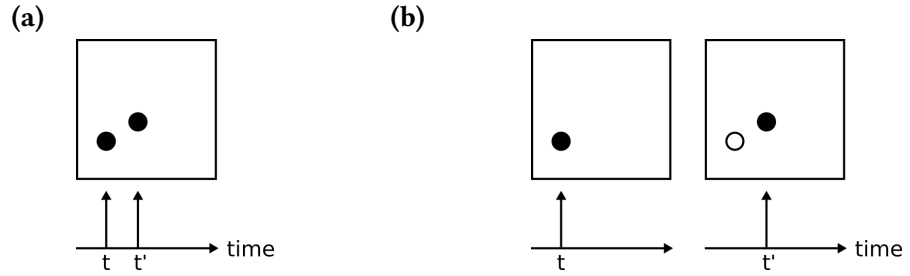

Figure 2.13: (a) Experimental principle for single-frame/double-exposure. The scattered light at time t and $t^{'}$ is captured on the same frame and analyzed via autocorrelation. **(b)** Double-frame/single-exposure principle. The second exposure is captured on a second frame and analyzed using cross-correlation.[150]

t and after a short delay time at $t^{'}$ on the same frame. If the particle has moved sufficiently, the second signal will show up at a different position of the frame. The velocity of the particle is then evaluated using an autocorrelation between the two signals. Since it is not known which of the signals belongs to t and which to $t^{'}$, the autocorrelation cannot determine an unambiguous direction of motion. Nevertheless, this technique rests on simple electronic equipment for detection and can be performed even with household digital cameras. Depending on the time delay between the two exposures, the 1F2E technique requires a camera with a rather fast frame rate, which increases the overall costs for the experiment. Compared to the autocorrelation of a single frame, the two frames acquired via 2F1E are evaluated using cross-correlation and since it is known, which particle signal belongs to the first exposure, the information obtained with 2F1E gives the velocity and the direction of the flow. Due to the non-uniformity of turbulent flows and the high amount of information provided by a large number of particles in the imaging plane, the cross-correlation is not performed on the whole image but rather in so-called interrogation areas which are evenly placed over the image.

Depending on the application, the flow can only be seeded to a certain degree because of interfering effects between tracer particles and reacting flow, e.g., PIV measurements around the edges of a flame. Figure 2.14 shows three different cases of seeding density. For low image density, individual particles can be detected and identified on consecutive images from the same measurement. The velocity is only determined at random locations in the image in contrast to higher seeding density methods, where the velocity is measured uniformly across the observation plane.[151]

In case of medium density, interrogation areas contain several particles, and identification of image pairs is not possible anymore. This leads to dividing the picture into interrogation areas and correlating the movement of the interrogation

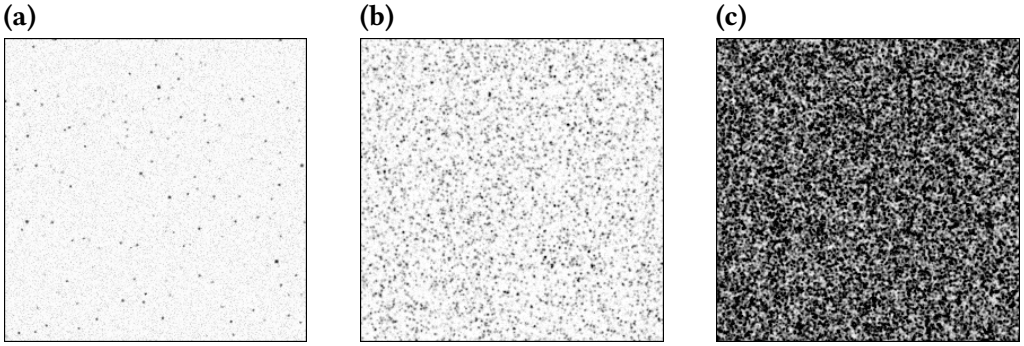

Figure 2.14: **(a)** Low particle density image showing individual particles used for Particle Tracking Velocimetry (PTV). **(b)** Medium-density image for Particle Image Velocimetry. **(c)** High density image, particles tend to overlap and cannot be distinguished anymore. All images were inverted.

area with each other independent of movement of single particles. For high density seeding, particles tend to overlap and form speckles, hence the name laser speckle velocimetry, and it is rather the speckles than the particles themselves that provide the information of movement.

2.2.2.2 Tracer particles and their fluid mechanical properties

Compared to indirect methods like hot wire anemometry or pressure probe techniques, PIV yields a direct measurement of two components, distance and time, by which the velocity in the investigated direction is defined. But as the detection technique of PIV relies on the scattered light of particles seeded into the flow and not of the flow itself, a direct measurement is only valid, if the fluid mechanical differences between the flow and tracer are negligible.

The particles effectiveness to follow the flow can be derived from basic fluid mechanical dynamics of a two-phase flow. To these ends, the particles are treated as spherical particles in a viscous fluid with low Reynolds number. The arbitrary translational motion under an external force $f(t)$ can be described using the Basset function:[152–154]

$$\begin{aligned}\frac{4}{3}\pi d_\mathrm{p}^3 \rho_\mathrm{p} \frac{\mathrm{d}U_\mathrm{p}}{\mathrm{d}t} =& f(t) - \underbrace{6\pi\mu_\mathrm{f} d_\mathrm{p} \left(U_\mathrm{f} - U_\mathrm{p}\right)}_{1} - \underbrace{\frac{2}{3}\pi\rho_\mathrm{f} d_\mathrm{p}^3 \frac{\mathrm{d}}{\mathrm{d}t}\left(U_\mathrm{f} - U_\mathrm{p}\right)}_{2} \\ & \underbrace{- 6\pi d_\mathrm{p}^2 \frac{1}{\sqrt{\pi\nu_\mathrm{f}}} \int_{-\infty}^{t} \frac{1}{\sqrt{t-\tau}} \frac{\mathrm{d}}{\mathrm{d}\tau}\left(U_\mathrm{f} - U_\mathrm{p}\right) \mathrm{d}\tau}_{3} \,.\end{aligned} \tag{2.41}$$

Here, ρ_p, d_p and U_p are the density, diameter and velocity of the particle and ρ_f, ν_f, μ_f and U_f are the density, dynamic and kinematic viscosity and the velocity of the fluid. The three terms on the right hand side represent the quasi-steady Stokes drag (1), the inertial drag due to added mass (2) and the Basset force (3), which accounts for the unsteadiness of the flow. For particles in a gaseous flow, the density of the particles is much higher than the fluid density, and Equation 2.41 is dominated by the Stokes terms and can be reduced to

$$\frac{\mathrm{d}U_\mathrm{p}}{\mathrm{d}t} = -\frac{18\mu}{\rho_\mathrm{p} d_\mathrm{p}^2}\left(U_\mathrm{p} - U_\mathrm{f}\right) . \tag{2.42}$$

The Stokes drag law can only be applied for particles with Reynolds numbers smaller than unity,[150,155]

$$Re_\mathrm{p} = \frac{\rho_\mathrm{f}\left(U_\mathrm{f} - U_\mathrm{p}\right) d_\mathrm{p}}{\mu_\mathrm{f}} = \frac{\left(U_\mathrm{f} - U_\mathrm{p}\right) d_\mathrm{p}}{\nu_\mathrm{f}} , \tag{2.43}$$

which holds true for small differences in velocity and small particles, e.g., tracer particles used for PIV. The velocity lag U_s of a particle exposed to a flow with the continuous acceleration a can be expressed as

$$U_\mathrm{s} = U_\mathrm{p} - U_\mathrm{f} = d_\mathrm{p}^2 \frac{\left(\rho_\mathrm{p} - \rho_\mathrm{f}\right)}{18\mu_\mathrm{f}} a . \tag{2.44}$$

The step response of the particle with a greater density than the flow generally follows an exponential decay,

$$U_\mathrm{p}\left(t\right) = U_\mathrm{f}\left[1 - \exp\left(-\frac{t}{\tau_\mathrm{p}}\right)\right] . \tag{2.45}$$

The relaxation time τ_p is one of the most important characteristics in selecting the seed material, since it describes the particles' tendency to follow the velocity fluctuations in the flow. It can be calculated using

$$\tau_\mathrm{p} = \frac{\rho_\mathrm{p} d_\mathrm{p}^2}{18\mu_\mathrm{f}} . \tag{2.46}$$

The rule of thumb for ideal tracers is a Stokes number S_p much smaller than unity. S_p is given by the ratio of the relaxation times of the particle τ_p and the flow τ_f,

$$S_\mathrm{p} = \frac{\tau_\mathrm{p}}{\tau_\mathrm{f}} , \tag{2.47}$$

where the time scale of the flow is related to its length L and velocity U_f,

$$\tau_\mathrm{f} = \frac{L}{U_\mathrm{f}} \,. \tag{2.48}$$

But even if a particle is small enough to follow the fluid flow, it is sometimes hard to find a compromise between ideal particle size and scattered light intensity on the recording device. The scattering depends on the ratio of both the refractive index of the particle and the surrounding, the particle size, shape and orientation, the polarization of the light and the angle of observation. If the (spherical) particle size is larger than the wavelength of the irradiation source, the Mie solution to Maxwell's Equations, often called Mie theory, can be applied. Figure 2.15 shows the polar distribution for the light scattering of a wavelength of $\lambda = 532$ nm at different sized oil particles in air. As it can be seen, the intensity of the scattered light at 90° increases by a factor of 10^4 for a $d = 10$ µm particle compared to $d = 1$ µm. At first

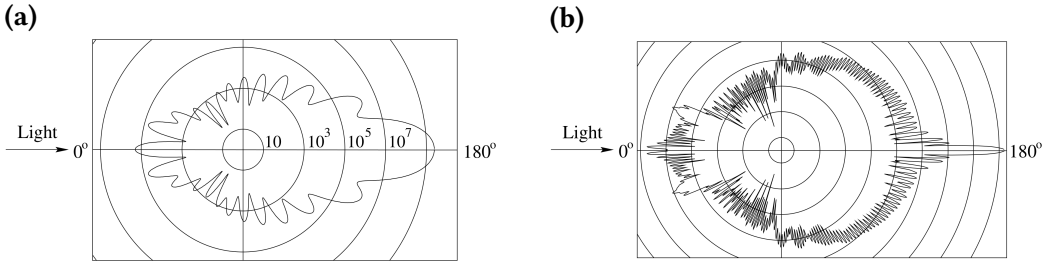

Figure 2.15: Radial intensity distribution for light scattered by a 1 µm oil particle **(a)** and 10 µm oil particle **(b)** in air. Each circle stands for an increase in intensity by a factor of 10^2.[150]

sight, it seems feasible to increase the particle diameter to get better signal-to-noise ratio, since the effect of particle size on the scattered light is much higher than increasing the intensity of the light source itself. But in reality, this approach fails for two reasons: First, the particle diameter is a property of the particle material and aerosol generator, which usually produces particles with a diameter distribution depending on the Laskin nozzle (see Fig. 2.16). Second, the response time of larger particles might be not sufficiently short enough to follow the rapid fluid fluctuations. The best way to get high-contrast images is an increase of the seeding density.

Table 2.3 gives on overview of common solid and liquid materials used as tracer particles. Besides the before mentioned oil, household olive oil or di-ethyl-hexyl-sebacate (DEHS) are used as liquid tracers, because of their non-toxic, color- and odorless characteristics. Both DEHS and olive oil offer a long lifetime and give almost spherical droplets, but are not stable at higher temperatures.

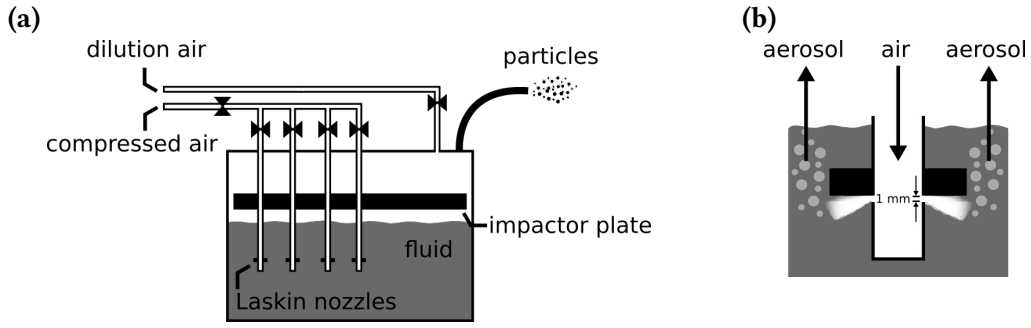

Figure 2.16: **(a)** Schematic drawing of an aerosol generator used for PIV. The aerosol is generated using a series of Laskin nozzles acting as atomizers. **(b)** Closeup of the Laskin nozzle.

The employed aerosol generator consists of two main parts: The reservoir, filled with the liquid tracer or a solution of the solid tracer, e.g., Al_2O_3 in water, and the high-pressure system and Laskin nozzle, submerged in the reservoir. The Laskin nozzle is a tube with four radial holes of 1 mm diameter. Above the holes, a ring is secured with four adjacent holes above the air exits. Compressed air flows at high velocity out of the radial holes and creates small air bubbles containing the tracer. When the bubbles reach the surface, they burst and release the particles to the air above the liquid. The flow rate can be increased by combining several Laskin nozzles and the by increasing the air pressure.[156]

Table 2.3: Examples of solid and liquid seeding materials used for tracer particles in gaseous flows.[150]

Type	**Material**	**Mean diameter/**µm
solid	polystyrene	0.5 - 10
	Al_2O_3	2 - 7
	glass micro-balloons	30 - 100
	granules for synthetic coating	10 - 50
	smoke	< 1
liquid	different oils	0.5 - 10
	di-ethyl-hexyl-sebacate (DEHS)	0.5 - 1.5
	helium-filled soap bubbles	1000 - 30000

2.2.2.3 Cross-correlation for double-frame/single-exposure images

To derive a mathematical description for the cross-correlation, some basic parameters have to be defined. All particles are located at random positions at a certain time t in a $3N$-dimensional space that is described by:

$$\mathbf{\Gamma} = \begin{pmatrix} \mathbf{\Psi}_1 \\ \mathbf{\Psi}_2 \\ . \\ . \\ . \\ \mathbf{\Psi}_N \end{pmatrix}, \mathbf{\Psi_i} = \begin{pmatrix} X_i \\ Y_i \\ Z_i \end{pmatrix} . \tag{2.49}$$

$\mathbf{\Psi}_i$ is the position vector of a particle i at a time t. Since all pictures are taken with a certain magnification factor, the particle position in the measurement plane is related to the 2-dimensional position in the imaging plane $\boldsymbol{\psi}$, defined by

$$\boldsymbol{\psi} = \begin{pmatrix} x \\ y \end{pmatrix}$$

according to $X_i = x_i/M$ and $Y_i = y_i/M$. The intensity distribution for an intensity field I can be written as

$$I(\psi, \mathbf{\Gamma}) = \sum_{i=1}^{N} V_0(\mathbf{\Psi_i}) \, \tau(\boldsymbol{\psi} - \boldsymbol{\psi}_i) , \tag{2.50}$$

where $\tau(\boldsymbol{\psi})$ describes the point spread function of the imaging lens and $V_0(\mathbf{\Psi})$ the shape, extension and location of the interrogation volume with respect to the light sheet intensity. For the second image at time $t' = t + \Delta t$, a constant displacement $\mathbf{\Delta}$ for all particles is assumed, which changes the particle location $\mathbf{\Psi}$ to

$$\mathbf{\Psi_i'} = \mathbf{\Psi_i} + \mathbf{\Delta} = \begin{pmatrix} X_i + \Delta_x \\ Y_i + \Delta_y \\ Z_i + \Delta_z \end{pmatrix} . \tag{2.51}$$

The particle image displacement $\boldsymbol{\delta}$ is given by

$$\boldsymbol{\delta} = \begin{pmatrix} M\Delta_x \\ M\Delta_y \end{pmatrix} . \tag{2.52}$$

It is treated as a simplified projection in the vicinity of the optical axis. The intensity field for second exposure then is similar to Equation 2.50,

$$I^{'}\left(\boldsymbol{\psi},\boldsymbol{\Gamma}\right)=\sum_{j=1}^{N}V_{0}^{'}\left(\boldsymbol{\Psi_{j}}+\boldsymbol{\Delta}\right)\tau\left(\boldsymbol{\psi}-\boldsymbol{\psi_{i}}-\boldsymbol{\delta}\right)\ . \tag{2.53}$$

To simplify the calculation, the light sheets and windowing characteristics are considered to be identical and the cross-correlation function can be written as

$$R_{\mathrm{II}}\left(\mathbf{s},\boldsymbol{\Gamma},\boldsymbol{\Delta}\right)=\frac{1}{a_{\mathrm{I}}}\sum_{i,j}V_{0}\left(\boldsymbol{\Psi_{j}}\right)V_{0}\left(\boldsymbol{\Psi_{j}}+\boldsymbol{\Delta}\right)\int_{a_{\mathrm{I}}}\tau\left(\boldsymbol{\psi}-\boldsymbol{\psi_{i}}\right)\tau\left(\boldsymbol{\psi}-\boldsymbol{\psi_{j}}-\mathbf{s}-\boldsymbol{\delta}\right)d\boldsymbol{\psi} \tag{2.54}$$

where a_{I} is the interrogation area and $\mathbf{s}$ the separation vector in the correlation plane. Assuming a Gaussian particle image density distribution, Equation 2.54 can be rewritten as

$$R_{\mathrm{II}}\left(\mathbf{s},\boldsymbol{\Gamma},\boldsymbol{\Delta}\right)=\sum_{i,j}V_{0}\left(\boldsymbol{\Psi_{j}}\right)V_{0}\left(\boldsymbol{\Psi_{j}}+\boldsymbol{\Delta}\right)R_{\tau}\left(\boldsymbol{\psi_{i}}-\boldsymbol{\psi_{j}}+\mathbf{s}-\boldsymbol{\delta}\right)\ . \tag{2.55}$$

All terms $i\neq j$ represent the correlation of different particles and only contribute to noise in the correlation plane, while all terms $i=j$ contain the displacement information. Therefore, the correlation function $R_{\mathrm{II}}\left(\mathbf{s},\boldsymbol{\Gamma},\boldsymbol{\Delta}\right)$ can be split into two parts

$$\begin{aligned}R_{\mathrm{II}}\left(\mathbf{s},\boldsymbol{\Gamma},\boldsymbol{\Delta}\right)=&\sum_{i\neq j}V_{0}\left(\boldsymbol{\Psi_{j}}\right)V_{0}\left(\boldsymbol{\Psi_{j}}+\boldsymbol{\Delta}\right)R_{\tau}\left(\boldsymbol{\psi_{i}}-\boldsymbol{\psi_{j}}+\mathbf{s}-\boldsymbol{\delta}\right)\\&+R_{\tau}\left(\mathbf{s}-\boldsymbol{\delta}\right)\sum_{N}^{i=1}V_{0}\left(\boldsymbol{\Psi_{i}}\right)V_{0}\left(\boldsymbol{\Psi_{i}}+\boldsymbol{\Delta}\right)\ .\end{aligned} \tag{2.56}$$

According to Keane and Adrian,[157] the cross-correlation function can be decomposed into three components,

$$R_{\mathrm{II}}\left(\mathbf{s},\boldsymbol{\Gamma},\boldsymbol{\Delta}\right)=R_{\mathrm{C}}\left(\mathbf{s},\boldsymbol{\Gamma},\boldsymbol{\Delta}\right)+R_{\mathrm{F}}\left(\mathbf{s},\boldsymbol{\Gamma},\boldsymbol{\Delta}\right)+R_{\mathrm{D}}\left(\mathbf{s},\boldsymbol{\Gamma},\boldsymbol{\Delta}\right)\ , \tag{2.57}$$

where $R_{\mathrm{D}}\left(\mathbf{s},\boldsymbol{\Gamma},\boldsymbol{\Delta}\right)$ represents the correlation component that corresponds to the correlation of particles obtained from the first image with the identical particles obtained from the second image $(i=j)$:

$$R_{\mathrm{D}}\left(\mathbf{s},\boldsymbol{\Gamma},\boldsymbol{\Delta}\right)=R_{\tau}\left(\mathbf{s}-\boldsymbol{\delta}\right)\sum_{i=1}^{N}V_{0}\left(\boldsymbol{\Psi_{i}}\right)V_{0}\left(\boldsymbol{\Psi_{i}}+\boldsymbol{\Delta}\right)\ . \tag{2.58}$$

The displacement is maximal for $\mathbf{s}=\boldsymbol{\delta}$ and its location gives the corresponding u and v velocity components of the flow. Compared to other methods like auto-

correlation in case of double-exposed single images, the cross-correlation results in only one peak, which can be unambiguously assigned to the particle's movement.

As mentioned before, it is not possible to identify individual particles and do the cross-correlation for every single particle. Therefore, the image is divided into square interrogation windows (IW). To correlate the interrogation windows of the two image pairs, the windows can be shifted around in the spatial domain, the so-called Direct Cross Correlation (DCC), or first can be fast-Fourier transformed into the frequency domain by the Discrete Fourier Transform (DFT) approach. The DCC methods uses IWs of different sizes, usually B is twice the size of A.[158] Interrogation window A is then shifted around over the area of B in x and y direction and for each shift the overlapping pixel intensities give one cross-correlation value $R_{\mathrm{II}}(x, y)$ (see Figure 2.17) forming a $(2M + 1) \times (2N + 1)$ matrix, with M and N the range of shifts in x and y direction. One major drawback of this method is the linearity of the DCC method, which allows no recovery of fluid rotation or deformation.[159,160] This can be overcome by choosing the IWs so small that these second-order effects can be neglected at the cost of an increased computational time.

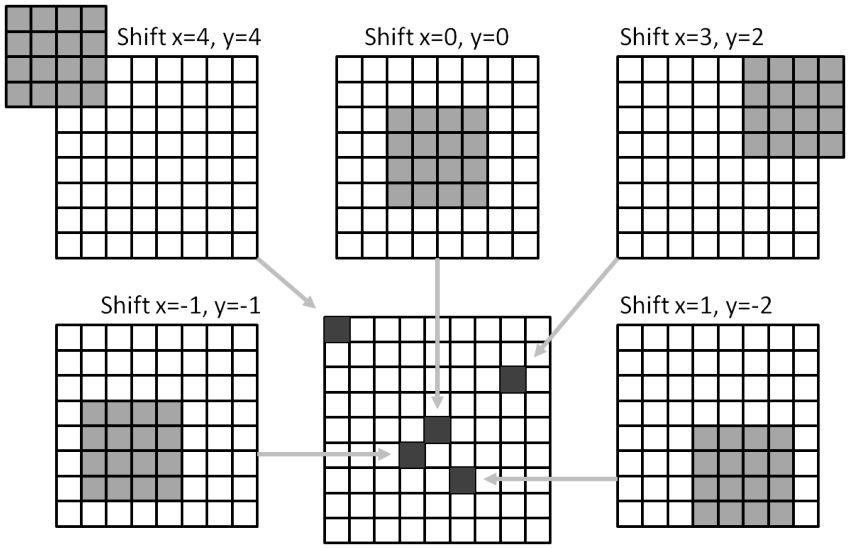

Figure 2.17: Schematic representation of the IW shifting to calculate the cross-correlation matrix. The second IW (4 × 4 pixels, filled gray squares) is shifted over the initial IW (8·8 pixels, white squares). This results in a final a 9 × 9 pixels cross correlation matrix. Adapted from Ref. [150] and [161].

The tedious two-dimensional correlation of the DCC method can be overcome using FFT with equal interrogation window sizes $N \times N$.[162–164] After a complex-conjugated multiplication of the Fourier coefficients, these are inversely Fourier transformed and yield an $N \times N$ correlation matrix. This reduces the computational costs from $\mathrm{O}[N^4]$ to $\mathrm{O}[N^2 \log_2 N]$, but increases the amount of background noise due to the displacement's loss of information. A second problem lies in the nature of the FFT itself, as the definition assumes that all interrogation windows are periodic

and repeat themselves in all directions. For displacements greater than half the size of the IW, the correlation peak will flip on the opposite site of the matrix, giving false results. This can be overcome by running several FFT calculations on the same data set, significantly increasing the signal-to-noise ratio.[165] Also, the decrease in time between frames, the increase of the interrogation window and a decrease in camera resolution can benefit the SNR, the latter with a decrease in information of the flow. An increase in resolution can be achieved by refining the interrogation area with every pass, using a large IW for the first pass to allow large particle displacements and decreasing the IW size with every step. During the work of this Thesis, the FFT method was used and will be explained in detail in the experimental Section.

Figure 2.18 shows the vector field (Fig. 2.18a) calculated from an artificial image pair with a high particle displacement and the corresponding cross-correlation maps for the vectors marked by the red (Fig. 2.18b) and blue (Fig. 2.18c) squares. The vector field was calculated using the FFT method and an initial IW size of 64×64 pixels with 32 pixels step size, refined by a second run with a IW size reduced by 50 %. The correlation map of Fig. 2.18c shows just one correlation maximum R_{D} for the displacement that can be unambiguously assigned to a valid vector. For low signal-to-noise ratio IWs or in case of high particle displacement, the correlation map in Fig. 2.18b exhibits more than one maximum and results in a bad vector.

2.2.2.4 Particle displacement and error sources

The accuracy of PIV measurements depends on a huge variety of factors, including the target flow field properties, the tracer particles, optical setup and data acquisition, and finally the data post-processing. One known experimental deficit of optical flow techniques in a two-dimensional plane is the instability to out-of-plane motion of the particles, which in the end leads to a loss of image correlation and consequently wrong velocity vectors. Especially in highly turbulent flows all two-dimensional techniques have to cope with strong three-dimensional movements with different velocities. The easiest way to prevent out-of-plane loss is the precise tuning of the laser pulse delay time to values as short as possible without neglecting the in-plane motion. A second, less applicable possibility, is the tuning of the light sheet. Although the demand for the light sheet is to be as small as possible, an increase in thickness can reduce the ratio of particle loss to overall amount of particles, thus leading to fewer erroneous correlations. Nevertheless, these two

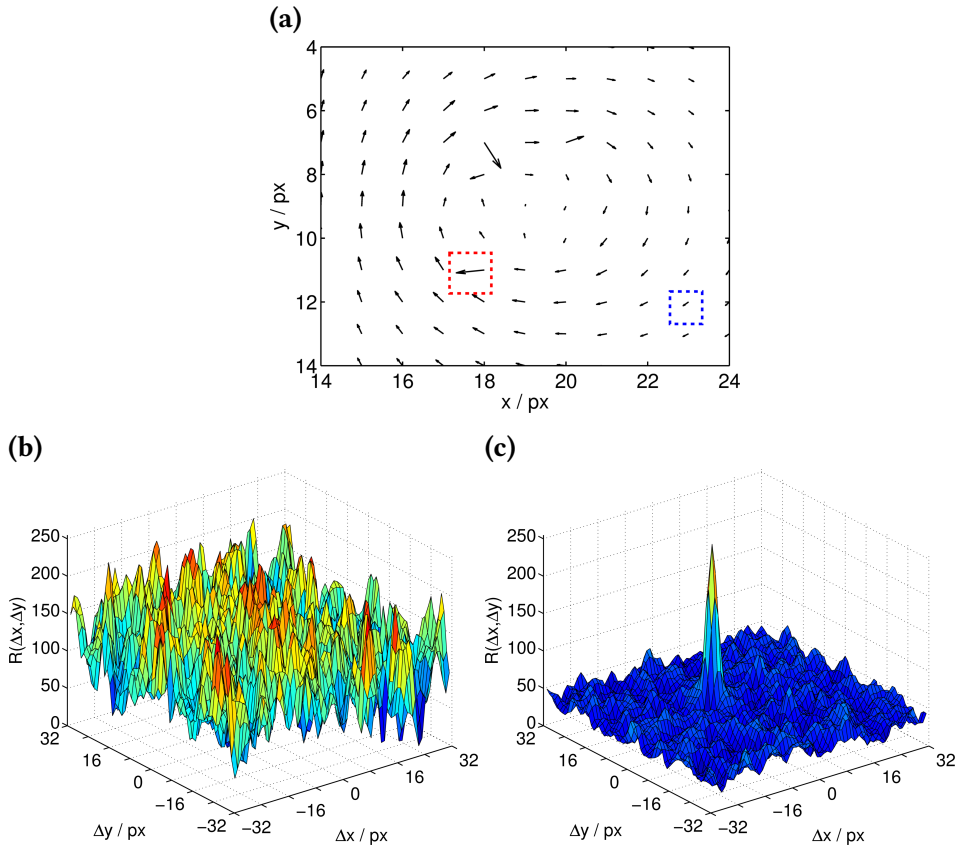

Figure 2.18: **(a)** Vector field calculated from an artificial image pair with high particle displacement. The vector marked by the red square represents a so-called bad vector without physical meaning. This is due to the lack of a clearly distinguishable cross-correlation peak for the interrogation window **(b)**. For sufficiently high signal-to-noise ratio or small particle displacement, only one cross-correlation peak is visible for interrogation window **(c)**.

parameters are not known at first and have to be tested for every experiment separately using a try-and-error approach.[150]

A possible error source lies in the mathematical method itself. The input data are discretized due to the camera pixels, thus the correlation value is only found for integral shifts and the highest correlation value can only be determined with an uncertainty of $\pm\frac{1}{2}$ pixel, if no other data evaluation method is applied. The cross-correlation is a statistical method and a lot of information is hidden underneath the correlation values. If an interrogation window contains ten particles with a mean displacement of 2.5 pixels, five particles will contribute with a displacement of 3 pixels and 5 with 2 pixels, respectively. To get a higher accuracy from the correlation value, a variety of methods estimating the real location of the peak, the so-called subpixel estimation methods, can be utilized. A simple way of doing this is the centroiding method that calculates the ratio of the first-order image moment to the zeroth-order image moment using a threshold to discriminate the correlation

values from the background noise, which is not always trivial as it was shown in Figure 2.18b).[150] Fitting a function to the correlation data provides a more robust method. Gaussian subpixel estimation is the common choice for particles described by an Airy intensity distribution. Usually a Gaussian-shaped function is fitted to three adjacent correlation peaks both in x- and y-direction separately. The subpixel value is then described by the maximum of the distribution (see Fig. 2.19)[163,166–168]

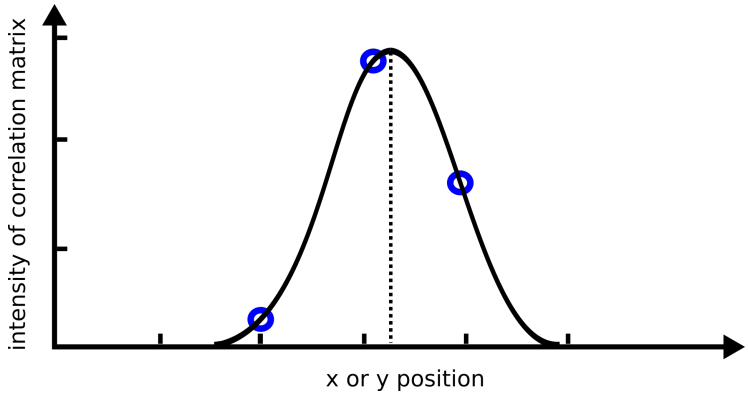

Figure 2.19: Subpixel estimation using 2×3 Gaussian profile. To get the exact position of the correlation peak, a one-dimensional Gaussian is fitted to the integer correlation intensities. The dashed line marks maximum of the Gaussian, which is used as the subpixel value.

Despite its advantages, subpixel estimation can lead to severe bias errors, the so-called peak locking, if the ratio of the particle diameter d_p to the pixel size d_pix is $d_\mathrm{p}/d_\mathrm{pix} < 2$. For small particle sizes, the images are under-resolved. The subpixel estimator cannot determine the exact position and tends to lock the value towards integer pixels.[168,169] The Gaussian estimator[170] and, even more so the sinc estimator[166] are known to mitigate the problems of peak locking and thus are superior to centroid or quadratic fits.

Random errors, often called root-mean-square (RMS) errors, are, apart from flow and tracer sources, affected by many factors, especially non-uniformity of illumination and reflection, detector dark current noise and hot pixel, readout noise from the cables and digitalization errors.[163] The right choice for the most appropriate or most accurate PIV treatment is still a not trivial task, because it is quite difficult to isolate the restrictive experimental and post-processing parameter for the accuracy of the PIV technique.[171]

2.2.2.5 Image decomposition for instantaneous velocity fields

The velocity fields, obtained from a single 2F1E experiment, are called instantaneous velocity fields that depict only one moment in time of an ongoing experiment. Statistical information on the experiment is often calculated using decomposition of ensemble averaging over a number of instantaneous fields. Nevertheless, a single instantaneous field itself can be used for decomposition, e.g., to reveal vortices hidden under the mean velocity field.[172] Therefore, the field is separated based on the scale of the fluid motion in space or time and the mean of the total velocity vector $\mathbf{u}$ is defined as

$$\mathbf{U}(\mathbf{x}, t) \equiv \langle \mathbf{u} \rangle \tag{2.59}$$

and calculated using either time or spatial averaging. The de-facto standard method for describing turbulent velocity by decomposition into mean fluctuation portions is the Reynolds decomposition. Depending on the choice of investigation and interest in information, different decompositions may offer better methods for visualization of the turbulent mechanics of the flow. If statistical relationships for improved Reynolds-averaged Navier-Stokes models are of interest, the Reynolds decomposition is the ideal choice. However, for the identification of small scale vortices hidden under the flow field, large eddy simulation (LES) decomposition, proper orthogonal decomposition (POD) or Galilean decomposition may be the method of choice.[173]

Reynolds decomposition: The Reynolds decomposition can be viewed as a scale decomposition in time or space, depending upon the definition of the mean. In general, the overall velocity field $\mathbf{u}$ is the sum of the scale velocity $\mathbf{U}$ and a fluctuating velocity part $\mathbf{u}'$:

$$\mathbf{u} = \mathbf{U} + \mathbf{u}' . \tag{2.60}$$

If the mean is determined by long-time averaging, the velocity field is decomposed into an infinite time-scale and a fluctuation part that contains all other components of shorter time scale. If the mean is calculated by averaging in one or more spatial dimensions, the mean can vary both in time and in the non-averaging directions. The velocity field is then decomposed in an infinite scale velocity and a part that fluctuates on finite scales and in time.

LES decomposition: If a sufficient amount of image pairs is not available or if the decomposition of a single image pair is of interest, the large eddy simulation

decomposition offers a more general approach. The separation of the velocity field is purely done in space and is defined as low-pass filtering the field as[174,175]

$$\overline{\mathbf{u}}\left(\mathbf{x},t\right)=\int\limits_{D}f\left(\mathbf{x},\mathbf{x}^{'}\right)\mathbf{u}\left(\mathbf{x}^{'},t\right)\mathrm{d}\mathbf{x}^{'} \tag{2.61}$$

to obtain the filtered large scale field $\overline{\mathbf{u}}$. f is the filtering kernel and D is the domain of the velocity field. The filtering kernel can be split into two groups: Homogeneous filtering using a shift-invariant kernel, e.g., Gaussian, or top hat filtering, when $f\left(\mathbf{x},\mathbf{x}^{'}\right)$ can be simplified to $f\left(\mathbf{x}-\mathbf{x}^{'}\right)$ and the total field is the sum of the low-pass filtered field $\overline{\mathbf{u}}$ and the smaller-scale part $\mathbf{u}^{''}$. To calculate $\mathbf{u}^{''}$, the filtered field is subtracted form the instantaneous velocity field

$$\mathbf{u}-\overline{\mathbf{u}}=\mathbf{u}^{''}\,. \tag{2.62}$$

A turbulent flow field is often characterized by statistically inhomogeneous directions, which a homogeneous filter cannot recognize. The advantage of proper orthogonal decomposition is its change as a function of the inhomogeneous coordinate. POD filters are constructed of a set of basis functions for an ensemble of data.[176] For a time-dependent, two-dimensional domain $\mathbf{x}=(x_1,x_2)$, the filtered velocity can be expressed as

$$\overline{u}_i\left(x_1,x_2\right)=\sum_{k=0}^{k}\sum_{n=0}^{n}H^{(k,n)}a^{(k,n)}\left(t\right)\Psi_i^{(k,n)}\left(\mathbf{x}\right)\,. \tag{2.63}$$

$H^{(k,n)}$ is a filter characteristic function that amplifies or attenuates the strength of each POD mode, Ψ is an orthogonal basis for the ith velocity component and a are the time-dependent expansion coefficients. Again, the velocity can be decomposed using Equation 2.62.

Galilean decomposition: Galilean transformation is the simplest method of decomposition. The total velocity $\mathbf{u}$ is represented by the sum of a constant convection velocity $\mathbf{U}_\mathrm{c}$ and the deviation $\mathbf{u}_\mathrm{c}$:

$$\mathbf{u}=\mathbf{U}_\mathrm{c}+\mathbf{u}_\mathrm{c}\,. \tag{2.64}$$

The convection velocity can either be a freely selected constant independent of time and space, or, if $\mathbf{U}_c$ corresponds to a local region, the convection velocity has the property of a moving-average low-pass filter.

Experimental Part

3

The experimental part of this Thesis is divided into four parts: First, the combustion chamber including the electronic controls and the gas supply system will be introduced. The second part deals with the combustion behavior for different fuel compositions under laminar and turbulent conditions, the third part focuses on the flame front expansion and the last part covers the particle image velocimetry measurements. Because all experiments are a novelty in this work group, a strong emphasis will be placed on the experimental setup and data evaluation procedures.

The basic setup of the experiments is shown in Figure 3.1. The chamber was equipped with a light barrier (LB) to measure the piston velocity and a pressure transducer (PT). Both were read out using an oscilloscope. All electronics were controlled using a homebuilt trigger box, which was synchronized with the Q-switch signal of a laser or, for measurements without laser, a 10 Hz frequency generator. The details of the components will be explained in the following Sections.

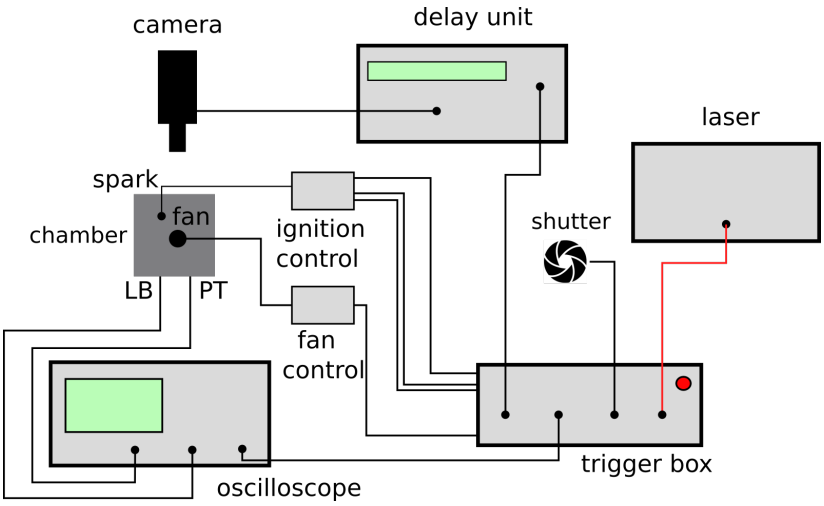

Figure 3.1: Schematic overview of setup used for pressure/piston velocity measurements and imaging experiments.

3.1 Combustion chamber

The engine used in this Thesis is a single-cylinder internal combustion engine that operates similar to a two-stroke IC engine. A metered amount of fuel is injected into a cylinder head filled with air at ambient conditions. The fuel-air mixture is ignited subsequently by a spark discharge. The expanding gas pushes a piston with a connected drive pin to the bottom of the cylinder. The piston is then lead back to its initial position, according to the top dead center (TDC) of a crank shaft engine. This happens either due to the underpressure generated by the movement of the piston or by using a small amount of exhaust gases pushing the piston to TDC.

The schematic setup of the chamber is shown in Figure 3.2 by a horizontal and a vertical cut through the cylinder and cylinder head. The cylinder head is equipped with an in- and outlet pipe to either flush the chamber with fresh air or fill it with premixed fuel-air compositions. Pure fuel can be injected using external cartridges (fuel cells, FC). A small electric motor equipped with a four bladed fan (d_{fan} = 61 mm) for fuel mixing and induction of turbulence is installed in the center of the head. The spark plug is placed at a distance of 14 mm from the wall. The spark gap is 6 mm. The volume of the cylinder head is V = 240 cm^3 for minimum insertion depth of the electric motor. The cylinder has a maximum stroke of 137.0 mm and is equipped with a piston, d_{pist} = 56.4 mm. All dimensions are summarized in Table 3.1.

Table 3.1: Dimensions of the internal combustion engine.

type	**part**	**dimension**
combustion chamber	width / depth / height	72.5 / 72.5 / 45.5 mm
	volume	240 cm^3
	fan diameter	61 mm
	fan height	10 mm
	spark plug distance from wall	14 mm
	spark gap	6 mm
cylinder	height	164.5 mm
	stroke	137.0 mm
	bore	56.4 mm

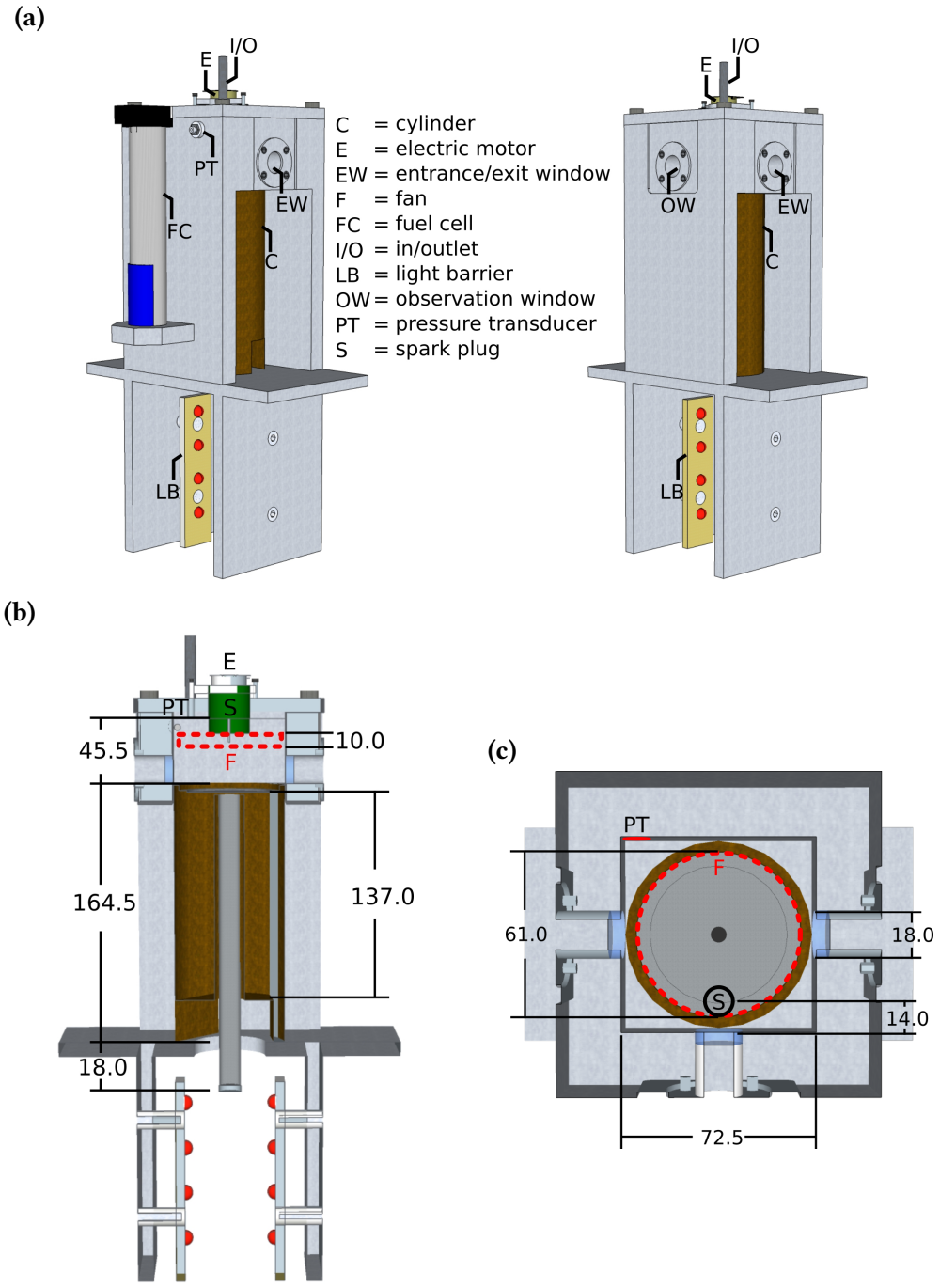

Figure 3.2: Schematic drawings of the combustion chamber. The fuel can be injected using external cartridges (fuel cells, FC) or the chamber is filled with premixed fuel-air compositions using the in-/outlet pipes. **(a)** Back and front view of the chamber and observation windows centered in the cylinder head. **(b)** Vertical cut through the chamber. **(c)** Horizontal cut through the cylinder head. All dimensions are given in mm. The position of the fan is marked by the dashed red line, the spark plug position is represented by the black circle.

For the pressure measurements, a modified cylinder head was used, which has a different position of the spark plug, as shown in Figure 3.3a. The spark plug

(**SP1**) is positioned slightly off-axis. For the experiments using dual-spark ignition, the cylinder head was equipped with a second spark plug (**SP2**) opposite of the first spark plug. Figure 3.3b shows the cylinder head used for the LIF and PIV measurements.

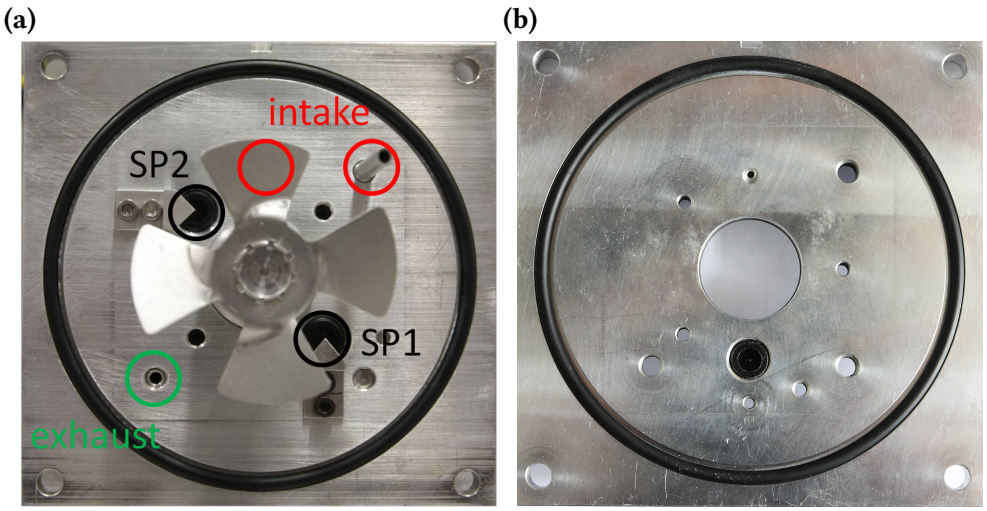

Figure 3.3: **(a)** Modified cylinder head used for the pressure measurements with the off-axis spark plug (**SP1**) position. For the experiments using dual-spark ignition, the cylinder head was equipped with a second spark plug (**SP2**) opposite of the first spark plug. **(b)** Cylinder head used for the LIF and PIV measurements with the spark plug positioned on the center axis.

3.1.1 Electronics setup

Due to the single-stroke nature of the original nail gun, it is not trivial to automatize the experiments for the combustion diagnostics. To achieve reproducible results, the electronics of the nail gun had to be re-designed to match the accurate timing needed for the synchronization of the laser and readout electronics. The timing and distribution of the electronic trigger signals were controlled using a homebuilt setup shown in Figure 3.4. The electric fan and spark generation were regulated using optical fibers (**a**–**d**), the incoming and outgoing TTL signals were distributed among BNC connectors (**1**–**5**). All timing delays were adjusted using the front panel in combination with a micro controller (ATMEL Mega 88).

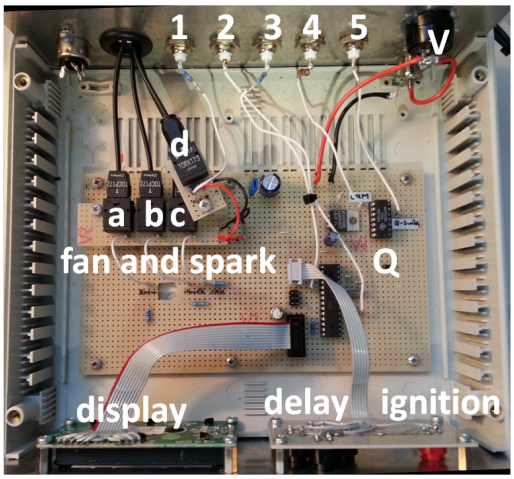

Figure 3.4: Electronic set-up of the trigger box. The circuit diagram can be found in the appendix.

3.1.1.1 Spark ignition system

To generate the spark, a coil ignition system in combination with a 12 V rechargeable battery was used. The battery powered both the spark system and the electric motor, which required a lower voltage of 6 V. For low battery charge conditions, the timing delay between the fan start and spark increased due to the high current required for the start of the electric motor. To stabilize the timing, the fan was powered by a separate 6 V accumulator, while the spark ignition system was connected to a 12 V power supply. Before the high voltage is built up in the secondary winding of the coil, a capacitor, forming a turned circuit with the primary winding, is charged to a voltage of $U_{\mathrm{cap}} \approx 200\,\mathrm{V}$. The voltage of the actual spark between the electrode gap was measured using a high voltage test probe (Tektronix P6015).

Before the ignition occurs, a gap voltage of $U_{\mathrm{max}} \lesssim 13000\,\mathrm{V}$ is applied during the pre-breakdown phase to initiate the breakdown phase. The voltage/time characteristics of the spark are shown in Figure 3.5. Depending on the maximum voltage of the pre-breakdown phase, the breakdown is finished after $t_{\mathrm{break}} \approx 3\,\mu\mathrm{s}$. Higher voltages in the pre-breakdown phase generally lead to longer breakdown times. The longest observed time for the breakdown was $t_{\mathrm{max}} \approx 5\,\mu\mathrm{s}$. The following arc phase shows a strong oscillating signal lasting for 7–10 µs. This can be attributed to the oscillations of the turned circuit or interfering signals picked up by the read-out electronics such as oscilloscope and BNC connectors. Depending on the maximum voltage, the arc phase lasts 40–70 µs. Due to the high voltage, the interfering signal generated by the spark superimposed all outgoing trigger signals of the timing control box. As shown in Figure 3.6a, the interference signal can be recorded up to 100 ns after the start of ignition. The maximum amplitude of 4–5 V

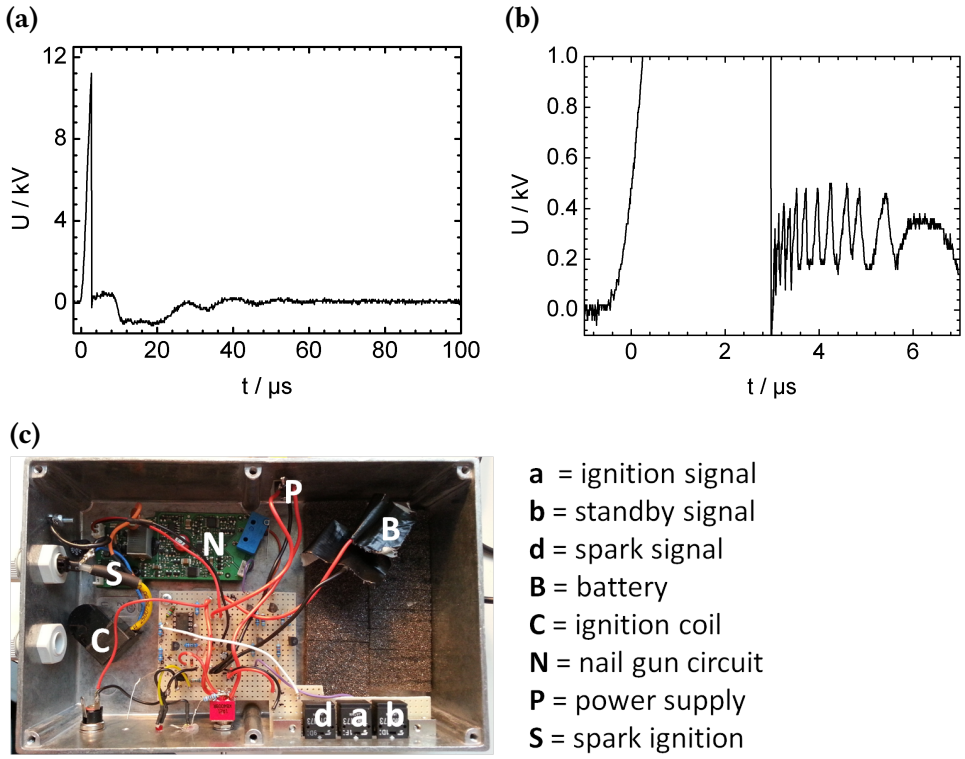

Figure 3.5: **(a)** Spark voltage characteristics for the first 100 µs after ignition. **(b)** Spark voltage for the first 14 µs. The breakdown-phase ($U_{\mathrm{gap}} \lesssim 13000\,\mathrm{V}$) of the spark is finished after $t_{\mathrm{break}} \approx 3\,\mu\mathrm{s}$. After the breakdown phase, the voltage rises back to $U_{\mathrm{arc}} \lesssim 300\,\mathrm{V}$ and shows strong oscillations due to electronic noise induced by the spark ignition. The arc phase and hence the whole ignition phase is finished after $t_{\mathrm{spark}} \approx 50\,\mu\mathrm{s}$. **(c)** Ignition box electronics using the nail gun circuit board **N**. The external signals for loading the coil **C** are received via fiber optics **a** and **a**. The trigger signal is send out via fiber **d**. The circuit diagram can be found in the appendix.

was sufficiently high enough to trigger all electric components, especially the iCCD camera used for chemiluminescence and LIF imaging. To reduce the signal intensity, the outgoing trigger pulses (5 V TTL) were filtered using an additional resistance of R = 50 Ω. The interference amplitude was reduced to less than 0.5 V, while the voltage of the TTL pulses was lowered to 2.5 V and the rise time of the signal was increased (see Fig. 3.6b). Furthermore, the control electronics was isolated from the high voltage generation using optical fibers to start the fan and enable the clearance for the spark.

Despite the spark gap being the shortest distance for the spark to travel, random events of spark impact on the cylinder head adjacent to the spark plug could be observed. Figure 3.7 shows the voltage (3.7a) and luminescence images (3.7b three spark discharges in air. Despite the different trajectories and thus different starting points of the flame kernel, no difference in combustion behavior could be observed in the pressure measurements, which indicates similar spark energies for

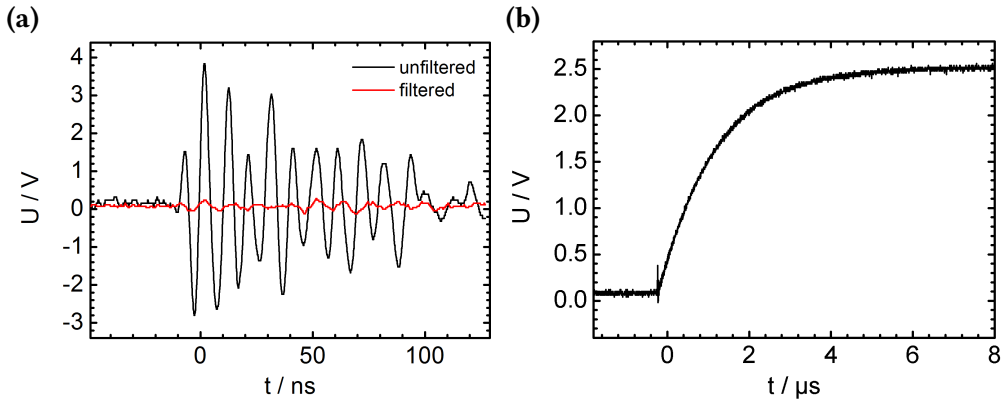

Figure 3.6: **(a)** Interference signal induced by the high voltage spark (black) and filtered signal (red) after passing it through a resistance of R = 50 Ω and a DG353 delay generator. **(b)** Example trigger signal generated by the 50 Ω filtering. The interference signal amplitude is reduced to $U \approx 0.5$ V, the TTL amplitude to 2.5 V. Additionally, the TTL rise time is increased to 6 µs.

each ignition event. The temporal differences in the breakdown phase shown in Figure 3.7a are negligible compared to the jitter of the experiment.

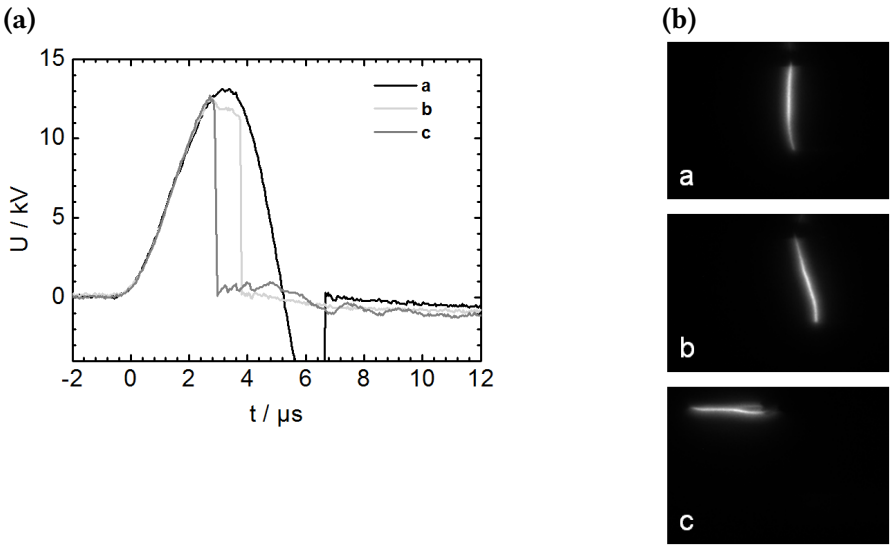

Figure 3.7: (a) Spark voltages measured in air for the three different spark kernels. **(b)** Corresponding plasma luminescence images for an ideal arc impact (a) and non-ideal impacts (b and c).

3.1.1.2 Electric fan

The fan (see Fig. 6.7) is powered by a small electric motor located at the center of the cylinder head. The electric motor (Maxon DC 936) operates at a nominal voltage of U = 6.00 V, resulting in a maximum power output of P = 5070 mW. The maximum

permissible speed of the motor without load is capped at $V_{\max}$ = 13600 rpm. With the fan equipped, the fan speed measured with a light barrier resulted in the same maximum velocity. Nevertheless, due to the load at the shaft, the electromechanical time constant, defined as the time needed to speed up from zero to a nominal no load (NL) speed, increased from τ_{NL} = 22.8 ms to τ_{L} = 130 ms. The roational speed of the fan for the first 1000 ms after start is shown in Figure 3.8a. After an unknown time delay to start the movement of the fan, the first full rotation occurs after Δt = 38.4 ms. The fan accelerates until $\Delta t \approx 800$ ms, showing the expected exponential increase in speed. At maximum speed, a full rotation takes $t \approx 4.5$ ms.

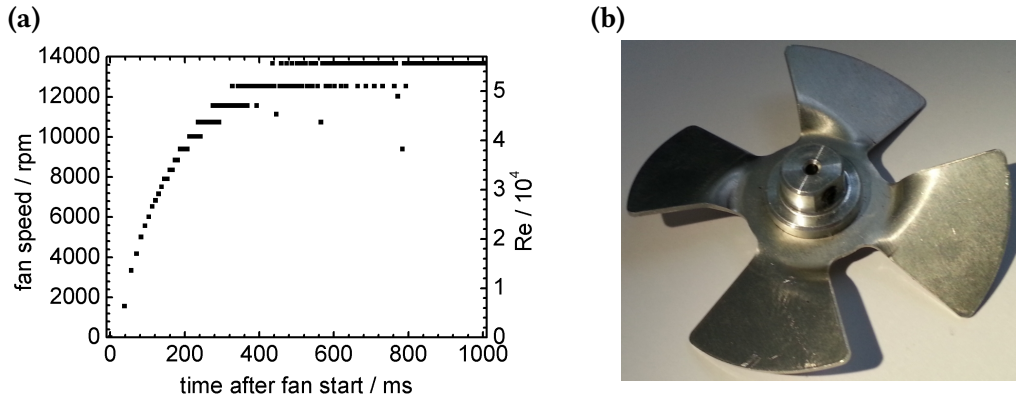

Figure 3.8: (a) Fan speed in rpm for the first 1000 ms after fan start and corresponding Reynolds number. The maximum speed of $v_{\max} \approx 13600$ rpm is reached after about $t \approx 800$ ms. The transition from laminar to turbulent conditions (Re > 10000) around the fan blades starts after $t \approx 65$ ms. **(b)** Fan used in the experiment. The fan has a diameter of d = 6.1 cm.

To quantify the turbulence induced by the movement of the fan, the Reynolds number of the flow was calculated according to

$$Re = \frac{\rho v \cdot L}{\mu} \tag{3.1}$$

For a cylindrical vessel equipped with a rotator centered in the vessel, the characteristic length scale L is the diameter of the rotor D. The velocity v of the rotator is its rotational speed N in rounds per seconds. The Reynolds number then is

$$Re = \frac{\rho N \cdot D^2}{\mu}\,, \tag{3.2}$$

where $\mu_{\mathrm{air}} = 1.818 \cdot 10^{-5}$ kg m s^{-1}[177] is the dynamic viscosity and $\rho_{\mathrm{air}} = 1.204$ kg m^{-3} the density of air at T = 293 K. With a diameter of D = 6.1 cm, the maximum Reynolds number for the fan is $Re \approx 56000$ (see Fig. 3.8a). For low fan speeds, the Reynolds number is assumed to be valid only in the vicinity of the blades,

because the rotation time of the fan is too low to affect the entire volume of the combustion chamber.

Table 3.2: Fan starting times Δt_{fan} investigated in the PIV measurements at an insertion depth of d_i = 9 mm. Each Δt_{fan} corresponds to a fan speed v_{fan} and Reynolds number of the fan Re_{fan}.

Δt_{fan} / ms	v_{fan} / rpm	Re_{fan}
50	3300	13500
100	6000	24500
150	7900	32200
200	9400	38100
300	11600	46900
400	12500	50900
500	13500	55700
700	13600	56000

3.1.2 Gas supply system

To operate the combustion chamber with premixed fuel/air mixtures, a gas supply system had to be developed. For the first preliminary experiments, just one mass flow controller (MFC) for propane was used and the chamber was filled with propane manually. The already present air served as oxidizer. Although this approach was suitable for initial measurements, an exact reproduction was not feasible, especially for experiments with low volume percentages of propane. Therefore, an additional MFC for synthetic air was installed to fill the chamber with a premixed gas composition. Figure 3.9 shows the scheme for the gas supply system. The gas flows of propane and air were controlled using MFCs with maximum flow rates of $\dot{m}_{\text{N}_2}$ = 1.00 slm (Advanced Energy Aera FC-7700CU) for synthetic air and $\dot{m}_{\text{He}}$ = 0.100 slm (Advanced Energy Aera FC-7700C) for propane. The MFCs were calibrated using the soap bubble method and adjusted using a homebuilt flow controller. Because of the difference in the flow rates, the mixing length for air and propane had to be set to 1.5 m and additional filters were introduced to the flow to increase the swirl for better mixing. Without filter and shorter pipes, mixtures with low propane flow could not be ignited due to the predominance of the air flow. After combining the two gas flows, they were passed through a filter system (HOKE 6300) and then directed to the combustion chamber. Depending on the flow rate of the MFC, the combustion chamber was flushed with the mixtures for

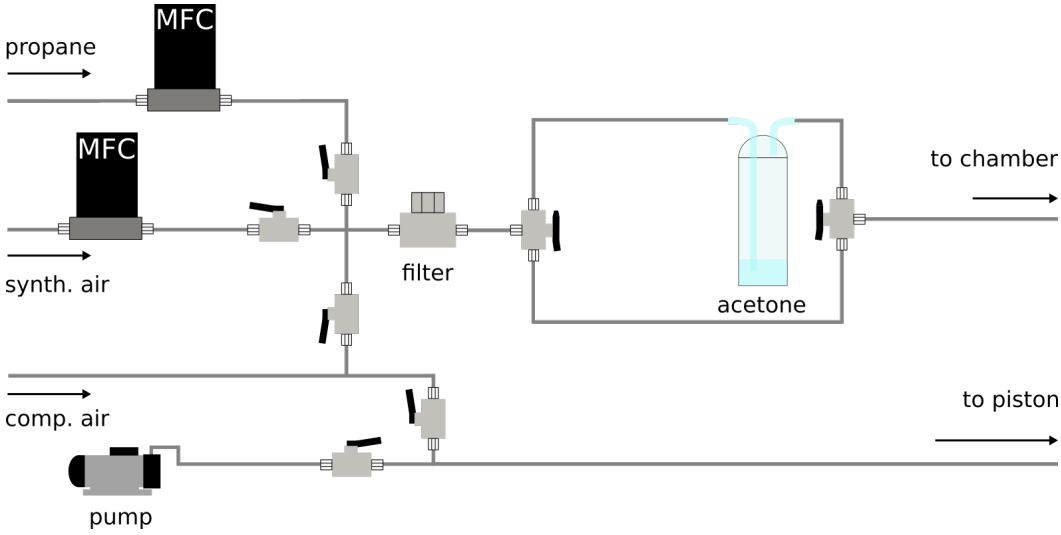

Figure 3.9: Gas supply system for the use with premixed fuel/air compositions. The synthetic air and propane mass flows were controlled using MFCs with a maximum flow rate of $\dot{m}_{N_2}$ = 1.00 slm for air and $\dot{m}_{He}$ = 0.100 slm for propane. The fuel/air mixture was either brought directly to the combustion chamber or passed through a washing flask filled with acetone for tracer LIF measurements. Compressed air from the laboratory was used to purge the system and to lift the piston to the original position.

at least 5 minutes to ensure a homogeneous filling of the chamber. The flushing corresponds to a tenfold volume exchange.

To ensure similar conditions for all combustion experiments, the chamber was purged after every ignition with compressed air. Additionally, the piston was set back to its initial position using a hydraulic lift. The hydraulic lift pressed the piston up until the chamber was finally filled with the premixed composition to avoid piston movement due to small overpressure during the filling. All the flows and the hydraulic lift were controlled manually using rocking lever valves (Swagelok).

For tracer LIF, the fuel gas flow could be passed through a washing flask filled with acetone via a three-way valve. To reduce the amount of seeded acetone, the flask was cooled using an ice bath.

In the commercially available nail gun, the fuel is provided using a small gas cartridge which automatically injects a small amount of gas and lubricant into the engine. Prior to the combustion, a valve is opened and the exhaust gases are ejected while new oxidizer in form of the surrounding air is sucked into the chamber. In the experiment, the same fuel cartridges are used (see Fig. 3.10).

Figure 3.10: Fuel cartridge containing Propene/1-Butene or Propane for external injection of fuel.

3.1.3 Piston velocity and pressure measurements

The velocity of the piston was measured using a homebuilt light barrier that was installed below the cylinder. The light barrier consists of four pairs of LEDs and photo diodes. The first barrier is located 5 mm below the top position of the piston, the next three are separated by 30 mm from each other. The lowest position of the piston, which is equal to the point of impact for the nail gun, is located 10 mm below the fourth light barrier, resulting in a traveling distance of 105 mm (see Fig. 3.11c). The light barrier is read out using an oscilloscope (Tektronix TDS 220) and the data were transfered to a PC via RS-232 serial connection. Figure 3.11a shows an example for the piston velocity measurements based on the light barrier voltage for the first 25 ms after start of combustion. The velocity of the piston for each light barrier was calculated as follows. The oscilloscope was started using the trigger signal of the ignition box and the time for passing each light barrier was determined at the half-maximum of the voltage drop, marked as the dashed gray line at t_{LB1} = 11.9 ms. The next light barriers are passed after intervals of 6.4 ms, 2.7 ms and 1.9 ms, resulting in velocities of v_{LB1} = 0.50 m s^{-1}, v_{LB2} = 6.40 m s^{-1}, v_{LB3} = 11.5 m s^{-1} and v_{LB3} = 15.8 m s^{-1}. After 24 ms, the piston moves up again due to the low pressure and is pressed down once more before it moves back to the initial position 160 ms after the start of combustion (see Fig. 3.11b).

To determine the pressure during the combustion, a piezo pressure transducer (Kistler 603B) was installed in the top corner of the chamber at a distance of d = 0.8 mm from the cylinder head and wall. The piezo was read out using a charge amplifier (Kistler 5007) and calibrated by a high precision manometer (MKS Baratron Type 390HA-00001) with an accuracy of about 0.1 %. The voltage of the pressure transducer was read out together with the light barrier voltage, transfered to a PC and analyzed in Origin 8.0. Figure 3.12 shows an example for the obtained pressure profiles. Depending on the combustion conditions, the pressure equalization lasts up to t_{eq} = 900 ms after ignition (Figure 3.12b), while the maximum pressure Δp_{max} is reached after a maximum pressure rise time of $t_{\Delta p_{\mathrm{max}}}$ = 20 ms (Figure 3.12a). The pressure starts to rise after a short delay time to a maximum of Δp_{max} = 1 bar due to the expansion of the hot gas while the steep pressure drop is caused by the expansion of the piston. The strong oscillations

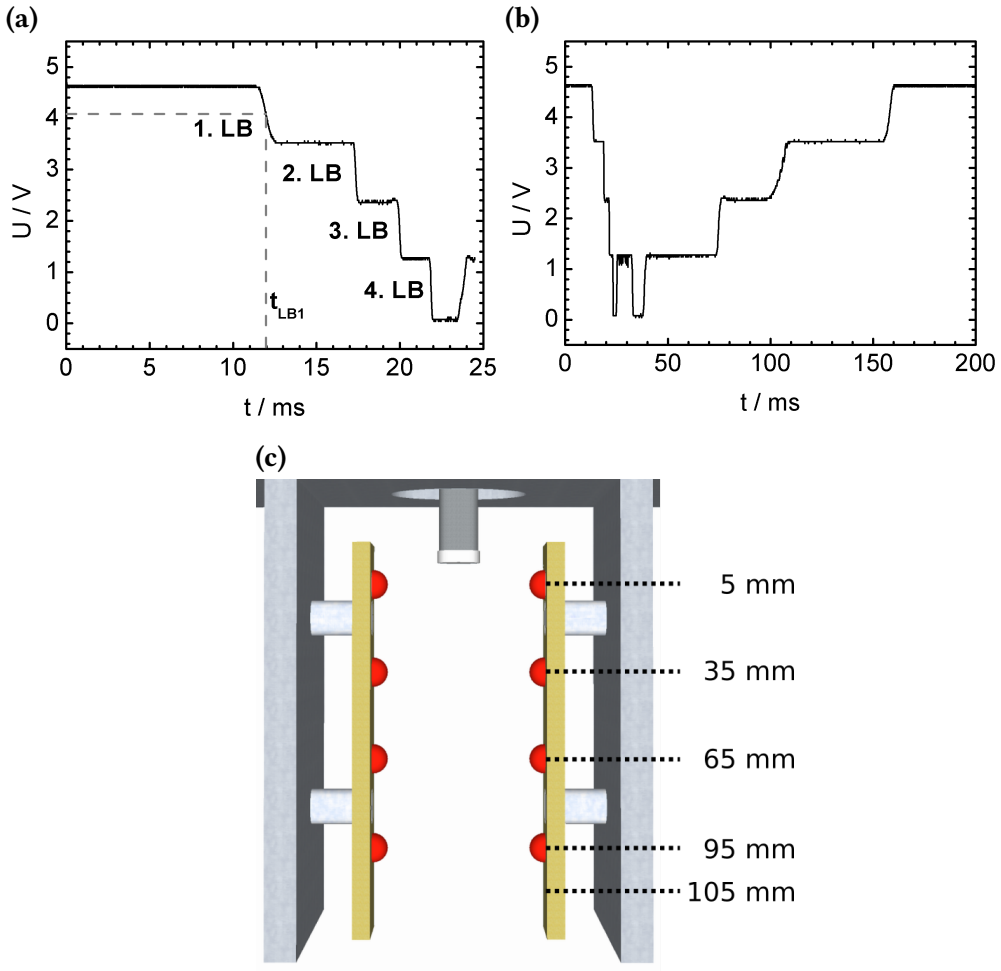

Figure 3.11: **(a)** Light barrier profiles for the first 25 ms after the start of combustion. Each drop in voltage represents the passing of one photodiode. The time for the passing of the barrier is measured at the half maximum of each voltage drop. **(b)** Light barrier profiles for 200 ms after ignition. Due to the underpressure resulting from the expansion, the piston moves up after reaching the bottom dead center. **(c)** Schematic representation of the light barrier. The first diode is located 5 mm below the top dead center position of the piston, the distance between the following diodes is 30 mm, the bottom dead center is reached 10 mm below the fourth diode.

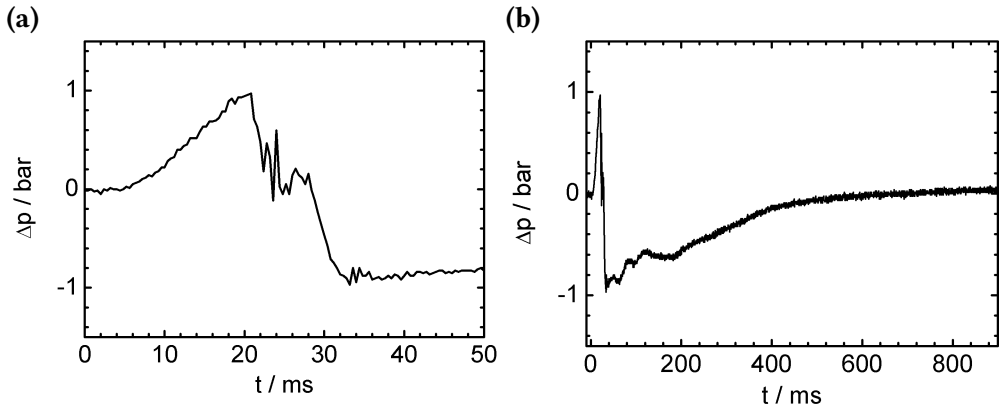

Figure 3.12: **(a)** Pressure profile for the first 50 ms after start of laminar combustion. **(b)** Pressure profile for one complete ignition event until pressure equalization is reached 900 ms after start of combustion.

during the pressure drop around $t = 23$ ms and 35 ms are probably caused by the sound waves of the expanding shock wave or impact of the piston crown. For most cases, these oscillations did not disturb the data evaluation and were left unaltered. For strong oscillations, the data was filtered using an FFT low-pass filter.

3.2 Optical setup for LIF and chemiluminescence imaging

3.2.1 Laser system

To excite the OH radicals at the $Q_1(6)$ band around $\lambda = 283.01$ nm, a dye laser system (Sirah Cobra Stretch) was set up. Figure 3.13 shows the optical setup used for the LIF measurements and will be explained in the following. To pump the dye laser, the fundamental wavelength $\lambda = 1064$ nm of a 20 Hz Nd:YAG laser (SpectraPhysics Quanta-Ray Pro 230) was frequency doubled using a second harmonic generation SHG KDP crystal to generate pulses with a wavelength of $\lambda = 532$ nm at a pulse length of $t = 8$ ns and a maximum energy of $E = 600$ mJ. The beam was coupled into the dye laser using two high-power dielectric mirrors.

The dye solution used for the excitation was Rhodamine 6G (Lambda Physics) in ethanol to generate pulses at a wavelength of $\lambda = 566.02$ nm with a pulse length of $t = 8$ ns and a spectral width of $\lambda = 1.2 \cdot 10^{-3}$ nm. The output of the dye laser was frequency doubled using an SHG crystal (BBO, 44 °, 380 nm $\geq \lambda \geq$ 280 nm). The fundamental wavelength was separated using a compensator and 4 Pellin-Broca prisms. The UV output of the dye laser was lowered to the optical table of the combustion chamber by a periscope. The output of the laser was measured behind the lower periscope mirror and set to approximately 14 mJ, which yielded an excitation energy of 10 mJ in front of the chamber.

After lowering the beam path, the beam diameter was horizontally reduced by a factor of 2.7 using a telescope system with two cylindrical lenses ($f_1 = 200$ mm, $f_2 = -75$ mm). A lens with negative focal length was chosen to avoid a focal point, which resulted in ionization of the air and hence a dramatic drop in excitation energy. The resulting beam diameter was determined by a knife edge scan and measured to be $d \approx 1$ mm. To generate the light sheet, the beam was expanded vertically using a single cylindric lens ($f = -30$ mm). The maximum height of the sheet was determined by cutting off the beam using the observation windows. Preliminary experiments were performed using a periscope with two cylindrical lenses to expand and collimate the beam. Due to the small diameter of the dye beam, the approximately Gaussian beam profile was stretched only by a small amount. Especially the areas at the edge of the profile, in this case mainly the area around the spark plug, suffered from low laser intensity. The single cylindrical lens resulted in a higher stretching of the beam profile and therefore a more homogeneous intensity distribution inside the chamber.

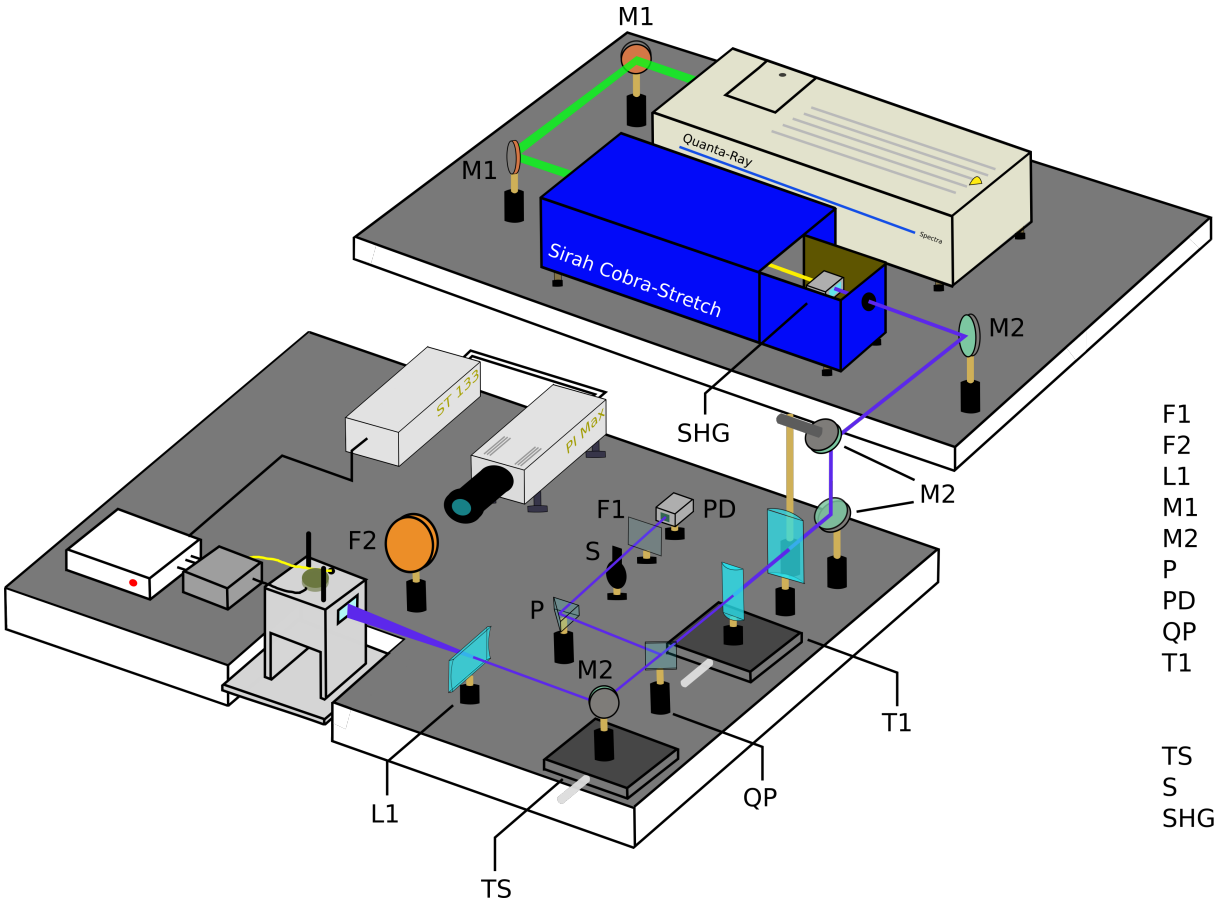

Figure 3.13: Optical setup used for the LIF experiment.

To separate the OH fluorescence from the excitation pulse, a filter (bk interferenzoptik, $d = 4$ cm, $t = 1$ cm) with a central wavelength of $\lambda = 315$ nm ($T_{max} = 76\%$) and a full width-half maximum (FWHM) of $\lambda = 35$ nm was placed in front of the imaging system.

The wavelength of the dye laser was calibrated using a UV pulsed wavemeter (Burleigh WA 5500). Additionally, a static Bunsen burner flame was used to select and test the $Q_1(6)$ excitation line, and the laser was accordingly tuned to get the highest signal intensity. Figure 3.14 shows the uncorrected LIF images obtained from a premixed and diffusion flame directly above the burner exit (white dashed line). The fluorescence intensity for single shot experiments (Figure 3.14a and 3.14b)

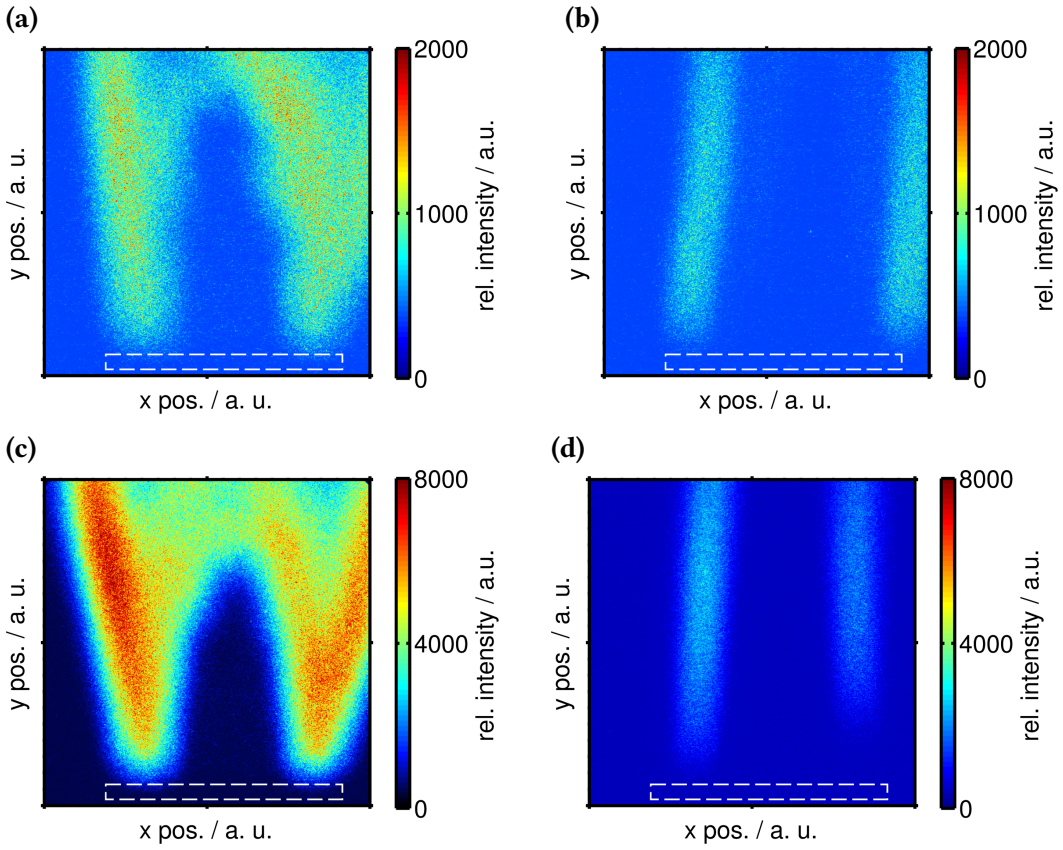

Figure 3.14: Bunsen burner flame used as steady flame for the excitation of OH radicals at $\lambda = 283.01$ nm, the position of the burner is marked by the white dashed line. To test and validate the setup, both a premixed Bunsen flame with open air inlet **(a)** and a diffusion flame with less oxygen content **(b)** where tested. Exposure time was set to $t_{exp} = 1\,\mu s$ (f/5.6, maximum gain). The excitation energy was $E \approx 4$ mJ, which resulted in a signal-noise-ratio of 3:1 for the flame with a higher OH radical concentration **(a)** and 2:1 for low concentrations **(b)**. **(c)** and **(d)** show the LIF intensity for 10 accumulated shots.

is two to three times higher than the background noise and therefore sufficient enough for the visualization of the flame front. Figures 3.14c and 3.14d show the

LIF intensity from 10 accumulated images for the same experimental conditions. For steady and laminar conditions, as is the case for the premixed flame, the single shot and accumulated only differ in signal-to-noise ratio, which is slightly higher for 10 accumulated images. Due to the shaky flame front in the diffusion flame, the accumulation of a low number of single shot measurements is not beneficial for the increase of the signal-to-noise ratio.

3.2.2 Image recording and post-processing

Flame front and LIF images were captured by an intensified charge-coupled device (ICCD) camera (Princeton Instruments PI Max 2) using a multi-channel plate (MCP) for intensification and a P43 phosphor screen. The camera was equipped with an 105 mm UV objective (f/4.5, UV Nikkor). The chip has a resolution of 1024 × 1024 pixels at a dimension of 12.8 × 12.8 µm^2 per pixel. The camera uses a Gen II image intensifier whose quantum efficiency is above 10 % in the UV range. The lens system was mounted via an f-mount and distance rings with a length of 8 cm. The camera recording and exposure time was controlled using the WinSpec 32 software (v 2.5.23.00). The MCP was set to the maximum gain of 255, the UV objective was stopped down to f/5.6. At an aperture of f/5.6 and a distance between objective and chamber of approximately 30 cm the depth of field is just a few millimeters. The exposure time for the chemiluminescence imaging was set to $t_{\mathrm{exp}} = 75\,\mu\mathrm{s}$, which was short enough to freeze the movement of the flame while maintaining a sufficiently high signal intensity. For the LIF measurements, the exposure time was reduced to $t_{\mathrm{exp}} = 1\,\mu\mathrm{s}$. While the majority of the chemiluminescence was removed using the filter, a small amount of light emitted by OH radicals not excited by the laser could only be suppressed using short exposure times. Prior to the measurements, the camera was cooled to $T = -20\,^{\circ}\mathrm{C}$ to reduce electronic noise. All raw images were corrected by subtracting an average background image with the laser turned off prior to each measurement. Hot pixels were identified by capturing 10 images with the shortest possible exposure time of $t_{\mathrm{exp}} = 10\,\mathrm{ns}$ and closed objective and for each image replaced by the average of the 24 surrounding pixels using a homebuilt ImageJ[178] script. The sheet intensity was measured before and after each measurement series and the averaged vertical intensity distribution was extracted to correct all fluorescence images using a homebuilt Mathematica script. To correct the images for pulse energy fluctuations, 1 % of the pulse energy was coupled out via a quartz plate in front of the last mirror and directed onto a photodiode using a quartz prism. To reduce the incident light intensity on the diode, the beam was attenuated with a filter (Schott, WG 320, $t = 1\,\mathrm{cm}$). A shutter was

inserted in front of the photodiode to detect only the pulse used for the imaging. The voltage output of the photodiode was measured before each experiment and correlated to the pulse energy measured with a power meter equipped with a pyro-electric head (Ophir Vega).

3.2.3 Timing of the components

The first experiments for the LIF imaging were based on a 10 Hz Nd:YAG laser as master clock. Thus, all the electronics and trigger signals were based on the 10 Hz frequency of the laser. While the laser could be operated in single-shot mode, the pulse energy for shots was not high enough and no fluorescence could be observed. To increase the pulse energy, the laser was operated in pulsed mode and the spark generation was based on the Q-switch TTL signal of the laser. Additionally, the trigger signal for the CCD camera was also coupled to the Q-switch signal, because the trigger signal of the spark showed a temporal deviation of a few µs. As seen in Figure 3.6b, the rise time of the filtered trigger signal for the camera was increased due to the filtering of interference signal. However, the time between Q-switch signal and laser pulse was shorter than the rise time for the 2.5 V signal and the OH fluorescence could not be imaged. Therefore, the camera signal was transmitted one period earlier and afterwards temporally delayed using a delay generator (Stanford Research DG535). Figure 3.15 shows the circuit diagram of the timing components (Figure 3.15a) and the used trigger scheme (3.15b). Both will be explained in the following. For the use of the 20 Hz laser, the trigger signal frequency was reduced to 10 Hz using a homebuilt frequency divider. Upon pressing the ignition button, the ignition box started the fan at a chosen delay of τ_{fan} = **c**. Depending on the desired delay between laser pulse and start of combustion, the spark was discharged at a delay of τ_{ign} = **a** before the laser pulse. The trigger signal for the camera was dispatched one Q-switch signal before the recorded laser pulse τ_{cam} = **b** and afterwards delayed by τ_{535} = **d** = 99.749749 ms using the delay generator. The trigger signal was picked up by camera controller (ST-133-5 MHz). To increase the signal-to-noise ratio, the camera was operated in gating mode which keeps the MCP biased off and switched it on only for the photocathode gating time. The shutter for the photodiode was opened for 49 ms and closed 15 ms after the recorded laser pulse.

The data of the photodiode was read out using an oscilloscope (Tektronix TDS2024C) and the data transfered to a PC running Windows XP using a LabVIEW software (Signal Express). The oscilloscope was triggered by the ignition box, which sent out a trigger signal starting with the spark discharge.

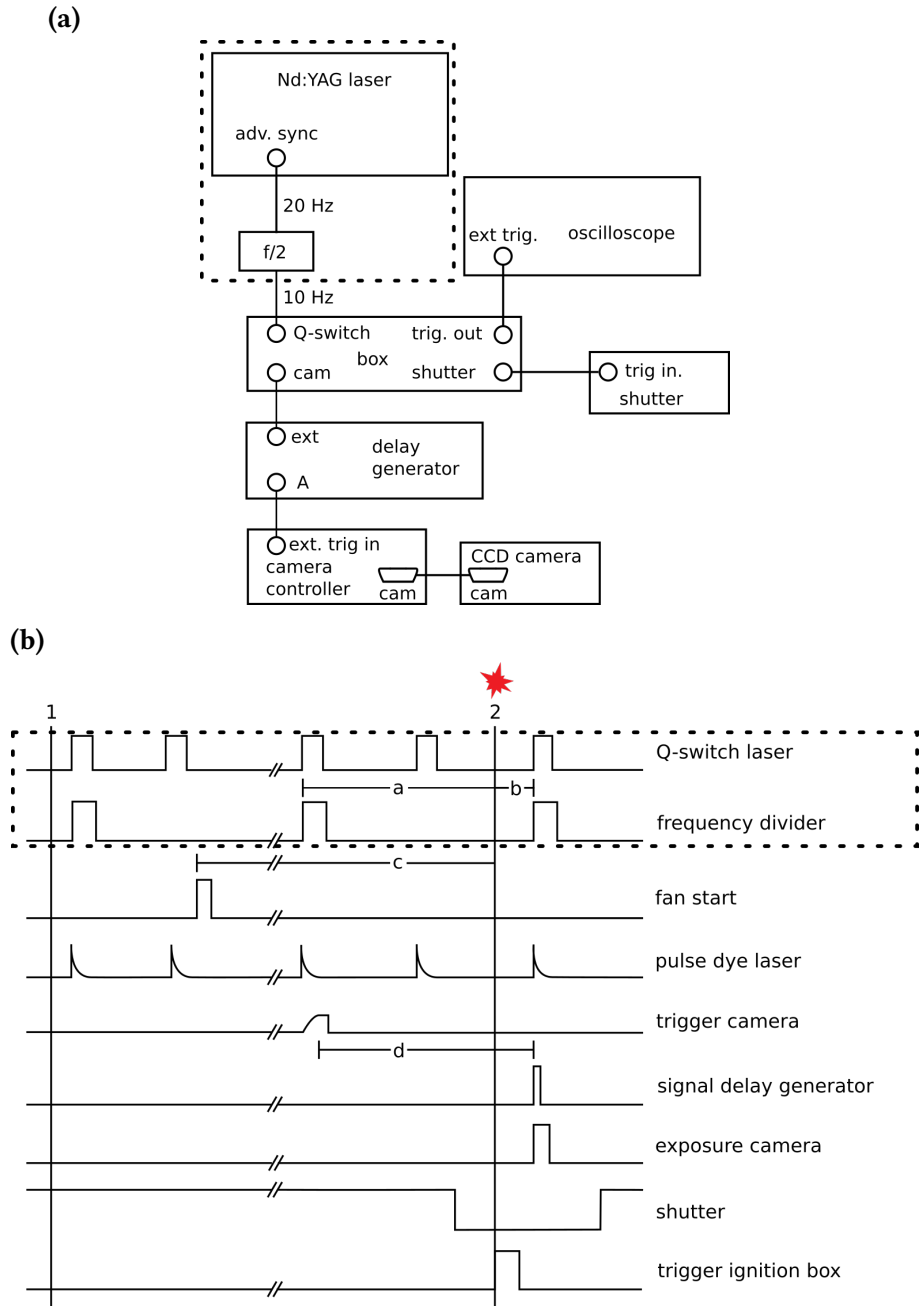

Figure 3.15: **(a)** Circuit diagram for the controlling of the LIF experiment and data recording using the frequency divided Q-Switch trigger signal of the laser as master clock (dashed box). **(b)** Resulting trigger scheme for the single-shot experiments. After pressing the ignition button at time $t = 1$, the trigger signal for the camera is sent out $t = \mathrm{a}$ before the ignition. The camera signal then is delayed using a delay generator by a time of $t = \mathrm{d} = 99.749749$ ms. The fan is started at $t = \mathrm{c}$ before the ignition. The image is recorded at a delay time of $t = \mathrm{b}$ after the start of ignition.

3.3 Reproducibility and error estimation

Because of the single-stroke principle of the investigated engine, it must be guaranteed that data from a single measurement are representative for the average combustion process. Therefore, a series of different methods were checked for their reproducibility. First, 25 consecutive pressure measurements were performed

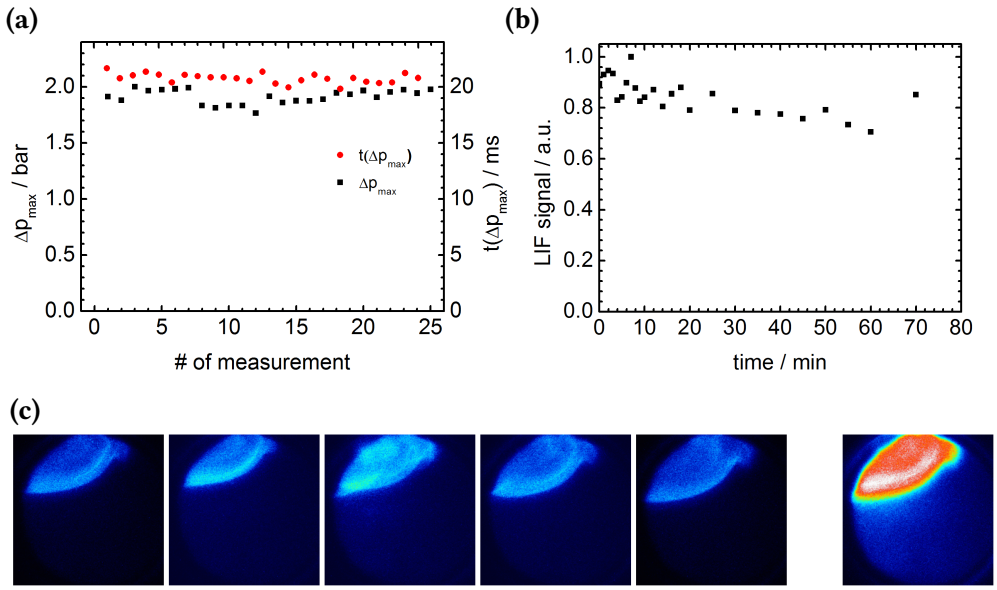

Figure 3.16: **(a)** Pressure rise time $t\,(\Delta p_{\max})$ and maximum pressure $\Delta p_{\max}$ for propane/air mixtures under laminar conditions from 25 consecutive measurements. **(b)** Normalized single-shot fluorescence signal over 70 minutes after filling the chamber with acetone and closing the valves. **(c)** Chemiluminescence images of a laminar flame front obtained at $t = 10$ ms after start of ignition and sum of the intensities.

using the cartridges and injected propane fuel with mounted fan. The pressure-time traces were analyzed in terms of maximum pressure and time to reach the maximum pressure. After each combustion, the chamber was flushed for $t = 5$ min with compressed air to remove all remaining exhaust gases. As seen in Figure 3.16a, the maximum pressure obtained with this setup was $\Delta p_{\max} = 2.0$ bar at a peak pressure time of $t\,(\Delta p_{\max}) = 22$ ms. Over the course of the measurements, a maximum pressure deviation of $\Delta\,(\Delta p_{\max}) = 0.3$ bar $\equiv 15$ % and peak pressure time of $\Delta t\,(\Delta p_{\max}) = 2$ ms $\equiv 9$ % were measured. To check for any fuel leaks, the chamber was filled with a fluorescence tracer. This was done by passing compressed air through a washing flask containing liquid acetone. After flushing the chamber for $t = 5$ min, all valves were closed. Every minute, the fluorescence signal of the acetone vapor after single-shot excitation at $\lambda = 283.01$ nm was detected using the LIF setup described in Section 3.2. The fluorescence signal was summed up and

normalized. The results are shown in Figure 3.16b. The LIF signal stays constant within the first 5 minutes after closing the vales. For higher standing times, the signal starts to decrease and reaches a minimum of 0.75 after one hour. From this, it can be concluded that the chamber housing is sealed well enough to guarantee a constant fuel amount and composition during the measurements. Additionally, flame front images were recorded under laminar conditions without obstacles. Five images recorded at $t = 10$ ms after start of the ignition and the sum of the chemiluminescence are shown in Figure 3.16c. The shape of the flame is equal in all 5 images. From the summed up intensity it can be seen that the highest intensity, which should resemble the flame front, is slightly broadened and located in the area of burned gases. The timing errors induced by the jitter of the spark electronic are usually less than 100 µs and thus below the errors of the pressure rise time.

3.4 Particle image velocimetry setup and experimental parameters

This Section describes the experimental setup, which has been built during the time of the Thesis. The Section is divided into four parts. (*i*) The properties and choice of tracer particles, (*ii*) the optical setup with emphasis on the beam alignment and shaping, (*iii*) the timing of the components and (*iv*) a description of the experimental data analysis procedure.

3.4.1 Tracer particles

As mentioned in Section 2.2.2.2, the particle size is the crucial parameter for every PIV measurement. The particle size must be small enough to follow the change of fluid velocity and direction because all velocity calculations arise from the movement of many particles in an interrogation window. Nevertheless, the particles must be large enough to scatter a sufficient amount of light onto the CCD array, thus increasing the signal-to-noise ratio, and to avoid undersampling. At high Reynolds numbers, the tracking ability of the particles can be estimated using the Stokes number

$$S_\mathrm{t} = \frac{\tau_\mathrm{p}}{\tau_\mathrm{f}}. \tag{3.3}$$

τ_f and τ_p are the response times of the fluid and tracer particle and can be calculated as

$$\tau_\mathrm{p} = \frac{\rho_\mathrm{p} d_\mathrm{p}^2}{18\mu_\mathrm{f}} \quad \text{and} \quad \tau_\mathrm{f} = \frac{L}{U_\mathrm{f}}, \tag{3.4}$$

with the particle density ρ_p and diameter d_p, the fluid kinematic viscosity μ_f, the macroscopic length scale of the experiment L and corresponding velocity U_f.[179,180] In this Thesis, two kinds of tracer particles were used: Solid particles generated from an aqueous solution of sucrose (ρ_suc = 1590 kg m^{-3}[181]) and liquid particles using undiluted olive oil (Rewe Bio Natives Olivenöl Extra, ρ_oil = 970 kg m^{-3}[150]). The size of the particles can be adjusted by varying the concentration of the stock solution, a lower concentration yields smaller particles. The oil particles have a mean diameter of $d_\mathrm{oil} \approx 1$ µm.[150,182] To obtain similar sizes for the sucrose particles, a solution with a mass concentration of 20 g L^{-1} was used.[183] To calculate the Stokes number for the macroscopic length scale, the initial parameters for the experimental length scale L and the velocity U_f have to be set. The macroscopic length L was chosen to be the fan diameter $d_\mathrm{fan} = 6.10 \cdot 10^{-2}$ m, as the largest

eddies are expected to be of the same size as the fan. The macroscopic velocity U_f was unknown prior to the start of the experiments and therefore had to be estimated using the rotational speed of the fan u_fan. The average fan speed in the first 1000 ms after start is $u_\mathrm{fan} \approx 12000$ rpm, resulting in a macroscopic time-scale velocity of $u_\mathrm{L} \approx 40\,\mathrm{m\,s^{-1}}$ and a time of τ_f=1.8 ms. Using the kinematic viscosity of air at $T = 294\,\mathrm{K}$ of $\mu_\mathrm{air} = 1.8481 \cdot 10^{-5}\,\mathrm{kg\,m\,s^{-1}}$, a sucrose density of $\rho_\mathrm{suc} = 970\,\mathrm{kg\,m^{-3}}$ and a mean particle diameter of $d_\mathrm{suc} = 1 \cdot 10^{-6}\,\mathrm{m}$, the particle response time is $\tau_\mathrm{p,suc} = 4.7\,\mu\mathrm{s}$, resulting in a Stokes number of $S_\mathrm{t,suc} = 2.7 \cdot 10^{-3}$. For the oil particles the response time and Stokes number are $\tau_\mathrm{p,oil} = 2.9\,\mu\mathrm{s}$ and $S_\mathrm{t,oil} = 1.6 \cdot 10^{-3}$, respectively. Since both Stokes numbers are well below unity, sucrose and olive oil particles are well suited to follow the macroscopic fluctuations of the flow. To

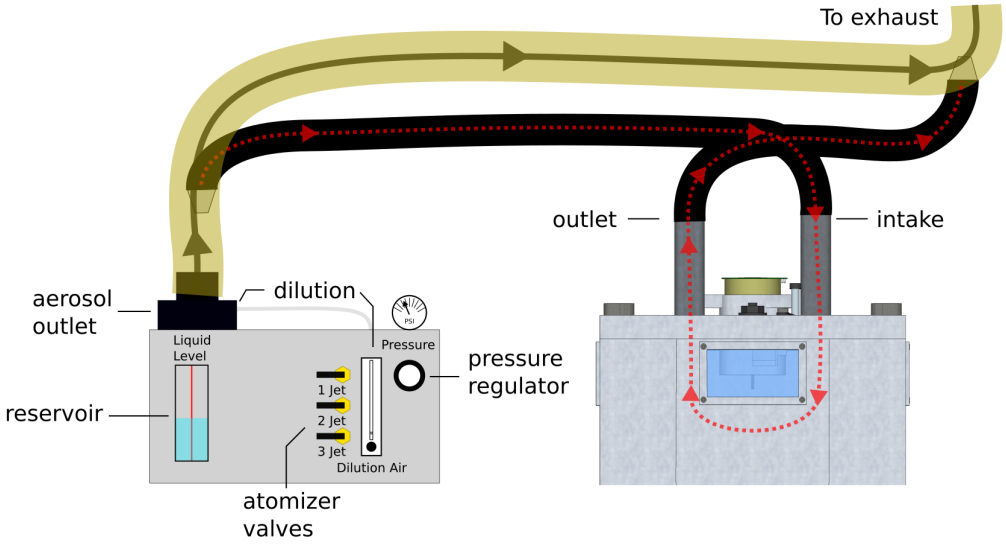

Figure 3.17: Scheme of the experimental setup for the aerosol seeding with the TSI six-jet 9603. A fraction of the main aerosol flow is directed through the combustion chamber.

generate the particles, a TSI 9306 six-jet aerosol generator was used. The amount of aerosol flow rate per atomizer valve could be adjusted between $2.4\,\mathrm{L\,min^{-1}}$ and $12\,\mathrm{L\,min^{-1}}$ using the pressure generator which was connected to the laboratory pressurized air. To alter the particle concentration, up to six valves could be opened, each producing a concentration greater than 10^7 particles/cm^3, or the particle flow could be diluted by adding a co-flow of dilution air. The flow rate was controlled with a rotometer. If particles are generated from an aqueous solution, the air co-flow was also used to dry the excess water.

To reduce the remaining particle concentration, a fraction of the aerosol flow was diverted from the main flow, passed through the chamber and later rejoined with the main flow, which was disposed to the laboratory exhaust. The flow rate for the oil and sucrose particles was set to roughly $4\,\mathrm{L\,min^{-1}}$, corresponding to an input

pressure of 83 kPa or 12 psi with one atomizer valve and was subsequently diluted using the air co-flow. The co-flow rate was increased until particles appeared in the chamber and finely adjusted to match the particle concentration shown in Figure 2.14b. Before every measurement, the chamber was rinsed for at least 5 minutes with the aerosol followed by a series of repeated starts of the fan to ensure a complete mixture inside the chamber. During the experiments, the aerosol flow was run continuously to avoid changes in particle density. Prior to the measurements, all optical windows were cleaned using lens tissue and isopropanol/acetone for the olive oil and water/acetone for the sucrose.

3.4.2 Optical setup

3.4.2.1 Laser system

Nowadays, commercially available PIV systems are often based on lasers equipped with one cavity operating in a so-called dual-pulse mode. This allows for the laser to emit two subsequent pulses from the same cavity with an adjustable time delay. A second method combines two cavities in one laser, where the two separated pulses have to be spatially overlapped in the laser housing. For the following experiments, two separate lasers were used to generate the double pulses needed for the particle exposure.

The lasers used for the PIV setup are a 20 Hz (Continuum Powerlite 8020) and 10 Hz (SpectraPhysics Quanta-Ray INDI 4010) Nd:YAG laser. The Indi was chosen over a 20 Hz Quanta-Ray Pro 230 because the Continuum and Indi offer similar beam properties. The beam diameter of the Pro 230 with $d \approx 18$ mm is 0.3 cm bigger and the beam shape and quality is, in terms of beam alignment, more crucial for the experiment than the possibility of easier synchronization. The fundamental beams of $\lambda = 1064$ nm were frequency doubled using an internal SHG KDP crystal to obtain laser pulses at $\lambda = 532$ nm. The fundamental and frequency-doubled pulses were separated using dichroic mirrors. The maximum pulse energy for the Indi was 230 mJ and 600 mJ for the Continuum, both at 532 nm with a pulse length of ≈ 8 ns and vertical polarization.

3.4.2.2 Imaging system

The particles were imaged using a macro lens system (Nikon Micro-NIKKOR, 105 mm, f/4) onto the the 14 bit CCD chip of a pco.1600 camera. The chip has a resolution of 1600×1200 pixels and a dimension of $7.4 \times 7.4\,\mu m^2$. The quantum efficiency has a maximum of 50 % at $\lambda = 545$ nm. The lens system was mounted via an f-mount to c-mount adapter with a length of 6 cm. The camera timing was controlled using the camware software (pco., V 3.11). To capture two consecutive images, the camera was operated in double shutter-mode with two analog-to-digital converters (ADC) operating at 40 MHz. Figure 3.18 shows the trigger scheme for the camera. After receiving the trigger signal and an internal delay $\tau_{d1} = 200$ ns, the camera sends out a TTL signal for the whole exposure of the two frames. The exposure of the first frame starts after a second delay of $\tau_{d2} = 5.3\,\mu s$ and can be set between 0.5 µs and 49 d. The exposure time for the second frame τ_{frame2} has a fixed value corresponding to the readout time of frame 1. The readout time depends on the configuration of the ADC. With two ADCs at 40 MHz the shortest possible readout time is $\tau_{readout} = 33.5$ ms. The exposure of the second frame starts after a short interframing time of $\tau_{if} = 180$ ns. To capture both laser pulses and get image pairs with comparable background noise, the exposure time was set to $\tau_{frame1} = 33.5$ ms and the first laser pulse was recorded before the end of exposure time. The second laser pulse arrived shortly after the interframing time. The exact timing of the components will be discussed in the next Section. The images were transferred to a computer using a camera link interface and camware software.

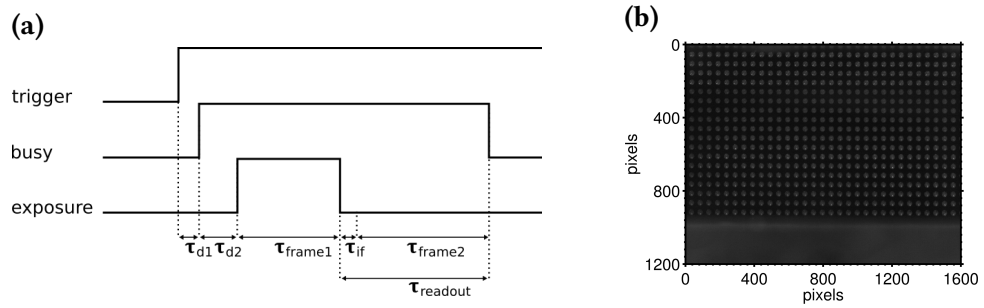

Figure 3.18: **(a)** Trigger scheme for the pco camera using the double-shutter mode. The exposure time of the second frame τ_{frame2} depends on the readout time $\tau_{readout}$, which was set to the shortest possible time of $\tau_{readout} = 33.5$ ms using 2 ADC. **(b)** Target used for the camera calibration. The distance between the center of the dots is 1.0 mm.

3.4.2.3 Timing of the components

The timing of the two laser beams is one of the key parameters for a successful PIV measurement. The easiest way to set up the system would be to use the 20 Hz laser as the master clock for the experiment and take the trigger signal of the laser for the timing of the 10 Hz laser. Unfortunately, both the flashlamp and Q-switch trigger signal of the Powerlite cannot be used for the timing because the signals show a change in phase over time and are thus not stable as master clock. While the jitter of the Indi TTL output signals is in the range of nanoseconds, the 10 Hz signals would have to be converted to 20 Hz using a frequency doubler. Compared to a frequency divider, the doubler offers less stable pulses and is not a suitable option for the timing.

Instead, a delay generator (Stanford Research DG 645) was used as an external trigger source for both lasers. The delay generator generates stable signals with jitters of less than 25 ps and allows for a separate timing of up to four channels including the width of the TTL pulses. A circuit diagram using the delay generator is shown in Figure 3.19, the complete pulse diagram for the trigger cascade is shown in Figure 3.20. The internal trigger was set to 20 Hz and the **AB** and **CD**

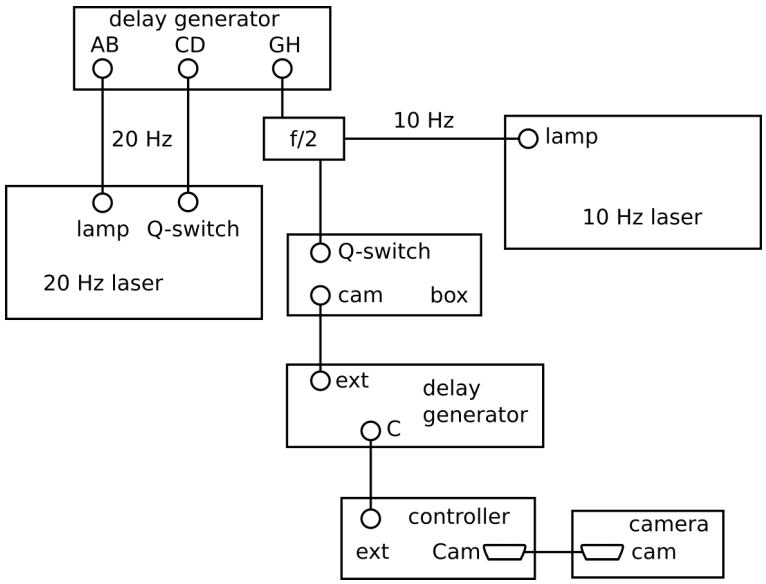

Figure 3.19: Circuit diagram for the controlling of the PIV experiment using the DG 645 delay generator for the timing of the two lasers.

channels used for the timing of the Continuum flash lamps and pockels cells of the Q-switch. A compromise between laser power and timing had to be found because the pulse energy of the Continuum laser depends dramatically on the Q-switch delay time. Additionally, the pulse energy can be tuned changing the delay timing between the flash lamps using the power supply of the Continuum. Fortunately,

the internal timing of the flash lamps does not change the delay between the first flash lamp and pockels cell **a**, which was set to a fixed value of **a** = 400 µs. The width of the TTL signals had to be set to 1 µs. The delay of the **GH** channel was used for the trigger of the 10 Hz laser and the input signal for the timing of the fan start and camera exposure via the ignition box. This delay **b** operated the timing between the two laser pulses and was determined experimentally by detecting the stray light with two photodiodes and monitoring on an oscilloscope (Tektronix TDS2024 C). The TTL signal with a pulse width of 1 ms triggered the flash lamp of the Indi. The opening of the pockels cell was controlled by setting the Indi to external mode and using the remote controllable Q-switch delay, which was set to a fixed value for maximum pulse energy. For a beam separation of 10 µs, the delay **b** had to be set to **b** = 215 µs.

All the laser timings were independent from the ignition box. The timing of the camera exposure and fan start was similar to the LIF setup. When the ignition button was pressed (**1**), the box waited for the next 10 Hz TTL pulse to calculate the fan start before ignition depending on the desired delay **c**. The delay between Q-switch signal of the Indi and ignition was set to 1 ms to avoid timing issues as mentioned before. Due to the spark plug interference, the camera was triggered using a Stanford Research DG 535 delay generator, similar to the LIF setup. The trigger signal for the delay generator was sent out 100 ms before ignition (**2**). The exposure start of the camera was controlled using the delay **d** of the **C** channel, which was set to a fixed value of **d** = 66.66 ms. With this timing, the first laser pulse always arrived 6 µs before the end of the first exposure, the arrival of the second pulse depended on the delay **b**.

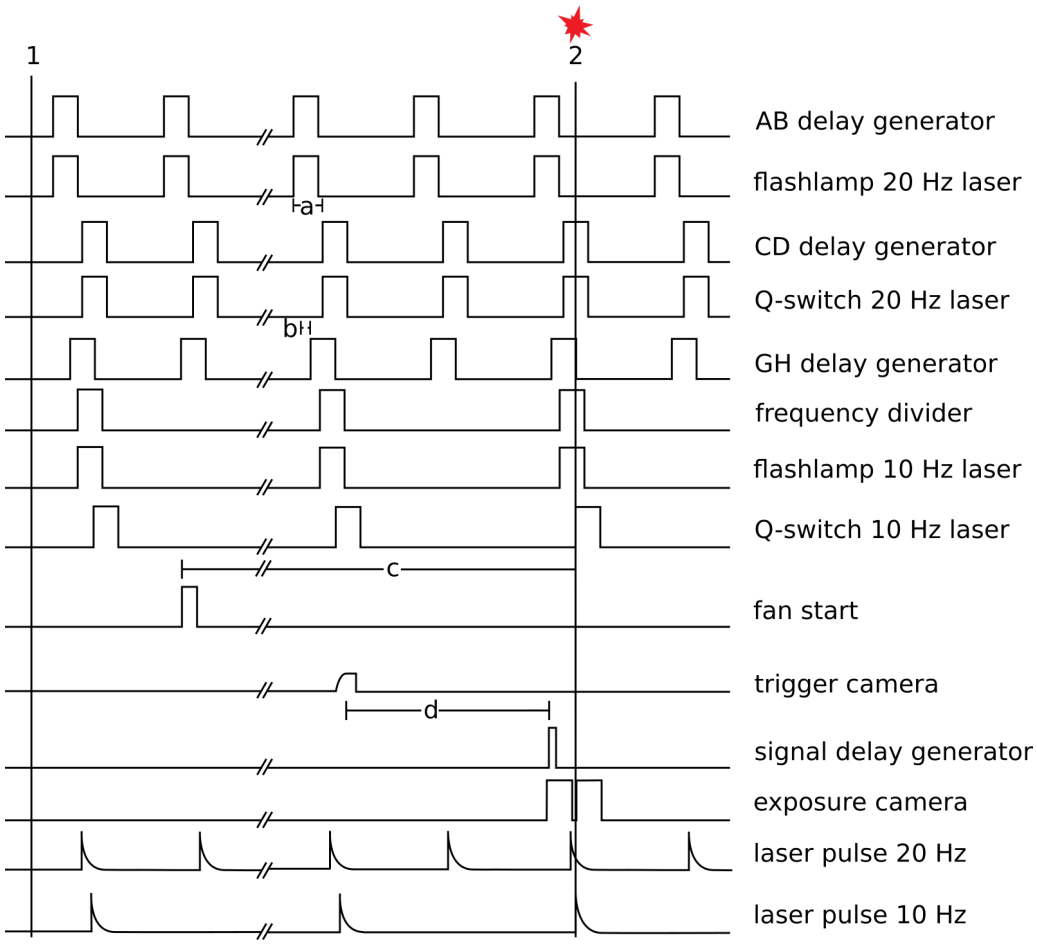

Figure 3.20: Pulse diagram for the used trigger scheme of the PIV experiments. The 20 Hz laser was triggered using the internal pulse generator of a DG 645 delay generator. The same delay generator in combination with a frequency divider was used to trigger the 10 Hz laser and the controlling of the ignition box (see Figure 3.15b). A DG 535 delay generator was used to trigger the camera. The laser pulse of the 20 Hz laser arrived 10 µs before the end of the first exposure, the timing of the second laser pulse was controlled using the CD output of the DG 645. **a** = 400 µs, **b** ≈ 200 µs,**c** = 50 ms-1000 ms, **d** = 66.66 ms.

3.4.2.4 Beam alignment and shaping

The following part describes the detailed procedure for the overlap of the two laser beams, because the crucial and most tedious part for the setup of the PIV experiment is to assure a near-perfect overlap. The optical setup of the experiment is shown in Figure 3.21.

Beam alignment: The $\lambda = 532$ nm beam of the Indi was used as the reference beam for the experiment and was always set up first. Due to the long path lengths of the experiment, the Indi beam showed a slight beam divergence 3 m behind the laser exit, which was near the combustion chamber. To reduce the beam divergence, a f = +5000 mm spherical lens was placed in front of the first mirror, 20 cm behind the laser exit. The beam was then reflected using a 50:50 high power beam splitter (Laser Components) and passed trough an iris **I1**, $d = 15$ mm. Due to the height difference of the optical tables, the beam was brought onto the combustion table using a periscope consisting of two $\lambda = 532$ nm high-reflective mirrors. After passing a second iris **I2** ($d = 15$ mm), the laser beam was reflected towards the chamber using a $\lambda = 532$ nm high-power mirror mounted on a translation stage **TS2**. The translation stage was used to set the position of the laser beam in the chamber, the parallel alignment of the beam to the chamber was adjusted using the mirror holder screws and removable pen markers above the chamber windows. The position of the beam was marked on a paper at the wall of the lab at a distance of $d \approx 4$ m away from the exit of the Indi laser. In addition, the back reflex of the beam splitter was marked at another position on the lab wall.

When the Indi beam was set, the beam path of the Continuum laser was aligned. First, the beam was passed through the two irises using the mirror mounted on the translation stage **TS1**. Then, the position of the second beam was overlapped with the marks of the first beam on the lab wall. This made sure that both beam are parallel at the beginning and the end of the beam combiner. The exact overlap of the two beams was determined as follows: The position of the first and second beam was measured behind iris **I2**, in front of the chamber and at the end of the table. The Continuum beam was then adjusted using the translation stage **TS1** and the horizontal mirror screw. The measurements of the beam position and diameter were done using a homebuilt knife-edge scan program (see Figure 3.22). To check the vertical overlap of the beams, the fluorescence of a solution of Rhodamine 6G in ethanol was captured at the position of the chamber.

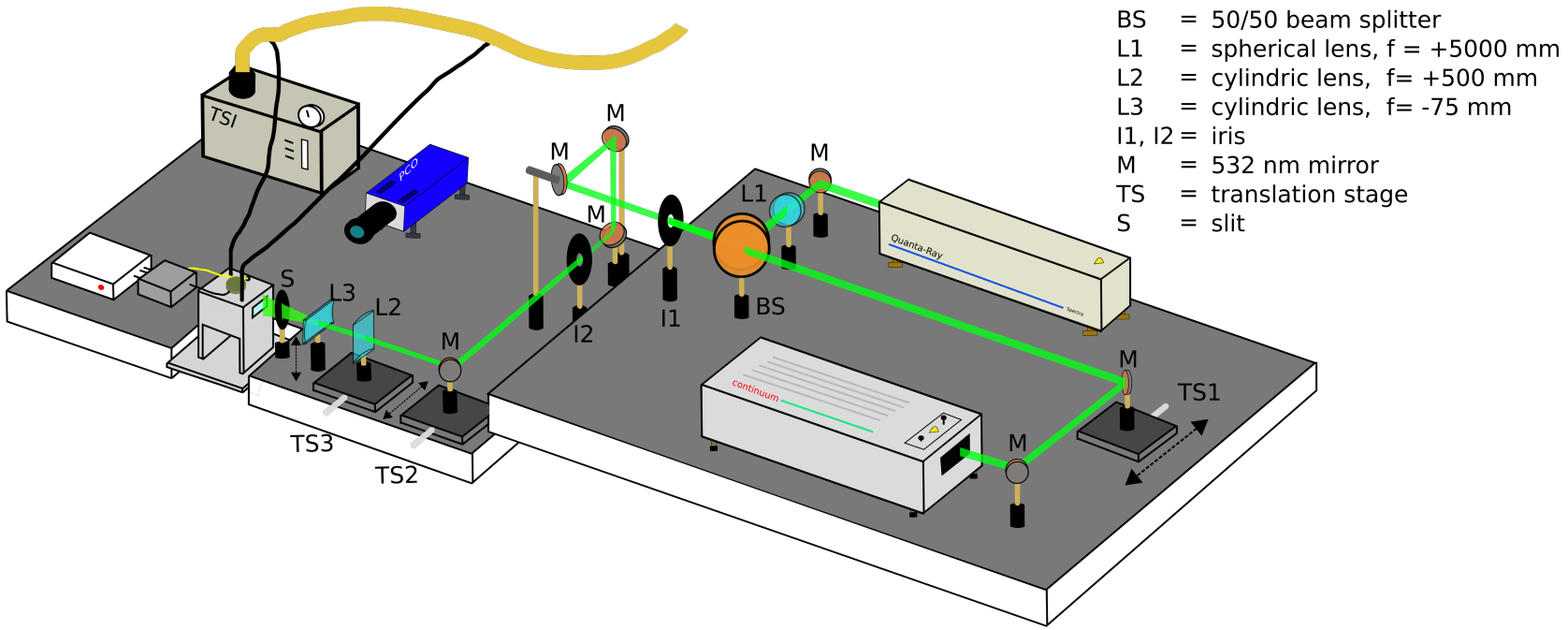

Figure 3.21: Optical setup used for the PIV experiment

Beam shaping: The beam was passed through a combination of f = +500 mm and f = -75 mm cylindric lenses to form the light sheet. The first lens, also mounted on a translation stage, was used to compress the beam in the horizontal plane. The focal point was positioned 10 mm behind the exit window of the chamber, resulting in a beam thickness of $d \approx 1$ mm inside the observation plane. While the focusing slightly reduced the beam thickness near the edge of the observation plane, the changes of $\Delta d \approx 0.1$ mm could be neglected. The use of a second cylindrical lens to collimate the beam did not increase the image quality and just made the alignment of the two beams more difficult. The adjustment of the beam path for inserting the focusing lens was done as follows: Two adjustable pinholes were placed in front of the chamber and 50 cm behind the chamber to mark the position of the beam, also the beam position at the wall of the lab was marked. Additionally, the relative position of the beam was measured using the knife-edge scan method at the position of the chamber. After the cylindric lens was inserted, the beam path was adjusted by eye, using the pinholes and wall position. The latter was just a rough estimation due to the diverging beam. Then, the lens was adjusted using the translation stage of the focusing lens to place the center of the beam on top of the unfocused beam position using the knife-edge scan. Each scan was repeated three times and the average beam positions were compared, until the beam position deviation was less than 50 µm. The negative cylindric lens then expanded the beam

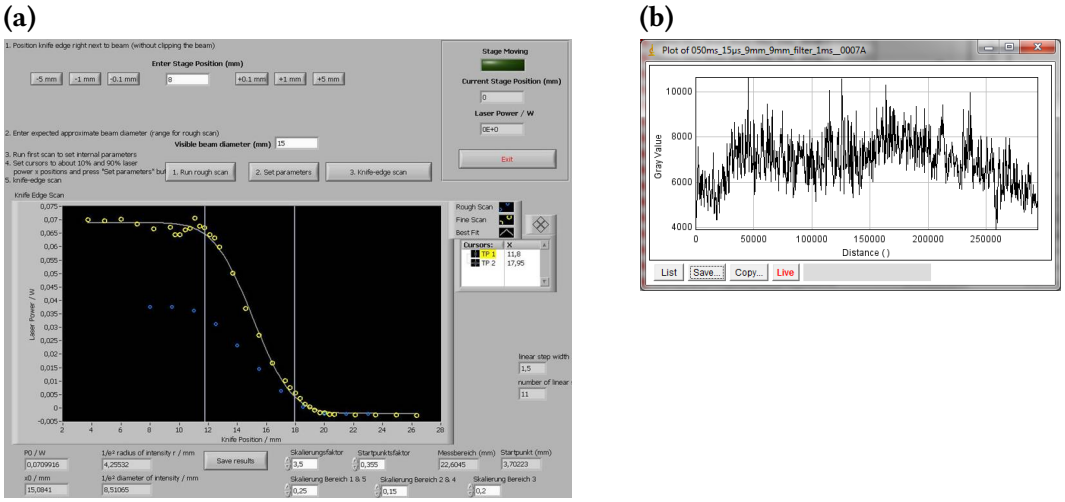

Figure 3.22: **(a)** LabVIEW program used for the knife edge scan to determine beam diameter and relative beam position. **(b)** beam profile aquired from a vertical slice trough the imaging plane.

in the vertical plane. The height of the light sheet inside the chamber was limited by the height of the observation windows, the remaining beam was cut off by the chamber walls. The position of the negative lens was chosen to generate a light sheet with a highly stretched Gaussian profile, resulting in minimal differences in

intensity distribution across the observation window. The intensity distribution was imaged using a cuvette filled with a solution of Rhodamine 6G in ethanol or by filling the chamber with aerosols and capturing the scattered light. Afterwards, the intensity cross-section of the observation window was measured using imageJ. To generate the optimal light sheet, approximately 30 % of the beam intensity were cut off. The energy in front of the entrance window was set to ≈ 40 mJ to 42 mJ, resulting in an effective pulse energy of ≈ 28 mJ to 30 mJ inside the chamber. The overall loss percentage of pulse energy for the PIV system considering all optical elements is 65 %, thus the maximum available laser energy at the chamber can be raised to ≈ 75 mJ if necessary. Due to the stretched and therefore non-Gaussian shape in the vertical direction, the light sheet height was not measured. When everything was set up, two particle scattering images were captured. The fan was not started and the delay between the pulses was set to $\Delta t = 5\,\mu s$, which should result in two nearly identical images both in intensity and particle distribution. To get images of nearly identical signal-to-noise ratio and light distribution, the two laser intensities were adjusted to achieve similar intensities and similar apparent particle distributions.

3.4.2.5 Chamber setup

The chamber used for the PIV measurement was similar to the LIF experiments and only small modifications were done. Due to the small diameter of the fuel in- and outtake, new inlet pipes for the aerosol flow were designed and placed opposite of the fuel supply to ensure an aerosol flow throughout the whole chamber. To reduce the amount of scattered light on the camera chip and to increase the signal-to-noise ratio, the highly reflective chamber surface had to be covered with anti-reflex coating. For the fan, a permanent coating (Nextel Velvet 811-21) was chosen.[184,185]. All other parts of the chamber were covered with a non-permanent soot layer. Despite the superior reflective properties of the coating, soot was chosen because the deposition of oil or sugar on the walls demanded a regular cleaning of the chamber, which led to an abrasion of the coating. Parts of the fan illuminated by the laser showed areas of coating ablation over the duration of an experiment due to the high laser fluence and were repaired before each experiment by applying a thin layer of soot from a household candle.

The total fan running time for the measurement of one image pair was set to $\Delta t = 800\,ms$, which allowed up to 20 consecutive measurements without a visible decrease in image quality. For higher fan running times, the amount of particle deposition on the windows increased dramatically and made a proper data

evaluation impossible. Afterwards, the chamber had to be cleaned as explained in Section 3.4.1. The whole chamber was cleaned on a daily basis and new soot applied before the start of new experiments. Three measurement planes were chosen for the PIV experiments, as shown in Figure 3.23a. Two light sheets passed the chamber from left to right. Light sheet **1** was positioned at the level of the spark electrode tip, sheet **2** passed the electrode at a distance of 4 mm. Sheet **3** was directed at the spark plug from the front. The modified and blackened cylinder head is shown in Figure 3.23b.

(a)

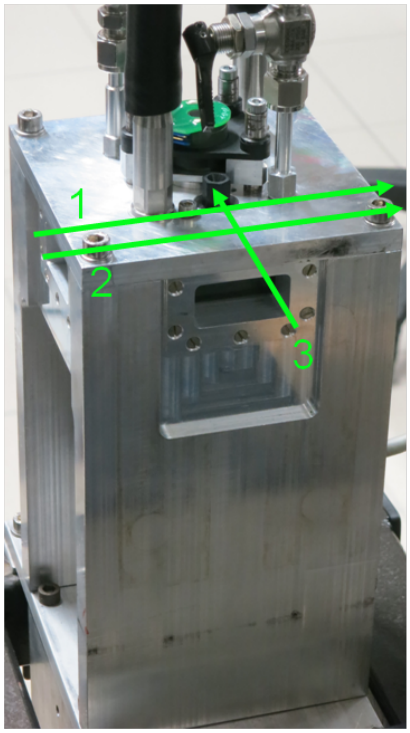

(b)

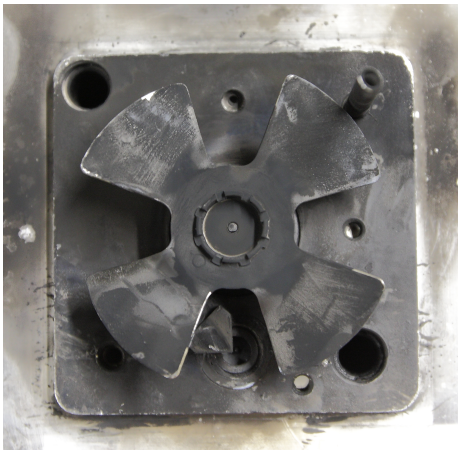

Figure 3.23: (a) Measurement planes for the PIV setup. **(b)** Modified and blackened cylinder head for the PIV measurements.

3.4.3 Image and data processing

The following Section describes the image and data processing for the evaluation of the velocity fields. The image pre-processing and calculation of the velocity data was carried out using non-commercial MATLAB GUI software (PIVlab),[75,162] additional flow properties were calculated using home-built MATLAB scripts.

3.4.3.1 Image pre-processing

The 16 bit raw images captured with the camware software were loaded into PIVlab. Usually, the signal-to-noise ratio is high enough to calculate a preliminary velocity field from the unmodified images, albeit the cross-correlation of two image pair results in > 20 % of erroneous vectors. To lower this value to < 10 %, a few modifications of the images have to be done. To capture the whole imaging window, parts of the surrounding chamber were still present at the top and bottom of the image. Depending on the position of the fan, parts of the image contained no information at all due to the blocked light sheet or pixel areas are saturated by scattered light. All parts without usable informations were masked (see Fig. 3.24). Three image

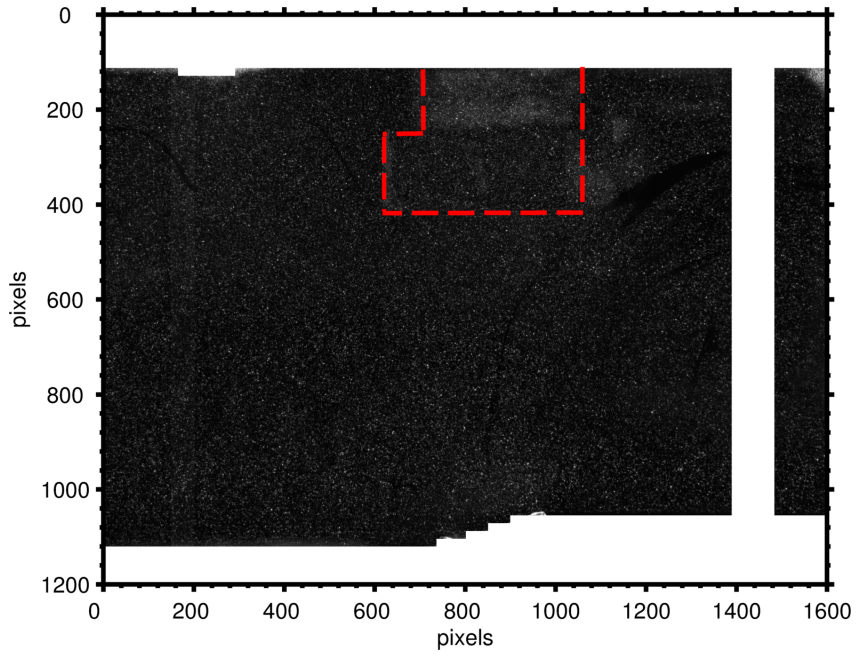

Figure 3.24: Raw image with applied mask (white areas) to the walls and part of the rotor. The position of the spark plug is noted in red.

enhancement features were used and combined: (*i*) High-pass filtering, (*ii*) intensity capping, and (*iii*) contrast limited adaptive histogram equalization (CLAHE).

The high-pass filtering was performed by applying a low-pass filter to the image and subtracting the filtered from the original image. While the low-frequency information does not influence the reflected light by the particles, it becomes problematic in areas with inhomogeneous illumination,[150] e.g.,caused by reflections from the spark plug, walls or rotor. The pixel size of the filter was adjusted to the image quality and was usually set between 50×50 and 100×100 pixels. High-pass filtering was applied to all image pairs used for cross-correlations.

Contrast limited adaptive histogram equalization has an advantage over common histogram equalization because it uses several histograms corresponding to different sections of the image. Regions of high and low contrast, resulting from non-uniform exposure of the image, are optimized independently.[186] The use of

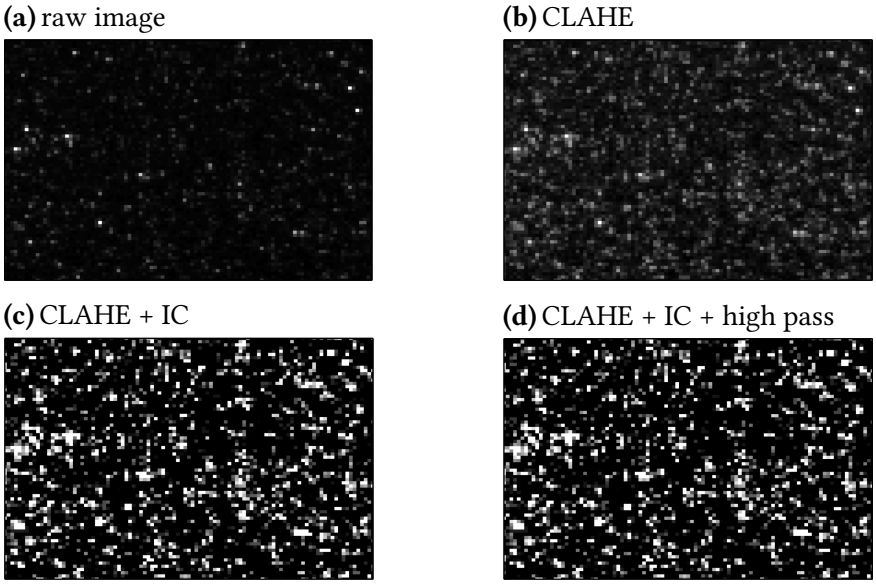

Figure 3.25: **(a)** 100 × 75 pixels cutout of the raw image. **(b)** Image after contrast limited advanced histogram equalization (CLAHE). **(c)** Image after CLAHE and intensity capping (IC). **(d)** Final image used for the cross-correlation, a 100 × 100 pixels high-pass filter was applied to remove scattered light around the walls of the chamber.

intensity capping also helps with the non-uniformly illuminated particles. Bright particles may result not only from coalesced or overlapping particles, but mainly due to individual particles located within the highly illuminated areas of the light sheet. These bright particles may contribute more to the cross-correlation peak than neighboring particles and if the movement of the bright particles differs from the mean movement inside the interrogation area, the resulting vector may be spurious.[187] The intensity capping applies an upper limit to the grayscale values, replacing all values above with the threshold value. Figure 3.25 shows the application of CLAHE, intensity capping and high-pass filtering to a 100 × 75 pixels cutout of an exemplary raw image. Usually, both CLAHE and intensity capping

were used for image enhancing, which lead to a strong reduction in discarded vectors. The amount of discarded vectors decreased from 4.5 % with high-pass filtering only to 2.7 % with high-pass filtering, CLAHE and intensity capping. Nevertheless, for measurements in highly turbulent conditions, e.g.,for fan start times of $\Delta t = 300$ ms before ignition, all image enhancement methods have to be checked separately by comparison of the results in order to avoid errors due to the change of image statistics. The adjustment of light sheet thickness and delay between laser pulses can also be used to enhance the image quality. While a delay of $\Delta t = 30$ µs was sufficient enough to calculate preliminary vector fields for fan start times of $\Delta t = 300$ ms, the amount of discarded vectors could be reduced from 30 % to less than 10 % by shortening the delay to $\Delta t = 5$ µs.

3.4.3.2 Cross correlation and data evaluation

As mentioned in Section 2.2.2.3, the FFT method using multi-pass analysis is the common method of choice for the cross-correlation. All data analysis was performed using an initial interrogation window size of 64×64 pixels with a step size of 32 pixels, resulting in 50 % overlap of the interrogation windows. The grid was refined using a second FFT pass with a window size of 32×32 pixels and 16 pixels step size. Additionally, a linear window deformation interpolator is used. While the simple cross-correlation method assumes that all particles within an interrogation window behave the same, this is not necessarily true in nature. Due to strong shear forces, the equally distributed particles in an interrogation window at t_1 would require a distorted interrogation window for the image at t_2 (see Fig. 3.26a.) The simplest approach for this problem is the so-called zeroth-order displacement predictor, which either uses different sizes of interrogation areas or multistep correlation with a discrete window offset (Fig. 3.26b). The first-order displacement predictor applies a linear deformation to the interrogation window based on the displacement distribution after the first cross-correlation pass.[188] If the interrogation windows are allowed to overlap during the correlation, additional information is present at the borders of the interrogation window. For an overlap of 50 %, eight displacement vectors around the central displacement can be calculated. Together with the central information, the pixel position inside the new window is linear interpolated (Fig. 3.26c). The new distorted IW is then used for the refined FFT pass.[75] The smallest interrogation window contains $\approx$ 25–30 particles. The subpixel estimation was performed using a 2×3 pixels Gaussian function. The FFT method in combination with the subpixel estimator is prone to produce peak locking effects and an increase of background noise (see Section 2.2.2.3) or

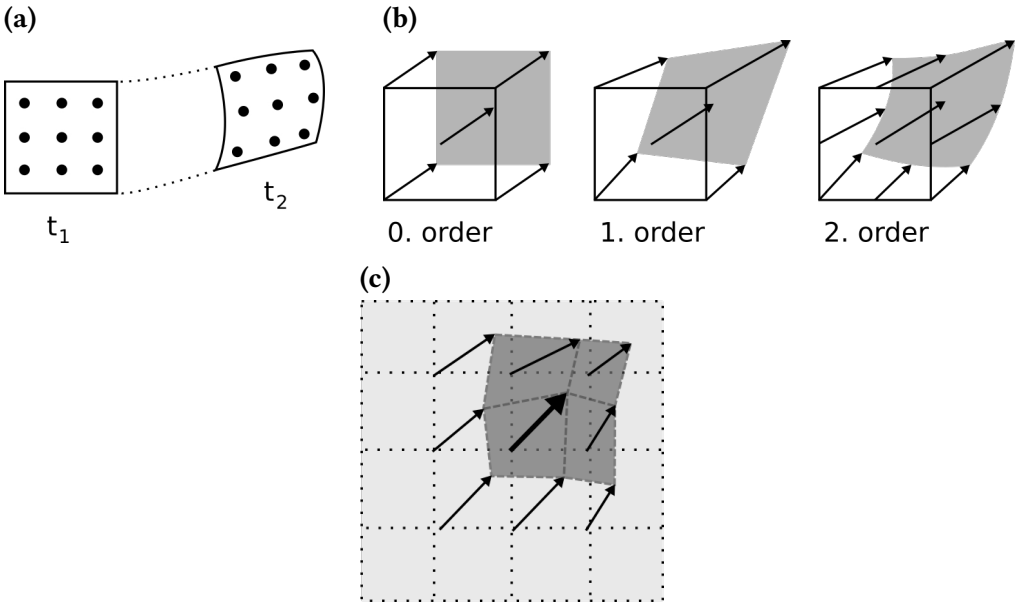

Figure 3.26: **(a)** Motion of fluid tracers inside an interrogation window leading to the deformation of the IW. **(b)** Effect of the window deformation depending on the order of interpolation. **(c)** Linear window interpolator used in PIVlab. An overlap of the IW of 50 % gives eight additional displacement vectors around the central displacement vector after the first cross-correlation. This information is then used to calculate the distorted interrogation window for the second cross-correlation pass.[75,188]

erroneous vectors, when the particle displacement becomes greater than half of the interrogation window size. The velocities for two different turbulence intensities obtained with the DCC and FFT method are displayed in Figure 3.27. For the DCC method, the interrogation window size was set to 32×32 pixels and 16 pixels step size, the FFT approach was carried out using the aforementioned two-pass procedure. While for low turbulence 100 ms after start of the fan (Figure 3.27a) the amount of vectors with apparently too high velocities, so-called spurious vectors, is nearly the same for the two methods, for higher turbulence intensities (Figure 3.27b) the two-pass FFT methods significantly reduces the number of spurious vectors. In addition to the reduction of noise, no signs of peak locking can be observed and the FFT was favored. A reduction of the final interrogation window to 16×16 pixels did not increase the resolution of the velocity data and lead to a higher degree of spurious vectors, which makes it harder to adjust velocity limits and filters. If the amount of spurious vectors becomes too high, some flow structures like vorticity cannot be resolved anymore, since the calculation of the flow field becomes highly inhomogeneous. Figure 3.29 shows the comparison of the vorticity calculated from the same image pair for different sizes of the final interrogation window, starting from an initial size of 64×64 pixels (3.29a) and subsequent correlation passes using 32×32 pixels (3.29b) and 16×16 pixel (3.29c).

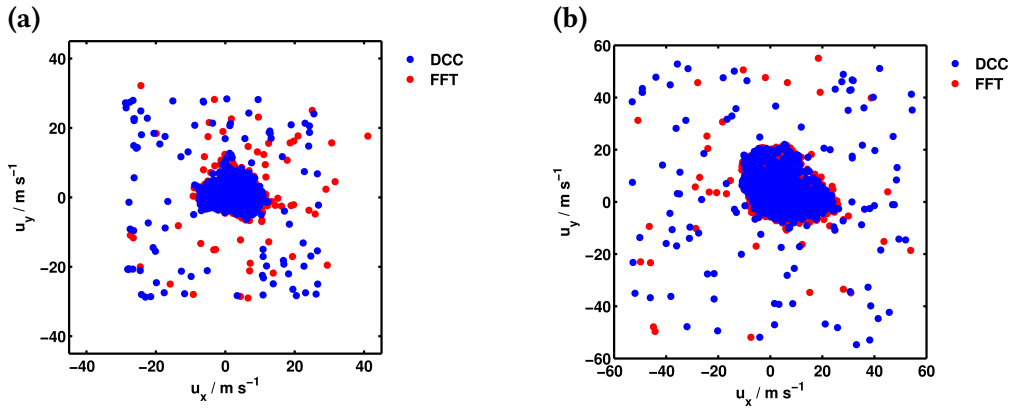

Figure 3.27: Comparison of the DCC and FFT methods for **(a)** low turbulence intensities (100 ms after fan start, $\Delta t = 10\,\mu s$) and **(b)** high turbulence intensities (700 ms after fan start, $\Delta t = 5\,\mu s$). The velocity components of the DCC method are shown in blue, the FFT results in red.

The bigger areas of vorticity are still visible both for 3.29a and 3.29b, but tend to break up for small interrogation window sizes, especially in regions with high velocity gradients. To refine the calculated velocities and eliminate spurious vectors, a limit was chosen for the axial and horizontal velocity components. The limits had to be set high enough not to eliminate physically reasonable vectors and were checked for every experimental conditions. A typical example of velocity limit refinement for low turbulent conditions corresponding to 50 ms after start of the fan is shown in Figure 3.28.

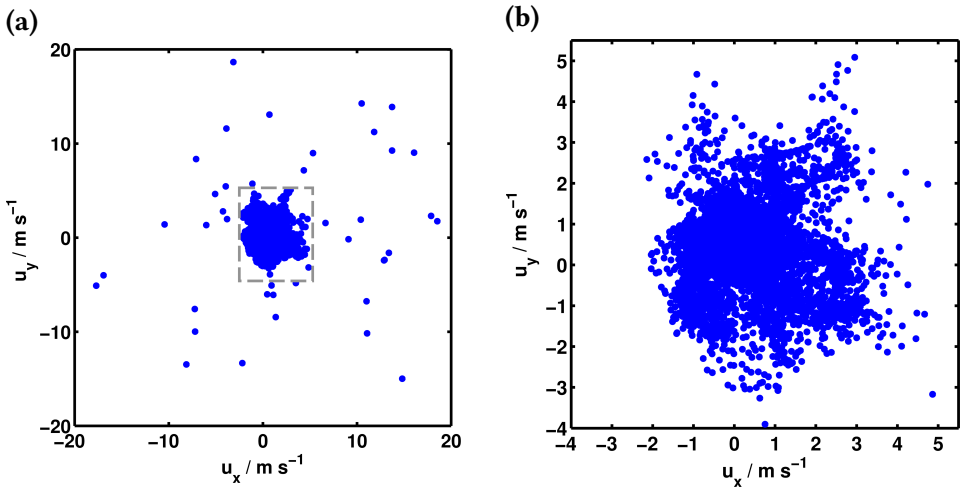

Figure 3.28: a): Velocity scatter plot for low turbulence 50 ms after start of the fan. All vectors outside the gray area are considered as erroneous and removed for further post-processing. **(b)**: Velocity field after filtering, the velocity limits were set to $-3.09\,m\,s^{-1} \leq u_x \leq 5.39\,m\,s^{-1}$ and $-3.89\,m\,s^{-1} \leq u_y \leq 5.17\,m\,s^{-1}$.

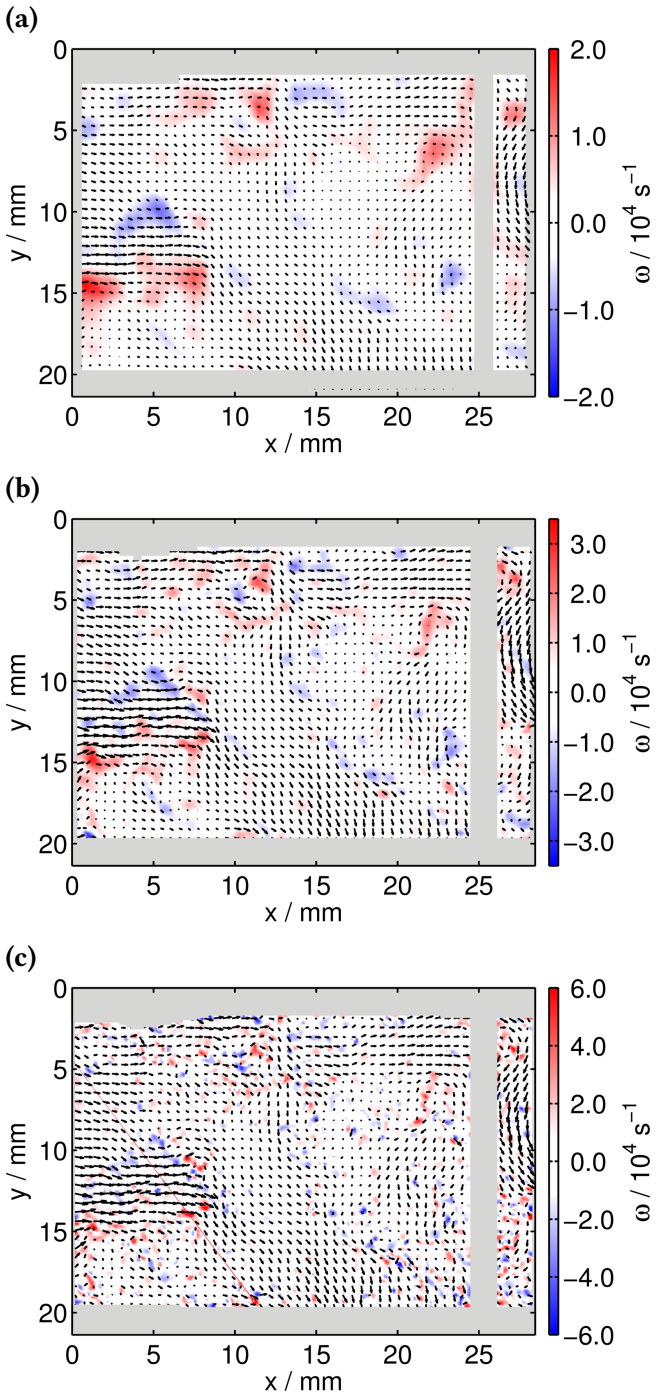

Figure 3.29: Comparison of the influence of different interrogation window sizes on the resolution of the fluid dynamical properties, in this case the vorticity. The final interrogation window size for the calculation was **(a)** 64×64 pixels, **(b)** 32×32 pixels and **(c)** 16×16 pixels. With a decrease in interrogation window size, the larger structures obtained from the 64 pixels calculation are still recognizable, but tend to be broken up due to the increase of spurious vectors, which lead to higher velocity gradients and hence to higher vorticity and smaller vortex areas.

A total of 5601 vectors were calculated and the limits were set to $-3.09\,\mathrm{m\,s^{-1}} \leq u_\mathrm{x} \leq 5.39\,\mathrm{m\,s^{-1}}$ and $-3.89\,\mathrm{m\,s^{-1}} \leq u_\mathrm{y} \leq 5.17\,\mathrm{m\,s^{-1}}$ to exclude 48 vectors (< 1%) that are supposed to be outliers.

Additionally, the velocity field was filtered using a standard deviation filter

$$u_\mathrm{std} = \bar{u} \pm n \cdot \sigma_\mathrm{u}. \tag{3.5}$$

The upper and lower boundaries for the filter were set to the sum of the average velocity component $\bar{u}_\mathrm{x}$ or $\bar{u}_\mathrm{y}$ and a multiple of the velocity standard deviation $n \cdot \sigma_\mathrm{u}$. Again, the parameter n was checked for different experimental conditions. To prohibit the filter from being too strict, n was usually set to values between $5 \leq n \leq 7$. All velocities were compared to the limit values u_std and velocities not within the filter range were rejected.

One should keep in mind that both the velocity limits and standard deviation filter rely on the experience of the experimenter and should be treated with caution. A more unbiased method for removal of outliers is the classic median test, which compares the evaluated vector to its surrounding neighbors, giving a 3×3 kernel. The vector is considered to be an outlier and removed if the residual, defined as $r_\mathrm{i} = |U_\mathrm{i} - U_\mathrm{m}|$, or the combination of both velocity component residuals is above a chosen threshold. The normalized residual is calculated using

$$r_0 = \frac{|U_0 - U_\mathrm{m}|}{r_\mathrm{m} + \epsilon}, \tag{3.6}$$

where U_0 is the displacement vector and U_m the median of the surrounding vectors $\{U_1, U_2, ...U_8\}$, divided by the median residual r_m of $\{r_1, r_2, ...r_8\}$. To compensate for uniform flows with an r_m close to zero, a minimum level of normalization ϵ is assumed. ϵ is usually chosen to be 0.1.[189]

The removal of spurious vectors becomes problematic during the calculation of fluid derivatives, e.g.,vorticity or strain rate. Velocity gradient calculations react very fragile to steep changes of velocities and hence erroneous vectors have to be replaced adequately. A common practice is using a 3×3 mean neighborhood interpolation, which tends to overshoot the replacement vector for images with a high degree of missing values, since it uses only the directly adjacent vectors. The interpolator used in PIVlab is based on a boundary value solver and is described in detail elsewhere.[161,190] While these methods are all able to detect and eliminate "wrong" vectors, they inherently fail to remove measurement noise. Therefore, PIVlab uses a penalized least squares method algorithm for data smoothing.[191,192]

Vorticity ω_z was calculated according to Equation 2.16, using the *curl* function implemented in MATLAB. According to the Stokes theorem, the vorticity at each

point is determined by computing the circulation Γ_{xy} around a closed contour with a path length $\mathbf{l}$ and reducing the value of the closed area A to zero:[193]

$$(\omega_z)_{xy} = \lim_{A\to 0} \frac{\Gamma_{xy}}{A} = \lim_{A\to 0} \frac{1}{A} \oint \mathbf{U} \cdot \mathrm{d}\mathbf{l}\,. \tag{3.7}$$

To visualize the strength of the velocity gradient in direction of the local velocity, which can be interpreted as stretching deformation, the simple strain rate S_{xy}, which is the difference of the S_{xx} and S_{yy} components of the strain rate tensor, and shearing rate component of the strain rate tensor $\dot{\gamma}_{xy}$ were calculated according to[182,194,195]

$$S_{xy} = \frac{\partial u}{\partial x} - \frac{\partial v}{\partial y} \tag{3.8}$$

and

$$\dot{\gamma}_{xy} = \frac{\partial v}{\partial x} + \frac{\partial u}{\partial y} \tag{3.9}$$

using the $gradient$ function of MATLAB.

3.4.3.3 Velocity decomposition for instantaneous velocity fields

As discussed in Section 2.2.2.5, the easiest way do decompose the instantaneous velocity fields is either to subtract a mean flow velocity or to apply a high-pass filter. In case of flows with a constant flowing direction, the first method usually produces accurate results, in the latter case, where the fluid tends to move in different directions in the observation plane, a mean flow velocity is only valid for smaller areas. Figure 3.30 shows the original and decomposed velocity field after subtraction of the mean velocities in u_x and u_y direction (Galilean method), $\bar{u}_x$ = 0.54 ms^{-1} and $\bar{u}_y$ = 0.32 ms^{-1}. The velocities were calculated 50 ms after start of the fan, resulting in a Reynolds number of $Re \approx 7000$.

While the decomposed velocities correspond well to stronger vortices, especially for the counter-rotating pair at x = 16 mm / y = 18 mm and the clockwise rotating vortex at x = 11 mm / y = 16 mm, the visualization fails for weak features like the vortex pair at x = 8 mm / y = 17 mm. Also the centers of the counter-rotating vortices do not correspond to the maximum of the calculated vorticity. Thus, the overall decomposition using the average velocity fails even for flows that are still in the transition from laminar to turbulent conditions. To solve the problems, the LES decomposition using a high-pass filter was applied to the instantaneous velocity fields. MATLAB offers a predefined filter and a built-in function for image

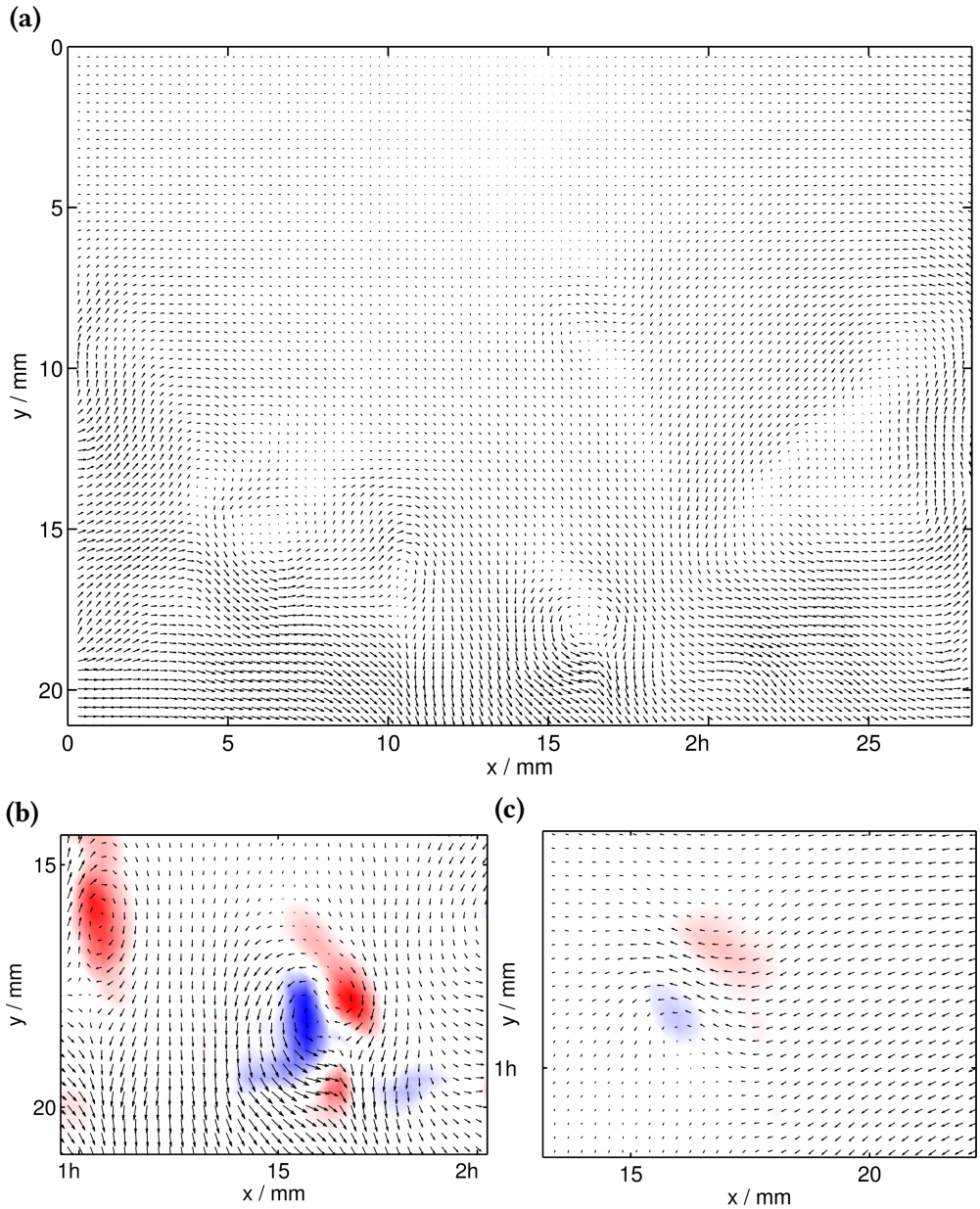

Figure 3.30: **(a)** Calculated velocity field 50 ms after start of the fan. The light sheet passed 4 mm in front of the spark plug, the distance between fan and cylinder head was 9 mm. **(b)**: Zoom of the velocity field. The velocity profile and vorticity plot for the stronger vortex pair are taken from the lower part of the vector field after $\bar{u}_\mathrm{x}$ and $\bar{u}_\mathrm{y}$ were subtracted. **(c)** Velocity profile and vorticity plot for the weaker vortex pair in the upper part of the vector field after $\bar{u}_\mathrm{x}$ and $\bar{u}_\mathrm{y}$ were subtracted.

processing. The Gaussian filter was created using the *fspecial* function, which first generates the Gaussian function

$$h_\mathrm{g}(n_1, n_2) = \exp\left(-\frac{n_1^2 + n_2^2}{2\sigma^2}\right) . \tag{3.10}$$

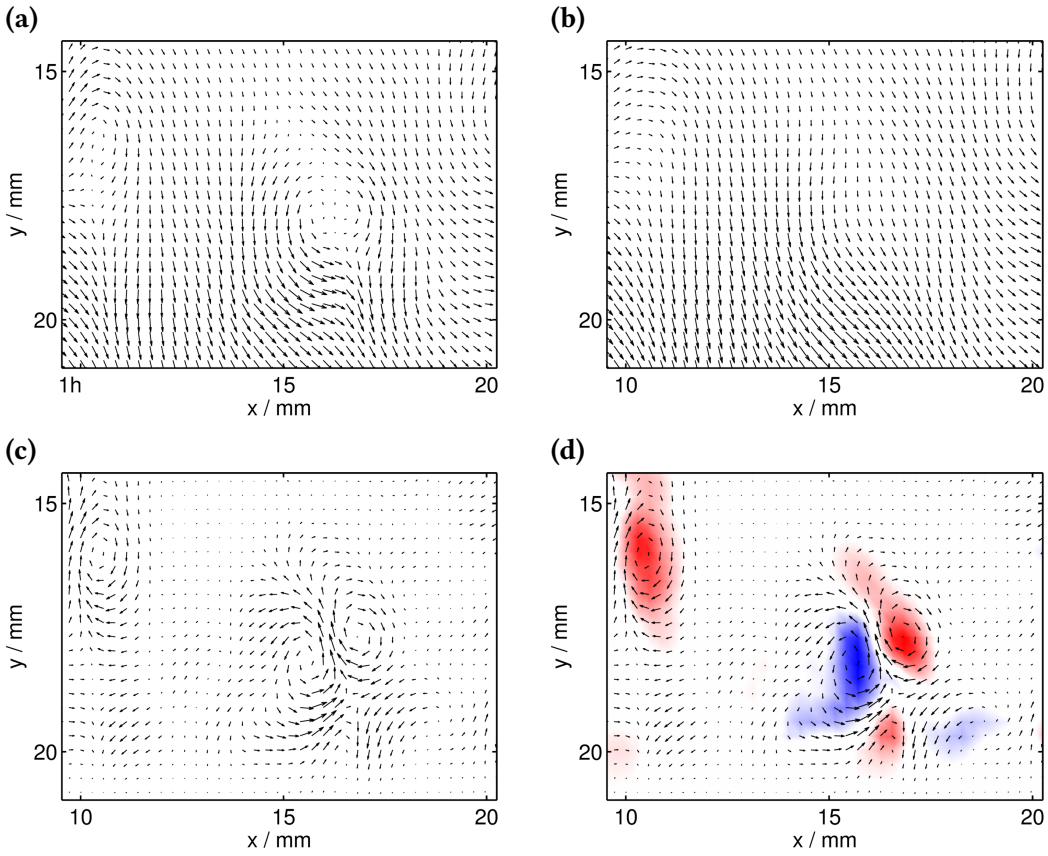

Figure 3.31: (a): Zoom of the velocity field around the counter-rotating vortex pair at x = 16 mm / y = 18 mm **(b)** Velocity field after convolution with a Gaussian function, kernel size 9 $\times$ 9 pixels. **(c)** Resulting velocity field after subtraction of convoluted field from the smoothed vectors. **(d)** High-pass-filtered velocity field overlayed on vorticity plot.

n_1 and n_2 represent the dimension of a matrix $n_1 \times n_2$, which defines the width of the Gaussian kernel in numbers of interrogation areas. In this Thesis, $n_1$and n_2 are equal in size, thus resulting in a square matrix. σ is the standard deviation. Afterwards, the smoothed velocities for x and y directions were separately convoluted using the function

$$h(n_1, n_2) = \frac{h_g(n_1, n_2)}{\sum_{n_1}\sum_{n_2} h_g}\,, \tag{3.11}$$

and afterwards subtracted from the smoothed vector field. This results in a high-pass-filtered vector field that reveals the smaller velocity fluctuations and vortices. The amount of filtering depends on the width n and standard deviation σ of the Gaussian filter and had to be checked for all individual images. If the parameters are chosen too big, not all high-frequency features will show up, if the kernel is too small, nearly all features will be cut off or smoothed out. Figure 3.31 shows the general procedure for high-pass filtering of an instantaneous velocity field. In this case a velocity field 50 ms after start of the fan with relatively slow moving

fluid particles was chosen. Again, the same counter-rotating vortices at x = 16 mm / y = 18 mm were used to verify the LES method.

The first picture shows the calculated low-pass filtered velocity field used for the decomposition. Compared to the Galilean method, the subtracted velocity field is homogeneously composed, accounting for the fluctuations of the velocity in the observation plane. After subtraction and low-pass filtering of the remaining vector field, the decomposed image clearly shows the underlying structure of the turbulent flow and corresponds very well to calculated vorticity. Note that the vectors are of different scale and thus not comparable with the original vector field.

Results and Discussion 4

Chapter 4 reports on the experimental results of the present work. It is divided into three major sections:

Section 4.1 presents the combustion behavior for pre-mixed fuel compositions and manually injected fuel. Propane/air and propene/1-butene/air fuel mixtures were burned and the chamber pressure and piston speed were measured. The influence of turbulence, mixing and the placement of obstacles in form of grids and the fan in the chamber were analyzed and compared to combustion under laminar conditions.

Section 4.2 presents the results for flame front imaging under laminar and turbulent combustion. Flames were investigated using chemiluminescence and laser-induced fluorescence imaging of OH radicals.

Lastly, Section (4.3) shows the results obtained by the particle image velocimetry for for turbulent flow without ignition. The flow in the chamber induced by the movement of the fan is analyzed at different fan speeds. Measurements were done at different positions in the chamber and for varying fan insertion depths.

4.1 Combustion behavior for different experimental conditions and fuel compositions

The combustion of various fuels was investigated under laminar conditions without obstacles. Different fuel compositions consisting of propane/air and injected fuels containing propane or propene/1-butene were ignited and pressure-time traces were recorded. Afterwards, the influence of obstacles on the combustion and finally the turbulence induced by the fan were investigated.

4.1.1 Laminar premixed and partially premixed combustion of propane and propene/1-butene fuel

Prior to each measurement, the chamber was flushed using compressed air followed by flushing the chamber with the desired mixture for at least 5 minutes. For

flushing times shorter than 2 minutes, a reduction of the maximum pressure could be observed. The raw pressure-time profiles for propane/air mixtures of 3.3 vol%, 3.5 vol%, 4.1 vol%, 5.0 vol%, 6.0 vol% and 6.5 vol% are shown in Figure 4.1. All traces were recorded between $t = 0$ ms and 80 ms after start of ignition without any additional obstacles present. Ignition of mixtures with low propane content (vol% < 3.5) yielded maximum pressures below $\Delta p_{\max} = 1$ bar. Mixtures containing 3.0 vol% of propane showed the lowest recorded pressure rise of 0.4 bar, while mixtures containing less than 3.0 vol% could not be ignited. The low peak pressure was observed at pressure rise times of $t\,(\Delta p_{\max}) > 28$ ms. The longest rise times were observed for the lowest propane content. For higher propane amounts, the maximum pressure increases to $\Delta p_{\max} > 1$ bar, while the rise times decrease. The maximum peak pressure and minimum rise time can be found for mixtures containing 4.5 vol% propane. For higher fuel-air-ratios, the maximum pressure decreases in combination with longer pressure rise times. Mixtures containing 6.5 vol% propane marked the maximum amount of ignitable fuel-content (see Fig. 4.2). All mixtures with maximum pressures above 1 bar only showed one

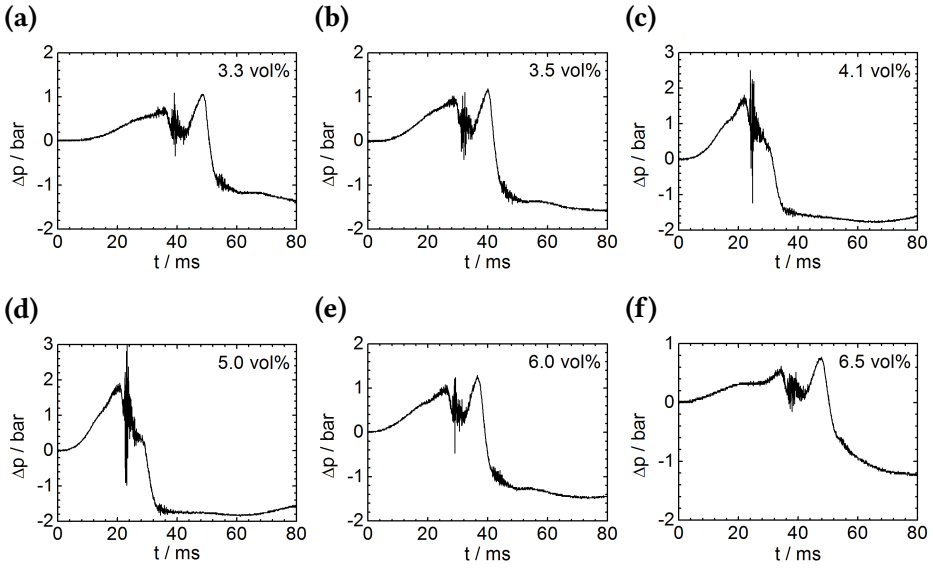

Figure 4.1: Pressure-time traces for the first 80 ms after ignition. Fuel compositions between 3.3 vol% and 6.5 vol% propane were burned under laminar conditions without obstacles in the chamber.

clearly identifiable maximum, while for lower maximum pressures a second peak was found between 15 – 20 ms after the first maximum. The maximum pressure of the second peak is of the same magnitude as the first, but characterized by a higher rate of pressure rise ($\mathrm{d}p/\mathrm{d}t$) as well as a steeper pressure drop. For all mixtures, the rate of pressure rise changes around half maximum of the first pressure peak. The combustion of the premixed fuels was compared to the combustion of injected

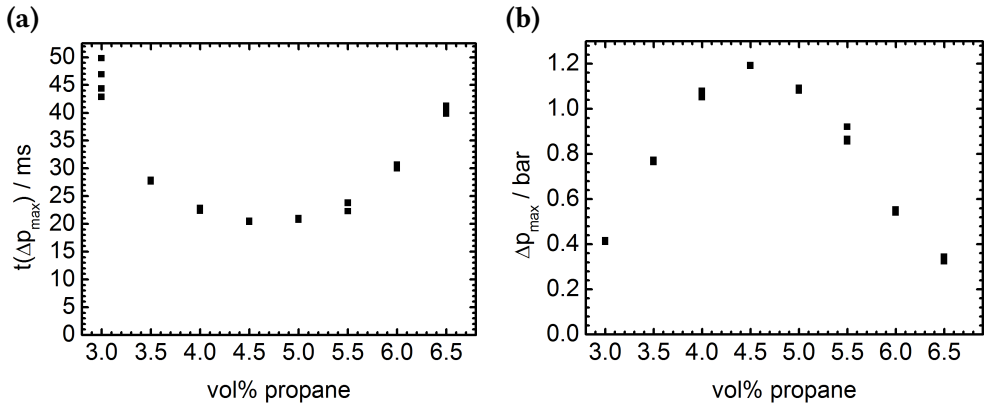

Figure 4.2: **(a)** Pressure rise time $t\,(\Delta p_{\max})$ and (b) maximum pressure $\Delta p_{\max}$ for propane/air mixtures under laminar conditions between 3.0 vol% and 6.5 vol%.

propane mixtures using the BeA cartridges (see Fig. 3.10). Pressure-time traces of BeA and 4.1 vol% propane fuel in air are shown in Figure 4.3. To ensure a homogeneous fuel distribution of the premixed composition, the fuel in the pre-filled chamber was stirred using two different grids that were of the same size as the cylinder and could be moved up and down manually in the chamber. The grids were made from perforated stainless steel plates with hole diameters of d_{big} = 3 mm or d_{small} = 1.5 mm. After stirring, they were positioned flush with the cylinder head. The mixtures investigated were BeA fuels after 10 and 20 fold stirring and premixed

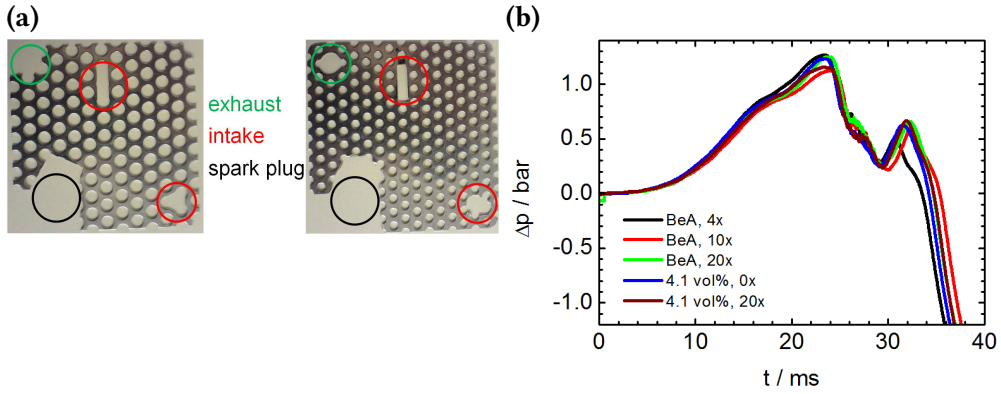

Figure 4.3: **(a)** Mixing grids used for homogenization of injected and premixed fuels. Recesses for intake (red), exhaust (green) and the spark plug are noted by the circles. **(b)** Pressure-time traces using BeA fuel and 4.1 vol% propane after different mixing processes.

propane without stirring and 20 fold stirring. In comparison, the combustion of BeA fuel without mixing is also shown. All pressure traces rise to a maximum pressure of $\Delta p_{\max} \approx 1.1$ bar after a rise time of t = 24 ms. Furthermore, all curves show a change in pressure rise at t = 17 ms and a second maximum between t = 30 ms and 33 ms.

The observations and conclusions for the measurements can be summarized as follows: The explosion limits for propane-air mixtures at ambient conditions are ≈ 2.5 vol% and 9.6 vol% for the lower flammability limit (LFL) and upper flammability limit (UFL), respectively.[55,196,197] With an LFL ≈ 3.3 vol% and UFL ≈ 6.5 vol%, the explosion limits obtained in this Thesis agree well with the literature values.[198,199] While the LFL and UFL could be extended to 3.0 vol% and 7.0 vol%, respectively, they were not part of experimental investigation, because they cannot be used for practical applications. Although mixtures approaching the LFL and UFL could be ignited, the detected pressure rise was too small to be considered relevant. Additionally, the reproducibility was significantly decreased for mixtures close to the LFL and UFL. A possible explanation for the decrease of ignition probability towards the flammability limits might be the position of the spark. The lower spark electrode is located close towards the surface of the cylinder head, while the upper electrode is placed inside the head. During the development of the flame kernel, the expanding sphere is susceptible to heat loss effects, which might occur given the proximity of a relatively cold surface. Due to the single-shot experiments, the walls of the combustion chamber have a temperature equal to the surrounding ambient air.

The highest pressure and rise time was not found for stoichiometric mixtures containing 4.1 vol% propane, instead the maximum of the pressure and time curves were both found in the richer regime. The maximum occurred between 4.5 vol% and 5.0 vol%, which is in good agreement with literature.[198] The different shapes and the second maximum of the pressure-time traces depending on the fuel amount can be explained by the expansion of the piston towards bottom dead center. A representative pressure trace of stoichiometric propane combustion is shown in Figure 4.4. The first change of slope and thus a decrease in the rate of pressure rise occurs at t = 15.8 ms after start of ignition. This corresponds to the piston reaching the first light barrier. Thus, the reduced pressure rise can be attributed to the expansion of the piston which decreases the pressure. The piston passes the third light barrier when the peak pressure is reached. Due to the rapid expansion of the piston, the pressure decreases strongly after the maximum. The oscillations after pressure decrease occur at the lowest piston position and can thus be attributed to shock waves induced by the impact of the piston crown at bottom dead center. Afterwards, the piston starts to move upwards, marked by the passing of the last light barrier and the second spike in the pressure traces. This happens due to the rapid expansion and creation of under pressure or the recoil induced by the impact. In case of higher fuel content, this second peak is less pronounced. The higher combustion rate and steeper pressure rise counteracts the upward motion of the piston and dampens the recoil. The change of pressure rise at t = 15.8 ms can also

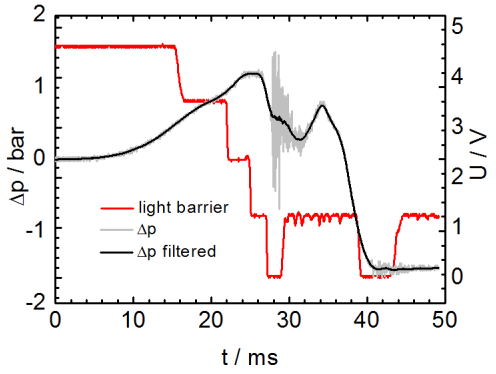

Figure 4.4: Exemplary pressure-time trace and signal after filtering in comparison with the light barrier voltage signal.

be attributed to another effect. It is known from pressure rise measurements of gaseous fuels in spherical or cylindrical closed vessels that the point of ignition can alter the combustion behavior and thus the pressure-time traces. For ignition close to the top of the vessel, the flame starts to propagate spherically or hemispherically, until it reaches the walls and starts to propagate downward. Thus, the second stage of pressure rise should result in a lower rate of pressure rise due to the heat loss to the walls.[200] An exemplary pressure rise diagram is shown in Figure 4.5. To

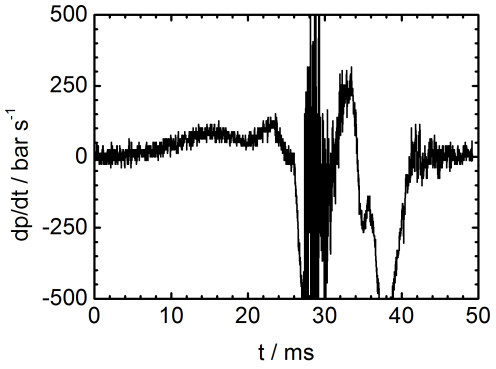

Figure 4.5: Derivative of the pressure rise ($\mathrm{d}p/\mathrm{d}t$) for the first 50 ms after ignition calculated from Figure 4.4.

calculate the derivative of the pressure rise ($\mathrm{d}p/\mathrm{d}t$) from the $p(t)$ diagrams, the data points were smoothed using the Savitzky-Golay method based on least squares quartic polynomial fitting in a 20 points moving window.[201] The first maximum pressure rise can be found at $t = 15$ ms. Due to the noisy data, the maximum rate could only be estimated to be at $(\mathrm{d}p/\mathrm{d}t)_{\mathrm{max}} \approx 90\,\mathrm{bar\,s^{-1}}$. Followed by a decrease of ($\mathrm{d}p/\mathrm{d}t$), a second maximum can be found at $t = 23$ ms. The rate of pressure increases to $(\mathrm{d}p/\mathrm{d}t)_{\mathrm{max}} \approx 120\,\mathrm{bar\,s^{-1}}$, which is in contrast to the aforementioned effect of heat loss to the walls. The rate of pressure rise does not only depend on the point of ignition, but also on the shape and volume of the explosion vessel. The maximum rate of pressure rise increases with decrease in volume of spherical

chambers, and is smaller for cylindrical chambers of similar size. The maximum pressure rise for a spherical bomb with a constant volume of $V = 520\,\mathrm{cm}^3$ was reported to be $(\mathrm{d}p/\mathrm{d}t)_{\max} = 1057\,\mathrm{bar\,s}^{-1}$[201] and thus significantly higher compared to the results obtained in this Thesis. Nevertheless, the rates of pressure rise at early times ($t < 30\,\mathrm{ms}$), obtained in experiments with a constant volume are of the same order of magnitude as presented in this Thesis and the difference can be attributed to the change of volume during the combustion.

The pressure-time traces can also be used to investigate the influence of non-laminar conditions on the flame propagation. If the flame front in small scale explosion is not disturbed, the combustion wave traveling through the mixture is supposed to be spherical.[202] For this case, a cubic law correlating the pressure increase during the constant volume combustion with time from ignition can be applied:

$$\Delta p = C \cdot p_0 \frac{u_l^3 t^3}{V_0} \equiv C' t^3 \,, \tag{4.1}$$

where p_0 is the initial pressure, V_0 the volume of the chamber, u_l the burning velocity and C a dimensionless constant depending on the mixture properties. To validate the model of a spherical expansion of the flame kernel for early stages of the combustion, the pressure variation Δp can be modeled according to Equation 4.1. To account for imprecision during the time measurements due to the jitter of the trigger and slight variations in the baseline of the pressure transducer, a modified law was applied:[203]

$$\Delta p = a + C' \left(t^n + b\right) \,. \tag{4.2}$$

Here, n was used as a free parameter to check for deviations from the cubic law. An exemplary fitted pressure profile is shown in Figure 4.6. Using equation 4.2, the pressure profile could be described very well up to the change in pressure rise at $t = 15\,\mathrm{ms}$. With a free fit parameter of $n = 3 \pm 0.04$, is it reasonable to assume

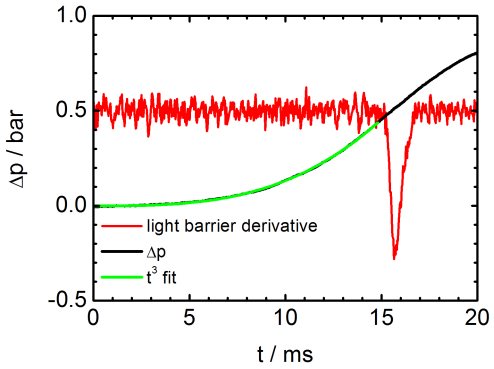

Figure 4.6: Exemplary pressure-time trace for the first 20 ms after ignition (black line) and data fit (green) until $t = 15\,\mathrm{ms}$ after ignition according to equation 4.2. The derivative of the light barrier voltage is shown in red.

a spherical expansion of the flame front at least for the first 15 ms after start of ignition.

The pressure-time traces for laminar combustion did not change for flushing times longer than 3.5 minutes and additional stirring. As seen from the measurement with different amounts of propane, a change in fuel composition results in drastic changes of the pressure curves. Hence it is reasonable to assume that the fuel-air mixture is equally distributed over the whole chamber volume for each measurement or the mixing ratio of fuel and air was constant for each composition. Nevertheless, the injected fuel, which is assumed to be partially premixed due to the injection process, showed the same combustion behavior as the premixed fuel. Due to manual operation of the chamber, a certain delay t_{inj} between fuel injection and ignition occurred. This delay was usually not longer than $t_{\mathrm{inj}} \approx 5$ s. For the injected fuel, a spherical expansion of the flame kernel for early times can also be expected.

4.1.2 Laminar premixed and partially premixed combustion of propane and propene/1-butene fuel with obstacles placed in the combustion chamber

As mentioned in Section 2.1, combustion can be enhanced by placing obstacles in the path of the expanding flame.[204] The first experiments were done using the mixing grid as stiff, non-moving obstacle. This was advantageous because the flat grid represents a more simple geometry in comparison to the twisted fan blades. Furthermore, the height of the grid inside the chamber can be easily changed. A lowering of the fan is always accompanied by a change in volume because the height of the fan blades can only be changed by lowering the housing of the electric fan. While the volume is also changed by lowering the grid, the effect of volume reduction due to the rod, which is connected to the grid, is negligible. Both mixing grids were investigated at insertion depths between $d_{\mathrm{i}} = 0$ mm (flush with the cylinder head) and 4.5 mm (flush with the cylinder bottom). The data are shown in Figure 4.7. The maximum pressure Δp_{max} and maximum velocity v_{max} at minimum insertion depth of the small grid are comparable to the values obtained at laminar conditions without any obstacles. A significant change in pressure and velocity can be found at an insertion depth of $d = 1$ mm. Here, the average maximum pressure and velocity increase to $\Delta p_{\mathrm{max}} = 1.8$ bar and $v_{\mathrm{max}} = 68\ \mathrm{km\,h^{-1}}$ measured at the fourth light barrier. The highest peak pressure and velocity occur at an insertion depth of $d = 2.5$ cm. The peak pressure increases to 2.5 bar, the maximum velocity

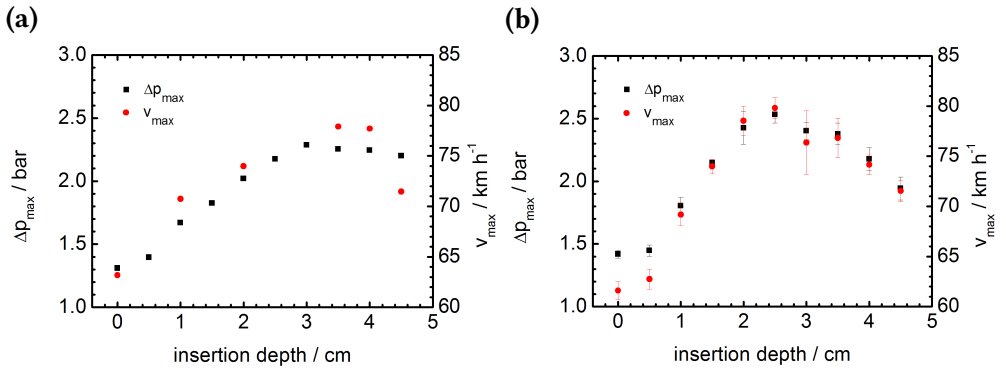

Figure 4.7: Maximum piston velocity $v_{\max}$ (red) and maximum pressure $\Delta p_{\max}$ (black) using the propane cartridges and the big grid, $d_{\text{big}} = 3$ mm **(a)** and the small grid, $d_{\text{small}} = 1.5$ mm **(b)**.

to 79 km h^{-1}. For lower insertion, peak pressure and velocity decrease towards $\Delta p_{\max} = 2$ bar and $v_{\max} = 72$ km h^{-1}, respectively. The insertion depth using the

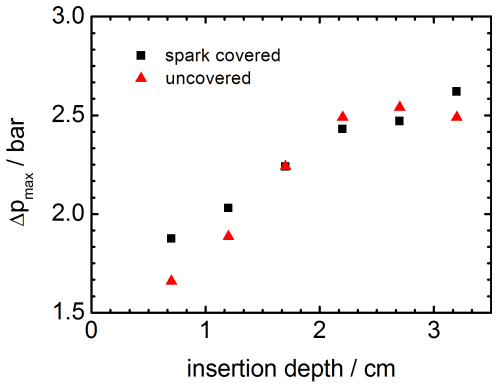

Figure 4.8: Maximum pressure of BeA fuel for different cases of insertion depth of the fan and positions of the fan as obstacle (non-rotating) blade relative to the spark plug.

non-rotating fan as stationary obstacle was set as the distance between the tip of the fan blade and the cylinder head. An insertion depth of 0 mm could not be realized because the spark electrode protruded in the chamber. Measurements were done with a spark electrode covered by a fan blade and uncovered (see Fig. 4.8).

A similar effect can be observed with mounted fan compared to the grids. A maximum peak pressure can be found at insertion depth around $d \approx 2.5$ mm for both covered and uncovered conditions. Nevertheless, the maximum pressure at lower insertion is slightly higher with mounted fan. The data also show a difference between combustion with covered and uncovered spark. Here, the maximum pressure is slightly higher for low insertion depths until $d = 1.7$ mm, where both are equal.

The results and conclusions can be summarized as follows: The measured pressures and piston velocities at the minimum insertion depth for the grids are

consistent with the data for the undisturbed flame expansion without obstacles. The only slight increase of pressure and velocity at $d = 0.5$ cm indicates a small flame kernel which passes through the cutout ($d_{\mathrm{cut}} = 0.9$ cm) without disturbance. The first interaction between flame front and obstacle can be found for an insertion depth of $d = 1.0$ cm suggesting a flame kernel with a diameter bigger than $d_{\mathrm{flame}} = 0.9$ cm. The highest effect of flame acceleration can be found for insertion depth between $d = 2.0$ cm and 3.0 cm. Here, the flame kernel is large enough to interact with the maximum number of grid holes. The increase of flame wrinkling results in an increase of flame surface and thus burning velocity. This effect can be seen in the pressure-time trace shown in Figure 4.9. The pressure rises until

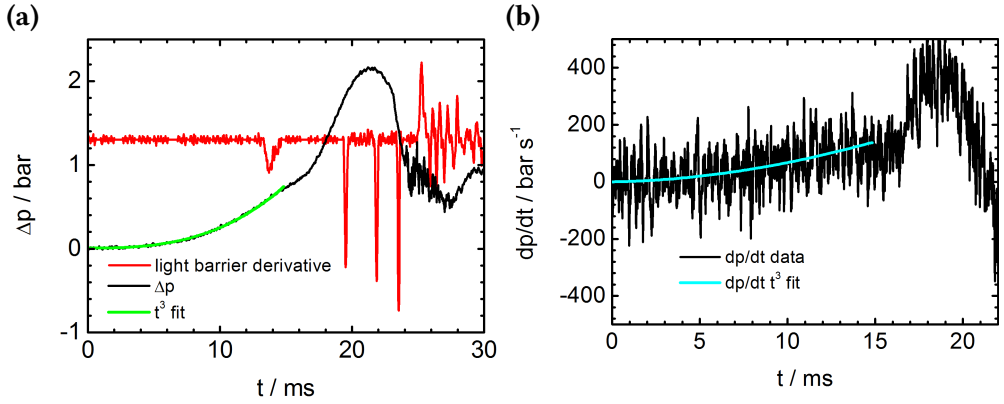

Figure 4.9: **(a)** Pressure diagram at an insertion depth of $d_{\mathrm{i}} = 2.5$ cm (black) and fitted data (green) until the inflection point at $t = 14$ ms. The according derivative of the light barrier voltage is shown in red. **(b)** Measured rate of pressure rise ($\mathrm{d}p/\mathrm{d}t$) (black) and rate calculated according to Equation 4.2 (blue).

$t = 14$ ms, which coincides with the piston reaching the first light barrier. According to equation 4.2, the fit results suggest a near spherical expansion of the flame with constant burning velocity u_{l}. Due to the expansion of the piston the rate of pressure rise drops first and increases strongly at $t = 17$ ms. Due to the noisy data, is not possible to calculate an exact rate of pressure rise for the flame-obstacle interaction. As seen in Figure 4.9b, the spherical flame model is in good agreement with the measured data and a maximum rate of pressure rise can be found at $(\mathrm{d}p/\mathrm{d}t) = 130$ bar s^{-1}, which corresponds to the rise rate measured for combustion without obstacles in Section 4.1.1. Although a steep increase in pressure rise at $t = 16$ ms can be unambiguously seen, the maximum rate of pressure rise can only be estimated. Between $t = 18$ ms and 19 ms, the rate is increased by a factor of 3 to $(\mathrm{d}p/\mathrm{d}t) \approx 360$ bar s^{-1}. Due to the expansion of the chamber, seen by the piston reaching the second light barrier during the maximum rate of pressure rise at $t = 19$ ms, the total chamber pressure and the subsequent rates of pressure rise decrease. The steady decrease of maximum pressure and piston velocity for higher

insertion depth might be due to the same mechanism. The rate of pressure rise and thus velocity of the moving flame is reduced before the flame front hits the obstacle. While an increase of the rate of pressure rise at this point is still visible, it does not reach the values obtained at lower insertion depths. The data obtained with the big grid show the same trend, albeit the pressure and velocity drop at higher insertion depths is less pronounced. In contrast to the small grid, all obtained values originate from single shot measurements, which tend to fluctuate more for non-laminar conditions, which can be assumed during the interaction of flame and turbulence caused by the grid.

In comparison to the grid pressures, the influence of the position of the fan inserted as obstacle seems to be similar as shown in Figure 4.8. A significant increase in pressure rise can be found at an insertion depth of $d \approx 1.0$ cm, indication of a slightly less important influence of wrinkling around the blades on the early development of the flame kernel. The maximum pressure can be found for insertion higher than 2.0 cm. In addition to that, the effect of increased pressure due to blocking the direct pathway beneath the spark plug vanishes. Nevertheless, the obstacles, in particular the fan, act as an important tool for flame acceleration and thus in increase in rates of pressure rise. An often seen influence of blocking ratio,[22,205–207] achieved using differently spaced grids, could not be observed. Because all obstacles increase the maximum pressure, the heat sink-like conditions of the cold metal surfaces[208] seem to be unimportant for the flame expansion mechanism.

4.1.3 Turbulent premixed and partially premixed combustion of propane and propene/1-butene fuel

To investigate the effect of higher degrees of turbulence on the combustion, all measurements were repeated while the fan was running. This was initially done using a fixed starting time of the fan before ignition, which was set to $\Delta t_{\mathrm{fan}} = 250$ ms. Preliminary measurements showed that the ignition probability for premixed fuels was close to zero when the fan position was at its highest insertion depth. The ignition probability for injected fuel was also slightly decreased, as not every single injection in fuel lead to a combustion event. Therefore, the measurements were performed with the fan positioned at a lower insertion depth of $d = 9$ mm.

As can be seen in Figure 4.10, the pressure-time traces with running fan differ drastically from the combustion under laminar conditions. Depending on fuel composition, the peak pressure is increased by a factor of 3–5 compared to

measurements without obstacles and a factor of 2 compared to measurements with stationary fan present, respectively. The time to reach peak pressure is shortened by a factor of 2 to $t\,(\Delta p_{\max}) < 10$ ms after ignition. Additionally, the maximum velocity of the piston increased to $v_{\max} \approx 130\,\mathrm{km\,h^{-1}}$. The pressure-

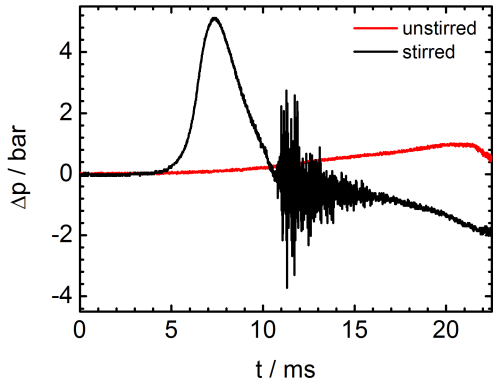

Figure 4.10: Comparison of the pressure-time traces between turbulent combustion (black line) and laminar combustion without obstacles (red line).

time traces were recorded for different propane/air compositions between 4.0 vol% and 6.0 vol% at a fan delay time of $\Delta t = 250$ ms (Figure 4.11). The ignition probability dropped significantly for mixtures containing less than 4.0 vol% and more than 6.0 vol%, hence which were not considered for systematic studies. All other experiments were repeated three times for each fuel composition. The highest peak pressure $\Delta p_{\max} = 4.2$ bar was observed for rich mixtures containing 5.0 vol% propane, with an average of $\Delta p = 4.0$ bar. Mixtures containing more or less propane showed a decrease of maximum pressure. A minimum can be found for 4.0 vol% at $\Delta p = 3.0$ bar. An inverse curve form occurred for the time to reach peak pressure. The shortest time of $t = 7.6$ ms occurs at 5.0 vol% propane, the average time is

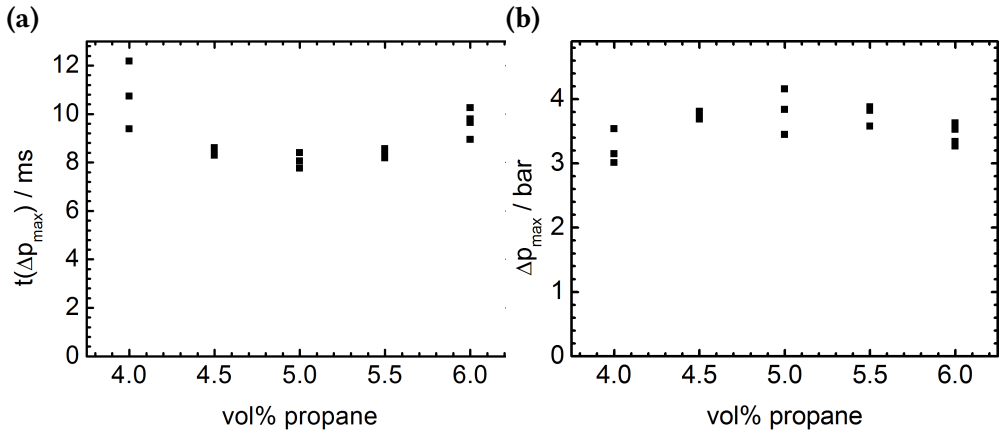

Figure 4.11: **(a)** Pressure rise time $t\,(\Delta p_{\max})$ and **(b)** maximum pressure $\Delta p_{\max}$ for propane/air mixtures under turbulent conditions between 4.0 vol% and 6.0 vol% at $\Delta t_{\mathrm{fan}} = -250$ ms.

$t \approx 8.0$ ms. For leaner and richer mixtures $t\,(\Delta p_{\max})$ increases to a maximum of $t = 12.2$ ms for 4.0 vol%. For lean mixtures, the peak pressure is scattered over a range of $\Delta\,(\Delta p) = 0.55$ bar, while the peak pressure time varies between 9.4 ms and 12.3 ms.

As it was known from these experiments that for a fan start of 250 ms before ignition the ignition probability drops for certain mixtures, the influence of fan running time on the combustion was investigated. Fuel mixtures of 4.0 vol%, 5.0 vol% and 6.0 vol% were ignited at fan starting times between $\Delta t_{\text{fan}} = 50$ ms and 500 ms before ignition. The results are shown in Figure 4.12. Prior to the measurements, the chamber was flushed for at least 5 minutes with the investigated mixture. Using flushing times of less than 2 minutes lead to a strong decrease of maximum pressure and for lean mixtures to a complete ignition failure. Flushing times longer than 5 minutes showed no effect on the pressure profiles. All curves

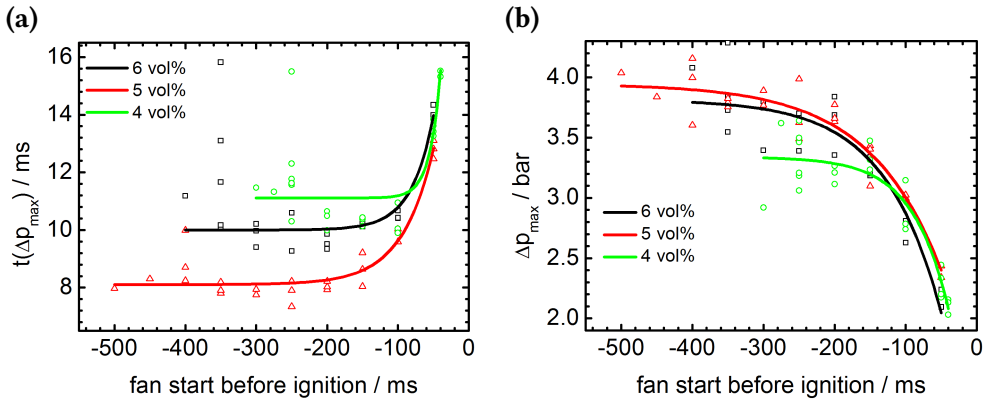

Figure 4.12: (a) Pressure rise time $t\,(\Delta p_{\max})$ and **(b)** maximum pressure $\Delta p_{\max}$ for propane/air mixtures for different fan starting times Δt_{fan}. Compositions of 4.0 vol%, 5.0 vol% and 6.0 vol% were investigated.

show a drastic increase in peak pressure and a decrease in pressure rise time up to fan delay times of $\Delta t = 100$ ms. For higher delays, the curves flatten and reach their maximum values around $\Delta t \approx 300$ ms. Overall, mixtures with 5.0 vol% propane have the highest peak pressures and shortest rise times, while for 4.0 vol% the values are considerably lower. Lean mixtures showed a steep decrease in ignition probability for fan delay times above $\Delta t = 250$ ms and drops to zero for $\Delta t > 300$ ms. A maximum fan running time without decrease in ignition probability can be found for mixtures containing 5.0 vol% propane. Here, the fan running time can be extended to $\Delta t = 400$ ms. At the edge of decreasing ignition probability, all mixtures showed a strong scattering of the values for peak pressure and pressure rise time.

Due to the change of the cartridge gas composition towards propane/1-butane, extended investigations of the combustion behavior of the injected propane could

not be done. Nevertheless, the general ignition probability under turbulent combustion condition was the same for both gases. The main difference after the change towards propene/1-butene could be observed in the pressure-time traces. Using these mixture, the maximum observed peak pressure was $\Delta\,(\Delta p) \approx 0.5$ bar higher, the rise times were decreased by $\Delta\,(\Delta t) \approx 1$ ms. As shown in Figure 4.13, the

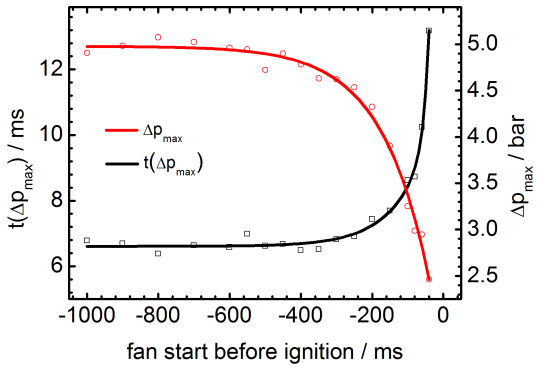

Figure 4.13: Pressure rise time $t\,(\Delta p_{\max})$ and maximum pressure $\Delta p_{\max}$ for propene/1-butene/air mixtures at different fan starting times Δt_{fan}.

peak pressure increases with increasing fan delay times and reaches a maximum at $\Delta p \approx 5.0$ bar around $\Delta t > 500$ ms. The shortest rise times of $t \approx 6.6$ ms can also be found for delay times longer than 500 ms. The steepest change of both values occurs between $\Delta t = 40$ ms and 200 ms. Ignition could be observed over the whole measurable delay time range of 1000 ms. At the shortest possible delay time $\Delta t = 40$ ms, the peak pressure and rise time are comparable to the values obtained from the obstacle measurements.

The results allow for the following conclusions: As seen from the pressure-time traces, the movement of the combustible mixture has a significant impact on the pressure-time traces. The peak pressure is increased by a factor of 3 for all fuel-equivalence ratios investigated. The maximum pressure rise and rise time was achieved for slightly richer mixtures and dropped towards the leaner and richer limits, similar to combustion under laminar conditions. Depending on the fan running time, the overall range of ignitable mixtures was severely narrowed down to 4.0 vol% on the lean side and 6.0 vol% as the rich limit. To calculate the rate of pressure rise, the pressure data were fitted according to Equation 4.2, with n as a free parameter. In contrast to the laminar combustion, the initial phase of pressure rise could not be approximated using $n = 3$. This indicates a strong deviation from the spherical expansion of the flame kernel. An exemplary comparison of the data and fit model is shown in Figure 4.14. The data could be well described instead using a value of $n = 7.4 \pm 0.2$. The drastic increase of $(\mathrm{d}p/\mathrm{d}t)$ with t^n is in good agreement with literature, where values of $n > 6$ were reported for turbulent combustion.[202] The rate of pressure rise was approximated using the derivative

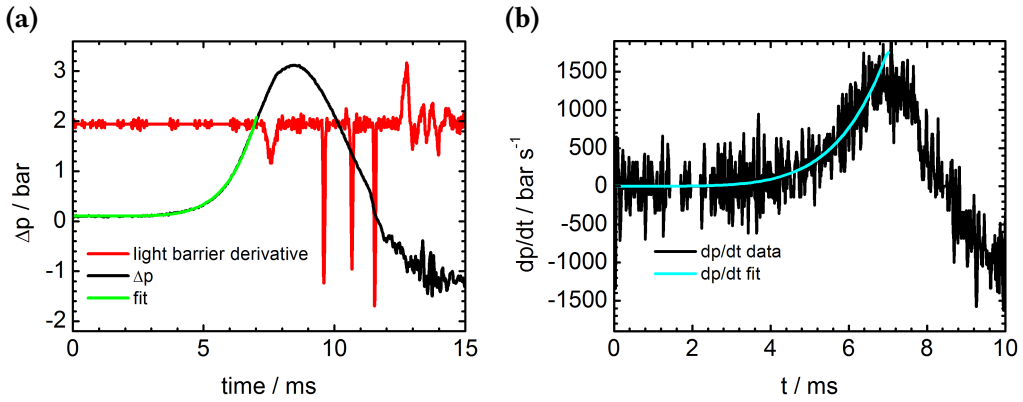

Figure 4.14: **(a)** Pressure diagram for turbulent combustion (black) and fitted data (green) until $t = 7$ ms. The according derivative of the light barrier voltage is shown in red. **(b)** Measured rate of pressure rise ($\mathrm{d}p/\mathrm{d}t$) (black) and rate calculated according to Equation 4.2 (blue).

of the measured data in combination with the fit model shown in Figure 4.14b. In comparison to the laminar conditions, the rate of pressure rise is increased by a factor of ≈ 10 to $(\mathrm{d}p/\mathrm{d}t) = 1300\,\mathrm{bar\,s^{-1}}$. The stronger expansion can be linked to an increase in the rate of fuel consumption during the reaction. The rate of fuel consumption $\mathrm{d}m_\mathrm{b}/\mathrm{d}t$ can be expressed as a function of flame surface area A_fl, unburned fuel/air density ρ_u, the laminar burning velocity u_l and turbulent velocity fluctuation u' [205]

$$\frac{\mathrm{d}m_\mathrm{b}}{\mathrm{d}t} = A_\mathrm{fl}\rho_\mathrm{u}\left(u' + u_\mathrm{l}\right) . \tag{4.3}$$

Due to the turbulence induced by the fan, it can be assumed that the initial spherical shape of the flame is severely distorted, which then leads to an increase of flame surface and thus higher burning ratio. From the comparison of the pressure increase and signal of the light barrier seen in Figure 4.14a, it is clearly visible that the pressure reaches its maximum value nearly identical to the time of the piston reaching the first light barrier. In this case, the effect of reduced maximum pressure due to the expansion of the piston is less pronounced for highly turbulent conditions. Another mechanism for the explanation of the resulting pressure-time traces and the effect of flame quenching is the change of turbulent burning velocity u_t. The increase of burning velocity can be estimated according to

$$\frac{u_\mathrm{t}}{u_\mathrm{l}} \approx \left(\frac{a + u'L}{a}\right) , \tag{4.4}$$

where a is the thermal diffusivity, u' the turbulence intensity and L the corresponding length scale.[19] For small scale turbulence, where the eddies do not exceed the

flame front thickness, the mechanism governing the increase in burning velocity is the enhancement of heat and mass transport. For high turbulence, the distorted flame front breakes up and forms pockets of burning gas, which then can brake away and enter the unburned gas. The flame thickness increases further, leading to a thicker reaction zone and hence a slower burning. This effect might cause the scattering of the peak pressure times at longer fan running times, as seen in Figure 4.12. Especially for the less stable mixtures, the peak pressure times can be increased from $t\,(\Delta p_{\max})$ = 11 ms to 16 ms, as seen for mixtures containing 4.0 vol% propane as well as 6.0 vol%.

The same effect, albeit less pronounced, can also be found for the peak pressures. For longer fan running times, the ignition probability decreases significantly. The influence of turbulence on the turbulent burning velocity of lean and rich propane-air mixtures has been investigated by many groups, most notably by Abdel-Gayed and coworkers.[209] They used a constant-volume bomb with central ignition source containing four fans to generate uniform and isotropic turbulence. They reported an increase of turbulent burning velocity with increase in fan speed for all investigated mixtures. The highest burning velocity of $u_{\mathrm{t}} \approx 6\,\mathrm{m\,s^{-1}}$ were found for rich propane-air mixtures containing 4.7 vol% propane, and a slight decrease to $u_{\mathrm{t}} \approx 5\,\mathrm{m\,s^{-1}}$ at 5.5 vol%. Leaner mixtures showed a trend of decreasing turbulent burning velocity with a decrease of fuel amount. Additionally, they found a quenching limit for lean mixtures that decreased towards lower fan speeds with a decrease of fuel amount. Similar results were obtained by Karpov and Severin, using a comparable setup with four agitators.[210] In theory, a flame is quenched if the flame front is broken up to the point where cold gas can enter the reaction zone. This can reduce the temperature of the flame and decrease the reaction rate, until the flame chemistry cannot sustain itself.[19,22] This can be described using the ratio of thermal diffusivity a to mass diffusivity D, which is defined as the Lewis number Le

$$Le = \frac{a}{D}\,. \tag{4.5}$$

Thus, flame quenching by turbulent strain occurs for $Le > 1$.[205] In contrast to the experiments performed by Adbel-Gayed, which are characterized by a low mean flow velocity with by high turbulence intensity,[211] these experimental conditions cannot be assumed for the experimental setup in this Thesis. Nevertheless, the general trend of stable propane mixtures in the rich regime and a lower quenching limit for lean mixtures could also be observed during the work here. As already discussed before, another influence on the combustion behavior is the geometry of the combustion chamber, e.g., spherical or cylindrical, and the point of ignition. The influence of chamber size on the pressure increase induced by turbulence

was shown by Harris, who did not observe a decrease of maximum pressure with increased turbulence.[212]

As mentioned in Section 2.1.2.1, the ignition probability of a certain mixture depends on several variables, e.g., the minimum ignition energy (MIE) and quenching distance (d_q). For laminar mixtures, the MIE is usually observed at fuel-equivalence ratios above stoichiometric mixtures and increases with increasing carbon number. This effect is attributed to lower diffusivities for molecules heavier than air, e.g., propane and propene. As shown in a variety of experiments,[48,213] the required MIE increases strongly for leaner and richer mixtures, resulting in u-shaped curves. This effect could also be observed for the quenching distance between two electrodes, which has a minimum for propane-air mixtures around 5.0 vol%.[42,48,214,215] When a combustible mixture is exposed to turbulence, the minimum of the MIE stays at the same fuel-to-air equivalence ratio, albeit the total value for the MIE and quenching distance are increased. The u-shaped curves are severely narrowed and thus show a strong increase for d_q.[47] It is thus possible that the energy deployed by the spark to the combustible mixture at high fan speeds is below the amount needed to establish a self-sustaining flame kernel. As the ignition energy provided by the spark electronics is unknown, a comparison of the distance between the spark electrodes used in the experiments with literature values is not possible. Nevertheless, quenching distances for quiescent mixtures of propane found in the literature are of similar orders of magnitude. For propane and propene fuels, the minimum quenching distance determined using a spherical bomb, are $d_{C_3H_8}$ = 1.7 mm[42,213] and $d_{C_3H_6}$ = 1.6 mm[216], respectively. Those values are still below the spark gap of d_{spark} = 4.0 mm, but may rise to higher values with increasing fan running times.

The use of propene/1-butene as fuels resulted in a higher peak pressure and pressure rise time, caused by an increase of laminar flame velocity. At the ideal fuel-to-air ratio, a flame velocity of u_l = 0.46 m s^{-1}[200] was measured at atmospheric conditions, while propane mixtures showed a maximum velocity of u_l = 0.40 m s^{-1}.[203,217] This resulted in an increase of the rates of pressure rise, as shown by Razus and co-workers.[200,201]

The difference in kernel stability can also be explained using the ignition delay time τ_{ign}. Ignition delay times were calculated using CHEMKIN and the USC Mech. II[218] mechanism for C_1–C_4 fuels and a 1D flame model at initial pressure of 1 bar. The ignition delay times were determined using the maximum of the OH radical concentration profiles calculated for 7 temperatures between 1000 K and 2500 K (see Table 4.1). At high temperatures, the ignition delay time of propane mixtures containing 5.0 vol% is shorter compared to richer or leaner mixtures. Because of this, a stable flame is built up faster and thus less susceptible to quenching conditions induced by turbulence. However, the temperature and

Table 4.1: Ignition delay times τ_{ign} in ms for propane/air and propene/1-butene/air mixtures between T = 1000 K and 2500 K calculated with CHEMKIN using the USC Mech. II[218]

1000/T (K^{-1})	1.0	0.9	0.8	0.7	0.6	0.5	0.4
3.0 vol%	56.9	10.3	1.45	0.169	0.0365	0.00958	0.00439
3.5 vol%	51.6	9.83	1.49	0.178	0.0360	0.00961	0.00482
4.0 vol%	47.5	9.39	1.53	0.187	0.0351	0.00953	0.00509
5.0 vol%	41.5	8.76	1.60	0.207	0.0332	0.00950	0.00382
6.0 vol%	37.3	8.29	1.68	0.237	0.0382	0.00980	0.00414
C3/C4	24.4	6.28	1.27	0.214	0.0390	0.00888	0.00406

pressure during the spark ignition for this experiment are unknown and the calculated delay times should not be used as absolute values.

4.1.4 Dual spark ignition

The purpose of two spark plugs used in engines often serves two purposes: (*i*) In aircraft engines, two spark plugs are implemented to serve as a redundant safety mechanism. In case of ignition failure or complete failure of a spark plug, the engine can still be operated. (*ii*) In car engines (Alfa's Twin Spark series, Honda L engine Series, modern Chrysler HEMI V8 engine), two spark plugs are used to generate two flame fronts leading to faster and ideally complete combustion. Depending on the configuration of the cylinder, the sparks may fire at the same time or at different intervals during the combustion. In this Thesis, the effect of two spark plugs, both firing at the same time or with a delay between spark discharge, were investigated for laminar and turbulent conditions, using injected and premixed fuel. The two spark plugs were driven by the same electronics used in the single spark configuration. The location of the second spark was chosen to be opposite of the first. Pressure and piston velocity measurements were performed firing the spark at the same time or inserting a delay up to Δt_{spark} = 15 ms. To check for effects of inhomogeneity between the high-voltage generation of the electronics, both sparks were alternatively used as the first to start the ignition.

The pressure-time profiles were again investigated for maximum pressure and the time to reach the maximum pressure. The results are shown in Figure 4.15a and 4.15b. The delay between spark 1 and spark 2 was increased in Δt = 0.1 ms increments up to 1 ms and afterwards changed in steps of Δt = 2 ms up to delays

of $\Delta t_{\mathrm{spark}} = 15$ ms, which is the maximum time of combustion determined under laminar condition using one spark. All measurements were performed without additional obstacles, i.e. without fan or mixing grid, using the propene/1-butene fuel. The maximum pressure Δp_{max} and shortest pressure rise time $t\,(\Delta p_{\mathrm{max}})$

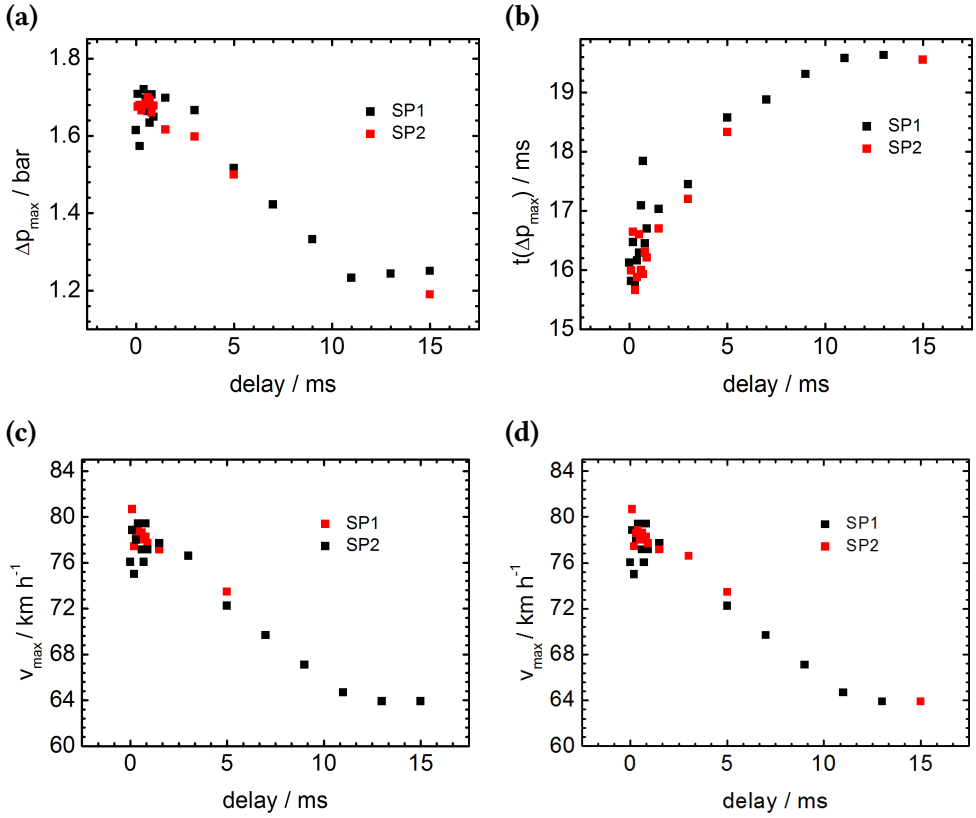

Figure 4.15: **(a)** Maximum pressure, **(b)** time of maximum pressure after ignition and **(c)** maximum piston velocity for propene/1-butene combustion depending on the delay between the spark discharge of the two spark plugs. Black squares: spark 1 fired first. Red squares: spark 2 fired first. **(d)** Pressure-time traces for turbulent combustion at $\Delta t = 800$ ms using propene/1-butene and 4.5 vol% propane.

were reached for simultaneous spark discharge. This behavior did not change up to a discharge delay of $\Delta t_{\mathrm{spark}} = 3$ ms. The average maximum pressure of 1.7 bar could be observed between 15.5 ms and 17 ms after start of combustion. A first significant change in the pressure-time traces could be observed at $\Delta t_{\mathrm{spark}} = 5$ ms, where the maximum pressure starts to decrease combined with an increase in pressure rise time. This trend continues until $\Delta t_{\mathrm{spark}} = 11$ ms, where the maximum pressure of 1.2 bar was reached after 19.5 ms. Further increase of spark delay time did not change the combustion behavior. This resulted in a maximum velocity of $v_{\mathrm{max}} = 78\,\mathrm{km\,h^{-1}}$ for delay times up to 3 ms and a minimum of $v_{\mathrm{max}} = 64\,\mathrm{km\,h^{-1}}$ at $\Delta t_{\mathrm{spark}} = 13$ ms. Using spark plug 2 as the first spark yielded similar results.

The dependence of spark delay time on the pressure-time traces under turbulent conditions could not be observed. Neither the maximum pressure nor the pressure rise time did change using two sparks. The maximum pressure for the propene/1-butene mixtures was reached for fan delay times bigger than 500 ms. For mixtures of 4.5 vol% propane in air, the ignition probability dropped for $\Delta t_{\mathrm{fan}} > 500$ ms. Nevertheless, ignition was possible in some cases for higher delay times, as can be seen in Figure 4.15d. Here, two ignition events using premixed fuel at $\Delta t_{\mathrm{fan}} = 800$ ms are compared to an ignition of propene/1-butene. For the injected fuel, the first pressure rise starts at 3 ms, while the pressure maximum is reached 7 ms after ignition. For both premixed events, the pressure rise is strongly delayed, the first increase in pressure occurs at 8 ms and 12.5 ms, respectively. Pressure maxima of comparable height can be observed 12 ms and 17 ms after ignition.

The results can be discussed and summarized as follows: The use of two spark plugs increases the maximum pressure only under laminar conditions. The maximum combustion enhancement can be achieved for simultaneous spark ignition and delay up to $t = 3$ ms. The pressure maximum is increased by a factor of 1.4, the piston velocity only by a factor of 1.2. A significant increase in combustion efficiency can only be found for spark delays of $t < 10$ ms. For higher delay times it can be assumed, that the first flame kernel has consumed nearly all fuel in the vicinity of the second spark. A second spark ignition thus produces either a small flame kernel or, for higher delays, no flame kernel at all.

Under turbulent conditions, a delayed combustion event could be observed for mixtures that were not ignitable for high fan running times. The similar shape and maximum pressure of the pressure-time traces suggest similar combustion mechanisms for all observed events. The use of two spark plugs fired simultaneously generates two flame kernels and thus doubles the probability of flame kernel survival. The delayed rise thus might be due to one flame kernel surviving the initial quenching conditions and combustion starts after stabilization of this kernel. Nevertheless, it was not possible to reproduce this effect reliably, which made further investigations impossible.

4.2 Imaging of the flame front: Chemiluminescence and OH fluorescence

The expansion of the flame under laminar conditions was studied using chemiluminescence and laser-induced fluorescence in the vicinity of the spark plug. Additionally, flame-obstacle interactions were investigated for different insertion depths. Further work focused on the influence of turbulence on the shape and propagation of the flame. Preliminary experiments on the flame propagation were carried out using a different placement of the observation windows, as can be seen in Figure 4.16. The windows have an open diameter of $d_{\mathrm{w}} = 18\,\mathrm{mm}$ and were

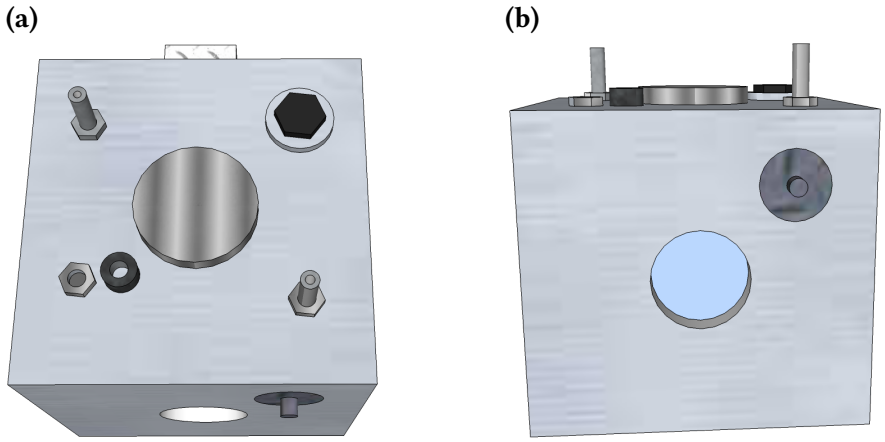

Figure 4.16: **(a)** Top view of the modified combustion chamber with the spark plug positioned on the diagonal of the cylinder head. The distance to the chamber is $d_{\mathrm{spark}} = 22.6\,\mathrm{mm}$, while the distance between the center of the spark and the center of the observation window line of sight is $d = 16\,\mathrm{mm}$. **(b)** Position of the observation window used for the chemiluminescence measurements. The diameter of the windows is $d_{\mathrm{w}} = 18\,\mathrm{mm}$. The center of the windows were positioned at a distance of $d_{\mathrm{I}} = 22\,\mathrm{mm}$ and $d_{\mathrm{II}} = 32\,\mathrm{mm}$ (center of window to cylinder head)

positioned at a distance of $d_{\mathrm{I}} = 22\,\mathrm{mm}$ or at $d_{\mathrm{II}} = 32\,\mathrm{mm}$ from the center of the window to the cylinder head. The windows at d_{II} were flush with the bottom of the chamber and primarily used for the obstacle measurements. In all experiments, the spark plug was positioned off-center, as seen in Figure 3.3b and 4.16a.

4.2.1 Laminar combustion

According to the pressure measurements presented in Section 4.1.1, six different fuel compositions between 3.3 vol% and 6.5 vol% of propane in air were investigated. Flame front images were taken at $t = 8$ ms after start of ignition at window position d_{I} (see Fig. 4.17). At the lowest investigated fuel amount 3.3 vol%, the flame front

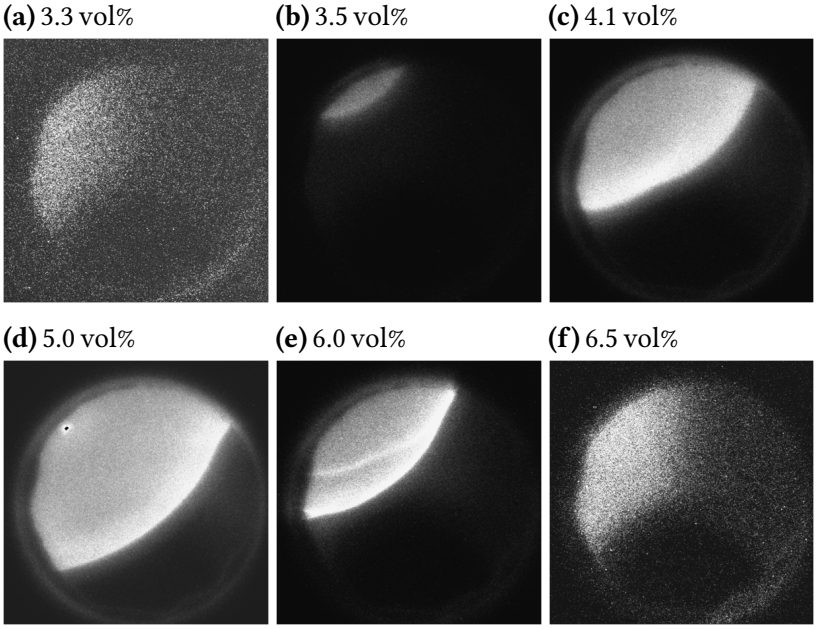

Figure 4.17: Chemiluminescence images of the flame front for different fuel compositions between **(a)** 3.3 vol% and **(f)** 6.5 vol%. All images were recorded at $t = 8$ ms after start of ignition using the windows at d_I.

has not yet reached the observation window, which can also be found for rich mixtures containing 6.5 vol%. For all others mixtures, an observable flame front appears after 8 ms. Small wrinkling of the front can only be found for 4.1 vol%. In all visible flames, the front shows the highest intensity, which then drops towards the burned part of the mixture. At 6.0 vol%, a second line of high intensity can be seen behind the flame front. They merge at the upper part of the observation window. For fuels containing 5.0 vol%, the flame has traveled the longest distance and appears in the middle of the observation window. All flames show a nearly spherical and undisturbed front. The development of the flame front directly after combustion can be seen in Figure 4.18. Flame fronts were captured from single-shot events between $t = 0.0$ ms and 3.6 ms after ignition.

The first signal of the flame can be seen directly at the start of combustion around $t = 0.0$ ms. The flame propagation starts at the top of the cylinder head, directly below the upper spark electrode. The most intense region can be found at the center of the flame kernel. Between $t = 0.2$ ms and 0.6 ms the flame starts

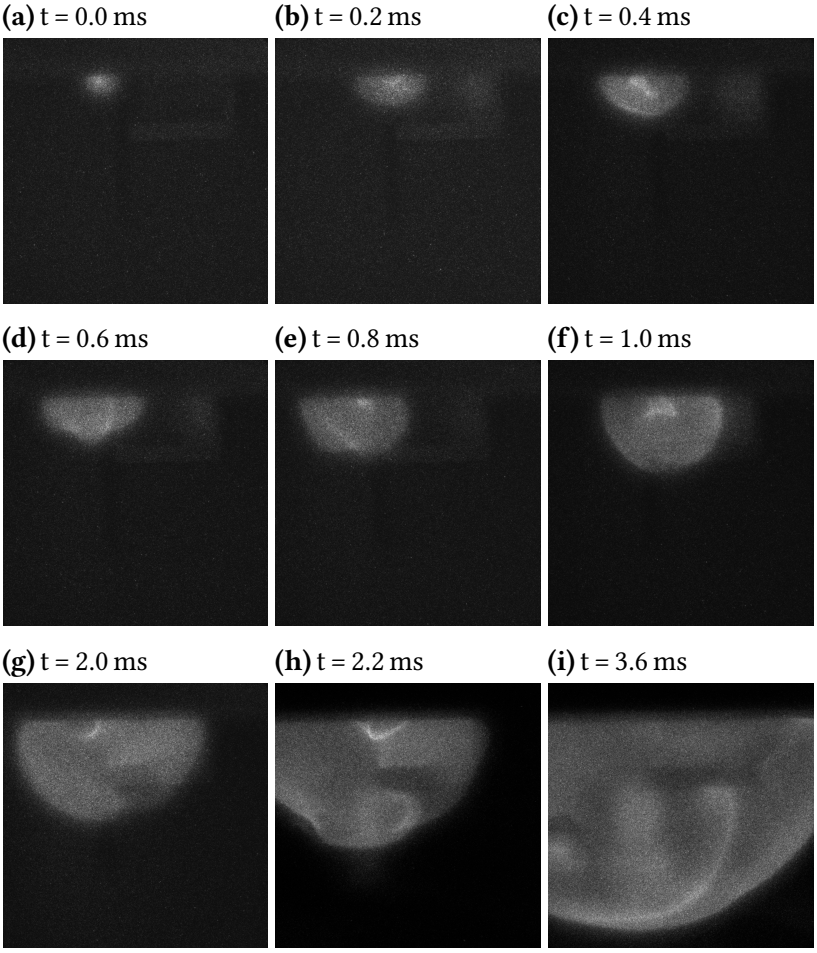

Figure 4.18: Chemiluminescence images of the flame front at different times between **(a)** t = 0.0 ms and **(i)** 3.6 ms after ignition. All images represent one event from a single-shot measurement. The images were recorded at the upper part of the chamber with the spark plug positioned in the upper central region of the image using propene/1-butene.

to expand hemi-spherically, until the flame front hits the lower spark electrode at t = 0.6 ms. During the expansion, the bright central region around the upper spark electrode is still visible. Between t = 0.6 ms and 1.0 ms, slight deviations from the spherical shape can be seen. After t = 2.0 ms, the flame front passes the spark electrode. During this time, a second flame front develops below the lower spark electrode. This flame front moves along the electrode and expands towards the bottom. At t = 3.6 ms, the second flame front merges with the main front in the lower right sector if the image, while the rest of the second flame expands spherical. This also marks the time after which the flame front has reached the bottom of the observation window.

The drawback of the chemiluminescence images lies in its two-dimensional projection of a three-dimensional shape; it provides information only in the x and y directions. From the images, the development of the flame kernel in the plane of

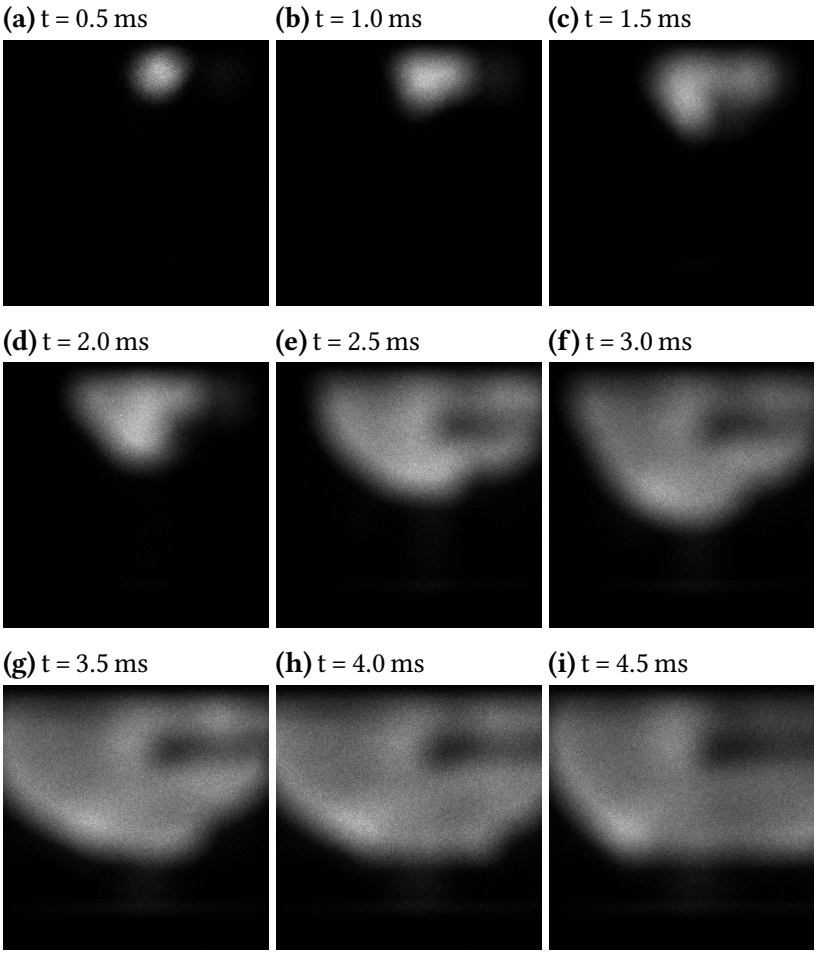

Figure 4.19: OH radical LIF images recorded between **(a)** $t = 0.5$ ms and **(i)** $t = 4.5$ ms after the start of ignition.

the spark electrode tip cannot be deduced. To overcome this disadvantage, laser-induced fluorescence images of the OH radical distribution in the aforementioned plane were recorded. Single-shot images between t = 0.5 ms and 4.5 ms after start of ignition are shown in Figure 4.19.

At t = 0.5 ms, the flame expands spherically, as seen from the chemiluminescence images. 0.5 ms later, the flame reaches the lower spark electrode. At t = 1.5 ms, residuals of OH radicals can be found above the electrode surface and in front of the tip, resulting in an „L"shaped structure. Afterwards, the area in front of the electrode shows a fluorescence signal, which at t = 2.5 ms can be found over the whole electrode area. At the tip, the fluorescence remains weak. The shape of the radical distributions on the left resembles a sphere, while the front below the spark shows a dip. Until t = 4.5 ms, the shape of the flame starts to expand further, until the whole observation window is filled, apart from the bottom left corner. The most intense fluorescence can be found at the lower part of the fluorescence, facing towards the unburned mixture. Between 3.5 ms and 4.5 ms, the fluorescence signal above the spark electrode decreases. Signals of OH fluorescence could be observed up to 25 ms after the start of ignition, albeit of lower intensity. The maximum of the fluorescence was found above the spark electrode.

The results for the laminar expanding flame can be summarized and discussed as follows: The measurements of the flame expansion for different fuel compositions is in good agreement with the results from the pressure measurements. The highest flame velocity and pressure rise were measured for the slightly rich mixtures. Here, the highest flame velocity occurs at 5.0 vol%. After 8 ms, the flame has traveled a distance of approximately $d_{\mathrm{flame}} \approx 27$ mm, which equals a flame velocity of $v_{\mathrm{flame}} \approx 3.4\,\mathrm{m\,s^{-1}}$. Due to the expansion by the hot gases behind the flame front, the flame velocity is increased by a factor of 10 compared to the laminar flame speed u_{l}. Towards the LFL and UFL, the flame velocity is drastically decreased, as it was expected from the low pressure rise times measured for the mixtures. For 5.0 vol% mixtures, the visible flame front is nearly spherical without any disturbance at short times after start of ignition. This supports the model of adiabatic spherical flame expansion used for the pressure rise rates. Nevertheless, the flame front for richer mixtures with 6.0 vol% shows a deviation from the spherical expansion and a second flame front appears behind the leading flame. The measurements at the spark plugs show the origin of this structure. When the expanding flame hits the electrode, the flame is wrinkled around the surface. The increase in flame surface due to the wrinkling leads to a small change of moving direction and increase in flame speed, as seen in Figure 4.18h and 4.18i. A merging of the flame fronts can be observed before the initial flame reaches the bottom of the chamber.

The LIF images show a high initial concentration of OH radicals at the location of spark ignition. The high amount of radicals is generated by the high temperatures during the spark phase, where the temperatures of up to 4500 K can generate OH mole fractions of more than 4%.[92] Dreizler and coworkers also reported that OH radicals and a growing spark kernel appear as early as t = 100 µs after spark ignition, similar to the results obtained from the chemiluminescence images. The LIF images show a low fluorescence signal at the location of the spark electrode, which usually occurs due to heat transfer of the spark heated volume to the metal surface. This leads to a decrease of reaction rate and thus production of radicals or even flame quenching. The decrease of fluorescence signal with time can also be found below the cylinder head, which is due to heat transfer and depletion of radicals. Nevertheless, LIF signals in the hot burned gas can be observed until a few ms after ignition, especially in the region between the spark electrodes, which is caused by the elevated mole fractions of OH radicals during the plasma generation of the spark signal. The combination of LIF and chemiluminescence images indicate that a flame kernel with the size of the spark gap is established after $t \approx$ = 0.5 ms after start of the ignition. This is up to ten times longer than the overall duration of the spark phase. As was observed by Maly and Vogel,[37] spark ignition might produce two flame fronts. The major front develops outside the shell induced by the plasma and a second one persists inside the plasma. The second flame front may cause an additional expansion of the major flame front due to an increase of temperature in the hot burned products behind the major flame front. This second flame front can also be observed in the chemiluminescence images up to 2.2 ms after ignition.

4.2.2 Chemiluminescence imaging of combustion with obstacles

The laminar flame expansion was also studied for the combustion using the small grid shown in Section 4.1.2 as obstacle with insertion depths between d = 0.5 cm and 4.5 cm. The chemiluminescence images for propene/1-butene combustion between t = 10 ms and 15 ms after ignition are shown in Figure 4.20. For comparison, the images for laminar flame expansion without obstacles are shown at the top.

The flame propagation at d = 0.5 cm shows the same behavior as the combustion without obstacles, as was already shown in the pressure time traces. At d = 1.0 cm, the flame front appearing in the observation window at t = 10 ms is disturbed 1 ms later and shows an increase of luminosity in the flame front, especially in the

top right corner. For insertion depths between d = 1.5 cm and 2.5 cm, the flame front is broken up, when the flame enters the visible region. Afterwards, a part of the flame expands spherically towards the bottom right, while islands of high intensities are formed behind the initial flame front at the origin of the flame front breakup. In all images with a visible obstacle, the flame wrinkles around the grid, after which the highest flame intensity appears directly below the obstacle at the point of flame-obstacle interaction.

This leads to the following conclusions: The results obtained from the flame front imaging are in very good agreement with the pressure measurements, which showed an increase in maximum pressure for insertion depths of $d \geq 1.0$ cm. At this insertion depth, the flame exhibits a strong increase in luminosity as a result of a combustion enhancement and burning rate. The flame wrinkling around the obstacle and chemiluminescence intensity has a maximum at d = 2.5, comparable to what was observed in the pressure measurements. The increase of wrinkling and breakup of the spherical flame surface happens between t = 10 ms and 15 ms. As seen in Figure 4.9, the pressure rise rate starts to increase again after 15 ms, which is attributed to the increase of flame surface due to the wrinkling around the holes in the obstacle. The complete breakdown of the connected flame surface is a consequence of microturbulence induced by the flame front moving through the obstacle. Although this effect is diminished for higher insertion depths, the flame front is now broken up by the rod connected to the grid, which can be seen at t = 13 ms at insertion depths between 3.5 cm and 4.5 cm.

4.2.3 Turbulent combustion

Chemiluminescence and LIF images were recorded for different fan starting times before ignition Δt, which correspond to different fan velocities, as shown in Table 3.2. The reader should keep in mind that the fan is still accelerating during the combustion. Especially for shorter fan starting times, Δt < -100 ms, the fan speed can increase by $\Delta u_{\text{fan}} \approx 1000$ rpm during the combustion. Thus, the fan starting times with respect to ignition at t_0 = 0 ms are given instead of exact fan velocities.

For fan starting times of Δt = -50 ms, according to a speed of $u_{\text{fan}} \approx 2500$ rpm and Δt = -150 ms ($u_{\text{fan}} \approx 7900$ rpm), the chemiluminescence of the flame was imaged, for Δt = -100 ms ($u_{\text{fan}} \approx 6000$ rpm) and Δt = -200 ms ($u_{\text{fan}} \approx 9400$ rpm), the fluorescence of OH radicals at the spark plug was recorded. Additionally, chemiluminescence images were recoded at Δt = -500 ms ($u_{\text{fan}} \approx 13500$ rpm) below the fan to track the flame evolution at the end of the combustion phase. The

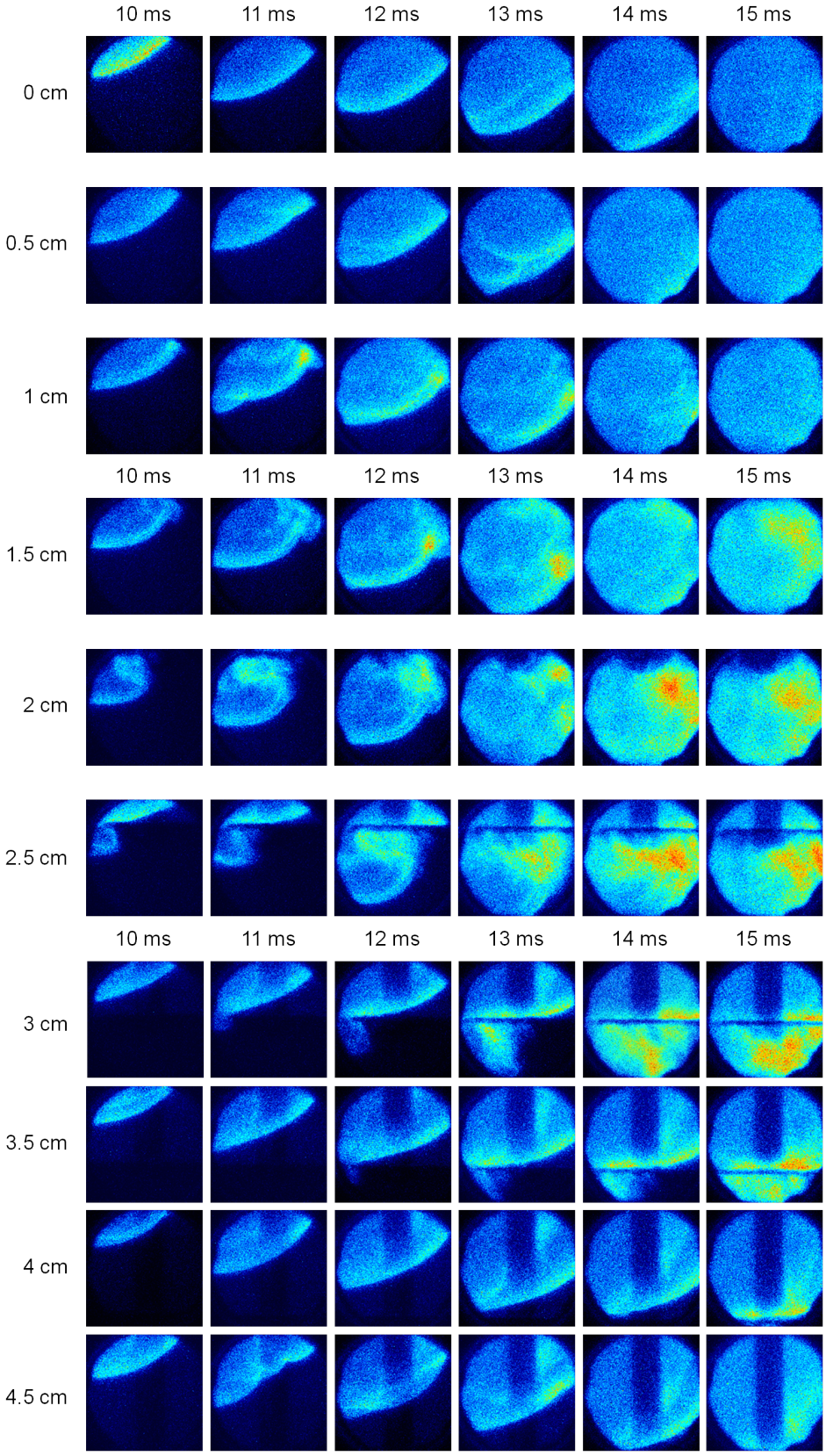

Figure 4.20: Flame front imaging for different insertion depths of the small grid. The measurement depths were altered between $d = 0$ cm and 4.5 cm in 0.5 cm steps. Single shot images were taken between 10 ms and 15 ms after start of ignition. All measurements were done using the fuels cells and at window position d_{II}. For a clearer comparison, all images are shown in false color.

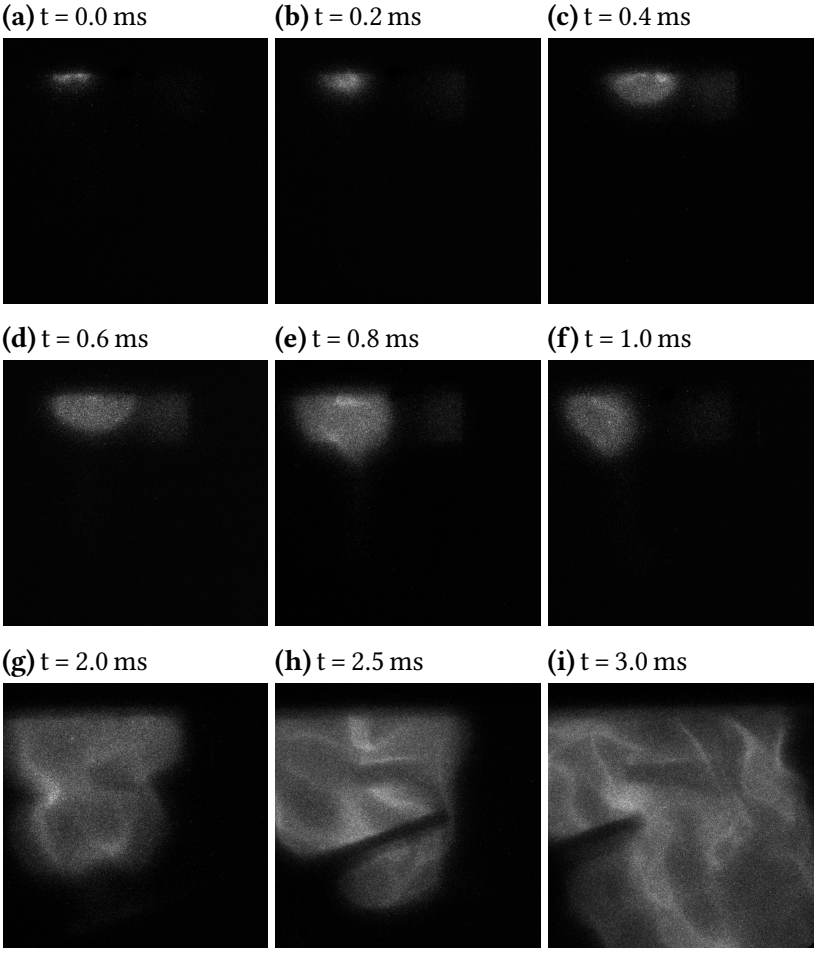

Figure 4.21: Chemiluminescence images of the flame front at different times between **(a)** t_0 = 0.0 ms and **(i)** 3.0 ms after ignition. The fan was started at Δt = -50 ms with respect to ignition at t_0. The images were recorded at the upper part of the chamber with the spark plug positioned in the upper central region of the image using propene/1-butene.

time-resolved chemiluminescence images at t_0 = 0.0 ms and t = 3.0 ms after ignition are shown in Figure 4.21. The fan was started at Δt = -50 ms with respect to ignition at t_0. The first flame signal can be found nearly simultaneously with the spark ignition. The flame starts to evolve from the upper spark electrode and expands until t = 0.6 ms in a spherical shape, until the flame front hits the lower spark electrode. This behavior is similar to the flame expansion found for laminar combustion. Nevertheless, the intensity of the chemiluminescence seems to be equally distributed over the flame surface. A strong signal in the flame front, as seen in the laminar flame expansion, cannot be identified. Between t = 0.8 ms and 1.0 ms, the expansion in horizontal direction stops, and the flame starts to propagate downwards. At t = 1.0 ms, the flame is severely stretched and cannot be approximated to be hemi-spherical anymore. After t = 2.0 ms, the flame has grown significantly in size and is stretched towards the bottom. At the height

of the spark electrode, a waist in the surface can be found. Additionally, the chemiluminescence is unevenly distributed across the flame. A region of high intensity appears at the left flame surface towards the unburned mixture. After 2.5 ms the downward stretching is increased further. Several areas of high intensity can be found distributed all over the flame surface. The flame surface in the right region is cut off at the end of the lower spark electrode. At t = 3.0 ms, the flame fills the whole observation window. All high-intensity areas, which are distributed non-uniformly across the incoherently connected flame surface, run in vertical direction. The region of highest intensity is located at the tip of the fan blade, around which parts of the flame are wrinkled.

The LIF images for a fan start at Δt = -100 ms with respect to ignition at t_0 show a spherical flame 0.2 ms after ignition (see Figure 4.22). At t = 0.3 ms, the flame moves to the right and a second fluorescence signal can be found below the spark plug. At higher delay times, the fluorescence distribution changes drastically.

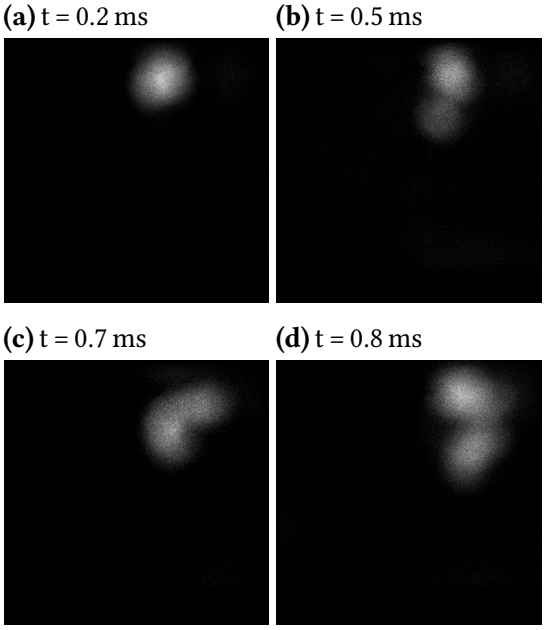

Figure 4.22: OH radical LIF images recorded between **(a)** t = 0.2 ms and (**d**) t = 0.8 ms after the start of ignition. The fan was started Δt = -100 ms before ignition at t_0.

For an even longer fan start of Δt = -150 ms before of ignition, the shape of the flame during combustion is even further disturbed, as shown in Figure 4.23. The difference from the spherical expansion can be seen as early as t = 0.4 ms after ignition. Between t = 0.6 ms and 1.0 ms, the flame kernel appears to be stagnant and stays mainly above the spark electrode, while small areas of chemiluminescence can also be found below the electrode at t = 1.0 ms. Both areas are connected by a small flame band, which is wrinkled counter-clockwise around the spark electrode. At a time 0.2 ms later, the flame intensity below the spark electrode is increased

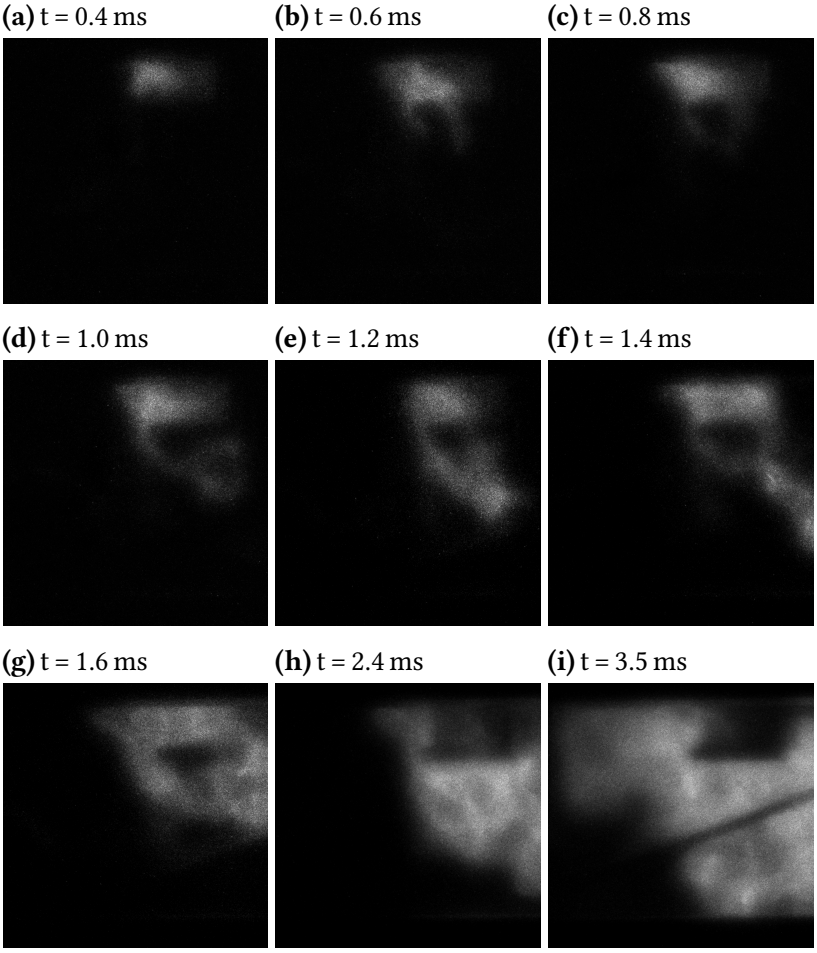

Figure 4.23: Chemiluminescence images of the flame front at different times between **(a)** t_0 = 0.0 ms and **(i)** 3.5 ms after ignition. The fan was started Δt = -150 ms before ignition at t_0. The images were recorded at the upper part of the chamber with the spark plug positioned in the upper central region of the image using propene/1-butene.

and the flame seems to be located behind the electrode. The whole burning surface is extended towards the bottom right part of the chamber. At t = 1.4 ms, most of the flame surface is still located behind the spark and moved further towards the right. Flame expansion against the moving direction of the fan can be found as early as t = 3.5 ms after start of the ignition. Between 2.4 ms and 3.5 ms, the non-illuminated surface of the spark electrode is clearly visible. The flame structures exhibits incoherently connected areas of high and low chemiluminescence intensity.

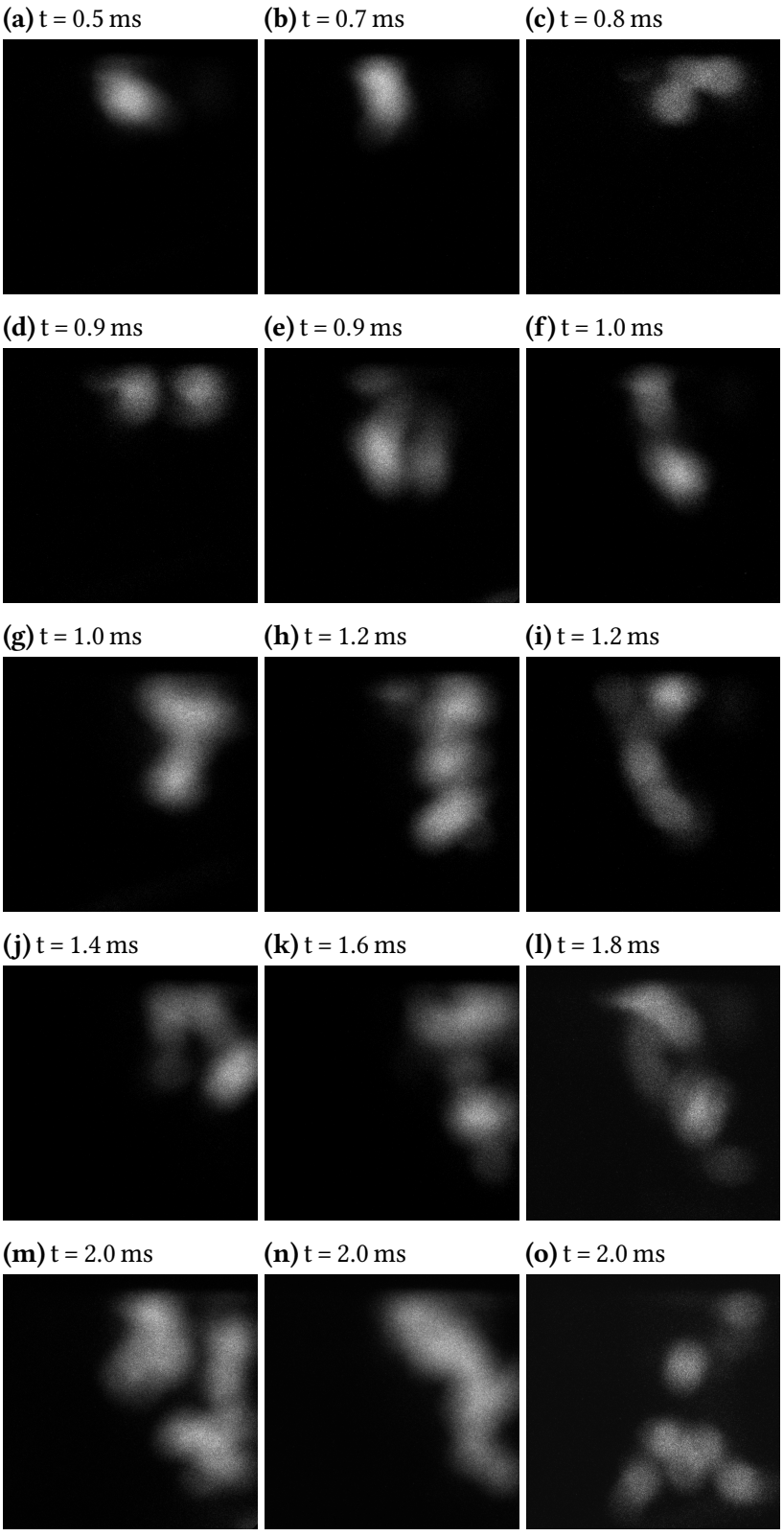

Figure 4.24: OH radical LIF images recorded between **(a)** $t = 0.5$ ms and (**d**) $t = 2.0$ ms after the start of ignition. The fan was started Δt = -200 ms before ignition. To account for the different flame expansion behavior for each individual combustion event, two or three images of the same recording time are shown.

The incoherent flame structure and expansion becomes even more apparent in the LIF images shown in Figure 4.24. The fan was started Δt = -200 ms before ignition. LIF images were recorded between t = 0.5 ms and 2.0 ms after ignition. The flame evolution in the first 0.8 ms after ignition is similar to the images at Δt = -100 ms. Nevertheless, for times longer than t = 0.9 ms, a reproducible flame front at each delay time could not be recorded. Figure 4.24d and 4.24e show flames recorded at t = 0.9 ms, which are completely different in shape. Regions of high fluorescence intensity can be found either above or below the spark electrode. Nevertheless, both images show non-connected areas of high OH radical concentration. This pattern can be found for nearly all following images. The majority of fluorescence can be found in the right part of the chamber next to the spark electrode and with increasing time also in the lower right part of the observation window. Three LIF images at t = 2.0 ms after ignition are shown in Figure 4.24m–o. Coherent flame structures can only be found in image (**n**), while in (**o**) many isolated islands with diameter of $d \approx 3$ mm are formed.

The flame propagation at high fan speeds (Δt = -500 ms, $u_{\mathrm{fan}} \approx 13000$ rpm) below the fan blades is shown in Figure 4.25. First chemiluminescence was recorded at t = 3.0 ms after ignition and appears at the top right corner of the observation window. The flame front is broken up and many small islands of burning fuel can be found. In the next 1.5 ms, the flame propagates from the top right to the bottom left. At t = 5.5 ms, the broken and wrinkled flame fills the whole observation window. Afterwards, the highest flame intensity can be found at the right part of the window, where the surface appears to be uniform. This uniform surface then moves towards to the right part of the chamber in direction of the fan movement, until the flame disappears for times longer than t = 7.0 ms.

The results obtained from the turbulent flame imaging can be discussed and summarized as follows: As seen in the images for short fan starting times of Δt = -50 ms and Δt = -100 ms (Figure 4.21a–4.21d and 4.22a), the initial growth of the flame kernel is not affected by turbulence. In the first case, the hemi-spherical expansion can be found until t = 0.6 ms after ignition, while at Δt = -100 ms, the flame stretching starts after t = 0.5 ms. At longer times after ignition, the flame surface grows rapidly and the flame is severely stretched. For short fan starting times of Δt = -50 ms, the flame still expands from the top of the chamber towards the bottom as seen under laminar conditions. However, chemiluminescence images show a strong wrinkling and denting of the flame surface. The nearly-uniform luminosity of the laminar flame is broken up and small islands of higher intensity are formed due to the increase in burning rate and temperature. For earlier fan start times Δt > 100 ms, the flame is displaced in the direction of the fan movement. This effect increases with longer fan starting times. While for low fan speeds,

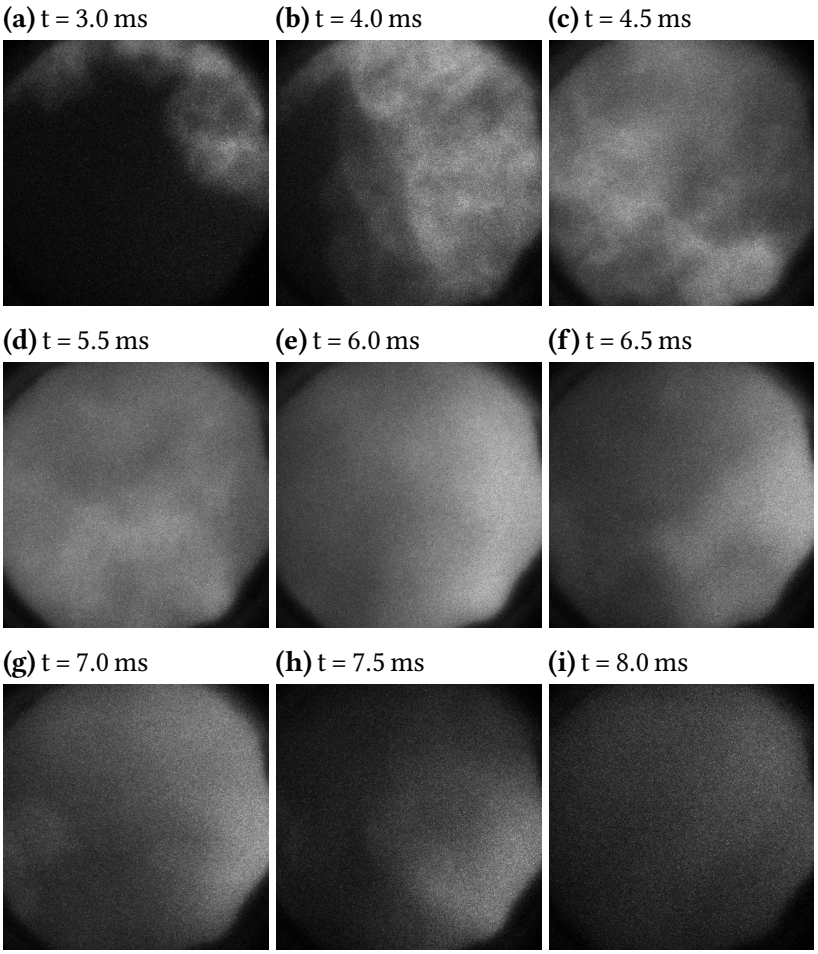

Figure 4.25: Chemiluminescence images of the flame front at different times between **(a)** t_0 = 3.0 ms and **(i)** 8.0 ms after ignition. The fan was started Δt = -500 ms before ignition. The images were recorded at the lower part of the chamber (d_{II}) using propene/1-butene. The spark electrode was located at the top left position of the chamber.

u_{fan} < 3000 rpm, the flame expands still centered in the observation window, at higher fan speeds the flame is first stretched horizontally towards the right area of the observation window within 1 ms after ignition and then starts to move vertically towards the bottom right. The chemiluminescence image recorded 3.5 ms after ignition shown in Figure 4.23i indicates that the flame moves towards the back of the chamber. The dark areas of the spark electrode at the cylinder head and the blade of the fan are clearly visible. Additionally, the chemiluminescence images recorded below the fan blade further suggest a swirl-like motion of the flame induced by the rotating fluid. Here, the flame enters the observation plane from the top right, moves towards the bottom left and vanishes in the right area of the chamber. The breakup of the flame surface into smaller burning islands and hence significant increase in flame surface is in good agreement with the pressure measurements. The pressure-rise rates increase significantly for starting times of the fan between Δt = -100 ms and -150 ms, which also can be found for the turbulent burning velocity. For longer fan starting times, Δt > -200 ms, the overall flame surfaces increases further and thus accelerates the burning rate of the fuel. The flame movement is not influenced by the expansion of the piston. As shown before, the piston expansion occurs at $t \approx 8$ ms after start of ignition, where the pressure maximum is reached. This coincides with the decrease of the flame luminosity due to the consumption of the fuel.

As seen in Figure 4.24, the LIF images recorded at t > 0.5 ms after start of the ignition exhibit a very poor reproducibility for each time step. This becomes even more apparent for longer delay times. At t = 2.0 ms, it was not possible to deduct a clear trend for the flame expansion and each image showed a different distribution of OH radicals. This can be attributed to two dominating mechanisms: The first effect is induced by the point of ignition at the spark electrode, which was shown in Figure 3.7. Due to the different trajectories of the arc, the initial flame kernel starts at slightly different positions inside the chamber. It can be assumed that at these positions the fluid movement differs in direction and speed and thus the flame kernel growth differently depending on the arc impact point. This effect can also be found in the chemiluminescence images at Δt = -150 ms shown in Figure 4.23. Here, the flame can be seen moving behind (Figure 4.23d) or in front of the lower spark electrode (Figure 4.23f and 4.23g). Second, and probably more important, due to the randomness of turbulence, the interaction between the flame surface and moving fluid are slightly different for each combustion event. This can lead to a difference in flame wrinkling and slight displacement of the expanding flame, which is illuminated by the thin laser light sheet. While this mechanism seems to be negligible for short times after ignition, t < 0.5 ms, it is more pronounced for longer times.

In the flame imaging measurements, the direct extinction of the flame kernel could not be observed. Yet, the drop of ignition probability with an increase of fan starting time before ignition seems to be coupled to the early stages of the flame kernel expansion. The increase of turbulence showed a strong impact on the flame kernel shape. Even within a few hundred microseconds after ignition, the kernel is stretched and wrinkled due to the strain induced by the turbulent medium.

As mentioned before, the quenching distance of a flame generated by spark ignition is coupled to the gap of the electrodes and increases with increasing turbulence. The different trajectories of the spark result in a change of length and shape of the plasma channel and thus a general spark gap is hard to define. Nevertheless, it is possible that for non-ideal spark trajectories shown in Figure 3.7 the flame kernel is not stable enough to survive the turbulent stress.

4.3 Particle image velocity of turbulent flows without ignition

The turbulent flow was measured at different positions in the chamber and for different insertion depths of the fan. At an insertion depth of $d_\mathrm{i} = 0$ mm, the housing of the fan was flush with the cylinder head. This resulted in a distance of 8 mm between cylinder head and fan. Additionally, two other configurations with insertion depths of 3 mm and 9 mm were investigated. This was done to decrease the amount of scattered light reflected by the fan, which was maximal for $d_\mathrm{i} = 0$ mm, and to avoid a cut-off of the light sheet by the fan blades. Depending on the position of the blades, up to half of the observation window could not be investigated. For the maximum insertion depth of $d_\mathrm{i} = 9$ mm, the fan position was leveled with the lower part of the observation window and resulted in a minimal influence on the light sheet. The position at 3 mm was chosen as compromise between the two positions. First, the images for insertion depth at $d_\mathrm{i} = 9$ mm will be presented, because they offer the highest data quality.

The influence on the calculated velocity by the temporal delay between the two laser pulses is shown in Figure 4.26. The average velocity magnitude $v_\mathrm{m,avrg}$ was calculated for turbulent conditions $\Delta t = 150$ ms after start of the fan at an insertion depth of $d_\mathrm{i} = 9$ mm and 4 mm away from the spark plug. Since there is no ignition as reference point t_0 in this Section, the fan running times are given as positives values here. The temporal delay between the PIV laser's shots was set to 10 µs (Figure 4.26a) and 7 µs (Figure 4.26b), respectively. An average of 17 image pairs was used for the calculation of magnitudes at longer delay time, 22 image pairs were used for the shorter. Since it is known that the fluid moves under the influence of turbulence, it is expected to find areas of low and high velocities in one instantaneous velocity field. Different delay times were chosen to check if areas of fast and quiescent moving particles can be represented by recording one image pair. The overall flow pattern is identical for both images. The general flow direction is from left to right, in accordance with the movement of the fan. A counter-clockwise rotating vortex is visible in the upper right corner of both images and the maximum velocity appears at the lower left sector. Nevertheless, the velocity distribution in Figure 4.26b seems to be more smooth compared to Figure 4.26a. Two explanations exist for this behavior: First, due to the limited number of image pairs for averaging, the method is prone to the random behavior of the turbulent motion and velocity extrema are more pronounced. Second, due

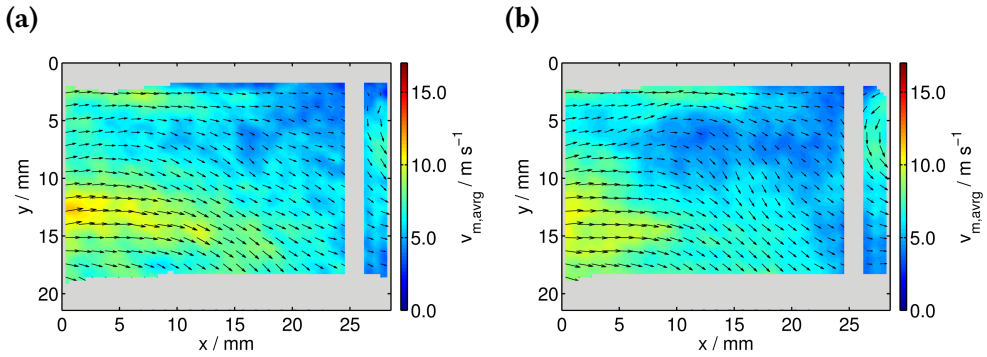

Figure 4.26: Comparison of the calculated averaged velocity at Δt =150 ms after fan start. The delay time between recorded frames was **(a)**: 10 µs and **(b)** 7 µs.

to the higher delay time, the amount of out-of-plane particle loss is increased and might lead to higher noise in the correlation maps as was seen in Figure 2.18b.

The flow of the aerosol without turbulence induced by the fan is shown in Figure 4.27. Due to the low velocity, the particles were illuminated by two pulses of the 20 Hz PIV laser, separated by 50 ms. The inlet port for the particles is located at the upper right part of the image and the flow is directed towards the outlet port at the upper left part. The maximum velocity of $v_{\max} \approx 0.04\,\mathrm{m\,s^{-1}}$ is located at the top left part of the chamber, below the outlet port. $v_{\max}$ is less than 2 % of the turbulent flow velocity, even at low turbulence intensities at $\Delta t = 50$ ms. Thus, the aerosol flow induced by the generator can be neglected and the generator was kept running during the measurements to ensure a continuous supply of particles.

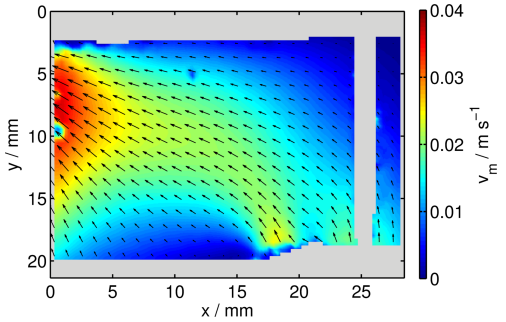

Figure 4.27: Velocity profile of the flow inside the chamber resulting from the aerosol generator. The temporal delay between the laser pulses was set to 50 ms. Due to the low maximum fluid velocity of $v_{\max} \approx 0.04\,\mathrm{m\,s^{-1}}$, which could be neglected compared to the turbulent fluid velocity, the aerosol generator was kept running during the measurements to ensure a continuous supply of particles.

4.3.1 PIV measurements 4 mm in front of the spark plug

The instantaneous velocity fields were recorded at fan starting times between Δt = 50 ms – 700 ms in time steps of of 50 ms between 50 ms – 200 ms and time steps of 100 ms up to 700 ms. As seen in Figure 4.28, this captures the strong acceleration time of the fan between 0 ms and 100 ms as well as the transition to constant speed around 500 ms, where turbulence is expected to be fully established.

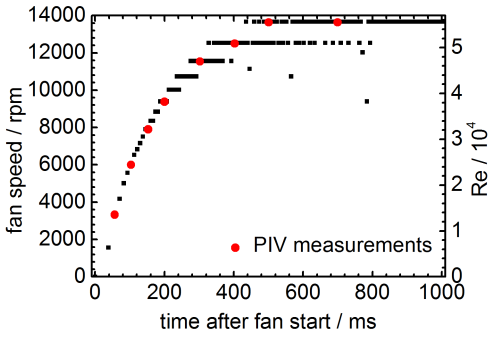

Figure 4.28: Temporal evolution of the fan speed for different times after fan start Δt. The delay times used for the PIV measurement are marked by the red dots.

4.3.1.1 Velocity fields at 9 mm fan insertion depth

For the maximum insertion depths, all values for Δt were investigated. The fan speed and corresponding Reynolds number are presented in Table 4.2. Due to the random nature of turbulence, especially for high turbulence intensities at Δt > 150 ms, it is not feasible to show all instantaneous velocity fields. Thus, for each delay time, a representative selection will be presented and discussed.

Four instantaneous velocity fields, i.e. the direction and magnitude v_m of the flow, and their corresponding vorticity ω for Δt = 50 ms are shown in Figure 4.29. For a better overview of the flow field, only every second vector is shown. The velocity magnitude was calculated according to

$$v_\mathrm{m} = \sqrt{u_\mathrm{x}^2 \cdot u_\mathrm{y}^2} \tag{4.6}$$

In these and the following pictures, the movement of the fan is from left to right. For this fan velocity and low turbulence intensity, all velocity fields show nearly identical flow patterns. A mostly quiescent area, $v_\mathrm{m} \ll 2\,\mathrm{m\,s^{-1}}$, is observed near the top of the chamber around x = 12 mm / y = 3 mm, which also marks the position of

Table 4.2: Times after start of the fan Δt investigated in the PIV measurements at an insertion depth of d_i = 9 mm. Each Δt corresponds to a fan speed v_{fan} and Reynolds number of the fan Re_{fan}.

Δt / ms	v_{fan} / rpm	Re_{fan}
50	3300	13500
100	6000	24500
150	7900	32200
200	9400	38100
300	11600	46900
400	12500	50900
500	13500	55700
700	13600	56000

the spark plug. The highest velocities occur at the bottom of the observation window near the blades of the fan, especially at the left and right corner of the window. All images show four distinctive flow features. The area between 0 mm < x < 8 mm is dominated by an increase in velocity and movement of the fluid upwards and direction of the fan. Above y = 6 mm, nearly no change of velocity and direction can be observed. The movement in the central region between 8 mm < x < 18 mm is, aside from some infrequent areas of higher velocity fluctuation for example in Figure 4.29a, directed downwards with relatively low velocities, v_m < 4 m s^{-1}. The region at x > 18 mm is dominated by a counter-clockwise rotating vortex with a diameter of d_{vort} ≈1 mm with velocity components below 2 m s^{-1} at its center and up to 4 m s^{-1} at the outer edge. The highest velocity components of v_m ≈ 6 m s^{-1} were measured exclusively around the position of the fan blades. The vorticity profiles (Fig. 4.29, right panels) show a similar pattern. The highest vorticity ω_{max} generally occurs at the left and right bottom of the observation window, apart from Figure 4.29a, where a strong counter-rotating vortex pair is visible at x = 16 mm / y = 18 mm. The central part of the image, especially around the spark plug, shows no fluid rotation, while the fluctuating fluid movement areas are accompanied by an increase of vorticity. Especially in the left sector, vortices occur as counter-rotating pairs, for example in Figure 4.29h at x = 17 mm / y = 7 mm. The counter-clockwise rotating vortex structure in the right sector is dominated by also counter-clockwise rotating areas of high vorticity ω > 2000 s^{-1}.

As shown in Section 3.4.3.3, is it not possible to reveal all flow features hidden underneath the instantaneous velocity fields displayed in Figure 4.29 using Galilean transformation. For a given velocity to be subtracted, only features with advection velocity close to the Galilean transformation can be exposed. Especially for low

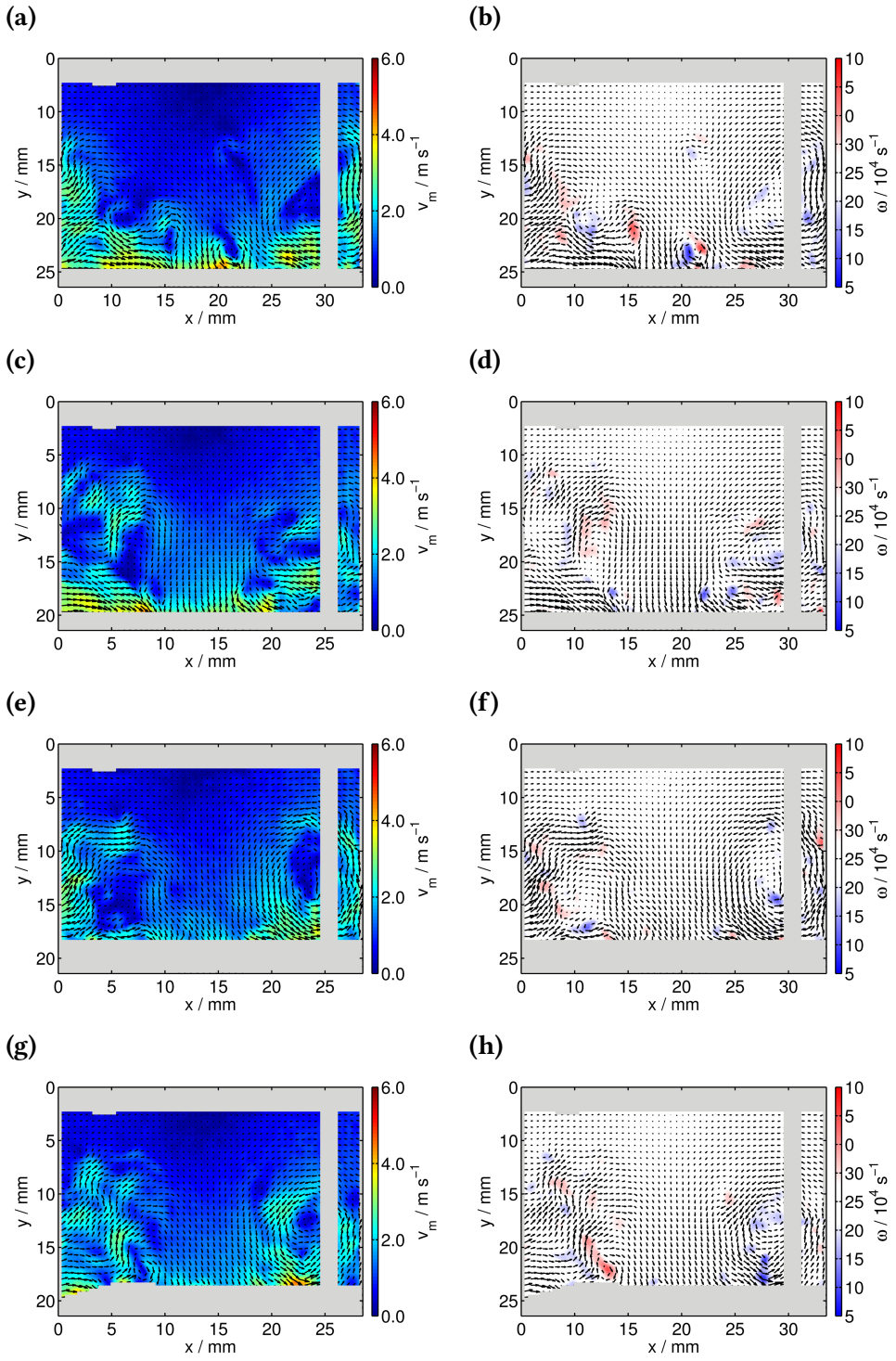

Figure 4.29: Four instantaneous velocity fields obtained Δt =50 ms after fan start. Images on the left represent the velocity magnitude v_m, images on the right the corresponding vorticity ω. To provide a better overview, only every second vector is shown.

turbulence intensities, there is no clear general motion of the fluid and thus, no average velocity to be subtracted. While it is possible to sequentially reveal the features using incremented average velocities, the number of increments becomes too high for complex multi-dimensional fields. All velocity fields were decomposed by subtracting a high-pass-filtered velocity field, resulting in spatially varying advection velocity, from the instantaneous images. For Δt = 50 ms, the filtered images are shown in Figure 4.30.

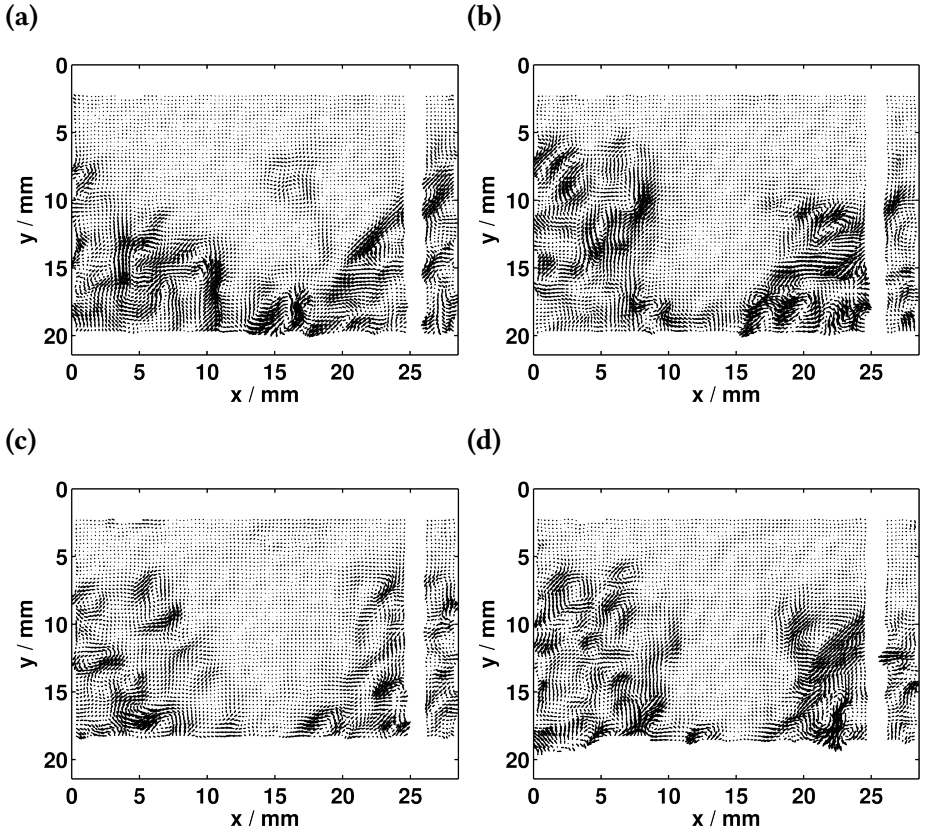

Figure 4.30: (a) – (d) High-pass-filtered instantaneous velocity fields at Δt = 50 ms.

As can be seen from all images, the bigger vortex structures visible in the instantaneous velocity fields consist of several smaller vortices with a size distribution of a few millimeters. The majority of the vortices shows a counter-clockwise rotation. Clockwise rotation is often coupled to adjacent CCW movement, which is clearly visible by the vortex pair at x = 16 mm / y = 7.5 mm in Figure 4.30a. This pair seems to be connected to two less intensive counter-rotating vortices at x = 16 mm / y = 16 mm. A similar pair, albeit with interchanged rotational direction, is exposed in Figure 4.30d around x = 18 mm / y = 10 mm and 4.30b at x = 20 mm / y = 12 mm.

For fan starting times of Δt = 100 ms (Fig, 4.31), the maximum velocity magnitude increases up to $v_{\max} \approx 12\,\mathrm{m\,s^{-1}}$. The flow pattern of the instantaneous velocity is in good agreement for all investigated image pairs and shows some recurring

features. Again, the lower part of the images shows the highest fluid velocity, but the relatively quiescent sector in the middle of the observation window is broken up and dominated by strong velocity fluctuations between $4\,\mathrm{m\,s^{-1}} < v_{\max} < 10\,\mathrm{m\,s^{-1}}$. The counter-rotating vortex on the right moves up towards the cylinder head and increases in intensity. The overall velocity around the spark plug increases and the fluid follows the movement of the fan towards the vortex structure. The movement of the fluid in the central bottom is no longer directed strictly downward, but instead starts to follow the fan movement. The decomposed velocity fields are shown in Figure 4.33 **a**–**d**. Together with an increase in the overall amount of vortices, they are no longer strictly localized at the left and right border of the plane and tend to be distributed over the whole observation plane. Larger coherent flow structures, especially in the lower part of Figure 4.31d show relatively few hidden vortices.

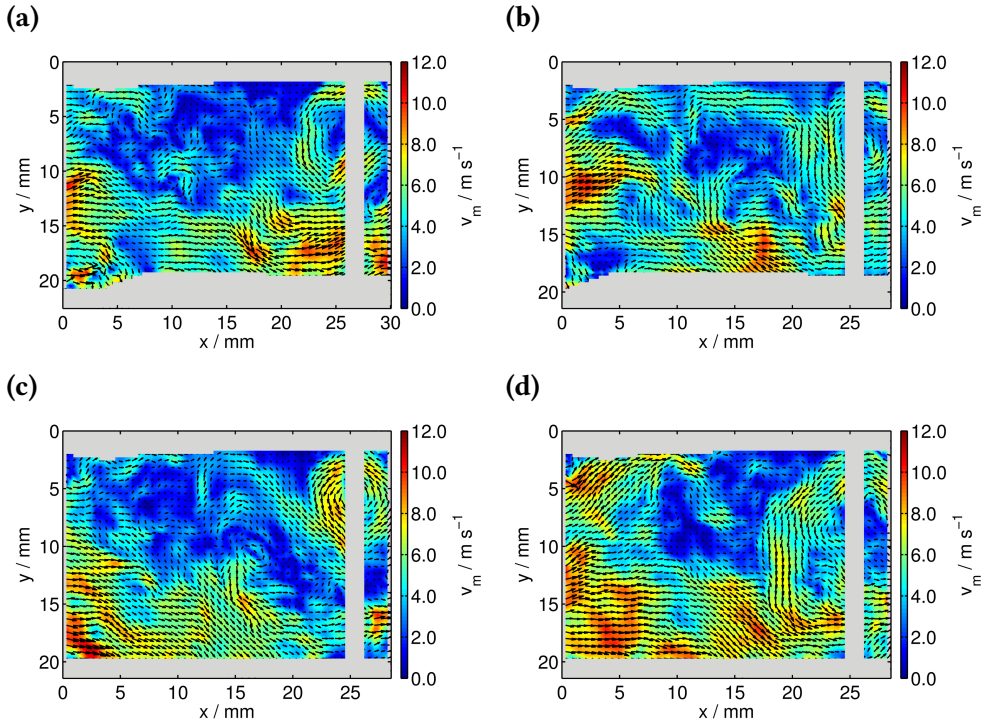

Figure 4.31: Four instantaneous velocity fields and velocity magnitude v_{m} obtained Δt =100 ms after fan start. Every second vector is shown.

At Δt = 150 ms (Figure 4.32), the velocity magnitude increases to $v_{\max} = 18\,\mathrm{m\,s^{-1}}$. Again, the highest velocities can be observed in the left sector of the observation window, with a fluid movement from left to right. The counter-clockwise rotating vortex is still visible, but cut at its center due to the shift towards the upper right corner of the flow field. The lowest velocity, $v_{\mathrm{m}} < 4\,\mathrm{m\,s^{-1}}$, is usually observed in the right sector of the image, but some instantaneous velocity fields have their lowest velocity slightly below the spark plug (Figure 4.32b and 4.32c). A general

trend can be observed at the boundary layer close to the cylinder head, $x \approx 12$ mm / $y \approx 2$ mm. The velocity is with $v_m \geq 8$ m s^{-1} significantly higher compared to the layer beneath.

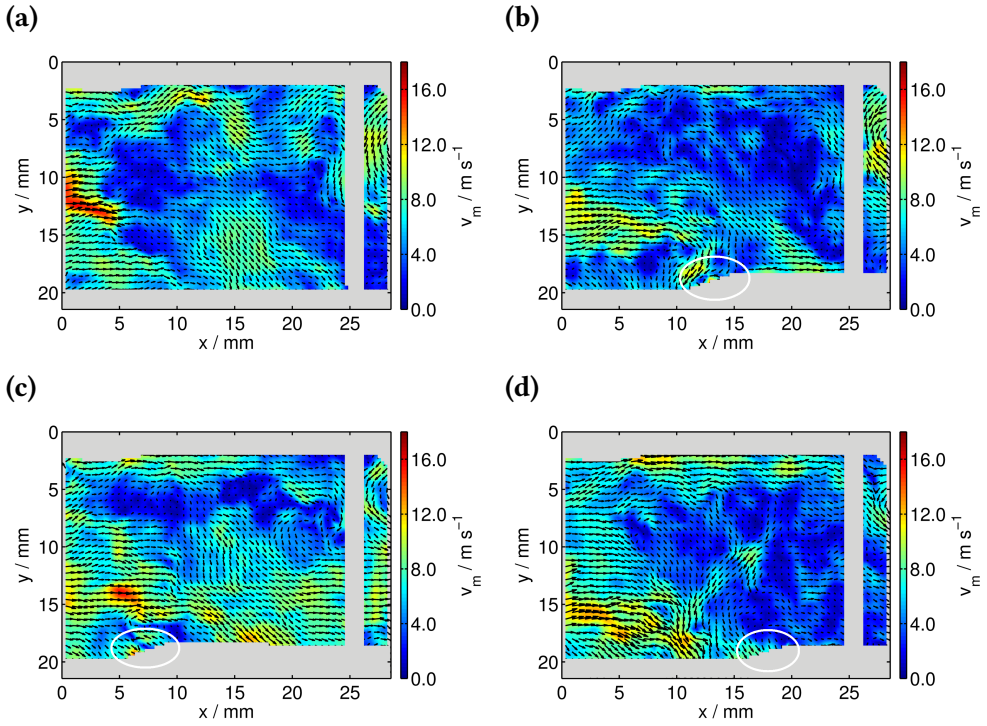

Figure 4.32: Four instantaneous velocity fields and velocity magnitude v_{m} obtained Δt =150 ms after fan start. Every second vector is shown. Insertion depth 9 mm. The tip of the fan blade is marked by the white circle.

Additionally, for each instantaneous velocity field, the fan masks part of the image at a different position in the chamber, as marked by the white circle. At this time, the fan speed is v_{fan} = 7900 rpm (see Table4.2) and thus significantly faster compared to Δt =50 ms and 100 ms. The starting position of the fan blades is slightly different for each experiment and in combination with the fan speed results in higher possibility of recording images with a fan blade moving into the observation plane. This "randomness" of the blade position during the imaging becomes even more pronounced for Δt >150 ms. Due to this effect, it is not feasible to show and compare multiple pictures for one fan starting time Δt. The instantaneous velocity fields for $\Delta t \geq 200$ ms are shown in Figure 4.34. The trend seen in the previous images continues: The velocity magnitude increases for every delay step and reaches a maximum of v_{max} = 25 m s^{-1} at Δt = 700 ms. Again, the areas of highest velocity are located in the left part of the image and the flow moves from left to right. The vortex in the upper right corner is still visible and the flow in the lower central region of the observation plane is directed downwards. The other areas are dominated by small islands of highly fluctuating velocity and flow direction and no

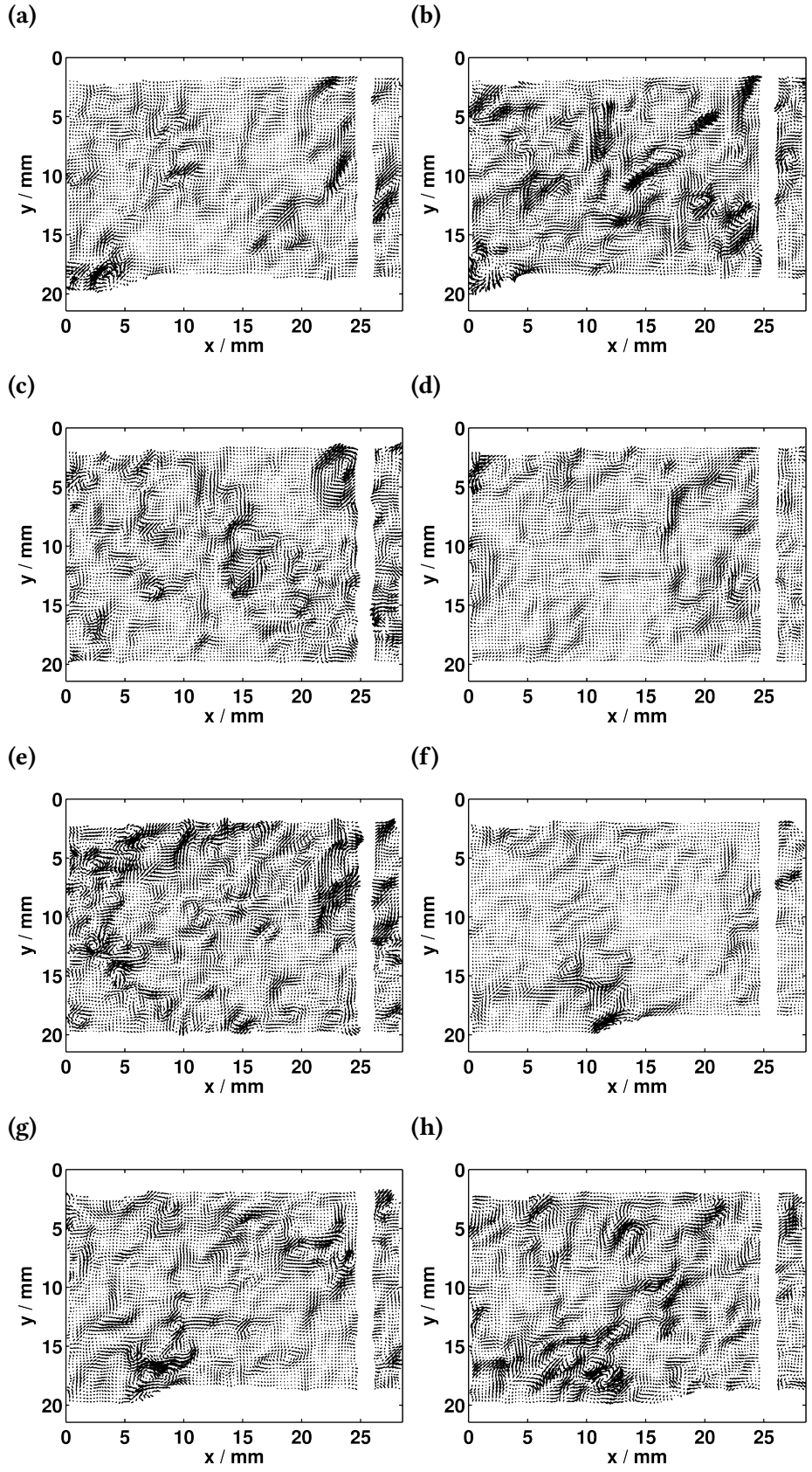

Figure 4.33: **(a)** – **(d)** High-pass-filtered instantaneous velocity fields at $\Delta t = 100\,\text{ms}$, **(e)** – **(h)** $\Delta t = 150\,\text{ms}$.

clearly identifiable pattern emerges from the flow. All images show features of very slow moving particles, $v_m < 4\,m\,s^{-1}$, that become nearly quiescent for the x and y direction. This can be seen not only for the whole right sector at $x > 25$ mm in Figure 4.34b, but also around $x = 20$ mm / $y = 10$ mm in Figure 4.34e. Two exemplary decomposed flow fields for $\Delta t = 200$ ms and 700 ms are shown in Figure 4.35. The amount of vortices in the region of the spark plug is increased for the instantaneous flow field at $\Delta t = 200$ ms. Nevertheless, the individual velocity fields cannot be distinguished from each other anymore based on the decomposed features.

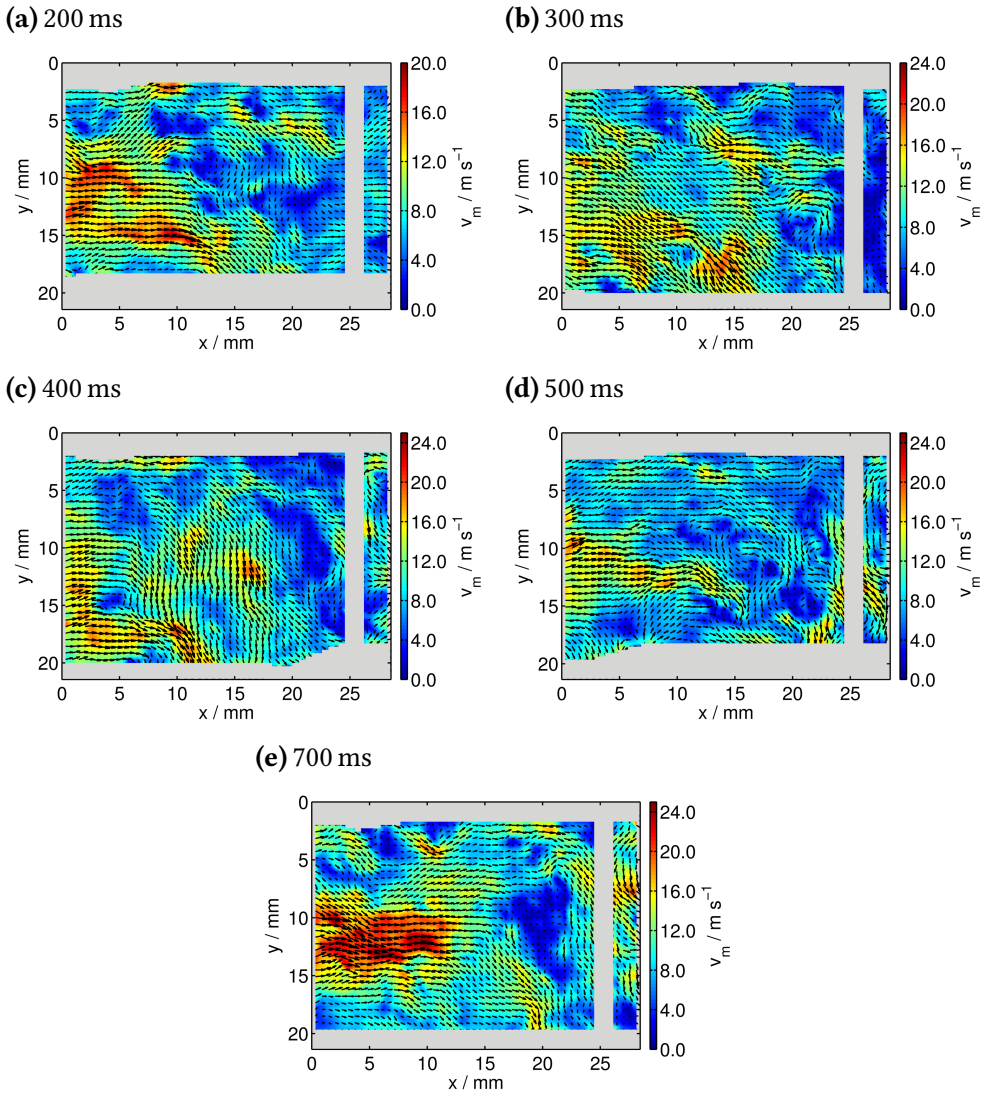

Figure 4.34: Instantaneous velocity fields and velocity magnitude v_m obtained between $\Delta t = 200$ ms and 700 ms after fan start. Every second vector is shown. Fan insertion depth 9 mm.

A clearer picture, especially at high turbulence, is provided by averaging the instantaneous velocity fields for a certain delay time Δt, the so-called ensemble averaging. All recorded images were checked for appropriate data quality, i.e. no

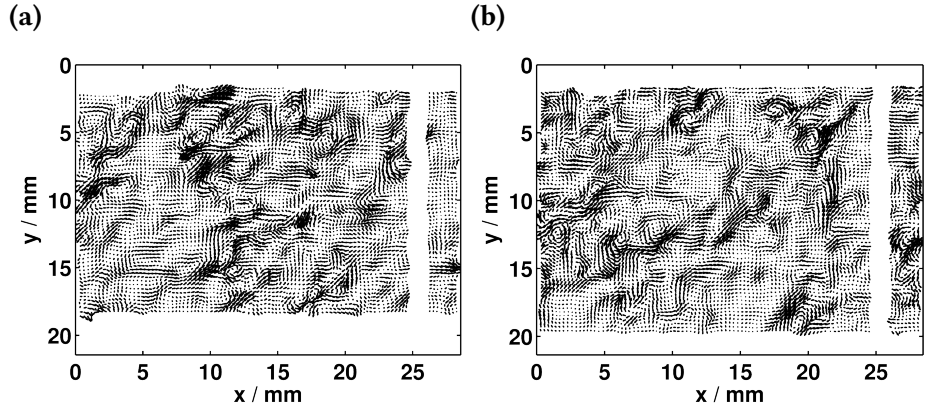

Figure 4.35: High-pass-filtered instantaneous velocity fields at **(a)** Δt = 200 ms and **(b)** Δt = 700 ms.

deposition of tracer particles on the window and low degree of scattered light. Together with the overall low amount of useful image pairs, this resulted in a number between $N_{\min}$ = 14 and $N_{\max}$ = 22 velocity fields available for the averaging. The averaged velocity as well as the vector field is shown shown in Figure 4.36. Due to the averaging, sudden change of flow direction do not occur and for clarity only every fourth vector is shown.

In comparison to the instantaneous velocity in Figure 4.29a at Δt =50 ms, all the previously described features of the flow can be found in the average velocity field, shown in Figure 4.36a, as well. The central part of the flow is dominated by a strictly downward flow ($u_{\mathrm{x}} \approx 0$), that increases in velocity from nearly quiescent areas around the spark plug to $v_{\mathrm{m}} \approx 4\,\mathrm{m\,s^{-1}}$ at the boundary layer above the fan. The highest velocities are observable at the left and right border of the observation window. Additionally, both area are dominated by rotating structures centered x = 7 mm / y = 12 mm and x = 23 mm / y = 12 mm, whose velocity magnitude increase in velocity towards the outside. The counter-clockwise rotating vortex in the right part is more pronounced than the clockwise rotating vortex on the left, but are both nearly equal in size, which spans the whole observation window. At Δt =100 ms (4.36b), the radius of the counter-clockwise vortex decreases to approximately 1 mm and moves upwards and to the right of the chamber. The central region, which is not clearly visible due to the scattered light, is shifted to x = 25 mm / y = 7 mm. The velocity increases to $v_{\mathrm{m}} \approx 6.5\,\mathrm{m\,s^{-1}}$ at the outer edge, while the velocity for the central region cannot be determined. The vortical structure in the left part vanishes and the flow pattern is nearly uniform with a dominating u_{x} velocity component. Here, the maximum velocity is increased by a factor of 2 compared to Δt =50 ms. Again, the lowest velocity components are found in the central region of the flow, while the velocity around the boundary layer at the cylinder head increases.

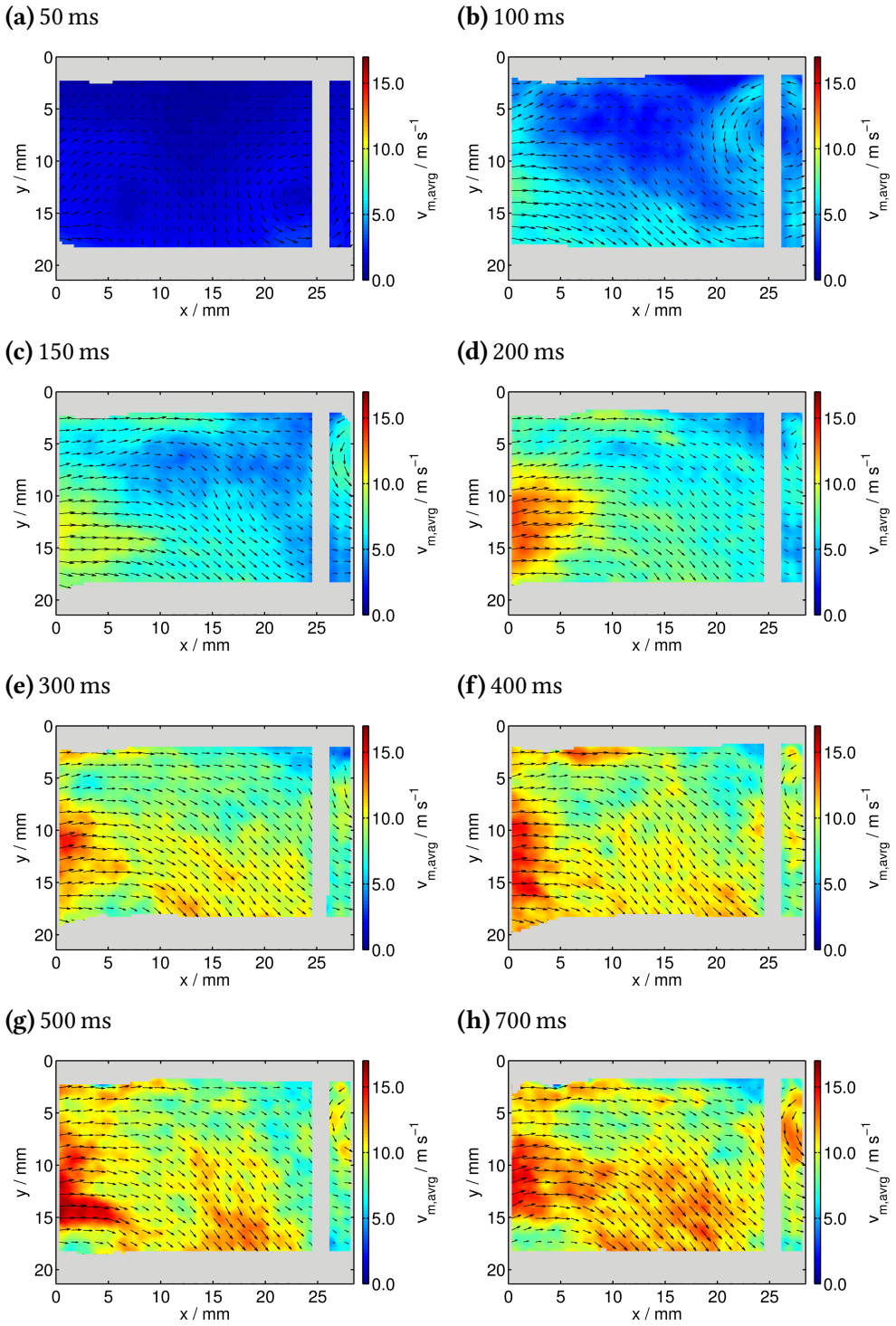

Figure 4.36: Ensemble averaged velocity $v_{\mathrm{m,avrg}}$ between Δt =50 ms 700 ms after fan start. All images were recorded at a fan insertion depth of 9 mm and a distance of 4 mm in front of the spark electrode. Every 4th vector is shown.

At Δt =150 ms, the vortex moves even further to the right and shows a further increase in velocity up to $v_\mathrm{m} \approx 9\,\mathrm{m\,s^{-1}}$ at the outer edge. The thickness of the cylinder head boundary layer shows a recognizable growth and the flow is characterized by a u_y component which is close to zero. A strong increase of the u_y velocity starts only at the outer edge of the vortex and below the boundary layer, which was dominated by nearly horizontal movement at Δt =100 ms. The area around x = 13 mm / y = 7 mm, which is directly below the spark plug, has velocity components with a magnitude of $v_\mathrm{m} \approx 5\,\mathrm{m\,s^{-1}}$, a factor of two smaller than the area at the left side of the flow. After Δt =150 ms, the overall pattern of the flow does not change anymore, as the flow velocity still increases. The maximum average velocity of $v_\mathrm{max} \approx 16\,\mathrm{m\,s^{-1}}$ is reached at Δt =500 ms at the left edge of the flow.

A similar pattern emerges from the average vorticity maps in Figure 4.37. At Δt =50 ms the right vortex has an area of high vorticity $\omega > -1500\,\mathrm{s^{-1}}$, while the vortical structure on the left is characterized by a positive vorticity with a maximum of $\omega > 1200\,\mathrm{s^{-1}}$, both around the central region. The area directly above the fan shows smaller regions of negative vorticity. The average vorticity around the spark plug is close to zero, with a small area of $\omega \approx 500\,\mathrm{s^{-1}}$ at x = 15 mm / y = 3 mm. For Δt =1000 ms, the vorticity does not only increase, but is also spread around the whole observation window. The boundary layer below the cylinder head shows mostly clockwise vorticity, even in the region of quiescent flow.

Horizontal cuts through the flow field were made at x = 12 mm (Figure 4.38a) and vertical y = 3 mm (Figure 4.38b), which is half the distance between the two spark electrode tips. Additionally, the average vorticity at y = 3 mm is shown in Figure 4.38c.

For the first delay time Δt = 50 ms, the velocity in horizontal direction drops to nearly 0 between $x \approx 10$ mm and 11 mm, but otherwise remains constant at $v_\mathrm{m} = 0.5\,\mathrm{m\,s^{-1}}$. In the vertical direction, the velocity at the top is close to zero and rises steady until $v_\mathrm{m} = 1.0\,\mathrm{m\,s^{-1}}$ at y = 17 mm. Below that position, the velocity increases strongly to a maximum of $v_\mathrm{m} = 4.0\,\mathrm{m\,s^{-1}}$. At Δt = 100 ms, the velocity drops from $5.0\,\mathrm{m\,s^{-1}}$ to $1.0\,\mathrm{m\,s^{-1}}$ until x = 20 mm and increases strongly over the length of 5 mm to $5.0\,\mathrm{m\,s^{-1}}$. The vertical velocity profile changes as well, a minimum can be observed around y = 7.5 mm. The drop-off in velocity starts below the boundary layer at y = 3 mm and increases towards the bottom. The distinctive drop of the velocity in horizontal direction and the occurrence of a minimum in vertical direction can be seen for all delay times. The x profiles at Δt = 150 ms and 200 ms are nearly identical in terms of absolute values and change of velocity, while all higher delay times are characterized by higher velocities, especially between x = 0 mm and 10 mm. In vertical direction, the minimum is shifted with increasing Δt towards the cylinder head and remains at x = 5.5 mm after Δt = 300 ms. With

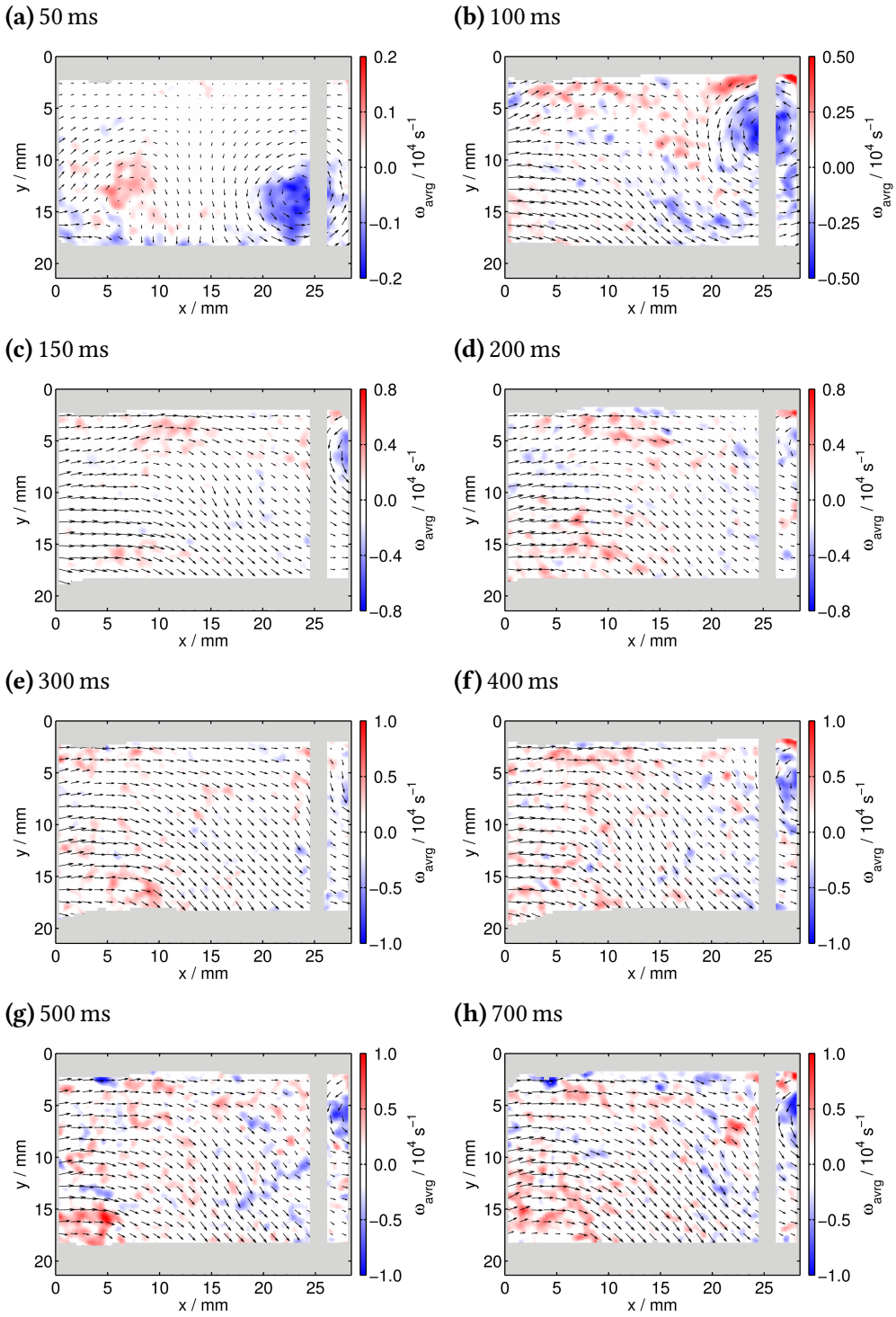

Figure 4.37: Ensemble averaged vorticity ω_{avrg} between Δt =50 ms 700 ms after fan start. All images were recorded at a fan insertion depth of 9 mm and a distance of 4 mm in front of the fan. Every 4th vector is shown.

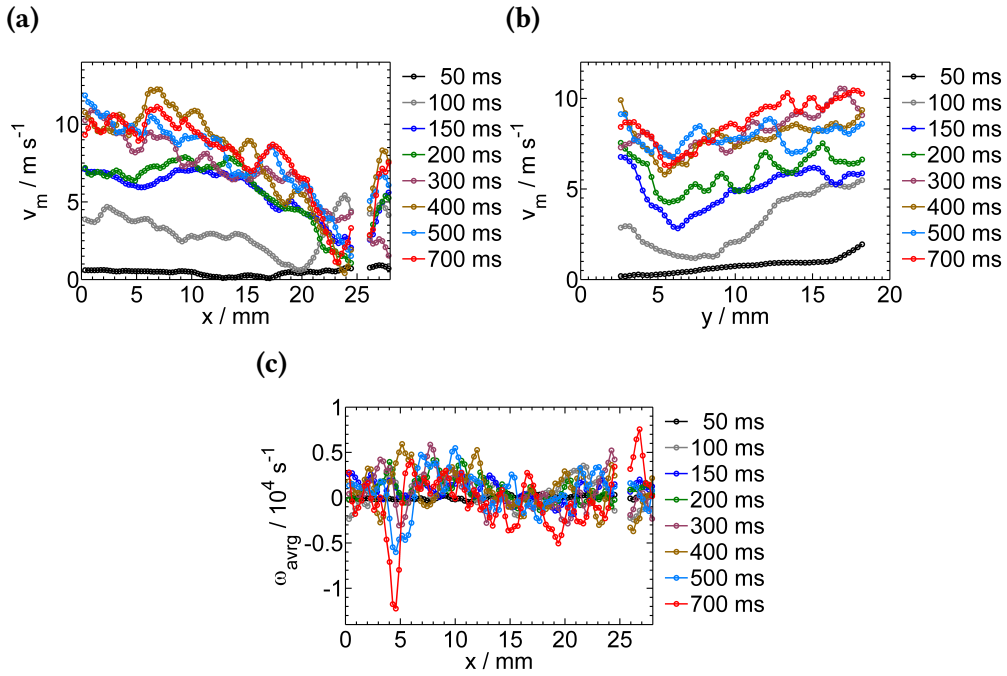

Figure 4.38: **(a)** Horizontal average velocity profile at $y = 3$ mm, **(b)** horizontal average velocity profile at $x = 12$ mm and **(c)** vertical average vorticity profile between $\Delta t = 50$ ms and 700 ms after start of the fan. Missing data points correspond to areas not accessible due to scattered light.

the high velocity boundary layer still intact, the steepest velocity drop can be observed at the top of the chamber. The velocity increases again at the lower parts of the y direction. Again, the profiles for $\Delta t = 150$ ms and 200 ms are nearly identical, as are the profiles for all higher Δt values.

This behavior is not observable in the vorticity slices. For Δt =50 ms, the vorticity is close to zero over the whole range. For higher delay times, $\Delta t \geq 100$ ms, the lowest vorticity can be observed between $x \approx 15$ mm and 18 mm. Between $x \approx 7$ mm and 11 mm ω is mostly positive. Otherwise, ω is randomly distributed and shows no clear trend. Especially at Δt =500 ms and 700 ms, areas with a strong positive vorticity are accompanied by sudden drops to negative values.

4.3.1.2 Turbulence intensity at 9 mm fan insertion depth

The average turbulence intensity $u_{\mathrm{x,rms}}$ and $u_{\mathrm{y,rms}}$ for different fan starting times Δt was calculated from the instantaneous velocity profiles. For each Δt, at least 14 image pairs were used for the calculation of the ensemble-averaged velocity components $\langle u_{\mathrm{x}} \rangle$ and $\langle u_{\mathrm{y}} \rangle$. Afterwards, the ensemble-averaged velocity was subtracted from the instantaneous velocity u_{x} and u_{y} to determine the turbulent velocity

fluctuation u_x' and u_y'. As mentioned in Section 2.1.4, the turbulence intensity is then calculated as root mean square value $u_{x,rms}'$ and $u_{y,rms}'$ according to

$$u_{i,rms}' = \sqrt{\langle u_i'^2 \rangle_{\Delta t}}. \tag{4.7}$$

The horizontal and vertical turbulence intensity between Δt = 50 ms and 200 ms is shown in Figure 4.39, the velocity maps for the horizontal component are on the left side. It should be noted that due to the small amount of available images, the turbulence intensities can only be used for a qualitative description of the flow field. Spikes in the fluctuating velocity component can lead to an overestimation of the average turbulence intensity.

For Δt = 50 ms, a minimum of the turbulence intensity for both components can be observed in the center of the observation window around x = 13 mm / y = 10 mm. Higher intensities, $u_{rms} \approx 3.0\ m\ s^{-1}$, appear in the lower left area and on the right side of the flow, where the two vortex structures are located. At Δt = 100 ms, the turbulence intensity increases for both velocity components to $u_{rms} > 4.0\ m\ s^{-1}$. The highest vertical turbulence intensity can be found predominantly in the right part of the chamber, x > 15 mm, slightly below the counter-clockwise rotating vortex. The turbulence intensity in horizontal direction is increased nearly everywhere and some areas of high velocity fluctuation appear at the lower part of the observation window. At Δt = 150 ms, both velocity maps show a gradient of turbulence intensity with lower values at the top and high intensity at the bottom. The maximum intensity for $u_{x,rms} > 5.0\ m\ s^{-1}$ is reached directly above the fan blades at x = 7.5 mm. Here, $u_{y,rms}$ is distinctly increased as well. The area of high intensity seen in Figure 4.39d is shifted upwards. The horizontal turbulence at Δt = 200 ms shows analog features, which are only increased in intensity to $u_{y,rms} = 6.0\ m\ s^{-1}$. This does not apply for the u_x component, where the intensity distribution changes significantly. The turbulence at the level of the fan is shifted upwards and covers nearly half of the left part. Additionally, the turbulence is considerably increased in the lower right area around x = 25 mm / y = 17 mm. From this delay time on, the turbulence fields for u_x differ drastically from the vertical component u_y. While for Δt > 200 ms the overall turbulence still increases up to 700 ms, the difference between u_x and u_y is clearly visible in Figure 4.40.

The highest turbulence in vertical direction can be observed in the lower left area below y = 10 mm and as far as x = 11 mm. Here, $u_{x,rms}$ increases to $10.0\ m\ s^{-1}$ at Δt = 700 ms, the average turbulence intensity is clearly above $6.0\ m\ s^{-1}$. The upper right corner, x > 22 mm / y < 5 mm is dominated by horizontal turbulence as well. Smaller areas of increased turbulence can be seen at the bottom right part, the u_x turbulence in between is significantly lower. In this area of apparent

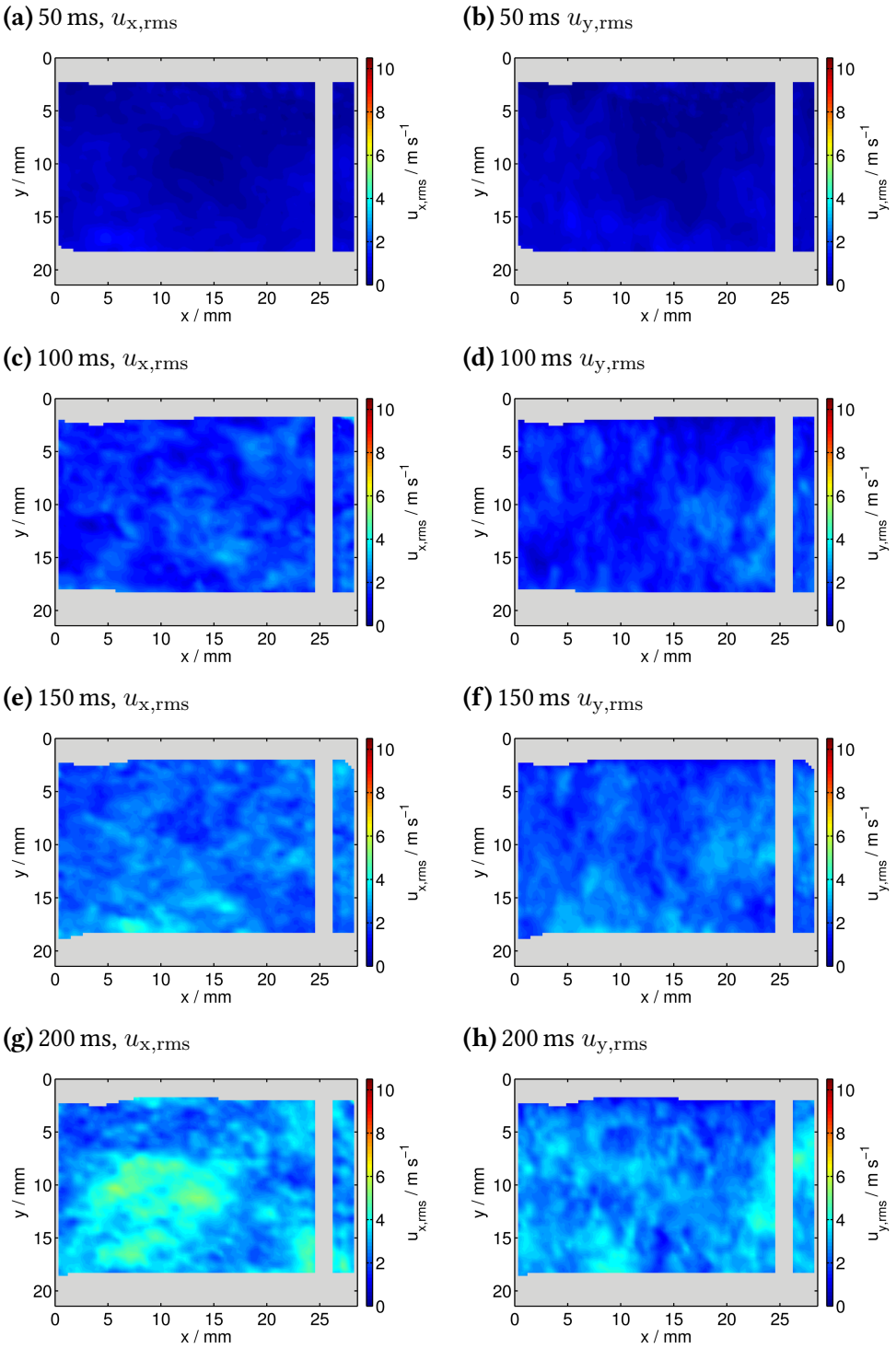

Figure 4.39: Average turbulence intensity u_{rms} between Δt =50 ms and 200 ms after fan start. The horizontal component of the turbulence intensity u_x is shown on the left, the u_y component on the right. All images were recorded at a fan insertion depth of 9 mm and a distance of 4 mm in front of the spark electrode.

low turbulence with a diameter of approximately 1 mm, the images show a strong increase of the vertical fluctuating velocity u_{y}. Complimentary to the the increase of $u_{\mathrm{x,rms}}$, the $u_{\mathrm{y,rms}}$ values in the lower left area of the images are substantially lower. Also, the vertical turbulence around the boundary layer of the cylinder head stays below 4.0 m s^{-1}, also the highest turbulence intensities are far off from the area of the spark plug.

The shape of the turbulence map correspond well with the velocity maps shown in Figure 4.36. The fluid in the left part of the image is influenced by a horizontal movement, reflected by the higher u_{x} turbulence. The counter-clockwise rotating vortex in the upper right corner has a strong vertical velocity component at its left edge, located at the same position of the highest u_{y} turbulence.

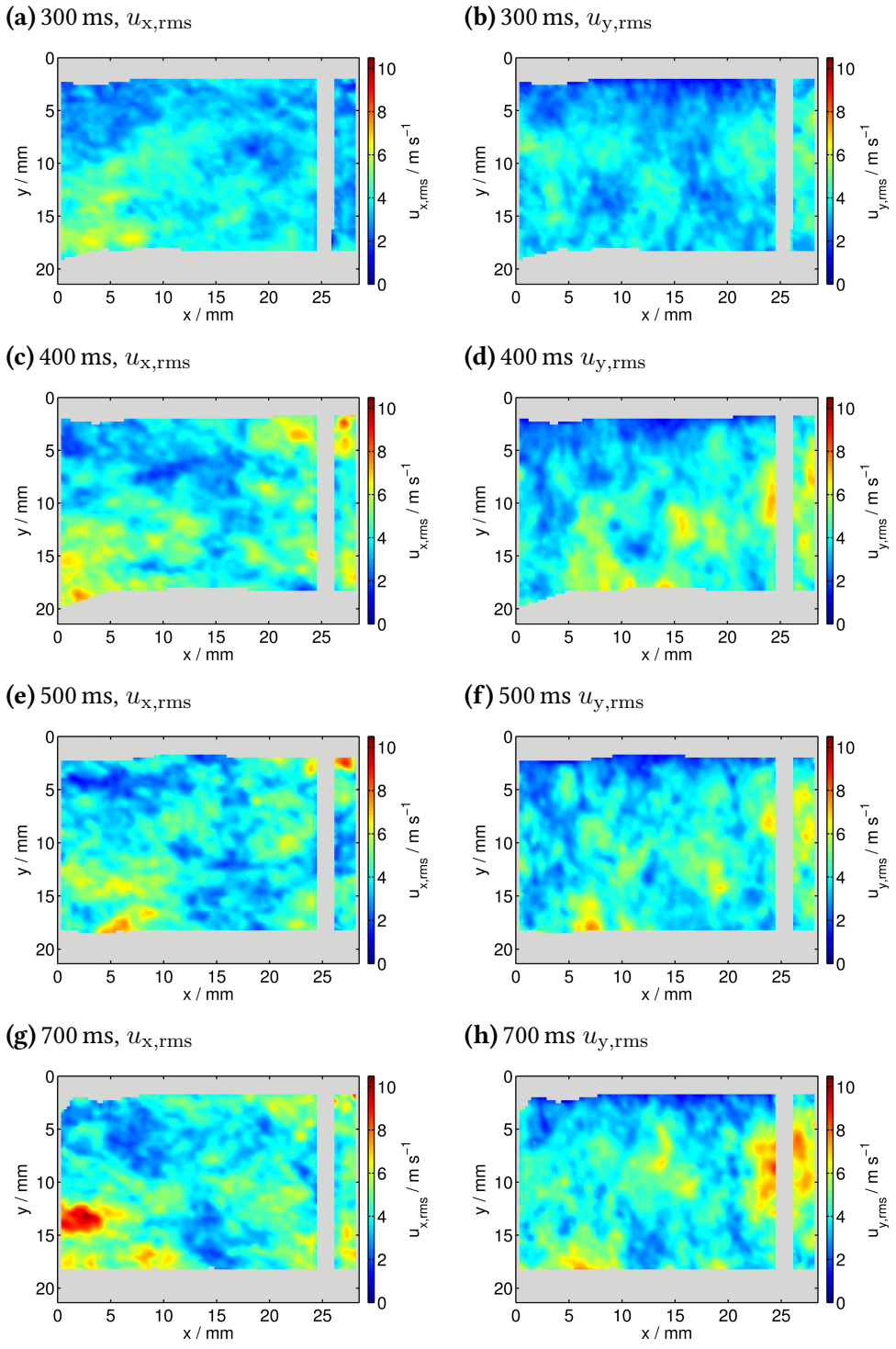

Figure 4.40: Average turbulence intensity u_{rms} between Δt =300 ms and 700 ms after fan start. The horizontal component of the turbulence intensity u_x is shown on the left, the u_y component on the right. All images were recorded at an insertion depth of 9 mm and a distance of 4 mm in front of the fan.

To provide a better overview of the turbulence at the level of the spark plug, again a horizontal and vertical velocity profile was extracted at $y = 3$ mm (Figure 4.41b and 4.41a) and $x = 12$ mm (Figure 4.41d and 4.41c). For each cut, both turbulence components $u^i_{\mathrm{x,rms}}$ and $u^i_{\mathrm{y,rms}}$ were examined. The superscript i denotes the direction of the cut.

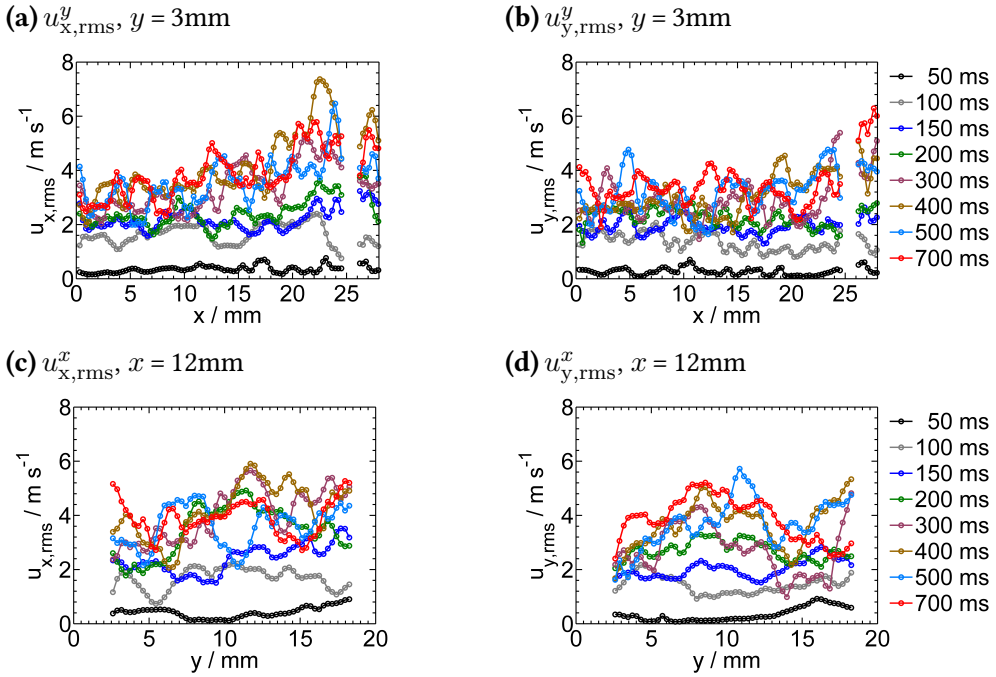

Figure 4.41: **(a)** and **(b)** Horizontal turbulence intensity profile for the $u_{\mathrm{x,rms}}$ and $u_{\mathrm{y,rms}}$ components. **(c)** and **(d)** Vertical turbulence intensity profiles are shown between 50 ms and 700 ms after start of the fan. Missing data points correspond to areas not accessible due to scattered light.

In horizontal direction, the turbulence intensity at $\Delta t = 50$ ms both for u_{x} and u_{y} stays around 1.0 m s^{-1} over the course of the chamber. For higher delay times, the turbulence intensity u_{x} tends to increase steadily from left to right, while the u_{y} component increases at $x = 20$ mm for fan running times longer than 300 ms. The highest increase in turbulence intensity, both for u_{x} and u_{y}, can be found between 50 ms and 100 ms. While the increase for longer Δt is hard to quantify due to the fluctuating velocities, two additional time ranges with similar behavior can be seen. The turbulence intensity between $\Delta t = 100$ ms and 200 ms tends to fluctuate around $u_{\mathrm{x},y} \approx 2.0$ m s^{-1}, especially towards the right side of the chamber. The highest turbulence intensities, $u_{\mathrm{x},y} > 2.0$ m s^{-1} are found in the third group, 300 ms < Δt < 700 ms.

For cuts in vertical direction, a similar trend is not observed. The turbulence intensity is below 1.0 m s^{-1} for $\Delta t = 50$ ms. Here, the intensity both for the u_{x} and u_{y} components increases from top to bottom and the highest values can be found

above the tip of the fan blades. The horizontal turbulence tends to increase for fan starting times between 150 ms and 500 ms from top to bottom as well, while at Δt = 100 ms the turbulence decreases towards the bottom. The vertical component u_y is nearly identical for all Δt > 100 ms at the boundary layer below the top of the chamber. At 100 ms and 150 ms, u_y stays at 2.0 m s^{-1} from top to bottom, while for longer fan running times the turbulence intensity has a maximum in the middle of the observation window at y = 10 mm.

The results can be discussed and summarized as follows: The recorded images clearly show the strong influence of the fan movement as early as Δt = 100 ms after fan start. The flow patterns of the instantaneous velocity fields reveal a relatively complex and inhomogeneous flow. The two-dimensional cut through a flow moving in three dimensions makes their interpretation even more difficult, yet the results reveal some general trends regarding the possible interaction between the movement of the fluid and the expansion of the flame.

At Δt = 50 ms, the flow around the spark electrode shows nearly no influence by the movement of the fan, as the fluid velocity is close to zero. As expected, the fluid is accelerated towards the fan, indicated by the velocity gradient in vertical direction. The vertical gradient becomes also apparent for the turbulent velocity fluctuations u_x' and u_y', which are significantly below 0.5 m s^{-1} in the horizontal direction. High turbulence can only be found around the bottom of the observation window and gradually increases both in x and y direction attributed to the movement of the fan. Due to the energy input by the fan, flow separation occurs at the left and right side of the windows where the fan blades enter and leave the observation plane, and the flow turns from laminar to turbulent. The counter-clockwise rotating vortex at the right side might emerge from the induced stall by the fan blades, which have a high angle of attack.

The transition towards turbulent conditions becomes also apparent in the decomposed velocity fields. All small vortices, which are hidden under the main flow, appear around the edges of the blade tips entering and leaving the observation plane. Due to the main flow traveling downwards, they mostly lack the velocity to disentangle themselves from the turbulent areas and cannot penetrate the laminar regions. Figure 4.30a shows one rare example, where a detached vortex pair becomes visible in the center of the observation window. As shown in the vorticity plots, the rotation of the smaller vortices is similar to the mean flow. The vorticity in the right sector of the image is mostly negative ($\omega \approx -1500$ s), whereas the net vorticity in the left sector is mostly positive ($\omega \approx 1000$ s), according to the fan blades entering and leaving the plane. These findings also correlate well with the fan Reynolds number of Re_{fan} = 13500, which lies in the transition regime towards turbulent conditions.

The general flow pattern is similar to the flame stretching observed in the chemiluminescence images shown in Figure 4.21. After ignition, the flame kernel grows as it is expected from a laminar flame. When the flame enters the acceleration zone in the center of the image, it is elongated due to the downstream flow. Afterwards, the flame starts to interact with the turbulent flow field around the laminar zone and the flame surface starts to wrinkle. The CCW rotating vortex also generates a recirculation zone, which provides the downward traveling flame with new fresh gas mixtures.

This flow pattern can only be observed at Δt = 50 ms, as the fan speed increases drastically within the next 100 ms, which marks its highest acceleration phase and an increase of fan Reynolds number from $Re_{100\mathrm{ms}}$ = 24500 to $Re_{150\mathrm{ms}}$ = 32200. During the strong acceleration phase, the transition towards fully turbulent conditions is supposed to be complete. This can be clearly seen in the vorticity maps and the LES decomposed velocity fields, which show an increase of underlying vortices. Additionally, the vorticity is enhanced by a factor of 2–3 to $\omega \approx 4000$ s. Vortices can now be found in all areas of the observation window and around the spark electrodes. This corresponds well with the strong increase of maximum combustion pressure $\Delta p_{\max}$ and maximum pressure time $t\,(\Delta p_{\max})$.

Due to the increase of turbulence, the flame expansion is influenced immediately after the establishment of a stable flame kernel at t = 0.4 ms after start of ignition (see Fig. 4.23). Furthermore, the expansion direction is changed due to the increase of the vertical flow velocity u_{x}, especially at the spark electrodes, and the flame first travels towards the right of the chamber, until it reaches areas with higher u_{y}.

As seen in the vorticity maps, there is no clear trend for the occurrence of clockwise or counter-clockwise rotating areas, apart from the big CCW vortex in the upper right corner. As a consequence, small CCW vortices with sized of less than 5 mm are often accompanied by CW rotating vortices. These areas are responsible for the strong wrinkling of the flame and the high strain induced to the flame front.

As mentioned in Section 2.1.2.1, a possible mechanism for flame quenching is the change of required minimum ignition energy with an increase of u'. A strong increase of the MIE occurs for turbulence u' much higher than the laminar flame speed u_{l}, $u' \geq 2u_{\mathrm{l}}$.[47,48] The horizontal and vertical slices at the spark electrodes show turbulence intensities above $u' > 2\,\mathrm{m\,s^{-1}}$ exceeding the laminar flame speed $u_l \approx 0.4$–$0.5\,\mathrm{m\,s^{-1}}$, which is typical for C_3 hydrocarbon flames.[200,203,217] For higher fan running times between Δt = 200 ms and 700 ms, the turbulence intensity increases to a maximum value of $u' \approx 5\,\mathrm{m\,s^{-1}}$, raising the turbulence-to-flame speed ratio u'/u_{l} above 10. Although the ignition energy is unknown, this

drastic increase of MIE can be a possible explanation for the flame quenching of propane-air mixtures, which showed a significant decrease in ignition probability for lean mixtures at fan running above $\Delta t = 200$ ms and $\Delta t \geq 300$ ms for rich mixtures.

Compared to the first 200 ms after fan start, only a small change of mean flow direction, maximum velocity and turbulence intensity can be observed for fan running times longer than $\Delta t = 200$ ms. This behavior is reflected by the same small changes in combustion enhancement, i.e. maximum pressure and pressure rise time, for the propene/1-butene fuel.

4.3.1.3 Integral length scale at 9 mm fan insertion depth

To understand the processes of energy dissipation in a turbulent flow, a definition of a characteristic length or time period for the largest turbulent scales is of importance. In some cases, e.g., for a pipe flow, the pipe diameter is of the size of the largest eddies and the ratio of pipe diameter to the mean velocity along the pipe can be used to estimate a characteristic time period of the flow. For more complex geometries, a similar estimation of the flow is rarely possible due to the non-homogeneity and unsteadiness of the flow and leads to the introduction of a so called integral scale. The integral scale Λ is often defined by measuring the longest connecting or correlating distance between two points in the flow. These points can be separated either by space r or time t. Λ is then defined by

$$\Lambda\left(r,t\right) = \int_{0}^{\infty} R_{ii}\left(r,t\right) d\left(r,t\right), \tag{4.8}$$

where $R_{ii}\left(r,t\right)$ is the autocorrelation function of a velocity component with itself. If $u_i^{'}\left(x\right)$ is the fluctuating velocity at a position x in a Cartesian frame, the correlation coefficient of this component measured simultaneously at position x and a moving position $x + r$ is defined as[219,220]

$$R_{ii}^{x}\left(r\right) = \frac{\left\langle u_i^{'}\left(x\right) \cdot u_i^{'}\left(x+r\right)\right\rangle}{\left\langle u_i^{'2}\left(x\right)\right\rangle} \tag{4.9}$$

Here, the superscript x refers to the axis of the flow component. By definition, the coefficient R_{ii}^{x} is unity for $r = 0$. Usually, this definition is applied for flows with a quasi-uniform RMS value.[221] If the moving position crosses different zones

for a given flow and thus changing RMS values of the flow are observed, the autocorrelation coefficient is often defined by[221,222]

$$R_{ii}^{x}(r) = \frac{\langle u_i'(x) \cdot u_i'(x+r) \rangle}{\sqrt{\langle u_i'^2 \rangle} \sqrt{\langle u_i'^2(x+r) \rangle}} \tag{4.10}$$

As shown in Equation 4.9, R_{ii}^{x} is unity for $r = 0$.

In Equation 4.8, the integral scale is determined by an infinite domain. This is often not possible for experimental data, especially for small numbers of ensemble averages and thus, different approaches were made to define a suitable integration domain. For autocorrelation functions with a negative region, the integration is often performed up to the first minimum value or to the first zero crossing.[223] Other methods are based on integration to the $1/e$ value or in case of low signal-to-noise ratio, estimating Λ by using the correlation length r where R_{ii}^{x} has the value $1/e$.[222] Due to the small amount of averaging, the latter method was used during the work of this Thesis. For homogeneous turbulence, the correlation curve is symmetric for displacements to the left ($r < 0$) and right ($r > 0$).[221] The integral

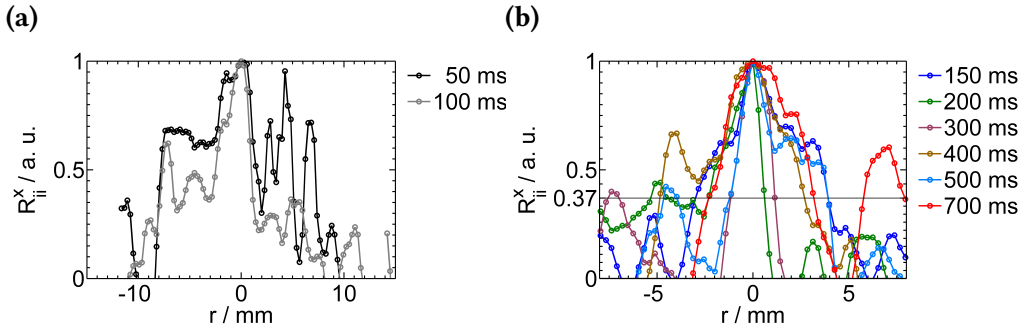

Figure 4.42: Autocorrelation values R_{ii}^{x} at the intersection of horizontal and vertical cuts, $x = 12$ mm / $y = 3$ mm shown in Figure 4.38. **(a)** 50 ms and 100 ms after start of the fan, **(b)** 150 ms – 700 ms after start of the fan.

length scale was calculated at the intersection of the horizontal and vertical slices at $x = 12$ mm / $y = 3$ mm. The correlation curves for $\Delta t = 50$ ms and 100 ms are shown in Figure 4.42a. As can be seen, both curves show a steep drop of R_{ii}^{x} for correlation to the right side of the chamber, $r > 0$. For longer distances, no clear correlation pattern can be observed and the correlation coefficient oscillates around $R_{ii}^{x} = 0.5$ for $\Delta t = 50$ ms and 0.25 for $\Delta t = 100$ ms. The first zero-crossing on the positive side occurs at $r_{50} = 9.5$ mm and $r_{100} = 8.0$ mm. Due to the oscillation values, the length at $R_{ii}^{x} = 1/e$ cannot be determined. For the correlation to the left side of the chamber, $r < 0$, the sharp drop-off in the first 2 mm is missing for $\Delta t = 50$ ms. The correlation coefficient stays constant between 2 mm $< r_{50} <$ 7 mm and decreases within 1 mm to zero. For $\Delta t = 100$ ms, the first zero crossing occurs at $r_{100} = 11$ mm.

For higher delay times and thus an increase in turbulence, the correlation curves tend to be more symmetrical around $r = 0$ and decay to zero until $|r| < 7$ mm, except for $\Delta t = 200$ ms. The correlation curve at this delay time decays to $R_{ii}^{x} = 0$ at 10.5 mm for $r < 0$ and 2.0 mm $r > 0$.

Due to the limited number of measurements, an exact calculation of the integral length scale was not possible. Nevertheless, the values obtained for l_t can be used for a rough estimation. The approximated integral length scales can be divided into two sections. For low turbulence ($\Delta t < 150$ ms), the integral length scale is $\delta_\mathrm{l} \approx 10$ mm, while at higher turbulence ($\Delta t > 150$ ms) the length scales drop to $\delta_\mathrm{l} \approx 5$ mm. These values are in reasonable agreement with the estimated length scales obtained from the LES decomposed instantaneous velocity fields and vorticity calculations. Additionally, the length scale values also partly support the finding from the previous section of inhomogeneous turbulence. In case of homogeneous turbulence, the integral time scale is inversely proportional to the turbulence intensity and suggests an integral length scale independent of fan speed. This was shown for different constant-volume combustion bombs and fan configurations.[224–226] Here, usually four or more fans opposed to each other are pointed towards the center of the combustion bomb, generating nearly homogeneous and isotropic turbulence (HIT).

Still, almost constant integral length scales were found for fan running times longer than $\Delta t = 150$ ms, which is in contrast to the velocity maps shown in Figure 4.40. Additionally, the correlation curves appear to be symmetrical around $r = 0$ mm, suggesting a homogeneous turbulence. One should keep in mind that the correlation functions shown in Figure 4.42 suffer from the limited amount of data points used for the averaging and thus the interpretation of their exact values is highly speculative.

Nevertheless, the integral length scales can be a useful parameter to characterize the interaction of flame and turbulence. As shown in Section 2.1.4.1, different regimes exist for premixed turbulent combustion. These are based on the ratio of turbulence intensity u' to laminar flame speed u_l and integral length scale l_t to laminar flame thickness δ_l, respectively. Depending on the turbulent conditions, the regimes are characterized by either disturbance of the laminar flame front or in the most extreme case a complete break-up of the flame front, which leads to flame quenching. The transition from the disturbed to the broken reaction zone is characterized by a Damköhler number of $Da < 1$.

The thickness of a laminar hydrocarbon-air flame δ_l is usually in the order of magnitude of the quenching distance d_q or slightly below.[25] The reported values for propane-air mixtures above stoichiometric conditions, $\phi \approx 1.2$, are of the order of $\delta_\mathrm{l} \approx 0.4$ mm.[30,227,228] The laminar flame speed at this conditions can

be approximated to be $u_l \approx 0.4\,\mathrm{m\,s^{-1}}$.[200,203,217] As seen in the previous Chapter, the turbulence intensities strongly depend on the fan speed and vary between $u'_{min} \approx 0.5\,\mathrm{m\,s^{-1}}$ for $\Delta t = 50\,\mathrm{ms}$ and $u'_{max} \approx 5\,\mathrm{m\,s^{-1}}$ for $\Delta t = 700\,\mathrm{ms}$. This leads to length scale rations of $12.5 < l_t/\delta_l < 250$ and velocity ratios of $1 < u'/u_l < 12.5$. The area of this approximation is marked in the Borghi diagram shown in Figure 4.43. Based on these values, the majority of the turbulent conditions can be placed in the

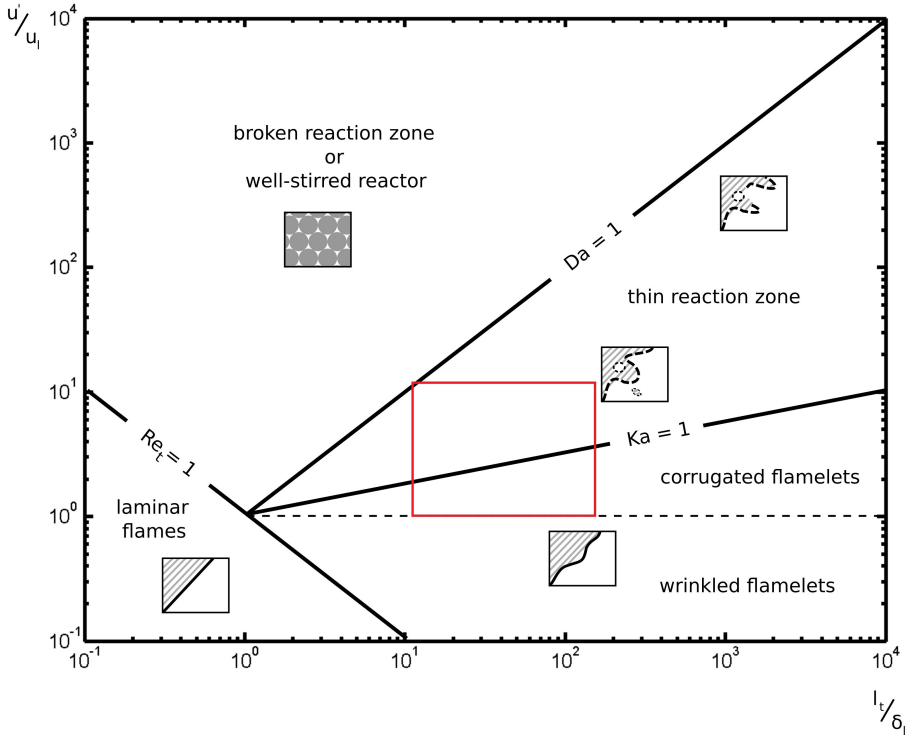

Figure 4.43: Borghi diagram to describe five different regions of combustion depending on the ratio of turbulence intensity to laminar flame velocity u'/u_l and microscale to flame thickness l_t/δ_l. The approximated regime for the turbulent combustion investigated in this Thesis is marked by the red rectangle.[69,70]

region of corrugated flamelets or the thin reaction zone, which is in good agreement with the flames observed in the chemiluminescence and LIF measurements.

For highly turbulent flows, the conditions approach the border towards the broken reaction zone and reach a Damköhler number of

$$Da = \frac{l_t \cdot u_l}{\delta_l \cdot u'} \approx 1 \tag{4.11}$$

For hydrocarbon-air mixtures deviating from the optimal conditions, $\phi > 1.2$, the laminar flame speed decreases while its thickness grows, which leads to Damköhler numbers smaller than unity and thus a transition to the broken reaction zone occurs.

This can explain the observations found for propane/air mixtures in Chapter 4.1.3. Here, the ignition probability decreased strongly for fan starting times times longer than Δt = 200 ms before ignition, which also marks the transition from low turbulent conditions (u' < 2 m s^{-1}) towards high turbulence. Due to the chamber operating at the stability limit in the Borghi diagram, small changes in turbulence intensity can lower the Damköhler number below unity and thus favor flame quenching. In contrast to propane/air flames, the laminar flame velocity is slightly higher for comparable 1-propene/butene mixtures and thus results in a higher Damköhler number.

4.3.1.4 Velocity fields at 3 mm fan insertion depth

The instantaneous velocity fields between Δt = 50 ms and 700 ms at an insertion depth of d = 3 mm are shown in Figure 4.44. Due to the higher position of the fan, the flow field behind the fan blades becomes visible. At Δt = 50 ms (Figure 4.44a), the highest velocity, $v_{\max}$ = 8.0 m s^{-1} can be found around x = 12 mm / y = 15 mm, directly behind the fan blade. The flow of this boundary layer is directed towards the blade surface at an angle of 45° and has a thickness of 3 mm. Left of the boundary layer, the velocity decreases below 6.0 m s^{-1} and the flow moves horizontally. Above the height of the fan, y < 12 mm, the velocity decreases significantly to $v_{\max}$ < 2.0 m s^{-1}. At the tip of the blade, the counter-rotating vortex can also be found at an insertion depth of d = 9 mm. In contrast to the maximum insertion, only few areas of quiescent fluid with small diameters below 2 mm can be found. The area in front of the spark plug is characterized by zones with velocities from < 2.0 m s^{-1} to ≈ 2.0 m s^{-1}. At x = 17 mm, the horizontal movement changes to a predominantly vertical flow.

At Δt = 100 ms, the velocity at the left part of the observation plane increases to v_m > 10.0 m s^{-1}, while the velocity at the blade stays between 6.0 m s^{-1} and 8.0 m s^{-1}. Nevertheless, the 45° layer increases in thickness. The CCW vortex in the top left corner mostly disappears, only the left region is visible at x = 30 mm / y = 5 mm. For all higher delay times, the flow pattern is similar apart from the velocity magnitude. The highest velocity can always be found in the left sector of the image. Here, the movement is predominantly horizontal, while the slow moving part in the right sector is mainly from top to bottom. The maximum velocity increases from 16.0 m s^{-1} at Δt = 150 ms to 24.0 m s^{-1} at Δt = 500 ms, after which the velocity stays constant.

The ensemble averaged flow fields shown in Figure 4.45 confirm the flow features from the instantaneous velocity fields. The CCW vortex is only visible at

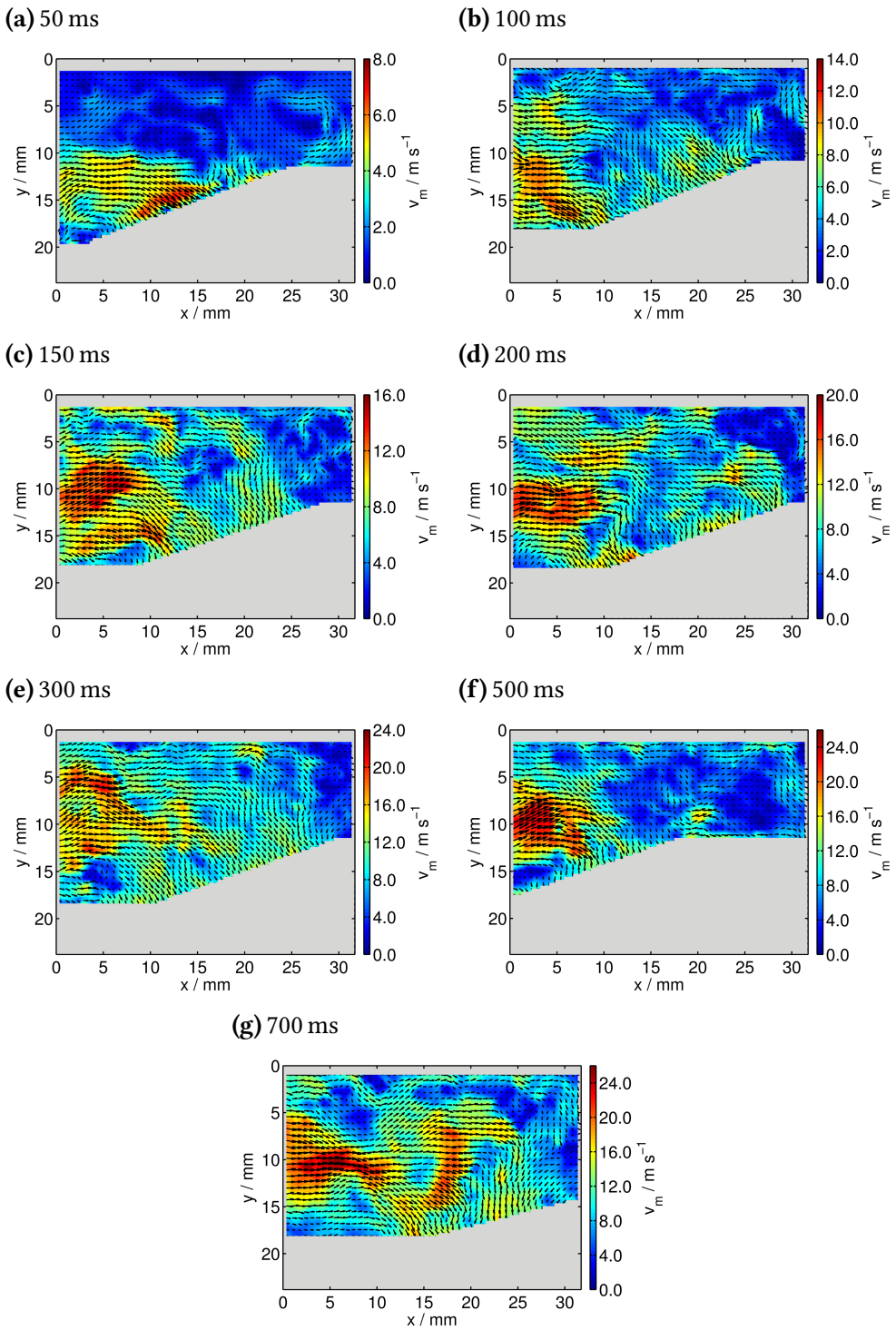

Figure 4.44: Instantaneous velocity fields and velocity magnitude v_{m} obtained between Δt =50 ms and 700 ms after fan start. Every second vector is shown. Insertion depth 3 mm.

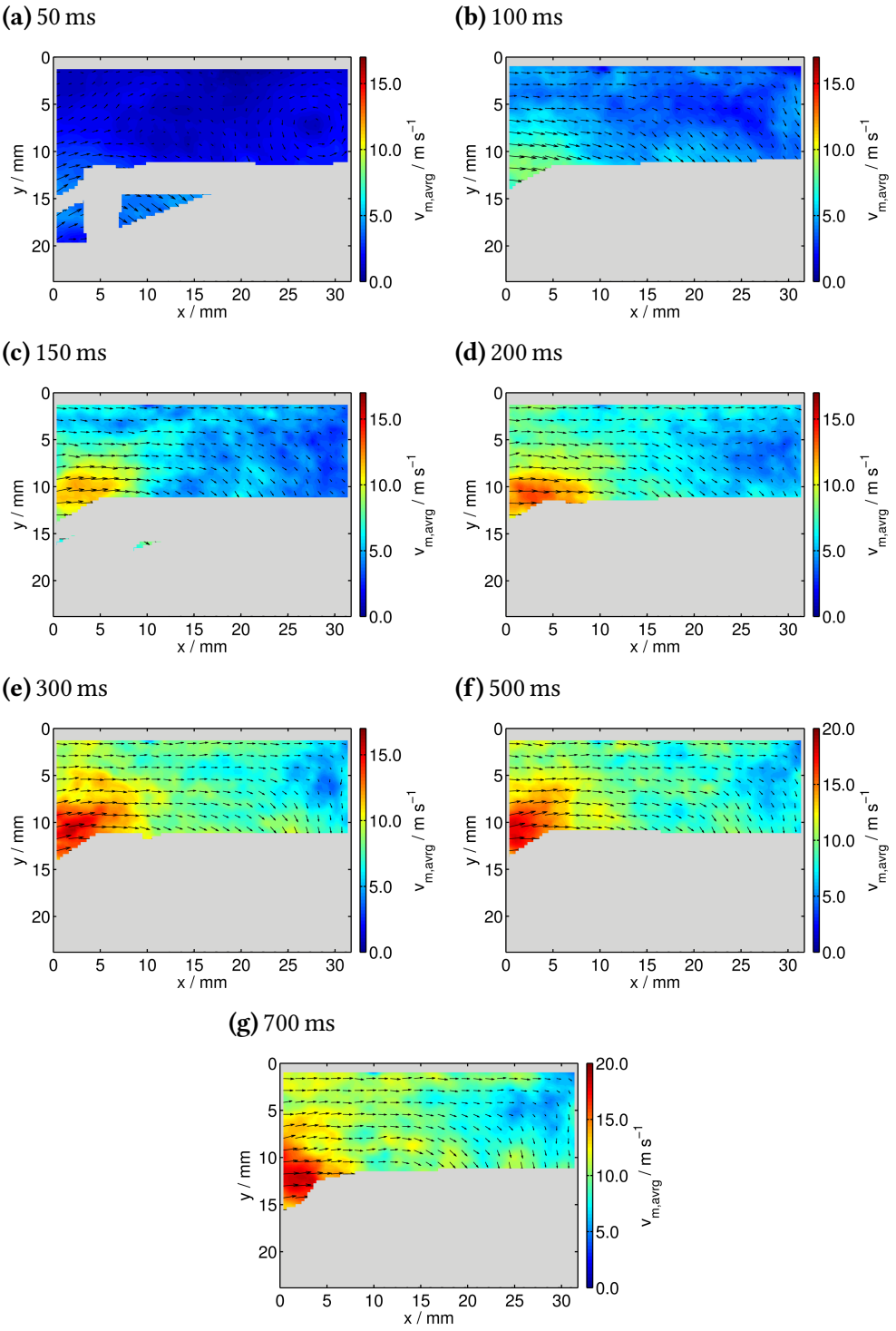

Figure 4.45: Ensemble averaged velocity $v_{\mathrm{m,avrg}}$ between Δt =50 ms and 700 ms after fan start. All images were recorded at a fan insertion depth of 3 mm and a distance of 4 mm in front of the spark electrode. Every 4th vector is shown.

Δt = 50 ms and vanishes afterwards. While the horizontal movement in the left part of the images changes direction at x = 15 mm at an angle of 45° towards the

bottom, a horizontally moving boundary layer at the top of the cylinder head with a thickness of d = 4 mm persists.

4.3.1.5 Velocity fields at 0 mm fan insertion depth

The instantaneous flow field at the minimum insertion depth of d = 0 mm is similar to the measurements performed at d = 3 mm. At Δt = 50 ms (Figure 4.46), the CCW rotating vortex can be found in the upper right corner. Again, the velocity at the center is significantly lower compared to its edge. In the center, the fluid movement is approaching 0 m s^{-1}, while the maximum velocity at the outer edge is slightly above 3.0 m s^{-1}. This feature is pronounced at the lower part of the vortex, which is connected to the 45° flow structure behind the fan blade. The fluid in this areas reaches a maximum velocity of v_{max} = 8.0 m s^{-1}. The area around the spark plug shows fluid movement with velocities up to 4.0 m s^{-1}.

At Δt = 100 ms, the CCW vortex starts to disappear and the maximum velocity of the flow behind the fan blade increases to v_{max} = 16 m s^{-1}. This also leads to a steep increase of the velocity around to spark plug, where v_m is enhanced by a factor of two. The areas of lowest fluid movement are usually located in the upper right and lower left corner. In the lower left corner, which is at the same level as the lower tip of the blade, the velocity in horizontal and vertical direction is below 8.0 m s^{-1}.

As can be seen from higher fan delay times, the maximum velocity increases significantly until Δt = 500 ms. Here, the highest observed velocity can be as high as v_{max} = 36 m s^{-1}. While these velocities can be found at the level of the fan, the area around the spark plug also shows a strong increase in velocity for Δt > 300 ms. As can be seen at Δt = 200 ms in Figure 4.46d, small pockets of slow moving particles (v_m < 8 m s^{-1}) remain at x = 15 mm / y < 5 mm. This behavior changes drastically for all higher delay times, as the velocity in this area increases to v_m > 20 m s^{-1} and can be as high as 26 m s^{-1} at Δt > 400 ms.

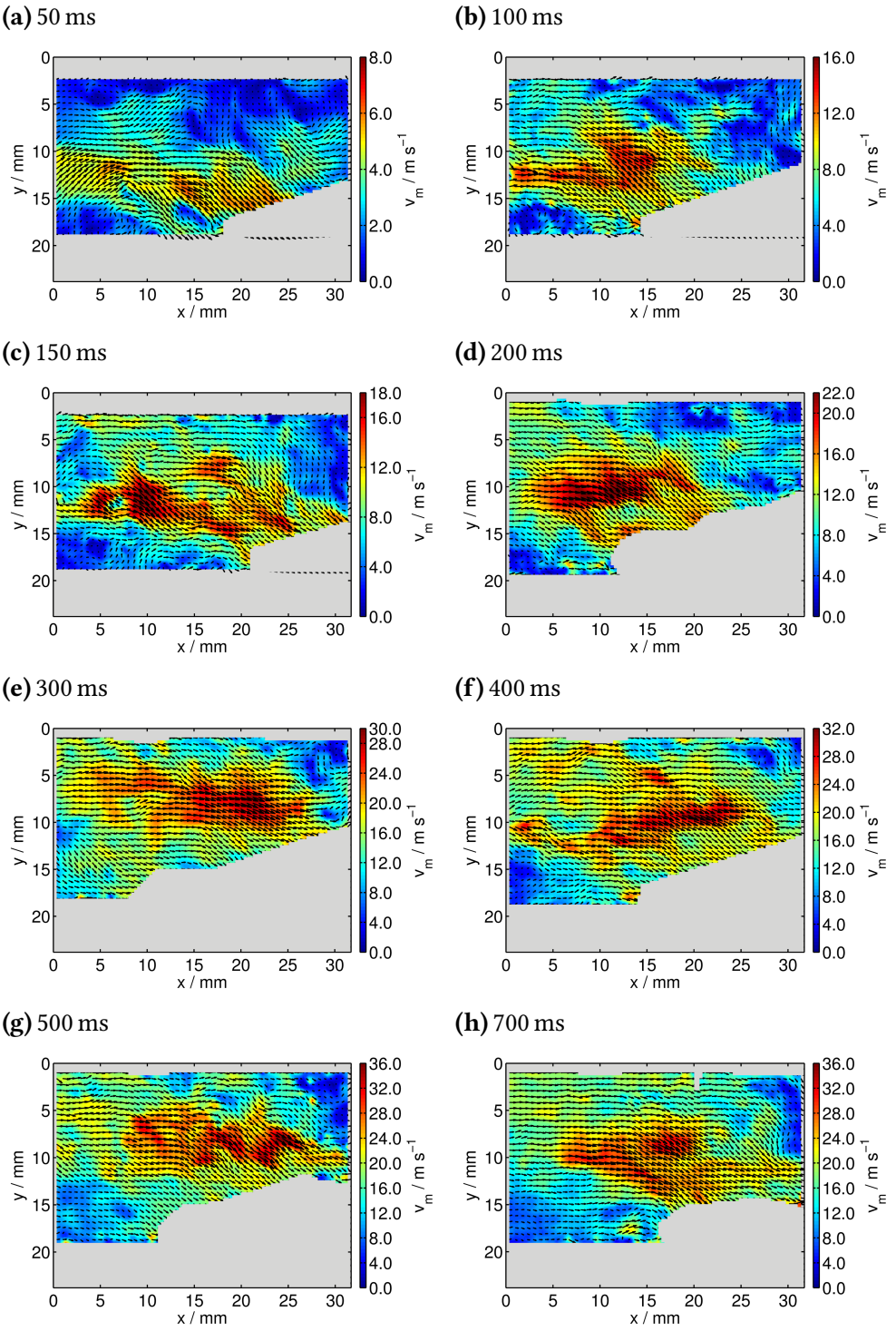

Figure 4.46: Instantaneous velocity fields and velocity magnitude v_m obtained between Δt =50 ms and 700 ms after fan start. Every second vector is shown. Insertion depth 0 mm.

In comparison to the maximum insertion depth of d = 9 mm, the general flow pattern shows some distinctive differences for lower insertion depths, especially for fan running times above Δt = 50 ms. Nevertheless, the measurements clearly demonstrate the evolution of the counter-clockwise rotating vortex in the upper

right corner. The fan movement towards the right pushes the fluid in front of it towards the upper right, while the fluid behind is dragged in direction of the fan movement towards the blade surface, as seen in Figure 4.44a. This creates a strong velocity gradient in the area above the surface and the previously upward moving fluid is sucked downwards. Due to the overall increased velocity at higher insertion depths, the vortex disappears for fan running times longer than Δt = 100 ms. As expected, the areas of higher velocity, which can be found slightly above the level of the fan blades, move upwards with a decrease of insertion depth. This leads to a significant increase of fluid velocity around the spark plug from $v_{\mathrm{m}} \approx 16\,\mathrm{m\,s^{-1}}$ to $v_{\mathrm{m}} \approx 26\,\mathrm{m\,s^{-1}}$, as shown in the instantaneous velocity fields recorded at Δt = 700 ms and insertion depths of 9 mm and 0 mm, respectively.

While not enough measurements were available for a sufficient calculation of the turbulent fluctuation u', it can be assumed that the overall higher velocity results in an increase of u' around the spark area as well. As mentioned in the last Section, a further increase of turbulence promotes the crossing of the transition regime towards the well stirred reaction as well as flame quenching, which appeared more frequently for lower insertion depths.

4.3.2 PIV measurements at the tip of the spark electrode

Due to the three-dimensionality of the flow, instantaneous velocity fields were also recorded directly in front of the spark electrode tip. The light sheet passed the chamber 4 mm further inside compared to the last measurement plane, as shown in Figure 3.23. The ensemble averaged velocity fields for three fan starting times (Δt = 150 ms, 200 ms and 500 ms) for all three insertion depths are shown in Figures 4.47, 4.48 and 4.49.

The position of the spark electrode is visible in all images, which is usually the area with the lowest calculated velocity. The majority of the recorded image pairs suffer from poor data quality at the lower spark electrode due to scattered light. This effect becomes particularly obvious at the ensemble averaged flow fields. Nevertheless, a small amount of instantaneous velocity fields with sufficient quality could be measured and gave insights into the flow between the electrodes. These images were also pre-evaluated by eye to estimate the flow and thus validate the calculated flow pattern. All averaged velocity fields are shown together with a representative instantaneous field.

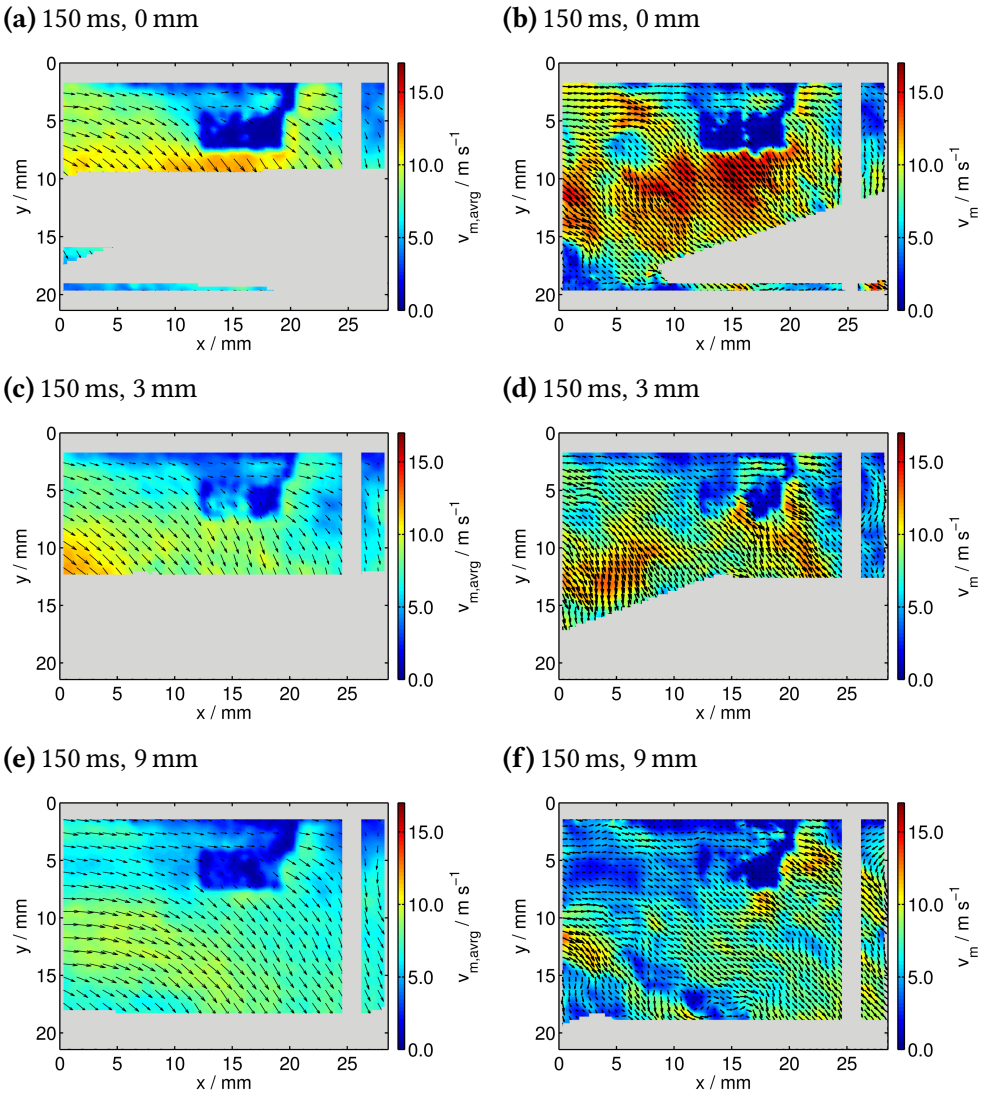

Figure 4.47: Ensemble averaged velocity fields (**(a)**, **(c)**, **(e)**) and instantaneous fields (**(b)**, **(d)**, **(f)**) at fan delay time $\Delta t = 150$ ms. Velocity fields are recorded for three insertion depths at $d = 0$ mm, 3 mm and 9 mm. Every fourth vector is shown for the averaged fields, every second for the instantaneous.

At $\Delta t = 150$ ms, the velocity magnitude follows the same trend seen for the first measurement plane. The ensemble averaged velocity around the cylinder head is usually the highest at minimum insertion depth (Figure 4.47). The magnitude right below the electrode reaches a maximum value of $v_{\max} \approx 12\,\mathrm{m\,s^{-1}}$ and decreases to $10\,\mathrm{m\,s^{-1}}$ and $8\,\mathrm{m\,s^{-1}}$ for $d = 3$ mm and 0 mm, respectively. Common for all insertion depths is a horizontal moving boundary layer between the spark electrodes. Below the electrodes, the vertical velocity component of the flow increases and dominates the right sector of the observation window. Figure 4.47c is a rare example of a reliable image for the flow at the electrode. It can be seen that the flow changed

direction at the electrode itself. A u_y component is visible over the the surface of the electrode around x = 15 mm / y = 7 mm.

At Δt = 200 ms (Figure 4.48), the average velocity increases further. Again, the highest velocities can be observed at the lowest insertion depth. Below the electrode, the fluid moves with a velocity of $v_{max} \approx 15\ m\ s^{-1}$. The velocity decreases to 13 m s^{-1} at d = 3 mm. At 9 mm, the highest average velocity below the electrode is slightly above 10 m s^{-1}. The instantaneous fields also show the general trends seen in the averaged images, where the highest velocities occur at the level of the fan blades. Nevertheless, while the areas of high velocity are often connected throughout the observation window, a broken zone can be found in Figure 4.48f, which corresponds to the maximum insertion depth. Here, the fast moving fluid in the lower left sector is adjacent to an area with velocities below 5 m s^{-1} centered at x = 16 mm / y = 13 mm. Above, the velocity increases again strongly to 15 m s^{-1} bordering to the spark electrode.

At Δt = 500 ms, the average velocity below the spark plug at minimum insertion increases to $v_{max} \approx 25\ m\ s^{-1}$ directly below the spark electrode. At d = 3 mm, the maximum velocity can be found in the left part of the image and decreases in horizontal direction from $v_{max} \approx 20\ m\ s^{-1}$ in the left area to $v_{max} \approx 15\ m\ s^{-1}$ in the area around the spark electrode. At the maximum insertion, areas of high velocity with $v_{max} \approx 14\ m\ s^{-1}$ are usually found in the left sector as well, but remain at 13 m s^{-1} in the area next to the CCW vortex in the right corner. As seen for the other measurement plane, this is the only insertion depth where the vortex is visible at high fan delay times. The same velocity distribution can also be found in the instantaneous velocity fields.

In contrast to the ensemble averaging, the instantaneous velocity fields show some similarities of the flow velocity at the right edge of the spark electrode around x = 20 mm. In all images, a fast velocity component above 10 m s^{-1} can be found, which is significantly higher compared to the flow in front of the electrode (x < 13 mm). In Figure 4.47d, this high velocity component can also be found on and above the electrode. The velocity changes within a distance of 3 mm from 7 m s^{-1} to 13 m s^{-1}.

The velocity fields measured at the tip of the lower spark electrode confirm the general trends obtained from the first measurement plane. The decrease of insertion depth leads to a significant increase of fluid velocity around the electrodes. Despite the reduced data quality at the spark electrodes, the splitting of the flow at the spark plug becomes apparent. This was also observed in the LIF and chemiluminescence measurements, where parts of the flame stayed below the cylinder head moving to the right, while the flame kernel below the spark electrodes expanded towards the bottom right. Despite the different blade positions for images recored for the

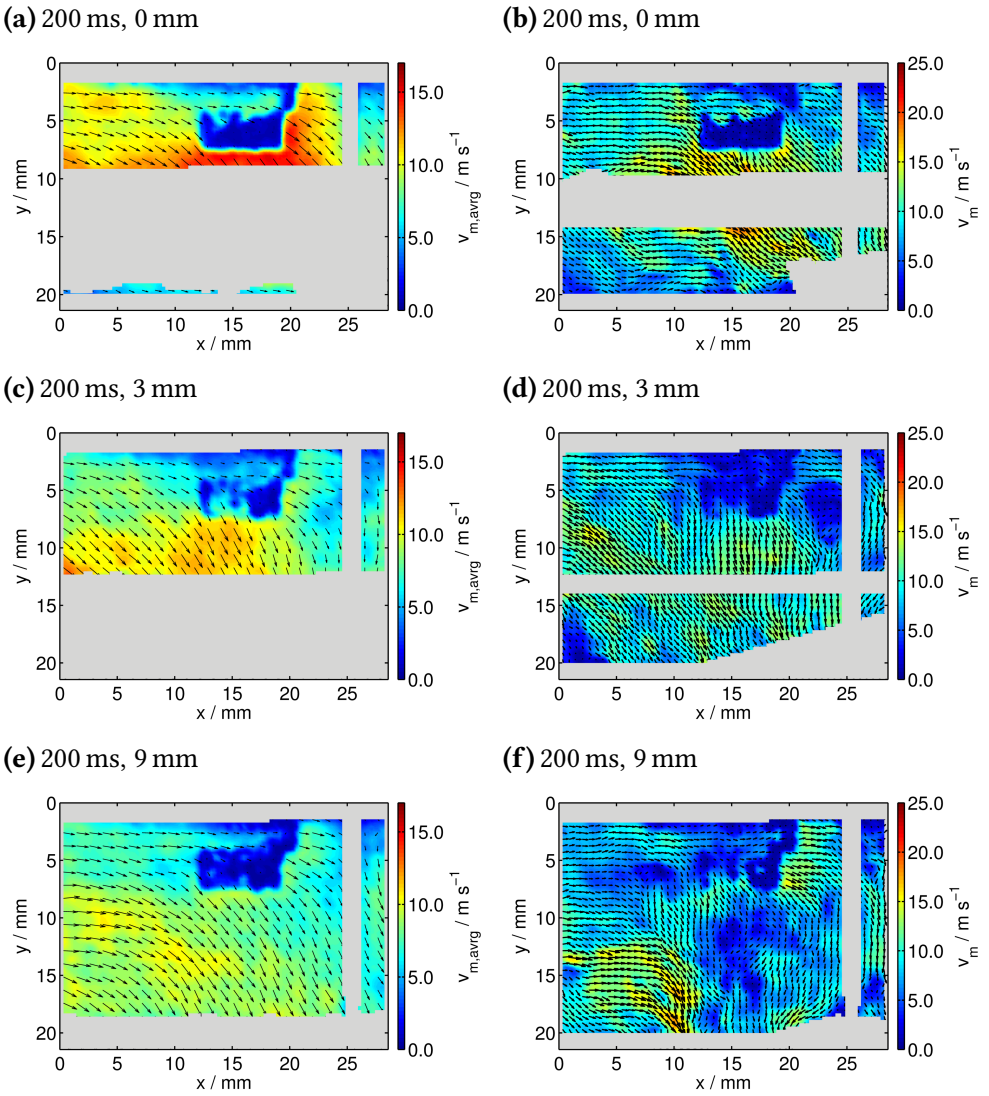

Figure 4.48: Ensemble averaged velocity fields (**(a)**, **(c)**, **(e)**) and instantaneous fields (**(b)**, **(d)**, **(f)**) at fan delay time $\Delta t = 200$ ms. Velocity fields are recorded for three insertion depths at $d = 0$ mm, 3 mm and 9 mm. Every fourth vector is shown for the averaged fields, every second for the instantaneous.

same time after fan start, the measurements suggest that averaging of velocity fields even for different fan positions is valid, especially in the region of the spark electrode. The data presented in this Section clearly show the similarity between the two measurement planes and suggest an overall consistent picture for both measurements. Therefore, the calculation of turbulence intensity and integral length scale 4 mm in front of the electrode can be used as reliable parameters for the discussion of the significant flow features in front of the electrode.

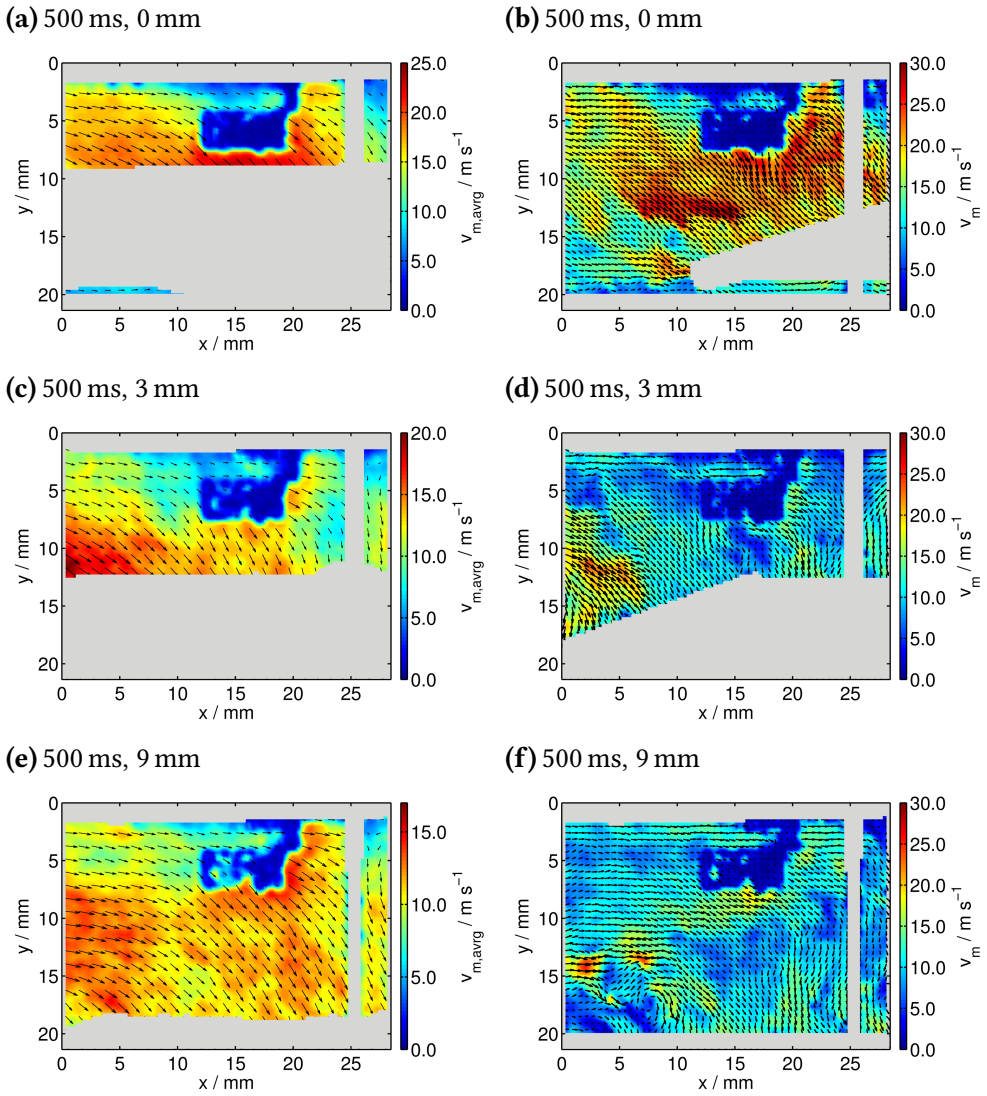

Figure 4.49: Ensemble averaged velocity fields (**(a)**, **(c)**, **(e)**) and instantaneous fields (**(b)**, **(d)**, **(f)**) at fan delay time $\Delta t = 500$ ms. Velocity fields are recorded for three insertion depths at $d = 0$ mm, 3 mm and 9 mm. Every fourth vector is shown for the averaged fields, every second for the instantaneous.

4.3.3 Velocity fields recorded perpendicular to the spark electrodes

Because of the three-dimensionality of the flow, PIV images were also recorded perpendicular to the flow shown in the last section. Due to fan blades appearing directly in the light sheet, most images suffer from high amounts of scattered light. Hence, only a small number of image pairs at different conditions were recorded and rough trends of the flow field will be presented.

Instantaneous velocity fields are shown in Figure 4.50 at Δt = 100 ms and 500 ms for insertion depths of 0 mm **(a)** and 9 mm (**b**–**d**). At 100 ms and d = 0 mm, the flow field is dominated by a strong clockwise rotation up to x = 8 mm and y = 17 mm, which also marks the vertical position of the fan tip. This area has the highest velocity magnitude with up to v_m = 8.0 m s^{-1}. The lowest velocity is generally observed under the fan blade. The particles move horizontally towards the left with a velocity below v_m < 2.0 m s^{-1}. Apart from the CW vortex and the area under the blade, the movement is directed towards the center of the chamber. Between the cylinder head and y = 5 mm, the boundary layer lacks a vertical velocity component. Directly below the spark electrode at x = 11 mm and y = 6 mm, the flows starts to move downwards with an initially high velocity that decreases to 2.0 m s^{-1}.

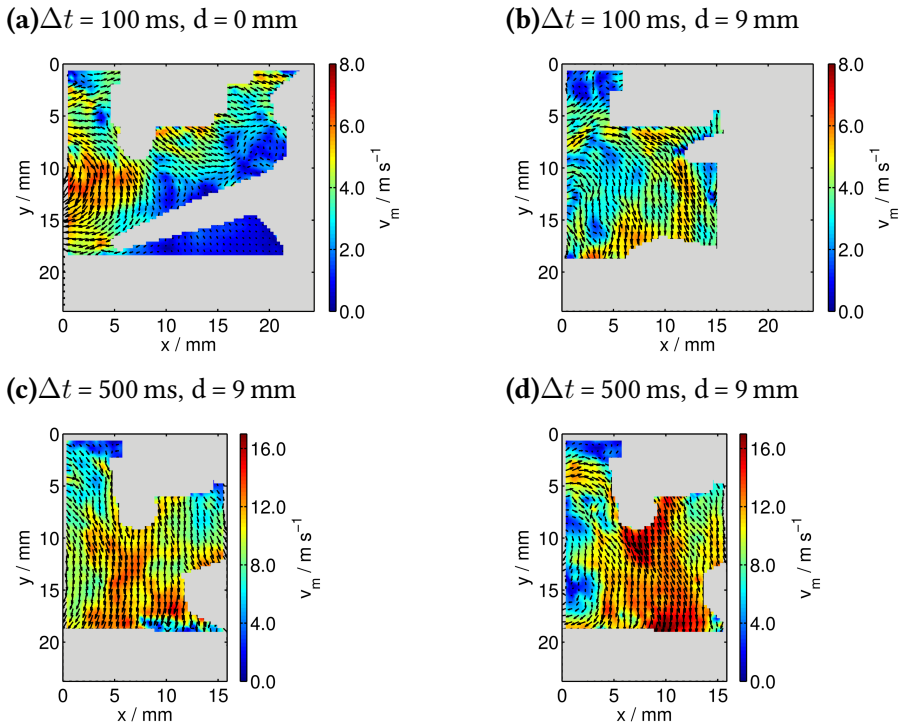

Figure 4.50: Instantaneous velocity fields recorded perpendicular to the main observation axis at **(a)** Δt = 100 ms, d = 0 mm, **(b)** Δt = 100 ms, d = 9 mm and (**c,d**) Δt = 500 ms, d = 9 mm.

At the maximum insertion depth, d = 9 mm, the flow exhibits similar features. The left area of the image shows a clockwise rotating feature that expands towards x = 15 mm. The boundary layer until x = 5 mm is not clearly visible due to light scattered by the metal housing of the fan. The overall velocity is again lower compared to the top position of the fan. While the fluid below the spark plug shows horizontal and vertical movement, the flow below x = 10 mm lacks the u_x velocity component. The overall flow pattern does not change for longer times after fan start. At Δt = 500 ms, the flow consists mainly of vertical movement. The

highest velocities can be observed below the spark electrode and in vicinity of the fan blades. Here, the velocity increases to $v_m > 15.0\ m\ s^{-1}$.

The ensemble-averaged velocity fields at $\Delta t = 100$ ms for both insertion depth and the associated vorticity are shown in Figure 4.51. For both insertion depths, the highest velocity magnitudes can be found at the tip of the fan blade. In both cases, the main component is in vertical direction u_y. At higher insertion depths, the velocity at the spark plug is decreased by a factor of two compared to $d = 0$ mm. Both vorticity plots (Figure 4.51b and 4.51d) show similar patterns. The areas of highest vorticity, $\omega > 4000\ s^{-1}$ are located at the top layer of the CW vortex. The vorticity is mostly positive, small patterns in CCW vortices can be found below the spark electrode.

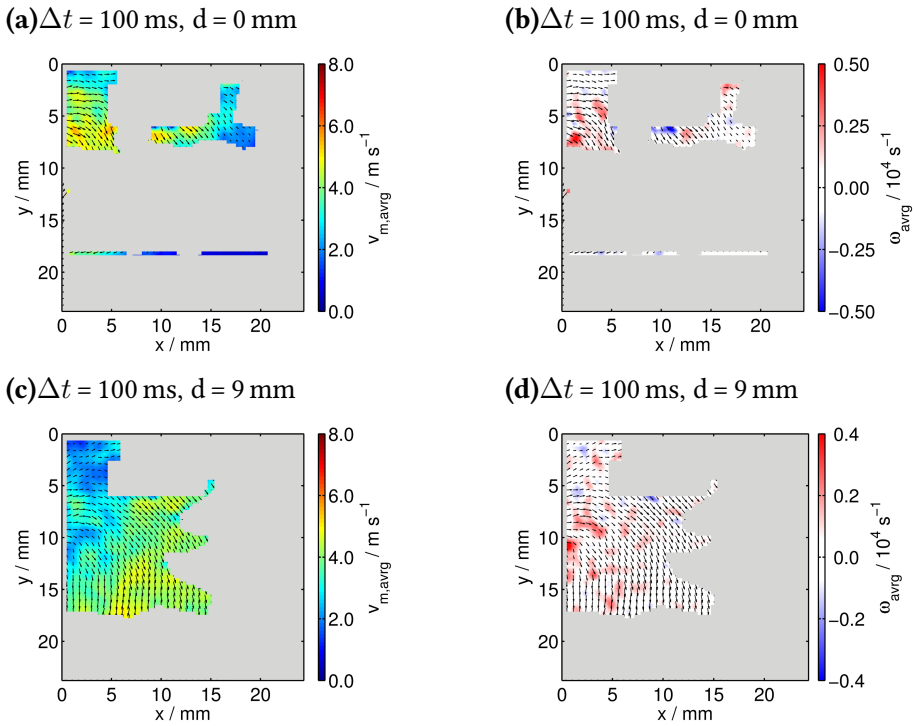

Figure 4.51: **(a)** Average velocity magnitude and **(b)** average vorticity at $\Delta t = 100$ ms, d = 0 mm. **(c)** and **(d)** $\Delta t = 100$ ms, d = 9 mm.

At $\Delta t = 500$ ms (Figure 4.52), the highest average velocity for $d = 0$ mm can be found in the region of the spark plug. Here, the maximum of $v_m > 14.0\ m\ s^{-1}$ appears directly below the spark plug and decreases strongly towards the center of the chamber. The flow pattern is identical to the one observed for a lower fan starting time $\Delta t = 100$ ms. The vorticity in the vicinity of the spark is still predominantly positive, while CCW rotating vortices can be found at areas of slower moving fluid at $x > 15$ mm.

At the maximum insertion, the flow pattern also is comparable to $\Delta t = 100$ ms. The velocity below the spark plug is drastically higher ($v_m > 10.0\ m\ s^{-1}$) compared to

the area above the lower electrode. Here, the flow tends to move strictly horizontal with a relatively small velocity, $v_{\mathrm{m}} < 5.0\ \mathrm{m\,s^{-1}}$. As seen in case of minimum insertion, the vorticity is mainly positive and frequent at the left part of the image. Below the spark electrode, the vorticity is close to zero.

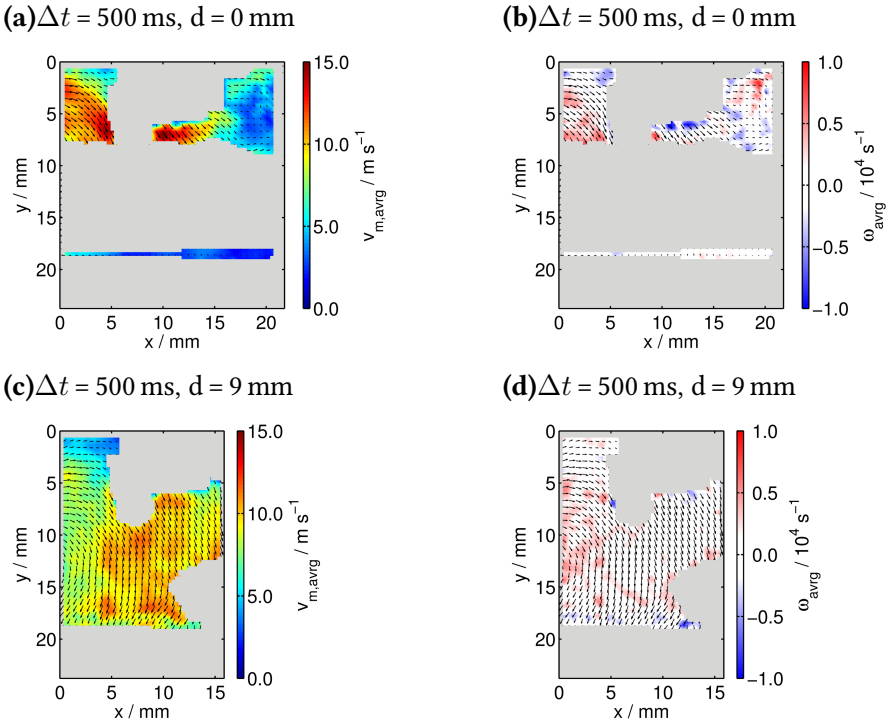

Figure 4.52: **(a)** Average velocity magnitude and **(b)** average vorticity at $\Delta t = 500$ ms, d = 0 mm. **(c)** and **(d)** $\Delta t = 500$ ms, d = 9 mm.

The overall results obtained at this measurement plane can be discussed and summarized as follows: A recurring observation for the second measurement plane of the flow is again a decrease of flow velocity with an increase of insertion depth. The effect is less pronounced, as in this observation plane the u_{x} velocity is the main flow component, which is less affected by the movement of the fan.

As seen in the vorticity plots, the eddy size is comparable to the eddies observed in the first plane and hence indicates similar integral length scales. The increase in flow velocity is also accompanied by an increase of vorticity, which on average has a positive sign. This is caused by a predominantly clockwise moving main flow. The rare CCW vortices appear around the spark electrode and thus most likely are due to bad vectors caused by the poor data quality around reflecting surfaces.

Due to the large blade surface, the flow velocity is relatively constant above the blades towards the center of the chamber. A significant velocity gradient appears primarily in front of the spark electrode towards the outer chamber wall and in the upper left corner. The latter effect is likely caused by the lower spark electrode acting as a shield, which prohibits the strong flow movement towards the center.

This effect is diminished for lower insertion depths due to the small gap between fan and cylinder head, similar to the other measurement planes.

Nevertheless, the horizontal velocity between chamber wall and tip of the spark electrode at x = 5 mm tends to be slower compared to the inside, which might affect the interpretation of the data presented in Section 4.3.1.1. The perpendicular measurements were performed along this slower moving area and thus cannot provide the exact flow field and turbulent conditions at the origin of the flame kernel growth. Due to the unknown inward velocity between the electrodes, it can only be assumed that the turbulence is increased, since the velocity below the electrode is significantly higher compared to the left area.

The strong horizontal flow movement around the spark electrodes enhances the substandard data quality due to low contrast at the reflective surfaces seen in Section 4.3.2. Most of the covered imaging area lacks the inward directed u_x component, resulting in a nearly ideal two-dimensional flow, while particles moving out of the observation plane enhance the amount of bad vectors during the cross-correlation calculations.

Despite the partly vague data, the combined measurement planes of the flow field resemble the movement of the flame very well. As shown in the chemiluminescence images (e.g., Fig. 4.23i), the flame front sometimes appears behind the spark electrodes and then starts to expand downwards. This is caused by the displacement attributed to the inward motion of the flow. The flame then is dragged by the flow and moves through the chamber in a spiral-like motion towards the bottom, which corresponds the flame movement seen in Figure 4.25.

Conclusion and Outlook 5

During the work of this Thesis, the combustion behavior of a gas-fueled one-cylinder internal combustion engine used in a commercially available nail gun (*BeA Gasnagler*) was analyzed. The main focus was laid on the difference in combustion under both laminar and turbulent combustion, the latter induced by a small electrical fan located in the top of the cylinder head, and for different fuel compositions, consisting of either propane-air or propene/1-butene-air. The results for turbulent combustion were investigated for flame quenching effects, as a strong decrease of ignition probability of premixed propane-air fuels was found for fan starting times longer than Δt_{fan} = -250 ms ignition, corresponding to a fan speed of $u_{\mathrm{fan}} \approx 10000$ rm and a Reynolds number of $Re \approx 40000$. This effect could not be observed for the unsaturated fuel, which was externally injected using pre-filled cartridges.

5.1 Experimental setup

A major part of the present Thesis was the design and setup of the required optical and electronic detection systems as well as the re-design of the engine electronics and housing for their implementation in the experimental systems. All measurements were done under single-shot conditions and thus required reliable reproducibility. For the reliable synchronization between engine and detection systems and decrease of spark-induced interference signals, the original spark ignition-, trigger-, and fan control electronic was galvanically separated. The modular approach of the control systems allows for a quick change of the components and conversion between the detection systems. The fan and camera timings with regard to the onset of the spark discharge can be controlled using the trigger box.

The combustion behavior was analyzed using the pressure profile inside the chamber, recorded by a piezo pressure transducer located in the top corner of the engine housing, and the piston velocity, measured by a light barrier. For a deeper understanding of the turbulence-flame interaction, the flame front was recorded using the chemiluminescence imaging technique, which provides a simple and straightforward approach for optical flame analysis.

For a more detailed investigation, a laser-induced fluorescence (LIF) setup was built. Here, the fluorescence of OH radicals, which appear abundant in the post-flame gases, was used as flame front markers. The LIF setup consists of a

Nd:YAG pumped dye laser probing the OH fluorescence at the $Q_1(6)$ band around $\lambda = 283.01$ nm and an ICCD camera for the detection at $\lambda = 314$ nm. Due to the thin light sheet of the LIF apparatus, a nearly two-dimensional cut through the expanding flame front could be realized.

For the correlation between turbulence induced by the fan movement and flame expansion mechanisms, the flow velocity was investigated using a two-dimensional particle image velocimetry (PIV) system. The PIV system was established by overlapping two separate Nd:YAG laser beams, whose delay timing can be easily adjusted using an external delay generator, and a dual-frame camera to record the scattered light of solid-particle aerosols introduced into the flow field. The PIV setup was used in single shot modus but in principle can be operated with a maximum repetition rate of 10 Hz, limited by the laser system and camera exposure time. Although the beam path of the PIV setup is fixed, the small form factor and the resulting mobility of the engine allow access to two perpendicular placed measurement planes. These were chosen to capture all three velocity components of the flow.

5.2 Laminar and turbulent combustion

The pressure measurements showed a strong increase of maximum pressure and pressure rise time by implementation of obstacles in the chamber. The combustion behavior was even more increased under turbulent conditions induced by the movement of the fan. Table 5.1 gives an overview of the most important parameters for the three investigated conditions.

In comparison to pre-mixed propane-air fuel mixtures, externally injected propene/1-butene fuel could be ignited independently from the time of fan start before ignition. For the propane fuels, the stability limits were highly dependent on the fuel-to-air ratio ϕ. The ignition probability for rich mixtures ($\phi \approx 1.2$, 5 Vol%) dropped at Δt_{fan} = -400 ms, for leaner and richer mixtures the ignitions limits were reduced to shorter times. The implementation of a second spark to initiate two simultaneous flame kernels improved the combustion under laminar conditions, but had no effect under fan-induced turbulence.

The chemiluminescence and LIF measurements revealed a hemi-spherical flame expansion for laminar conditions, while for the combustion with obstacle and even more important under turbulent conditions the flame is severely wrinkled. The increased flame surface enhances the burning velocity, which was seen in the pressure-measurements. For higher fan running times, the flame front was locally

Table 5.1: Maximum pressure $\Delta p_{\max}$, maximum pressure time $t\,(\Delta p_{\max})$, maximum piston velocity $v_{\max}$ and rate of pressure rise ($\mathrm{d}p/\mathrm{d}t$) for different combustion conditions. Turbulent combustion was recorded with a fan insertion depth of d_{i} = 0.9 cm, the parameters for the combustion using obstacles are shown for the highest combustion enhancement at d_{i} = 2.5 cm.

	turbulent d_{i} = 0.9 cm	obstacle d_{i} = 2.5 cm	laminar no obstacle
$\Delta p_{\max}$	5.0 bar	2.5 bar	1.5 bar
$t\,(\Delta p_{\max})$	7 ms	14 ms	20 ms
$v_{\max}$	130 km h^{-1}	79 km h^{-1}	61 km h^{-1}
$(\mathrm{d}p/\mathrm{d}t)$	1300 bar s^{-1}	360 bar s^{-1}	120 bar s^{-1}

broken up due to turbulence. The flame follows the movement of the flame and travels in a spiral-like trajectory through the chamber.

The combustion behavior and phenomena seen in the pressure-time traces and flame front images are in good agreement with the results of the PIV measurements. Several possible fluid-dynamical mechanisms for the flame expansion and increase of burning rate were found, which can be responsible for the combustion enhancement:

i Elongation of the flame for low turbulence and short fan running times ($\Delta t_{\mathrm{fan}} \leq$ -50 ms).

ii Penetration of big vortices into the area of flame kernel stabilization ($\Delta t_{\mathrm{fan}} \geq$ -50 ms).

iii Decrease of vortex size and increase of counter-rotating vortices, which induce flame strain.

iv Increased flame surface due to inhomogeneous flow field and strain.

v Vortices and inhomogeneous flow field induce a recirculation zone and supply of fresh gas mixtures.

With regard to ignition failures under high turbulent conditions, several reasons for flame quenching can be derived from the turbulent velocity fields. The strong increase of vorticity strains the flame and thus may quench the flame locally. The fan-induced turbulence exceeds the laminar flame velocity of typical hydrocarbon flames by a factor of $u'/u_{\mathrm{l}} \approx 10$, which can increase the required minimum ignition energy to form a self-sustainable flame kernel. In combination with an increase of u', a decrease of the integral length scale l_{t} could be observed. According

to the Borghi classification, the engine operates at the transition regime from the wrinkled flame regime towards the well stirred reactor, as indicated by a Damköhler number close to unity or smaller. Due to the higher laminar flame speed, the propene/1-butene fuel proved to be the more stable fuel in comparison to propane, whose lower laminar flame speed makes the flame expansion more susceptible for turbulent velocity spikes.

5.3 Outlook

While all these results provide a basis for a better understanding of the mechanisms responsible for the increased combustion efficiency and eventual flame quenching due to the fan induced turbulence, a direct prove of the extinction of the flame kernel could not be found. Due to the single shot operation, the amount of flow field data were not sufficient enough for an undisputed calculation of the important flow characteristics, i.e. turbulent velocity and integral length scale. The next step for further improvement would be the redesign of the engine electronics towards a automated fan start/stop, which results a higher repeatability of the PIV measurements. This would also enable the access to a quasi time-resolved measurement during the acceleration phase of the fan.

Time-resolved chemiluminescence and LIF measurement of the flame expansion cannot be realized using the current setup, as one single combustion event is finished after 12 ms. This is much faster than the repetition rate of both the camera and laser systems. Additionally, the automated LIF measurement would require a timed fuel-injection and flushing mechanism to rinse the remaining exhaust gases.

To measure all three velocity components of the flow at the same time, the system could be easily extended by implementing a second camera. The system would operate according to the so-called stereoscopic principle similar to the human eye and enables the identification of transverse velocities, which are known to exist from the two measurement planes investigated in this Thesis.[229–231]

A combination of LIF measurements for CH_2O and OH can provide the direct observation of the heat release rate during the flame expansion and would only require a second camera, as the already present Nd:YAG laser could be easily converted to $\lambda = 355$ nm.

Literature

[1] U.S. Energy Information Administration (EIA), „Total Primary Energy Consumption“, http://www.eia.gov/cfapps/ipdbproject/IEDIndex3.cfm?tid=44&pid=44&aid=2 (accessed May 12, 2016), **2012**.

[2] Bundesministerium für Wirtschaft und Energie (BMWi), „Energiedaten: Gesamtausgabe“, http://bmwi.de/DE/Themen/Energie/Energiedaten-und-analysen/Energiedaten/gesamtausgabe,did=476134.html, (accessed May 12, 2016), **2016**.

[3] European Climate Foundation (ECF), „Roadmap 2050 “, http://www.roadmap2050.eu/, (accessed May 12, 2016).

[4] European Commission, „Road transport: Reducing CO_2 emissions from vehicles“, http://ec.europa.eu/clima/policies/transport/vehicles/index_en.htm (accessed May 12, 2016), **2016**.

[5] European Commision, „Reducing CO_2 emissions from Heavy-Duty Vehicles “, http://ec.europa.eu/clima/policies/transport/vehicles/heavy/index_en.htm (accessed May 12, 2016), **2016**.

[6] eurostat, „Greenhouse gas emission statistics “, http://ec.europa.eu/eurostat/statistics-explained/index.php/Greenhouse_gas_emission_statistics (accessed May 12, 2016), **2015**.

[7] Bundesministerium für Wirtschaft und Energie (BMWi), „Die Energie der Zukunft - Erster Fortschrittsbericht zur Energiewende“, http://www.bmwi.de/DE/Mediathek/publikationen,did=672424.html (accessed May 10, 2016), **2014**.

[8] J. Turner, A. Popplewell, R. Patel, et al., „Ultra Boost for Economy: Extending the Limits of Extreme Engine Downsizing“, *SAE Int. J. Engines* **2014**, *7*, 387–417.

[9] „Downsizing lohnt sich nur begrenzt“, http://www.auto-motor-und-sport.de/news/downsizing-lohnt-sich-nur-begrenzt-auch-kleine-motoren-sind-durstig-4969466.html (accessed May 12, 2016), **2012**.

[10] B. Schmitt, „Dieselgate At GM? Defeat Devices Claimed To Be Found In Opel Cars“, http://www.forbes.com/sites/bertelschmitt/2016/05/12/dieselgate-at-gm-report-finds-defeat-devices-in-opel-cars/ (accessed May 12, **2016**.

[11] M. Rosenbach, G. Traufetter, „Modell Zafira: Experten weisen Opel weitere Abgasmanipulationen nach“, http://www.spiegel.de/auto/aktuell/opel-experten-finden-weitere-abschalteinrichtungen-a-1091959.html (accessed May 12, 2016), **2016**.

[12] „Manipulierte Verbrauchswerte: Mitsubishi hat bei fast allen Modellen betrogen“, http://www.spiegel.de/auto/aktuell/mitsubishi-hat-bei-fast-allen-modellen-betrogen-a-1091795.html (Accessed May 12, 2016), **2016**.

[13] R. D. Reitza, G. Duraisamy, „Review of high efficiency and clean reactivity controlled compression ignition (RCCI) combustion in internal combustion engines“, *Prog. Energy Combust. Sci.* **2015**, *46*, 12–71.

[14] K. Verbiezen, A. Donkerbroek, A. van Vliet, W. Meerts, R. Klein-Douwel, N. Dam, J. ter Meulen in Proceedings of the European Combustion Meeting, Orleans, **2003**, paper 88–1/6.

[15] M. Nikolich, Combustion gas powered fastener driving tool, US Patent 4,403,722, **1983**.

[16] „Combustion gas powered fastener driving tool, US 4403722, forward citations“, https://www.google.com/patents/US4403722#forward-citations (accessed May 18, 2016), **2016**.

[17] „Haftennagler R35-654E Produktblatt “, http://www.bea-group.com/bea/katalogdownloads/12100589-DE-Productsheet.pdf (accessed May 12, 2016).

[18] A. G. Gaydon, H. G. Wolfhard, *Flames, Their Structure, Radiation, and Temperature*, Fourth Edition, Chapman & Hall Ltd., London, **1979**.

[19] J. A. Barnard, J. N. Bradley, *Flame and combustion*, Chapman and Hall, London, New York, **1984**.

[20] F. A. Williams, *Combustion Theory*, Second Edition, The Benjamin/Cummings Publishing Company, Inc., Menlo Park, **1985**.

[21] J. C. Jones, *Combustion Science: Principles and Practice*, Millennium Books, Newtown, **1993**.

[22] *Handbuch des Explosionsschutzes*, (Ed.: H. Steen), Wiley-VCH, Weinheim, **2000**.

[23] J. Warnatz, U. Maas, R. W. Dibble, *Combustion - Physical and Chemical Fundamentals, Modeling and Simulation, Experiments, Pollutant Formation*, Fourth Edition, Springer-Verlag Berlin Heidelberg, **2006**.

[24] I. Glassman, R. A. Yetter, *Combustion*, Elsevier, **2008**.

[25] S. McAllister, J.-Y. Chen, A. C. Fernandez-Pello, *Fundamentals of Combustion Processes*, Springer-Verlag New York, **2011**.

[26] J. Warnatz, „The Structure of laminar alkane-, alkene-, and acetylene flames“, *Symp. (Int.) Combust. [Proc.]* **1981**, *18*, 369–384.

[27] J. Warnatz, „Resolution of gas phase and surface combustion chemistry into elementary reactions“, *Symp. (Int.) Combust. [Proc.]* **1992**, *24*, 553–579.

[28] M. Frenklach, H. Wang, „Detailed modeling of soot particle nucleation and growth“, *Symp. (Int.) Combust. [Proc.]* **1991**, *23*, 1559–1566.

[29] S. A. Skeen, H. A. Michelsen, K. R. Wilson, D. M. Popolan, A. Violic, N. Hansen, „Near-threshold photoionization mass spectra of combustion-generated high-molecular-weight soot precursors“, *J. Aerosol Sci.* **2013**, *58*, 86–102.

[30] A. Lipatnikov, *Fundamentals of Premixed Turbulent Combustion*, CRC Press, **2012**.

[31] Y. B. Zeldovich, D. A. Frank-Kamenentsky, „Theory of uniform flame propagation“, *C.R. Acad. Sci. U.R.S.S.* **1938**, *19*, 693–697.

[32] N. N. Semenov, „Thermal theory of combustion and explosion. III. Theory of normal flame propagation“, *Adv. Phys. Sci. Moscow* **1940**, *24*, 433–486.

[33] N. Peters, *Turbulent Combustion*, Cambridge University Press Cambridge, **2004**.

[34] T. Kathrotia, U. Riedel, J. Warnatz in Proceedings of the European Combustion Meeting, **2009**.

[35] A. Gaydon, *The Spectroscopy of Flames*, Springer Netherlands, **1974**.

[36] A. Kvaran, A. H. Haraldsson, T. I. Sigfusson, „Spectroscopy of flames: luminescence spectra of reactive intermediates“, *J. Chem. Educ.* **2000**, *77*, 1345–1347.

[37] R. Maly, M. Vogel, „Initiation and propagation of flame fronts in lean CH_4-air mixtures by the three modes of the ignition spark“, *Symp. (Int.) Combust. [Proc.]* **1979**, *17*, 821–831.

[38] J. B. Heywood, *Internal Combustion Engine Fundamentals*, McGraw-Hill, Inc., **1988**.

[39] *Flow and Combustion in Reciprocating Engines*, (Eds.: C. Arcoumanis, T. Arcoumanis), Springer Berlin Heidelberg, **2009**.

[40] S. Kondo, A. Takahashi, K. Tokuhashi, „Calculation of minimum ignition energy of premixed gases“, *J. Hazard. Mater.* **2003**, *A103*, 11–23.

[41] A. H. Lefebvre, *GAS Turbine Combustion*, CRC Press, **1998**.

[42] B. Lewis, G. von Elbe, *Combustion, Flames and Explosions of Gases*, Academic Press, **1987**.

[43] R. K. Eckhoff, *Explosion Hazards in the Process Industries*, Gulf Publishing Company, Houston, Texas, **2005**.

[44] L. G. Britton, *Avoiding Static Ignition Hazards in Chemical Operations*, American Institute of Chemical Engineers, New York, **1999**.

[45] D. Bradley, F. K.-K. Lung, „Spark Ignition and the early stages of turbulent flame propagation“, *Combust. Flame* **1987**, *69*, 71–93.

[46] C. C. Swett, R. H. Donlon, „Spark Ignition of flowing gases III: Effect of turbulence promoter of energy required to ignite a propane-air mixture“, *NACA Research Memorandum* **1953**, RM E52 – J28.

[47] D. R. Ballal, A. H. Lefebvre, „The influence of flow parameters on minimum ignition energy and quenching distance“, *Symp. (Int.) Combust. [Proc.]* **1975**, *15*, 1473–1481.

[48] D. R. Ballal, A. H. Lefebvre, „Ignition and Flame quenching in flowing gaseous mixtures“, *Proc. R. Soc. Lond. A* **1977**, *357*, 163–181.

[49] H. P. Lenz, *Mixture Formation in Spark-Ignition Engines*, Springer-Verlag Wien-New York and Society of Automotive Engineers, Inc., **1991**.

[50] L. J. Spadaccini, M. B. C. III., „Ignition delay characteristics of methane fuels“, *Prog. Energy Combust. Sci.* **1994**, *20*, 431–460.

[51] J. Hult, U. Meier, W. Meier, A. harvey, C. F. Kaminski, „Experimental analysis of local flame extinction in a turbulent jet diffusion flame by high repetition 2-D laser techniques and multi-scalar measurements“, *Proc. Combust. Inst.* **2005**, *30*, 701–709.

[52] S. F. A. F. S. Ahmed, PhD thesis, University of Cambridge, **2006**.

[53] V. Manente, B. Johansson, W. Cannella, „Gasoline partially premixed combustion, the future of internal combustion engines?“, *Int. J. Engine Res.* **2011**, *12*, 194–208.

[54] R. B. Gupta, *Hydrogen Fuel: Production, Transport, and Storage*, CRC Press, **2008**.

[55] K. L. Cashdollar, I. A. Zlochower, G. M. Green, M. Hertzberg, „Flammability of methane, propane and hydrogen gases“, *J. Loss Prev. Process Ind.* **2000**, *13*, 327–340.

[56] S. Seo, „Combustion instability mechanism of a lean premixed gas turbine combustor“, *KSME International Journal* **2003**, *17*, 906–913.

[57] M. R. Johnson, L. W. Kostiuk, R. K. Cheng, „A ring stabilizer for lean premixed turbulent flames“, *Combust. Flame* **1998**, *114*, 594–596.

[58] L. Yang, V. Franco, A. Campestrini, J. German, P. Mock, NO_x control technologies for EURO 6 diesel passenger cars, tech. rep., International Council on Clean Transportation, **2015**.

[59] N. Rott, „Note on the history of the Reynolds number“, *Annu. Rev. Fluid Mech.* **1990**, *22*, 1–11.

[60] O. Reynolds, „An experimental investigation of the circumstances which determine whether the motion of water shall be direct or sinuous, and of the law of resistance in parallel channels“, *Phil. Trans. R. Soc. Lond.* **1883**, *174*, 935–982.

[61] *Albright's Chemical Engineering Handbook*, (Ed.: L. F. Albright), CRC Press, **2008**.

[62] O. Reynolds, „On the dynamical theory of incompressible viscous fluids and the determination of the criterion“, *Phil. Trans. R. Soc. A* **1895**, *186*, 123–164.

[63] S. D. Pope, *Turbulent Flows*, Cambridge University Press Cambridge, **2000**.

[64] J. Mathieu, J. Scott, *An Introduction to Turbulent Flow*, Cambridge University Press Cambridge, **2000**.

[65] L. F. Richardson, *Weather prediction by numerical process*, Cambridge University Press, **1922**.

[66] A. N. Kolmogorov, „The local structure of turbulence in incompressible viscous fluid for very large reynolds numbers“, *Dokl. Akad. Nauk SSSR* **1941**, *30*, 301–305.

[67] A. N. Kolmogorov, „The local structure of turbulence in incompressible viscous fluids for very large reynolds numbers“, *Proc. R. Soc. Lond. A* **1991**, *434*, 9–13.

[68] G. I. Taylor, „Statistical theory of turbulence“, *Proc. R. Soc. London Ser. A* **1935**, *151*, 421–444.

[69] *Recent Advances in the Aerospace Sciences*, (Ed.: C. Casci), Plenum Press, New York, **1985**.

[70] N. Peters, „The turbulent burning velocity for large-scale and small-scale turbulence“, *J. Fluid Mech.* **1999**, *384*, 107–132.

[71] T. Poinsot, D. Veynante, *Theoretical and Numerical Combustion*, R.T. Edwards, Inc, **2005**.

[72] M. A. Liberman, *Introduction to Physics and Chemistry of Combustion*, Springer-Verlag Berlin Heidelberg, **2008**.

[73] *Turbulent Combustion Modeling*, (Eds.: T. Echekki, E. Mastorakos), Springer Netherlands, **2011**.

[74] J. F. Driscoll, „Turbulent premixed combustion: Flamelet structure and its effect on turbulent burning velocities“, *Prog. Energy Combust. Sci.* **2008**, *34*, 91–134.

[75] W. Thielicke and E. J. Stamhuis, PIVlab - Time-Resolved Digital Particle Image Velocimetry Tool for MATLAB (v. 1.4), http://dx.doi.org/10.6084/m9.figshare.1092508 (2014).

[76] N. Peters, „Laminar flamelet concepts in turbulent combustion“, *Symp. (Int.) Combust. [Proc.]* **1986**, *21*, 1231–1230.

[77] A. M. Steinberg, J. F. Driscoll, „Straining and wrinkling processes during turbulence–premixed flame interaction measured using temporally-resolved diagnostics“, *Combust. Flame* **2009**, *156*, 2285–2306.

[78] Y. Yeh, H. Z. Cummins, „Localized flow measurements with an He-Ne laser spectrometer“, *Appl. Phys. Lett.* **1964**, *4*, 176–178.

[79] Y. Yeh, H. Z. Cummins, „Measurement of localized flow velocities in gases with a laser Doppler flowmeter“, *Appl. Phys. Lett.* **1965**, *7*, 77–78.

[80] L. V. King, „On the convection of heat from small cylinders in a stream of fluid: Determination of the convection constants of small Platinum wires with application to hot-wire anemometry“, *Proc. R. Soc. A* **1914**, *214*, 373–732.

[81] A. C. Eckbreth, *Laser diagnostics for combustion temperature and species*, CRC Press, **1996**.

[82] N. M. Laurendeau, „Temperature measurements by light-scattering methods“, *Prog. Energy Combust. Sci.* **1988**, *14*, 147–170.

[83] K. Kohse-Höinghaus, „Laser techniques for the quantitative detection of reactive intermediates in combustion systems“, *Prog. Energy Combust. Sci.* **1994**, *20*, 203–279.

[84] J. W. Daily, „Laser induced fluorescence spectroscopy in flames“, *Prog. Energy Combust. Sci.* **1997**, *23*, 133–199.

[85] S. W. Allison, W. P. Partridge, *Laser-Induced Fluorescence Imaging*, Encyclopedia of Imaging Science and Technology, **2002**.

[86] C. Schulz, V. Sick, „Tracer-LIF diagnostics: quantitative measurement of fuel concentration, temperature and fuel/air ratio in practical combustion systems“, *Prog. Energy Combust. Sci.* **2005**, *31*, 75–121.

[87] J. Luque and D. R. Crosley, LIFBASE, Database and spectral simulation for diatomic molecules (v.2.1.1), SRI International Report MP-99-009 **1999**.

[88] J. M. Seitzman, R. K. Hanson, „Two-line planar fluorescence for temporally resolved temperature imaging in a reacting supersonic flow over a body“, *Appl. Phys. B* **1993**, *57*, 385–391.

[89] J. Hult, I. S. Burns, C. F. Kaminski, „Two-line atomic fluorescence flame thermometry using diode lasers“, *Proc. Combust. Inst.* **2005**, *30*, 1535–1543.

[90] M. Luong, R. Zhang, C. Schulz, V. Sick, „Toluene laser-induced fluorescence for in-cylinder temperature imaging in internal combustion engines“, *Appl. Phys. B* **2008**, *91*, 669–675.

[91] M. Tanahashi, S. Murakami, G.-M. Choi, Y. Fukuchi, T. Miyauchi, „Simultaneous CH–OH PLIF and stereoscopic PIV measurements of turbulent premixed flames“, *Proc. Combust. Inst.* **2005**, *30*, 1665–1672.

[92] A. Dreizler, S. Lindenmaier, U. Maas, J. Hult, M. Aldén, C. F. Kaminski, „Characterisation of a spark ignition system by planar laser-induced fluorescence of OH at high repetition rates and comparison with chemical kinetic calculations“, *Appl. Phys. B* **2000**, *70*, 287–294.

[93] D. Č Radenović, A. J. A. van Roji, S.-M. Wu, J. J. ter Meulen, D. H. Parker, M. P. J. van der Loo, G. C. Groenenboom, „Predissociation of the $A^2\Sigma^+(v' = 3)$ state of the OH radical“, *Phys. Chem. Chem. Phys.* **2009**, *11*, 4754–4760.

[94] R. Stocker, PhD thesis, Technische Universität München, **2004**.

[95] R. Stocker, Combustion Database, http://www.combustion-database.com, Technische Universität München, 2003.

[96] A. Cessou, U. Meier, D. Stepowski, „Applications of planar laser induced fluorescence in turbulent reacting flows“, *Meas. Sci. Technol.* **2000**, *11*, 887–901.

[97] A. Hoffmann, F. Zimmermann, H. Scharr, S. Krömker, C. Schulz, „Instantaneous three-dimensional visualization of concentration distributions in turbulent flows with crossed-plane laser-induced fluorescence imaging“, *Appl. Phys. B* **2005**, *80*, 125–131.

[98] T. S. Cheng, C.-Y. Wub, C.-P. Chen, Y.-H. Li, Y.-C. Chao, T. Yuan, T. S. Leu, „Detailed measurement and assessment of laminar hydrogen jet diffusion flames“, *Combust. Flame* **2006**, *146*, 268–282.

[99] H. Becker, A. Arnold, R. Suntz, P. Monkhous, J. Wolfrum, R. Maly, W. Pfister, „Investigation of flame structure and burning behaviour in an IC engine simulator by 2D-LIF of OH radicals“, *Appl. Phys. B* **1990**, *50*, 473–478.

[100] R. Collin, J. Nygren, M. Richter, M. Aldén, L. Hildingsson, B. Johansoon, „Simultaneous OH- and Formaldehyde-LIF Measurements in an HCCI Engine“, *SAE Transactions Journal of Fuels and Lubricants* **2003**, *112*, 2479–2486.

[101] P. G. Aleiferis, M. F. Rosati, „Flame chemiluminescence and OH LIF imaging in a hydrogen-fuelled spark-ignition engine“, *Int. J. Hydrogen Energy* **2012**, *37*, 1797–1812.

[102] A. Arnold, R. Bombach, B. Käppeli, A. Schlegel, „Quantitative measurements of OH concentration fields by two-dimensional laser-induced fluorescence“, *Appl. Phys. B* **1997**, *64*, 579–583.

[103] B. Atakan, J. Heinze, U. E. Meier, „OH laser-induced fluorescence at high pressure: spectroscopic and two-dimensional measurements exciting the A-X (1,0) transitions“, *Appl. Phys. B* **1997**, *64*, 585–591.

[104] I. Boxx, C. Heeger, R. Gordon, B. Böhm, M. Aigner, A. Dreizler, W. Meier, „Simultaneous three-component PIV/OH-PLIF measurements of a turbulent lifted, C_3H_8-Argon jet diffusion flame at 1.5 kHz repetition rate“, *Proc. Combust. Inst.* **2009**, *32*, 905–912.

[105] F. Diez, L. P. Bernal, G. M. Faeth, „PLIF and PIV measurements of the self-preserving structure of steady round buoyant turbulent plumes in crossflow“, *Int. J. Heat Fluid Flow* **2005**, *26*, 873–882.

[106] C. P. Fenimore, „Formation of nitric oxide in premixed hydrocarbon flames“, *Symp. (Int.) Combust. [Proc.]* **1971**, *13*, 373–380.

[107] M. Aldén, J. Bood, Z. Li, M. Richter, „Visualization and understanding of combustion processes using spatially and temporally resolved laser diagnostic techniques“, *Proc. Combust. Inst.* **2011**, *33*, 69–97.

[108] J. Kiefer, Z. Li, J. Zetterberg, M. Livin, M. Aldén, „Simultaneous laser-induced fluorescence and sub-Doppler polarization spectroscopy of the CH radical“, *Opt. Commun.* **2007**, *270*, 347–352.

[109] C. Moreau, E. Therssen, P. Desgroux, J. F. Pauwels, A. Chapput, M. Barj, „Quantitative measurements of the CH radical in sooting diffusion flames at atmospheric pressure“, *Appl. Phys. B* **2003**, *76*, 597–602.

[110] C. M. Vagelopoulos, J. H. Frank, „An experimental and numerical study on the adequacy of CH as a flame marker in premixed methane flames“, *Proc. Combust. Inst.* **2005**, *30*, 241–249.

[111] K. A. Watson, K. M. Lyons, C. D. Carter, J. M. Donbar, „Simultaneous two-shot CH planar laser-induced fluorescence and particle image velocimetry measurements in lifted CH_4/air diffusion flames“, *Proc. Combust. Inst.* **2002**, *29*, 1905–1912.

[112] R. Bombach, B. Käppeli, „Simultaneous visualisation of transient species in flames by planar-laser-induced fluorescence using a single laser system“, *Appl. Phys. B* **1999**, *68*, 251–255.

[113] P. H. Paul, J. E. Dec, „Imaging of reaction zones in hydrocarbon–air flames by use of planar laser-induced fluorescence of CH“, *Opt. Lett.* **1994**, *19*, 998–1000.

[114] M. M. Mansour, N. Peters, Y.-C. Chen, „Investigation of scalar mixing in the thin reaction zones regime using a simultaneous CH-LIF/Rayleigh laser technique“, *Symp. (Int.) Combust. [Proc.]* **1998**, *27*, 767–773.

[115] Z. S. Li, J. Kiefer, J. Zetterberg, M. Livinz, A. Leipertz, X. S. Bai, M. Aldén, „Development of improved PLIF CH detection using an Alexandrite laser for single-shot investigation of turbulent and lean flames“, *Proc. Combust. Inst.* **2007**, *31*, 727–735.

[116] P. H. Paul, H. N. Najm, „Planar laser-induced fluorescence imaging of flame heat release rate“, *Symp. (Int.) Combust. [Proc.]* **1998**, *27*, 43–50.

[117] H. N. Najm, P. H. Paul, C. J. Mueller, P. S. Wyckoff, „On the adequacy of certain experimental observables as measurements of flame burning rate“, *Combust. Flame* **1998**, *113*, 312–332.

[118] A. P. Alshuller, J. J. Bulifani, „Photochemical aspects of air pollution: A review“, *Environ. Sci. Tech* **1971**, *5*, 39–64.

[119] M. Musculus, R. Reitz, C. Genzale, „Effects of piston bowl geometry on mixture development and late-injection low-temperature combustion in a heavy-duty diesel engine“, *SAE Int. J. Engines* **2009**, *1*, 913–937.

[120] S. Böckle, J. Kazenwadel, T. Kunzelmann, D.-I. Shin, C. Schulz, J. Wolfrum, „Simultaneous single-shot laser-based imaging of formaldehyde, OH and temperature in turbulent flames“, *Proc. Combust. Inst.* **2000**, *28*, 279–286.

[121] A. Burkert, W. Paa, M. Reimert, K. Klinkov, C. Eigenbrod, „Formaldehyde LIF detection with background subtraction around single igniting GTL diesel droplets“, *Fuel* **2013**, *111*, 384–392.

[122] A. J. Donkerbroek, A. P. van Vliet, L. M. T. Somers, P. J. M. Frijters, R. J. H. Klein-Douwel, N. J. Dam, W. L. Meerts, J. J. ter Meulen, „Time- and space-resolved quantitative LIF measurements of formaldehyde in a heavy-duty diesel engine“, *Combust. Flame* **2010**, *157*, 155–166.

[123] F. Hildenbrand, C. Schulz, J. Wolfrum, F. Keller, E. Wagner, „Laser diagnostic analysis of NO formation in a direct injection diesel engine with pump-line-nozzle and common rail injection systems“, *Proc. Combust. Inst.* **2000**, *28*, 1137–1143.

[124] K. Verbiezen, R. Klein-Douwel, A. van Vliet, A. Donkerbroek, W. Meerts, N. Dam, J. ter Meulen, „Attenuation corrections for in-cylinder NO LIF measurements in a heavy-duty Diesel engine“, *Appl. Phys. B* **2006**, *83*, 155–166.

[125] J. Dec, R. Canaan, „PLIF Imaging of NO Formation in a DI diesel engine“, *SAE Technical Paper* **1998**, *980147*.

[126] M. Haudiquert, A. Cessou, D. Stepowski, A. Coppalle, „OH and soot concentration measurements in a high-temperature laminar diffusion flame“, *Combust. Flame* **1997**, *111*, 338–349.

[127] A. T. Hartlieb, B. Atakan, K. Kohse-Höinghaus, „Temperature measurement in fuel-rich non-sooting low-pressure hydrocarbon flames“, *Appl. Phys. B* **2000**, *70*, 435–445.

[128] M. Tamura, J. Luque, J. E. Harrington, P. A. Berg, G. P. Smith, J. B. Jeffries, D. R. Crosley, „Laser-induced fluorescence of seeded nitric oxide as a flame thermometer“, *Appl. Phys. B* **1998**, *66*, 503–510.

[129] K. Hayashida, K. Amagai, M. Arai, „LIF thermometry in sooty flames using NO $D^2\Sigma^+ \leftarrow X^2\Pi$ (0,1) and OH $A^2\Sigma^+ \leftarrow X^2\Pi$ (3,0) bands“, *Energy* **2005**, *30*, 497–508.

[130] B. Atakan, A. T. Hartlieb, „Laser diagnostics of NO reburning in fuel-rich propene flames“, *Appl. Phys. B* **2000**, *71*, 697–702.

[131] J. Nygren, J. Engström, J. Walewski, C. F. Kaminski, M. Aldén, „Applications and evaluation of two-line atomic LIF thermometry in sooting combustion environments“, *Meas. Sci. Technol.* **2001**, *12*, 1294–1303.

[132] S. Einecke, C. Schulz, V. Sick, „Measurement of temperature, fuel concentration and equivalence ratio fields using tracer LIF in IC engine combustion“, *Appl. Phys. B* **2000**, *71*, 717–723.

[133] J. E. Dec, J. O. Keller, „High speed thermometry using two-line atomic fluorescence“, *Symp. (Int.) Combust. [Proc.]* **1986**, *21*, 1737–1745.

[134] H.-O. Berten, K. Kleinermanns, „Determination of spatial temperature distributions in a laminar premixed ethylene/air flame by laser-induced atomic fluorescence“, *Appl. Phys. B* **1995**, *61*, 605–610.

[135] P. R. Medwell, Q. N. Chan, P. A. Kalt, Z. T. Alwahabi, B. B. Dally, G. J. Nathan, „Development of temperature imaging using two-line atomic fluorescence“, *Appl. Opt.* **2009**, *48*, 1237–1248.

[136] B. Cheung, R. Hanson, „CW laser-induced fluorescence of toluene for time-resolved imaging of gaseous flows“, *Appl. Phys. B* **2010**, *98*, 581–591.

[137] C. Schulz, V. Sick, „Tracer-LIF diagnostics: quantitative measurement of fuel concentration, temperature and fuel/air ratio in practical combustion systems“, *Prog. Energy Combust. Sci.* **2005**, *31*, 75–121.

[138] J. D. Koch, R. K. Hanson, „Temperature and excitation wavelength dependencies of 3-pentanone absorption and fluorescence for PLIF applications“, *Appl. Phys. B* **2003**, *76*, 319–324.

[139] J. D. Koch, J. Gronkib, R. K. Hanson, „Measurements of near-UV absorption spectra of acetone and 3-pentanone at high temperatures“, *J. Quant. Spectrosc. Radiat. Transfer* **2008**, *109*, 2037–2044.

[140] D. Galley, S. Ducruix, F. Lacas, D. Veyante, „Mixing and stabilization study of a partially premixed swirling flame using laser induced fluorescence“, *Combust. Flame* **2011**, *158*, 155–171.

[141] M. Cundy, P. Trunk, A. Dreizler, V. Sick, „Gas-phase toluene LIF temperature imaging near surfaces at 10 kHz“, *Exp. Fluids* **2011**, *51*, 1169–1176.

[142] M. C. Thurber, F. Grisch, B. J. Kirby, M. Votsmeier, R. K. Hanson, „Measurements and modeling of acetone laser-induced fluorescence with implications for temperature-imaging diagnostics“, *Appl. Opt.* **1998**, *37*, 4693–4978.

[143] Y. Nakamura, S. Manome, H. Yamashita in 13th Int. Symp. on Applications of Laser Techniques to Fluid Mechanics, **2006**.

[144] R. A. Bryant, J. M. Donbar, J. F. Driscoll, „Acetone laser induced fluorescence for low pressure/low temperature flow visualization“, *Exp. Fluids* **2000**, *28*, 471–476.

[145] N. T. Clemens, P. H. Paul, „Effects of heat release on the near field flow structure of hydrogen jet diffusion flames“, *Combust. Flame* **1995**, *102*, 271–284.

[146] J. Trost, M. Löffler, L. Zigan, A. Leipertz, „Simultaneous Quantitative Acetone-PLIF Measurements for Determination of Temperature and Gas Composition Fields in an IC-Engine“, *Physics Procedia* **2010**, *5*, 689–696.

[147] S. Nakaya, M. Kasahara, M. Tsue, M. Kono, „Velocity measurements of reactive and non-reactive flows by NO-LIF method using NO_2 photodissociation“, *Heat Trans. Asian Res.* **2005**, *34*, 40–52.

[148] R. K. Hanson, J. M. Seitzman, P. H. Paul, „Planar laser-fluorescence imaging of combustion gases“, *Appl. Phys. B* **1990**, *50*, 441–454.

[149] C. Brossard, J. C. Monnier, P. Barricau, F. X. Vandernoot, Y. L. Sant, F. Champagnat, G. L. Besnerais, „Principles and applications of particle image velocimetry“, *Aerospace Lab* **2009**, *1*, 1–11.

[150] M. Raffel, C. E. Willert, J. Kompenhans, *Particle Image Velocimetry*, (Eds.: R. J. Adrian, M. Gharib, W. Merzkirch, D. Rockwell, J. H. Whitelaw), Springer-Verlag Berlin Heidelberg, **2007**.

[151] A. K. Prasad, „Particle Image Velocimetry“, *Curr. Sci.* **2000**, *79*, 51–60.

[152] L.-S. Fan, C. Zhu, *The Handbook of Fluid Dynamics*, (Ed.: R. W. Johnson), Springer Berlin Heidelberg and CRC Press Boca Raton, **1998**.

[153] J. Feng, D. D. Joseph, „The unsteady motion of solid bodies in creeping flows“, *J. Fluid. Mech.* **1995**, *303*, 83–102.

[154] R. Mei, „Velocity fidelity of flow tracer particles“, *Exp. Fluids* **1996**, *22*, 1–13.

[155] A. Melling, „Tracer particles and seeding for particle image velocimetry“, *Meas. Sci. Technol.* **1997**, *8*, 1406–1416.

[156] C. Kähler, B. Sammler, J. Kopenhans, „Generation and control of tracer particles for optical flow investigations in air“, *Exp. Fluids* **2002**, *33*, 736–742.

[157] R. D. Keane, R. J. Adrian, „Theory of cross-correlation analysis of PIV images“, *Appl. Sci. Res.* **1992**, *49*, 191–215.

[158] E. J. Stamhuis, „Basics and principles of particle image velocimetry (PIV) for mapping biogenic and biologically relevant flows“, *Aquatic Ecol.* **2006**, *40*, 463–479.

[159] H. T. Huang, H. E. Fiedler, J. J. Wang, „Limitation and improvement of PIV, part I: Limitation of conventional techniques due to deformation of particle image patterns“, *Exp. Fluids* **1993**, *15*, 168–174.

[160] H. T. Huang, H. E. Fiedler, J. J. Wang, „Limitation and improvement of PIV, part II: Particle image distortion, a novel technique“, *Exp. Fluids* **1993**, *15*, 263–273.

[161] W. Thielicke, PhD thesis, Rijksuniversiteit Groningen, **2014**.

[162] W. Thielicke, E. J. Stamhuis, „PIVlab - Towards user-friendly, affordable and accurate digital particle image velocimetry in MATLAB“, *Journal of Open Research Software* **2014**, *2:e30*.

[163] H. Huang, D. Dabiri, M. Gharib, „On errors of digital particle image velocimetry“, *Meas. Sci. Technol.* **1997**, *8*, 1427–1440.

[164] J. Soria, „An investigation of the near wake of a circular cylinder using a video-based digital cross-correlation particle image velocimetry technique“, *Exp. Therm Fluid Sci.* **1996**, *12*, 221–233.

[165] M. P. Wernet in Planar Optical Measurement Methods for Gas Turbine Components, RT0 Lecture Series 217, **1999**, RTO–EN–6, paper 2.

[166] T. Roesgen, „Optimal subpixel interpolation in particle image velocimetry“, *Exp. Fluids* **2003**, *35*, 252–256.

[167] M. Stanislas, K. Okamoto, C. Kähler, „Main results of the First International PIV Challenge“, *Meas. Sci. Technol.* **2003**, *14*, R63–R89.

[168] J. Chen, J. Katz, „Elimination of peak-locking error in PIV analysis using the correlation mapping method“, *Meas. Sci. Technol.* **2005**, *16*, 1605–1618.

[169] K. T. Christensen, „The influence of peak-locking errors on turbulence statistics computed from PIV ensembles“, *Exp. Fluids* **2004**, *36*, 484–497.

[170] J. Westerweel, „Fundamentals of digital particle image velocimetry“, *Meas. Sci. Technol.* **1997**, *8*, 1379–1392.

[171] B. Lecordier, D. Demare, L. M. J. Vervisch, J. Réveillon, M. Trinité, „Estimation of the accuracy of PIV treatments for turbulent flow studies by direct numerical simulation of multi-phase flow“, *Meas. Sci. Technol.* **2001**, *12*, 1382–1391.

[172] M. Fischer, M. Wiegel, T. Herberg, G. Heidrich, „Flow field decomposition applied to experimental data obtained for a transitional boundary layer“, *Appl. Sci. Res.* **1996**, *56*, 103–112.

[173] R. J. Adrian, K. T. Christensen, Z.-C. Liu, „Analysis and interpretation of instantaneous turbulent velocity fields“, *Exp. Fluids* **2000**, *29*, 275–290.

[174] A. Agrawal, A. K. Prasad, „Properties of vortices in the self-similar turbulent jet“, *Exp. Fluids* **2002**, *33*, 565–577.

[175] A. Agrawal, A. K. Prasad, „Measurements within vortex cores in a turbulent jet“, *J. Fluids Eng.* **2003**, *561*, 561–568.

[176] Z.-C. Liu, R. J. Adrian, T. J. Hanratty, „Reynolds number similarity of orthogonal decomposition of the outer layer of tubulent wall flow“, *Phys. Fluids* **1994**, *6*, 2815–2819.

[177] R. B. Montgomery, „Viscosity and thermal conductivity of air and diffusivity of water vapor in air“, *J. Atmos. Sci.* **1947**, *4*, 193–196.

[178] Rasband, W.S., ImageJ, U. S. National Institutes of Health, Bethesda, Maryland, USA, http://imagej.nih.gov/ij/, **1997-2015**.

[179] E. Loth, „Numerical approaches for motion of dispersed particles, droplets and bubbles“, *Prog. Energy Combust. Sci.* **2000**, *26*, 161–223.

[180] H. Xu, E. Bodenschatz, „Motion of inertial particles with size larger than Kolmogorov scale in turbulent flows“, *Physica D.* **2008**, *237*, 2095–2100.

[181] G. V. Barbosa-Cánovas, E. Ortega-Rivas, P. Juliano, H. Yan, *Food Powders*, Springer US, **2005**.

[182] *Springer Handbook of Experimental Fluid Mechanics*, (Eds.: C. Tropea, A. L. Yarin, J. F. Foss), Springer-Verlag Berlin Heidelberg, **2007**.

[183] S. Ahmed, J. Hart, J. Nikolov, C. Solnordal, W. Yang, J. Naser, „The effect of jet velocity ratio on aerodynamics of a rectangular slot-burner in the presence of cross-flow“, *Exp. Therm Fluid Sci.* **2007**, *32*, 362–374.

[184] D. Janßen, J. Lohrengel, "Investigation and development of a method for the measurement of the emissivity of glass", final report on contract 1497/1/0/102/85-1-BCR-D(30), bcr information, EUR 13 487 EN, Luxembourg, Office for Official Publications of the European Communities **1991**.

[185] E. T. Kwor, S. Matteï, „Emissivity measurements for Nextel Velvet Coating 811-21 between -36 °C and 82 °C“, *High Temp. - High Pressures* **2001**, *33*, 551–556.

[186] S. M. Pizer, E. P. Amburn, J. D. Austin, R. Cromartie, A. Geselowitz, T. Greer, B. ter Haar Romeny, J. B. Zimmermann, K. Zuiderveld, „Adaptive histogram equalization and its variations“, *Comput.Gr.Image Process.* **1987**, *39*, 355–368.

[187] U. Shavit, R. J. Lowe, J. V. Steinbuck, „Intensity capping: a simple method to improve cross-correlation PIV results“, *Exp. Fluids* **2007**, *42*, 225–240.

[188] F. Scarano, „Iterative image deformation methods in PIV“, *Meas. Sci. Technol.* **2002**, *13*, R1–R19.

[189] J. Westerweel, F. Scarano, „Universal outlier detection for PIV data“, *Exp. Fluids* **2005**, *39*, 1096–1100.

[190] J. D'Errico, inpaint_nans (http://www.mathworks.com/matlabcentral/fileexchange/4551-inpaint-nans), MATLAB Central File Exchange. Retrieved August 13, **2012**.

[191] D. Garcia, „Robust smoothing of gridded data in one and higher dimensions with missing values“, *Comput. Stat. Data Anal.* **2010**, *54*, 1167–1178.

[192] D. Garcia, „A fast all-in-one method for automated post-processing of PIV data“, *Exp. Fluids* **2011**, *50*, 1247–1259.

[193] Y. Li, H. Zhao, Z. Peng, N. Ladommatos, „Particle image velocimetry measurement of in-cylinder flow in internal combustion engines-experiment and flow structure analysis“, *Proc. Inst. Mech. Eng. D J. Automob. Eng.* **2002**, *216*, 65–81.

[194] A. Okubo, „Horizontal dipersion of floatable particles in the vicinity of velocity singularities such as convergences“, *Deep-Sea Res.: Oceanogr. Abstr.* **1970**, *17*, 445–454.

[195] A. Okubo, C. C. Ebbesmeyer, „Determination of vorticity, divergence and deformation rates from analysis of drogue observations“, *Deep-Sea Res.: Oceanogr. Abstr.* **1976**, *23*, 349–352.

[196] *Handbook of Loss Prevention Engineering, Volume 1*, (Ed.: J. M. Haight), John Wiley & Sons, **2013**.

[197] *GPSA Engineering Data Book*, Gas Processors Suppliers Association, **2004**.

[198] M. Mitu, V. Brinzea, A. Musuc, D. Razus, D. Oancea, „Deflagration parameters of propane-air mixtures in a closed cylindrical vessel“, *U.P.B. Sci. Bull. Series B* **2011**, *73*, 17–26.

[199] A. S. Huzayyin, H. A. Moneib, M. S. Shehatta, A. M. A. Attia, „Laminar burning velocities and explosion index of LPG-air and propane-air mixtures“, *Fuel* **2008**, *87*, 39–57.

[200] D. Razus, C. Movileanu, D. Oancea, „The rate of pressure rise of gaseous propylene-air explosions in spherical and cylindrical enclosures“, *J. Hazard. Mater.* **2007**, *A139*, 1–8.

[201] D. Razus, V. Brinzea, M. Mitu, C. Movileanu, D. Oancea, „Temperature and pressure influence on maximum rates of pressure rise during explosions of propane-air mixtures in a spherical vessel“, *J. Hazard. Mater.* **2011**, *190*, 891–896.

[202] R. Dobashi, „Experimental study on gas explosion behavior in enclosure“, *J. Loss Prev. Process Ind.* **1997**, *10*, 83–89.

[203] D. Razus, D. Oancea, C. Movileanu, „Burning velocity and evaluation from pressure evolution during the early stage of closed-vessel explosions“, *J. Loss Prev. Process Ind.* **2006**, *19*, 334–342.

[204] Y. K. Pu, J. Mazurkiewicz, J. Jarosinski, C. W. Kauffman, „Comparative study of the influence of obstacles on the propagation of dust and gas flames“, *Symp. (Int.) Combust. [Proc.]* **1988**, *22*, 1789–1797.

[205] *Combustion Phenomena: Selected Mechanisms of Flame Formation, Propagation, and Extinction*, (Eds.: J. Jarosinski, B. Veyssiere), CRC Press Florida, **2009**.

[206] *The Modes of Gaseous Combustion*, (Ed.: N. M. Rubtsov), Springer, **2015**.

[207] B. Fan, Z. Ying, Z. Chen, J. Ye, „Observations of flame behavior during flame-obstacle interaction“, *Process Saf. Prog.* **2008**, *27*, 66–71.

[208] R. K. Kumar, H. Tamm, W. C. Harrison, „Combustion of hydrogen at high concentrations. Including the effect of obstacles“, *Combust. Sci. Technol.* **1983**, *35*, 175–186.

[209] R. G. Abdel-Gayed, D. Bradley, M. N. Hamid, M. Lawes, „Lewis number effect on turbulent burning velocity“, *Symp. (Int.) Combust. [Proc.]* **1984**, *20*, 505–512.

[210] V. P. Karpov, E. S. Severin, „Turbulent burn-up rates of propane-air flames determined in a bomb with agitators“, *Combust. Explos. Shock Waves* **1978**, *14*, 158–63.

[211] S. S. Shy, W. J. Lin, J. C. Wei, „An experimental correlation of turbulent burning velocities for premixed turbulent methane-air combustion“, *Proc. R. Soc. Lond. A* **2000**, *456*, 1997–2019.

[212] G. Harris, „The effect of vessel size and degree of turbulence on gas phase explosion pressures in closed vessels“, *Combust. Flame* **1967**, *11*, 17–25.

[213] M. V. Blanc, P. G. Guest, G. von Elbe, B. Lewis, „III. Minimum ignition energies and quenching distances of mixtures of hydrocarbons and ether with oxygen and inert gases“, *Symposium on Combustion and Flame and Explosion Phenomena* **1948**, *3*, 363–367.

[214] C. R. Ferguson, J. C. Keck, „On laminar flame quenching and its applications to spark ignition engines“, *Combust. Flame* **1977**, *28*, 197–205.

[215] D. R. Ballal, A. H. Lefebvre, „Flame quenching in turbulent flowing gaseous mixtures“, *Symp. (Int.) Combust. [Proc.]* **1977**, *16*, 1689–1698.

[216] D. Oancea, D. Razus, F. Chirila, N. I. Ionescu, „Pressure and temperature dependence of the quenching distance for propylene-air mixtures“, *Revue Roumaine de Chimie* **1997**, *42*, 571–578.

[217] S. G. Davis, C. K. Law, „Determination of and fuel structure effects on laminar flame speeds of C_1 to C_8 hydrocarbons“, *Comb. Sci. Tech.* **1998**, *140*, 427–449.

[218] H. Wang, X. You, A. V. Joshi, S. G. Davis, A. Laskin, F. Egolfopoulos, C. K. Law, USC Mech Version II. High-Temperature Combustion Reaction Model of H2/CO/C1-C4 Compounds, http://ignis.usc.edu/USC_Mech_II.htm, **May 2007**.

[219] P. Carlotti, P. Drobinski, „Length scales in wall-bounded high-Reynolds-number turbulence“, *J. Fluid Mech.* **2004**, *516*, 239–264.

[220] P. L. O'Neill, D. Nicolaides, D. Honnery, J. Soira in 15th Australasian Fluid Mechanics Conference, **2004**.

[221] H. Belmabrouk, M. Michard, „Analysis of the swirl effect on turbulent length scales in an ICE cylinder by two-point LDV“, *Int. J. Heat Fluid Flow* **2001**, *22*, 417–423.

[222] T. Ishima, T. Obokata, T. Nomura, Y. Takahashi in 12th Int. Symp. on Applications of Laser Techniques to Fluid Mechanics, **2002**.

[223] G. G. Katul, M. B. Parlange, „Analysis of Land Surface Heat Fluxes using the orthonormal wavelet approach“, *Water Resour. Res.* **1995**, *31*, 2743–2749.

[224] V. Sick, M. R. Hartman, V. S. Arpaci, R. W. Anderson, „Turbulent Scales in a Fan-stirred Combustion Bomb“, *Combust. Flame* **2001**, *127*, 2119–2123.

[225] T. D. Fansler, E. G. Groff, „Turbulence Characteristics of a Fan-Stirred Combustion Vessel“, *Combust. Flame* **1990**, *80*, 350–354.

[226] B. Galmiche, N. Mazellier, F. Haler, F. Foucher, „Turbulence characterization of a high-pressure high-temperature fan-stirred combustion vessel using LDV, PIV and TR-PIV measurements“, *Exp. Fluids* **2014**, *55*, 1636–1656.

[227] L.-K. Tseng, M. A. Ismail, G. M. Faeth, „Laminar Burning Velocities and Markstein Numbers of Hydrocarbon/Air Flames“, *Combust. Flame* **1993**, *95*, 410–426.

[228] F. J. Weinberg, „The Thickness of Laminar Flames in Pre-Mixed Reactants: Optical Considerations“, *Proc. R. Soc. Lond. A* **1957**, *243*, 107–118.

[229] A. K. Prasad, „Stereoscopic particle image velocimetry“, *Exp. Fluids* **2000**, *29*, 103–116.

[230] B. Wieneke, „Stereo-PIV using self-calibration on particle images“, *Exp. Fluids* **2005**, *39*, 267–280.

[231] D. Michaelis, B. Wieneke in 14th Int. Symp. on Applications of Laser Techniques to Fluid Mechanics, **2008**.

Appendix

6

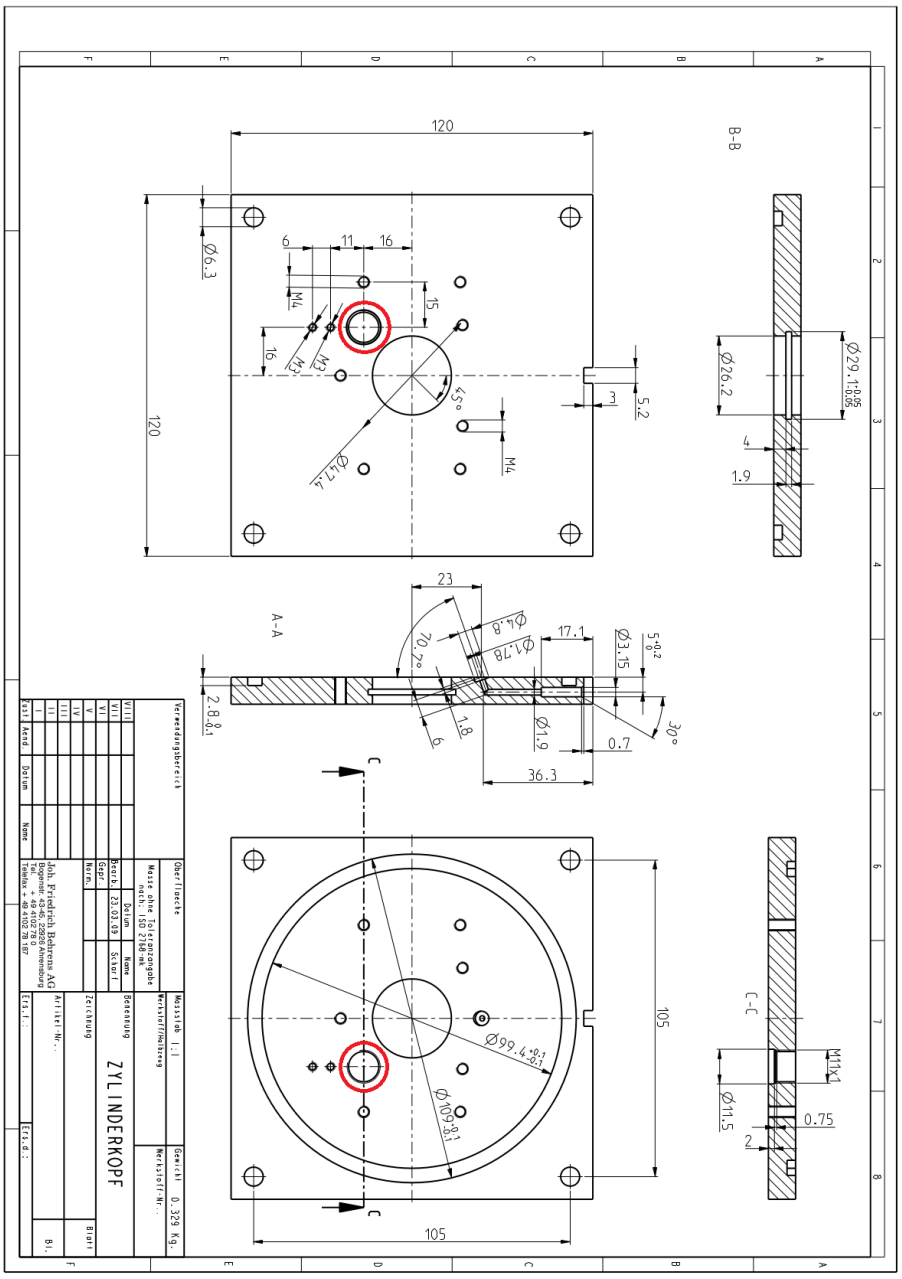

Figure 6.1: Schematic drawing of the cylinder head used for the pressure measurements. The position of the spark is marked by the red square.

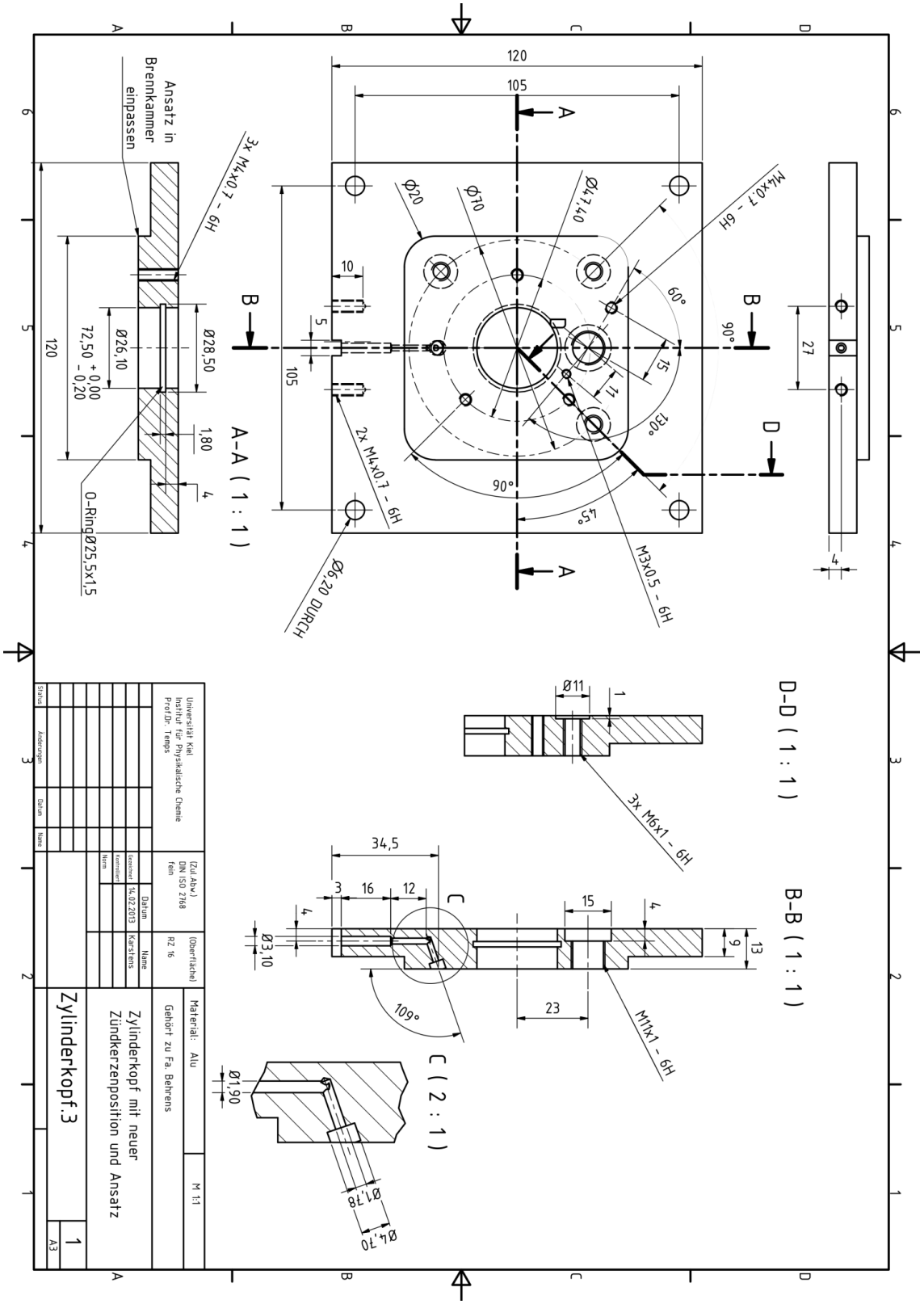

Figure 6.2: Schematic drawing of the cylinder head used for LIF and PIV measurements.

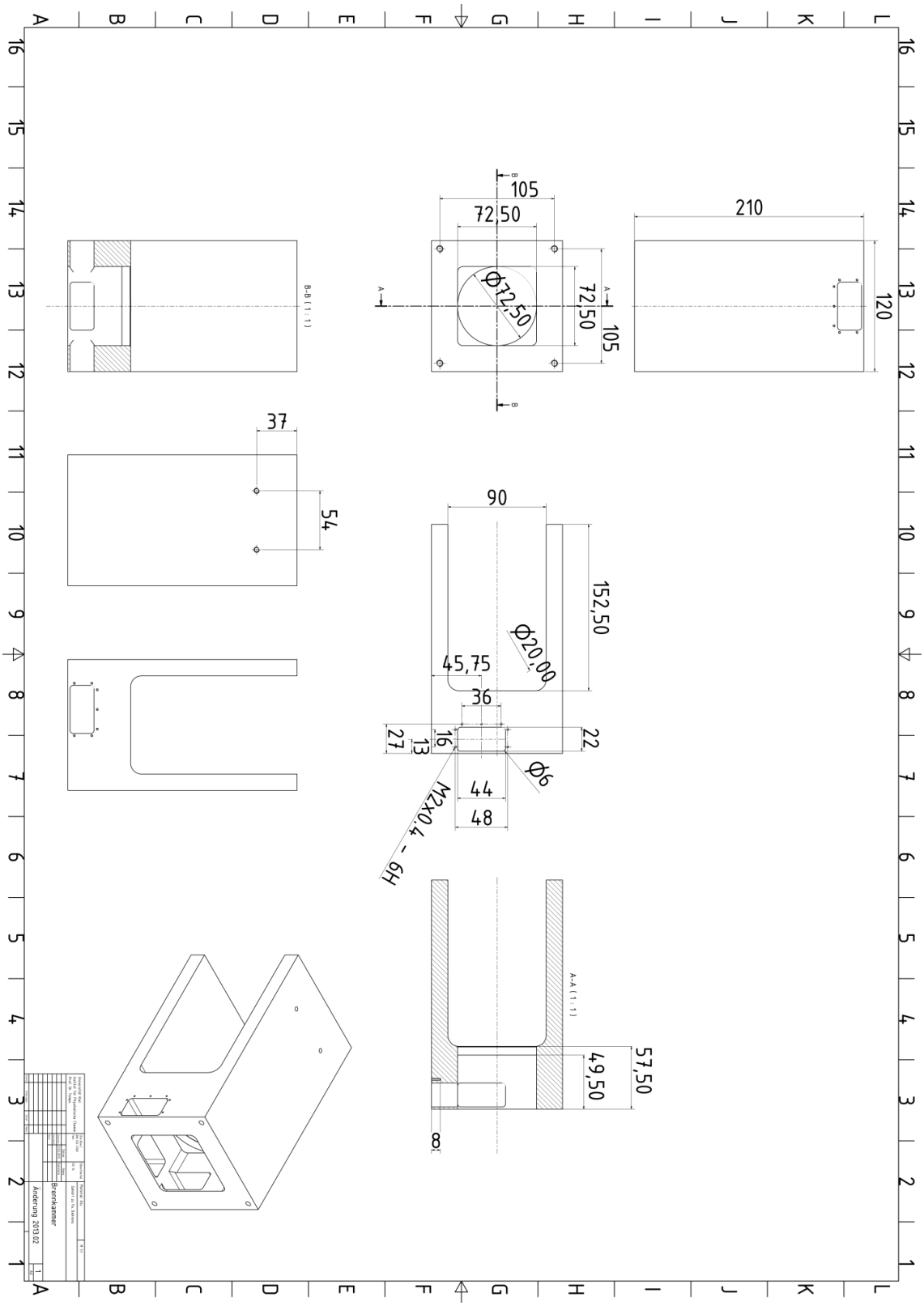

Figure 6.3: Schematic drawing of the chamber used for the PIV and LIF measurements.

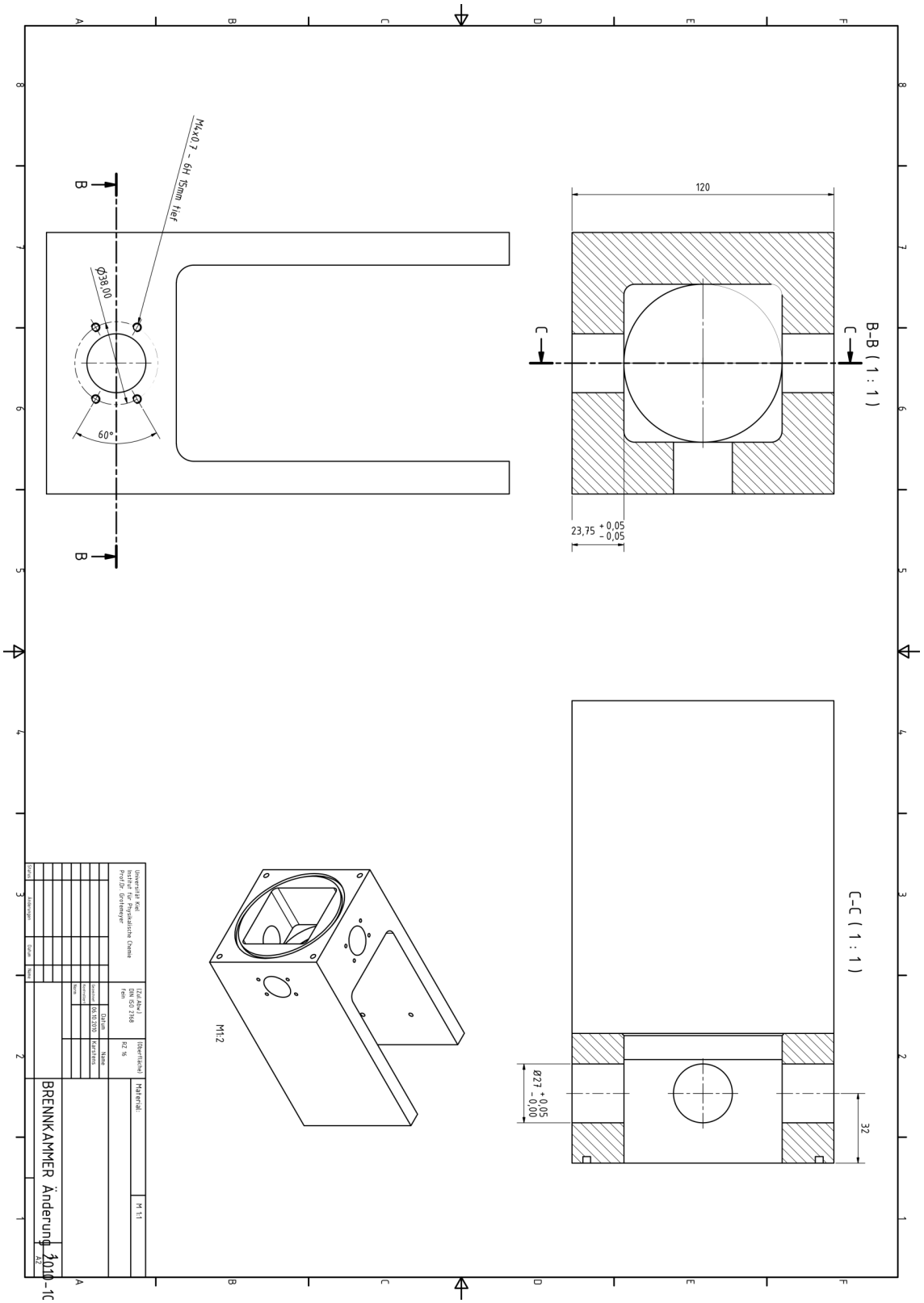

Figure 6.4: Schematic drawing of the chamber used for the pressure measurements.

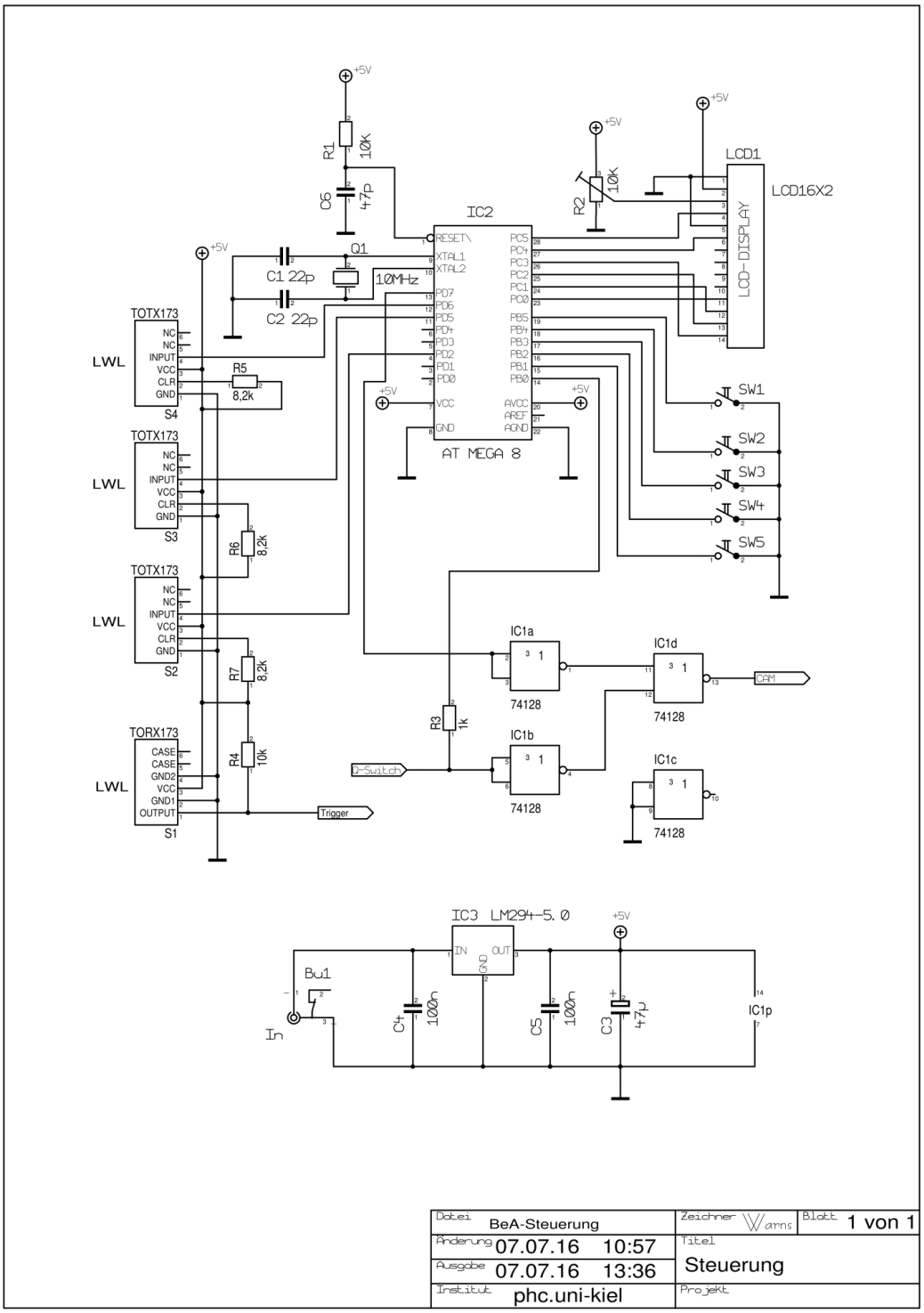

Figure 6.5: Circuit diagram of the control electronics inside the trigger box.

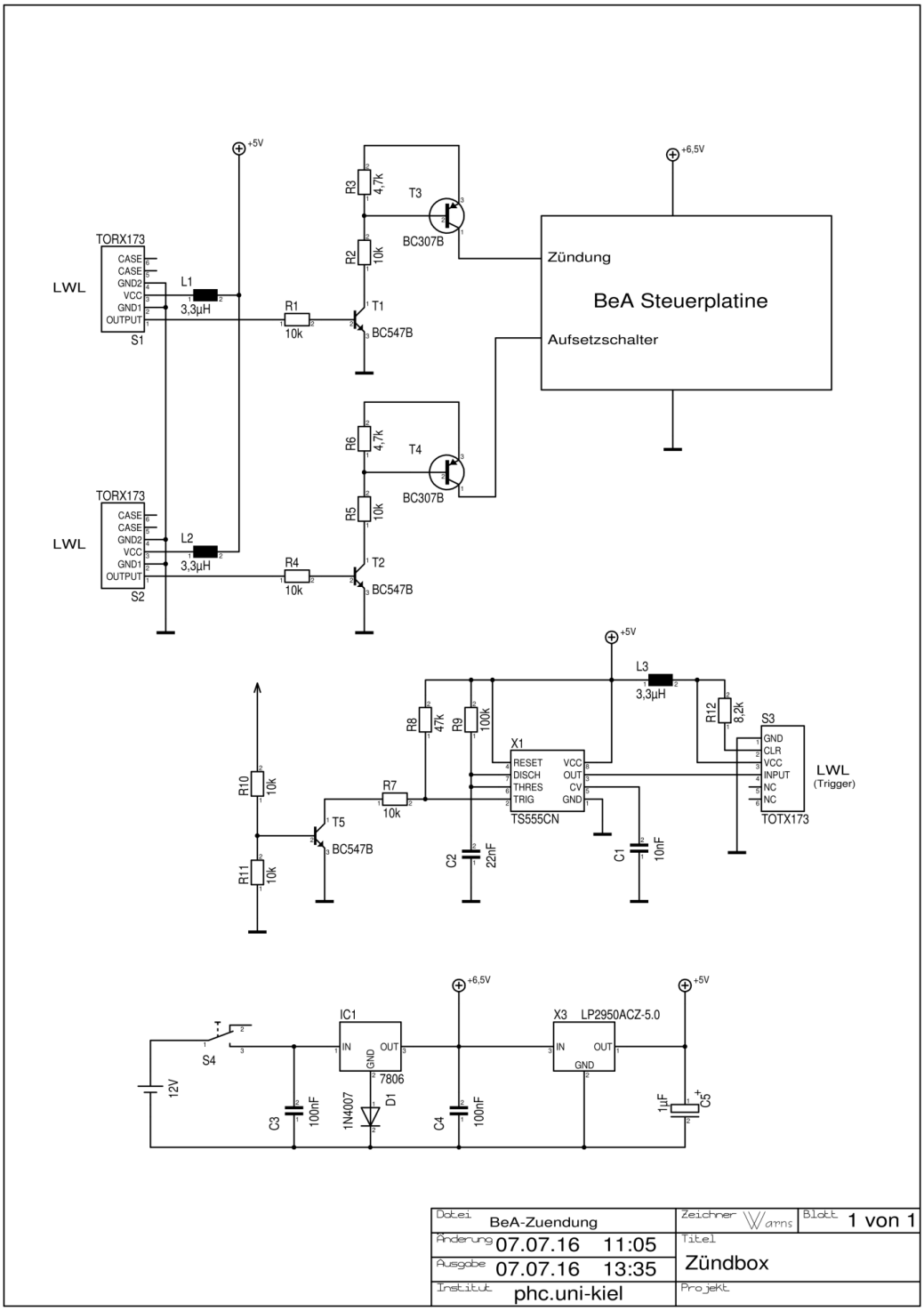

Figure 6.6: Circuit diagram of the ignition electronics based on the original electronics from the nail gun (*BeA Steuerplatine*).

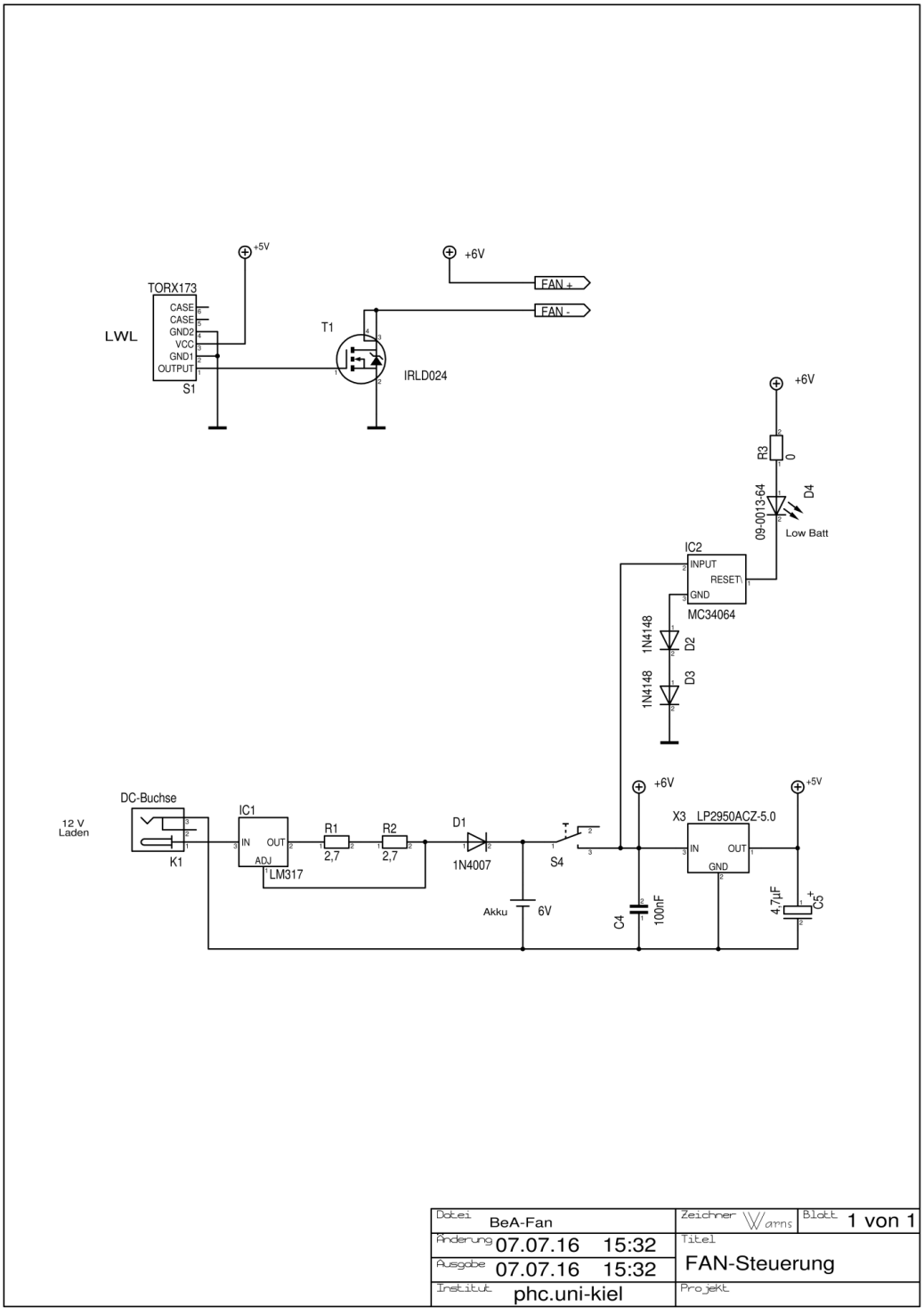

Figure 6.7: Circuit diagram of the fan electronics.

Danksagung

Und auch wenn in der Erklärung steht, dass diese gesamte Arbeit meine Eigene ist, möchte ich dennoch einigen Menschen für die wahnwitzigen letzten sechs Jahre danken.

Als erstes möchte ich mich bei meinem Doktorvater Herrn Prof. Friedrich Temps bedanken, für die Möglichkeit, auf einem Thema zu arbeiten, das noch viel breitgefächerter war, als ich es mir am Anfang vorgestellt habe, für die damit verbundenen vielfältigen Freiräume, die Geduld der letzten Jahre und die Unterstützung.

Joachim Bauer und der Joh. Friedrich Behrens AG danke ich für die Zusammenarbeit, Finanzierung und Bereitstellung des Motors.

Herrn Prof. Sebastian Kaiser danke ich für die zwar kurzen, aber dafür umso fruchtbareren Einblicke in die Feinheiten der Particle Image Velocimetry.

Ein großer Dank geht auch an Dr. Joachim Gripp für die Hilfe bei jeder Laborkleinigkeit und jedem Rumzicken des Lasers, sowie dem Galgenhumor, wenn mal wieder irgendwas nicht so funktionierte wie es sollte.

Ebenfalls bedanken (und eventuell auch ein wenig entschuldigen) möchte ich mich bei unser Institutswerkstatt, Timo Görgens, Frank Herzog, Frank Laasch, Andreas Sievers, Olaf Wendt und Klaus-Dieter Will. Ob es nun um „Könnt ihr das Loch hier ausbauen und da wieder einsetzen?“, „Ich hab wieder ’ne Schraube abgebrochen...“ oder um irrsinnige Fräsarbeiten ging, am Ende haben wir dann doch alle gelacht. Gleiches gilt auch für Michael Karstens, der oft für die irren Ideen verantwortlich war.

Ebenfalls danke ich unserer Elektronikwerkstatt, Kerstin Stolschewski und Klaus Warns, für die Beseitigung jeglicher Spannungsabfälle und die Hilfe bei jedem noch so dummen „Ich brauch was, da muss Strom rauskommen und idealer Weise auch ’n Rechteckpuls“.

Gemäß der alten Tradition danke ich auch Alexander Thrun für die Hilfe bei sämtlichen Latexproblemen. Und meinem einzigen Matlabbuddy Ribbi für jede ausufernde Diskussion und das gegenseitge (Un)Verständnis.

Danke auch an unsere Sekretärinnen Ursula, Tanja und Sonja, vor allem für die Hilfe bei allen großen und kleinen Problemen bezüglich des echten Lebens fernab der Forschung.

Danke an alle Opfer der FL3002-Laser, für den seelischen Beistand und die Hilfe bei jedem Laserproblem und danke an alle Korrekturleser, ich hoffe, ihr habt dabei einiges dazugelernt!

Gruß und Kuss an mein altes Büro in der LMS6 (Anja + Alex, coolstes Büro der Welt, besser als Katharina + Julia!) und den Pumakäfig in der MES1, Grüßchen und Küsschen an den Rest vom Arbeitskreis, ihr seid schon ganz ok, nur total unordentlich. Räumt doch auch mal den Geschirrspüler aus.

Gerno Mousepolice danke dafür, dass ihm eh alles egal ist. Milo Aukerman danke ich für die Erkenntnis, das Haus in der Vorstadt haben zu wollen und trotzdem nicht erwachsen zu werden. Allen meinen Freunden danke für alles andere, wisst schon.

Und vor allem meiner Familie für Alles und noch so viel mehr. Danke!